

UNIVERSIDADE DE SÃO PAULO  
INSTITUTO DE QUÍMICA DE SÃO CARLOS

Vivianne Karina Ocampo Restrepo

***Ab Initio* Investigation of the Adsorption and Reduction of  
CO<sub>2</sub> on 3d Transition Metals Finite-size Particles**

São Carlos

2022

**Vivianne Karina Ocampo Restrepo**

***Ab Initio* Investigation of the Adsorption and Reduction of  
CO<sub>2</sub> on 3d Transition Metals Finite-size Particles**

Thesis presented to the Graduate Program  
in Chemistry at the Instituto de Química de  
São Carlos, Universidade de São Paulo, to  
obtain the degree of Doctor in Science.

Concentration area: Physical Chemistry

Advisor: Prof. Dr. Juarez Lopes Ferreira da  
Silva

**Exemplar revisado**

**O exemplar original encontra-se em acervo reservado na Biblioteca do  
IQSC-USP**

**São Carlos**

**2022**

Autorizo a reprodução e divulgação total ou parcial deste trabalho, por qualquer meio convencional ou eletrônico para fins de estudo e pesquisa, desde que citada a fonte.

**Assinatura:**

**Data:**

*Ficha Catalográfica elaborada pela Seção de Referência e Atendimento ao Usuário do SBI/IQSC*

Ocampo Restrepo, Vivianne Karina

Ab Initio investigation of the adsorption and reduction of CO<sub>2</sub> on 3d transition metals finite-size particles / Vivianne Karina Ocampo Restrepo. — São Carlos, 2022.

134 f.

Tese (Doutorado em Físico-Química) — Instituto de Química de São Carlos / Universidade de São Paulo, 2022.

Edição revisada

Orientador: Prof. Dr. Juarez Lopes Ferreira da Silva

1. CO<sub>2</sub> activation. 2. CO<sub>2</sub> reduction. 3. Transition metals clusters. 4. Adsorption. I. Título.





*To my mother Alba Lucía and my father Alonso.*

*For their unconditional love and inspire me to be always my best version.*

## ACKNOWLEDGEMENTS

This work would not have been possible without the constant support, guidance, and assistance of my advisor Professor Dr. Juarez Lopes Ferreira da Silva. His prompt feedback pushed me to improve constantly and brought my work to a higher level. Many thanks to Dr. Larissa Zibordi-Besse for her technical and academic support at the beginning of my doctoral research and Dr. Lucas G. Verga for the thoughtful discussions and valuable contributions to this research.

I would like to thank all my lab mates for providing me with a high qualified working environment, several helpful comments, and suggestions. Especially, some of them with who I shared more time: Rafael Besse, Naidel A. M. S. Caturello, Mailde S. Ozório, Paulo C. D. Mendes, Julian F. R. V. Silveira, Tuanan C. Lourenço, Priscila Felício-Sousa, Jonathan Mucelini, Rafael Alves. Thank you so much for the great memories and the time together. Also, to Jaqueline Oliveira, who deserves special thanks because of her administrative labor, always available to help and support me efficiently and kindly.

I want to express my sincere gratitude to my life partner, Alfredo Calderón Cárdenas, for his companionship along this journey and for support me during my studies. Our meaningful academic discussions, for the advice, and unconditional help contributed to my personal and professional growth. Many thanks to my friends, Gisela Ibañez, Maria José Dávila, David Palomino, and Enrique Paredes, for their company during this process, always offering support. Last, but not least, my warm thanks to my mother Alba Lucía, my father Alonso, and my siblings Javier and Felipe for the love and confidence they had given to me. Thank you all!



## ABSTRACT

Ocampo-Restrepo, Vivianne K. ***Ab Initio* Investigation of the Adsorption and Reduction of CO<sub>2</sub> on 3d Transition Metals Finite-size Particles**. 2022. 134p. Doctoral Thesis ( Physical Chemistry) - Instituto de Química de São Carlos, Universidade de São Paulo, São Carlos, 2022.

The use of CO<sub>2</sub> as carbon feedstock to obtain value-added chemicals like fuels motivates the searching for catalysts actives to make its conversion efficient: fast catalytic conversion, low cost, high products selectivity, etc. In this context, the materials based on 3d transition metals are actives for this purpose and are especially attractive because of their abundance and cheapness. This thesis contributed to understanding the catalytic conversion of CO<sub>2</sub> on finite-size particles based on late 3d transition metals by density functional theory calculations combined with the climbing image-nudged elastic band algorithm and the computational hydrogen electrode method. This study addressed the adsorption and activation of CO<sub>2</sub> and other small molecules, the CO<sub>2</sub> reduction via carboxyl and redox routes within the reverse water-gas shift reaction, and the late stages in the reaction paths toward acetaldehyde, ethanol, and ethylene. The results of the CO<sub>2</sub>, CO, H<sub>2</sub>O, and H<sub>2</sub> adsorption on Fe<sub>13</sub>, Co<sub>13</sub>, Ni<sub>13</sub>, and Cu<sub>13</sub> clusters allowed us to identify the structural characteristics of molecule upon adsorption as the most relevant atomistic descriptors for characterize their activation. Particular, The CO<sub>2</sub> and CO activation was driven by the charge transferred from the TM via C atom. By investigating the C–O bond dissociation of the CO<sub>2</sub>, the minimum energy path followed on all TM<sub>13</sub> clusters was via the redox route and, the Co<sub>13</sub> provided the smaller activation energy a consequence to its capability to strongly adsorb the CO<sub>2</sub> and the O. Also, the activation energies for the carboxyl routes become closer to the redox as moving from the Fe<sub>13</sub> to Cu<sub>13</sub>. The H–TM interaction strength explains that effect since it decreased in the same direction, facilitated the COO–H bond formation. Regarding descriptors for C–O bond dissociation, the CO<sub>2</sub> and *trans*-COOH species characterize the redox and carboxyl routes, respectively. Regarding the late stages of the reaction paths to C<sub>2</sub> products studied on Cu<sub>55</sub> and Cu<sub>42</sub>Zn<sub>13</sub>, the preferred path to the formation of ethanol via acetaldehyde and ethylene shared a common intermediate in both clusters: CH<sub>2</sub>CHO. However, ethanol formation would occur at smaller overpotentials than ethylene, which is consistent with previous studies predicting this behavior on under coordinates sites. The effect of the alloy on the late stages of the reaction path to ethanol affects the adsorption strength of the intermediates, being stronger compared to the Cu<sub>55</sub>, which was a consequence of the *d* states from the Zn that reinforce the interaction with the adsorbed species providing more exergonic steps.

**Keywords:** CO<sub>2</sub> activation. CO<sub>2</sub> reduction. Transition metals clusters.



## RESUMO

Ocampo-Restrepo, Vivianne K. **Investigação *Ab Initio* da Adsorção e Redução do CO<sub>2</sub> em Partículas de Tamanho Finito de Metais de Transição 3d**. 2022. 134p. Tese (Doutorado em Físico-Química) - Instituto de Química de São Carlos, Universidade de São Paulo, São Carlos, 2022.

O CO<sub>2</sub> como matéria-prima de carbono para obtenção de produtos químicos de valor agregado tem motivado a busca por catalisadores ativos que tornem sua conversão eficiente: rápida conversão, baixo custo, alta seletividade de produtos, etc. Neste contexto, materiais baseados em metais de transição 3d são ativos para esta finalidade e são especialmente atraentes devido à sua abundância e baixo custo. Essa tese visa contribuir no entendimento da conversão do CO<sub>2</sub> em partículas de tamanho finito baseadas em metais de transição 3d por meio de cálculos da teoria do funcional da densidade combinados com o algoritmo de banda elástica com imagem de escalada e o método computacional do eletrodo de hidrogênio. Foram abordadas a adsorção de CO<sub>2</sub> e outras moléculas pequenas, a redução de CO<sub>2</sub> via rotas carboxil e redox dentro da reação de deslocamento reverso água-gás e os estágios finais nos caminhos da reação até acetaldeído, etanol e etileno. Os resultados da adsorção CO<sub>2</sub>, CO, H<sub>2</sub>O e H<sub>2</sub> em conglomerados de Fe<sub>13</sub>, Co<sub>13</sub>, Ni<sub>13</sub> e Cu<sub>13</sub> permitiram identificar as características estruturais da molécula após adsorção como os descritores atomísticos mais relevantes para caracterizar sua ativação. Particularmente, a ativação de CO<sub>2</sub> e CO foi impulsionada pela carga transferida do TM via átomo C. Ao investigar a dissociação da ligação C–O do CO<sub>2</sub>, o caminho de mínima energia em todos os TM<sub>13</sub> segue a rota redox e, o Co<sub>13</sub> forneceu a menor energia de ativação a consequência à sua capacidade de adsorver fortemente o CO<sub>2</sub> e o O. Além disso, as energias de ativação para as rotas carboxila tornam-se mais próximas do redox quando se comparan desde Fe<sub>13</sub> para Cu<sub>13</sub>. A força da interação H–TM explica esse efeito, pois diminui na mesma direção, facilitando a formação da ligação COO–H. Sobre os descritores para a dissociação da ligação C–O, as espécies CO<sub>2</sub> e *trans*-COOH caracterizam as rotas redox e carboxil, respectivamente. Em relação aos estágios finais das vias de reação aos produtos C<sub>2</sub> estudados em Cu<sub>55</sub> e Cu<sub>42</sub>Zn<sub>13</sub>, o caminho preferencial para a formação de etanol e etileno compartilhou um intermediário comum em ambos os clusters: CH<sub>2</sub>CHO. No entanto, a formação de etanol ocorreria em sobrepotenciais menores que o etileno, o que é consistente com estudos anteriores que preveem esse comportamento em locais de baixa coordenação. O CuZn afeta a força de adsorção dos intermediários, sendo mais forte em relação ao Cu<sub>55</sub>, consequência dos estados *d* do Zn que reforçam a interação proporcionando etapas mais exergônicas.

**Palavras-chave:** Ativação do CO<sub>2</sub>. Redução do CO<sub>2</sub>. Conglomerados de metais de transição.

## LIST OF FIGURES

Figure 1 – Optimized structures for CO <sub>2</sub> , CO, H <sub>2</sub> O, and H <sub>2</sub> along with their bond lengths and angles, and the lowest energy structures for Fe <sub>13</sub> , Co <sub>13</sub> , Ni <sub>13</sub> , and Cu <sub>13</sub> clusters. Below each structures are their space groups and the numbers in parenthesis are the binding energies ( $E_b$ ) in eV/atom. . . .	47
Figure 2 – The left side displays the bond lengths of the CO <sub>2</sub> , CO, H <sub>2</sub> O, and H <sub>2</sub> as a function of their charge state, while the right side shows the angles for the triatomic molecules as a function of their charge state. . . . .	49
Figure 3 – Diagram for the HOMO and LUMO of CO <sub>2</sub> , CO <sub>2</sub> <sup>-</sup> , H <sub>2</sub> O, and H <sub>2</sub> O <sup>-</sup> . . .	50
Figure 4 – Representation for adsorption sites identified in this study. The interactions between the molecule and TM <sub>13</sub> are 1-fold sites (top), 2-fold sites (bridge), and 3-fold sites (hollow) when this interaction is directly with one, two, or three atoms of the TM <sub>13</sub> , respectively. Example for CO <sub>2</sub> /Fe <sub>13</sub> . . . . .	50
Figure 5 – Adsorption energy ( $E_{ad}$ ) for all calculated configurations. Open and solid symbols are results with PBE and PBE+TS calculations, respectively. . . . .	51
Figure 6 – Lowest energy structures for the Mol/TM <sub>13</sub> systems. The adsorption energy ( $E_{ad}^{PBE+TS}$ ) is below each structures in eV. . . . .	53
Figure 7 – Electron density difference for CO <sub>2</sub> , CO, H <sub>2</sub> O, and H <sub>2</sub> on the TM <sub>13</sub> clusters. Blue and gray colors represent the charge accumulation and depletion, respectively. The charge transfer from cluster to molecule obtained from the Hirshfeld charge density analysis is below the structure in the number of $e$ . The charge density used for the isosurface plots was $1.50 \times 10^{-2} e \text{ \AA}^{-3}$ . . . . .	56
Figure 8 – Angles and bond lengths for CO <sub>2</sub> , CO, H <sub>2</sub> O, and H <sub>2</sub> upon adsorption on each TM <sub>13</sub> as a function of $\Delta q_{Mol}$ . The lines for each molecule connect the more negative or less positive with the more positive value of $\Delta q_{Mol}$ . . . . .	57
Figure 9 – Infrared spectra of molecules, TM <sub>13</sub> , and Mol/TM <sub>13</sub> . The infrared intensities for the TM <sub>13</sub> clusters were multiplied by 50 for visualization purposes. . . . .	60
Figure 10 – The relative change for bond lengths of adsorbed molecules regarding to the gas-phase configuration, as a function of net charge at molecule upon adsorption ( $\Delta q_{Mol}$ ), deformation energy for the molecules ( $\Delta E_{tot}^{Mol}$ ), interaction energy ( $E_{int}$ ), and adsorption energy ( $E_{ad}$ ). . . . .	61

Figure 11 – Lowest and high energy structures for adsorbed and co-adsorbed systems. The TM atoms highlighted with white $\mathbf{x}$ are the preferred sites for the lowest energy $\text{CO}_2$ chemisorption. Numbers below the structures are the adsorption energies ( $E_{ad}$ ) and in parentheses the adsorption energy for $\text{CO}_2$ and $\text{CO}$ ( $E_{ad}^{\text{CO}_2, \text{CO}}$ ) obtained due to the co-adsorption effect. . . . .	66
Figure 12 – C–O bond lengths ( $d_{\text{C-O}}$ ) for all optimized structures of $\text{CO}_2$ and $\text{COOH}$ upon adsorption on $\text{TM}_{13}$ as a function of the relative energy ( $\Delta E_{tot}$ ). Open circles and triangles symbols for $\text{CO}_2$ bonds; open squares and diamonds symbols for $\text{COOH}$ bonds. Yellow, red, green, and blue indicates the $\text{Fe}_{13}$ , $\text{Co}_{13}$ , $\text{Ni}_{13}$ , and $\text{Cu}_{13}$ clusters, respectively. The dashed (dashed-dots) lines are the C–O (C–OH) bonds length in gas-phase. . . . .	67
Figure 13 – Potential energy profiles for C–O dissociation: a) via redox route; b) via carboxyl route on $\text{TM}_{13}$ . The structures for all intermediates and transition states are at the bottom and top of their potential energy diagram, respectively. The activation energies ( $E_a$ ) values are the number below boxes, while the $\text{CO}$ desorption energy is the number in parenthesis. For comparison purposes, we aligned the transition states for the same elementary step, and the black arrows indicate the vibrational movement in the direction of the reaction coordinate. . . . .	69
Figure 14 – BEP and TSS relations for: $\text{CO}_2$ dissociation in a), d); $\text{COOH}$ formation in b), e); and for $\text{CO-OH}$ dissociation in c), f). $E_a$ is the activation energy, while $E^\ddagger$ is the transition state energy obtained by: $E^\ddagger = E_{tot}^\ddagger - E_{tot}^{\text{TM}_{13}} - \sum E_{tot}^{\text{reactants}}$ . The products and reactants are represented by $P$ and $R$ , respectively, and the equation inside each plot comes from the linear regression. . . . .	73
Figure 15 – Comparison of the activation energies ( $E_a$ ) between $\text{CO}_2$ dissociation, $\text{CO}_2$ hydrogenation, and $\text{CO-OH}$ dissociation on $\text{TM}_{13}$ represented by open bar, diagonal line filled bar, and squares filled bar, respectively. . . . .	74
Figure 16 – Species in gas-phase that participate in the reaction paths studied, where the carbon, oxygen, and hydrogen atoms are the gray, red, and white balls, respectively. The number below each species is the binding energy with $E_{energy}^{\text{ZPE}}$ correction ( $E_b^{\text{ZPE}}$ ) in eV per atom. . . . .	78
Figure 17 – $\text{Cu}_{55}$ and $\text{Cu}_{42}\text{Zn}_{13}$ cluster models with their projected density of states (PDOS). The dashed line in each PDOS plot refers to the HOMO energy. . . . .	80
Figure 18 – Possible reaction pathways via proton-coupled electron transfer steps after $\text{CH-CO}$ coupling for $\text{CO}_2\text{RR}$ or $\text{CORR}$ toward ethylene, acetaldehyde, and ethanol production. The final products are highlighted in blue for ethanol and acetaldehyde and red for ethylene and water. . . . .	82

Figure 19 – Free energy diagram from CHCO to a) CH <sub>3</sub> CH <sub>2</sub> OH and b) C <sub>2</sub> H <sub>4</sub> on Cu <sub>55</sub> . The steps with positives $\Delta G$ are indicated with their values in eV. Black lines connect the preferred reaction path, while red and blue lines connected other paths explored. . . . .	83
Figure 20 – Free energy diagram from CHCO to a) CH <sub>3</sub> CH <sub>2</sub> OH and b) C <sub>2</sub> H <sub>4</sub> on Cu <sub>42</sub> Zn <sub>13</sub> . The steps with positives $\Delta G$ are indicated with their values in eV. Black lines connect the preferred reaction path, while red and blue lines connected other paths explored. . . . .	84
Figure 21 – a) Free energy diagram for the preferred path from CHCO to CH <sub>3</sub> CH <sub>2</sub> OH on Cu <sub>55</sub> and Cu <sub>42</sub> Zn <sub>13</sub> . The steps with positives $\Delta G$ are indicated with their values in eV. Black lines connect the preferred reaction path on Cu <sub>55</sub> , while blue lines connected preferred path on Cu <sub>42</sub> Zn <sub>13</sub> . b) Structures for the adsorbed species on the preferred path toward ethanol. The numbers are the adsorption energies in eV ( $E_{ad}$ ). . . . .	86
Figure 22 – Projected density of states (PDOS) of C, O, and the TM atoms involved in the adsorption of the species on Cu <sub>55</sub> and Cu <sub>42</sub> Zn <sub>13</sub> clusters. Only the species in the preferred path toward ethanol were analyzed. . . . .	87
Figure 23 – Total energy convergence test for small molecules using different basis set functions. . . . .	109
Figure 24 – Reaction path of CO <sub>2</sub> $\longrightarrow$ CO + O on Fe <sub>13</sub> with NEB method using different force constants: red square for 20 eV $\text{\AA}^{-1}$ (iteration 91), green diamond for 15 eV $\text{\AA}^{-1}$ (iteration 245), and black circle for 10 eV $\text{\AA}^{-1}$ (iteration 100). All calculations used 7 images and a residual forces threshold at 0.15 eV $\text{\AA}^{-1}$ . . . . .	111
Figure 25 – Comparison for set of parameters A and B for CHCO and CHCHO adsorbed on Cu <sub>55</sub> <sup>ICO</sup> and Cu <sub>42</sub> Zn <sub>13</sub> <sup>ICO</sup> . Circle orange and <b>X</b> green highlight the lowest energy structure obtained by set A and B, respectively. . . . .	117
Figure 26 – Example for the control.in file for CI-NEB calculations. . . . .	118
Figure 27 – Example for the chain.in file for CI-NEB calculations. . . . .	119
Figure 28 – Permission request process to re-use published material in the Chapter 3.	121
Figure 29 – Adsorption structures of CO <sub>2</sub> /TM <sub>13</sub> . Here is presented all the representative structures studied in relation to their adsorption energy. The number close to the structure is the minimum distance in $\text{\AA}$ from one atom of the molecule to one atom of the cluster. The dashed lines are used to represent the long-range interaction between molecule and cluster.	122

- Figure 30 – Adsorption structures of CO/TM<sub>13</sub>. Here is presented all the representative structures studied in relation to their adsorption energy. The number close to the structure is the minimum distance in Å from one atom of the molecule to one atom of the cluster. The dashed lines are used to represent the long-range interaction between molecule and cluster. 123
- Figure 31 – Adsorption structures of H<sub>2</sub>O/TM<sub>13</sub>. Here is presented all the representative structures studied in relation to their adsorption energy. The number close to the structure is the minimum distance in Å from one atom of the molecule to one atom of the cluster. The dashed lines are used to represent the long-range interaction between molecule and cluster. 124
- Figure 32 – Adsorption structures of H<sub>2</sub>/TM<sub>13</sub>. Here is presented all the representative structures studied in relation to their adsorption energy. The number close to the structure is the minimum distance in Å from one atom of the molecule to one atom of the cluster. The dashed lines are used to represent the long-range interaction between molecule and cluster. 125
- Figure 33 – Permission request process to re-use published material in the Chapter 4. 126
- Figure 34 – Potential energy profiles for CO<sub>2</sub>\* → CO + O\*. The energy reference for redox path is the total energies sum of TM<sub>13</sub> with CO<sub>2</sub>. For comparison purposes, common transition-states are aligned. All intermediates and transition-state structures are under and over the boxes, respectively. For each transition-state, black arrows indicate the vibrational movement along the reaction coordinate. The number under transitions-states are the activation energies,  $E_a$ , for solid boxes paths connected by dashed lines, and in parenthesis are the values for the alternative paths represented by open boxes connected by solid lines. The CO desorption energy is the number throughout the last step. When two structures are possible, we highlight them with a dashed square for the solid boxes paths and a solid square for the open boxes paths. . . . . 127

Figure 35 – Potential energy profiles for $(\text{CO}_2 + \text{H})^* \longrightarrow \text{CO} + \text{OH}^*$ on $\text{TM}_{13}$ . The energy reference for carboxyl path is the total energies sum of $\text{TM}_{13}$ , $\text{CO}_2$ , and H. For comparison purposes, common transition-states are aligned. All intermediates and transition-state structures are under and over the boxes, respectively. For each transition-state, black arrows indicate the vibrational movement along the reaction coordinate. The number under transitions-states are the activation energies, $E_a$ , for solid boxes paths connected by dashed lines, and in parenthesis are the values for the alternative paths represented by open boxes connected by solid lines. The CO desorption energy is the number throughout the last step. When two structures are possible, we highlight them with a dashed square for the solid boxes paths and a solid square for the open boxes paths. . . . .	128
Figure 36 – TSS relations for all the processes studied. $E^\ddagger$ is the transition-state energy as a function of the adsorption energies ( $E_{ad}$ ). . . . .	129
Figure 37 – $\text{Cu}_{55}$ clusters models. Structures with high and low-symmetry were included, namely: icosahedron (ICO), cuboctahedron (CUB), disordered reduced-core (DRC), that includes models with 7 to 11 atoms in the core, tetrahedral-like models (THL), and a fragment of the FCC structure (FCCf) [1]. . . . .	130
Figure 38 – $\text{Cu}_{42}\text{Zn}_{13}$ ICO clusters models. Core-shell type core Cu-rich, $C_{Cu}S_{Zn}$ ; core-shell type core Zn-rich, $C_{Zn}S_{Cu}$ ; and segregated cluster, $Seg_{Cu-Zn}$ . . . . .	130
Figure 39 – Properties of $\text{Cu}_{42}\text{Zn}_{13}$ ICO clusters models as a function of basis function and functionals. Energetic, structural, and electronic properties for $\text{Cu}_{42}\text{Zn}_{13}$ ICO clusters. Relative energy ( $\Delta E_{tot}$ ); binding energy ( $E_b$ ); highest occupied molecular orbital (HOMO); lowest unoccupied molecular orbital (LUMO); HOMO-LUMO gap (Gap); average effective coordination number ( $ECN_{av}$ ); average interatomic distance ( $d_{av}$ ); Radius (Radius); chemical order parameter ( $\sigma$ ); total magnetic moment ( $m_{tot}$ ). . . . .	131
Figure 40 – Superficial charge distribution analysis for $\text{Cu}_{55}$ and $\text{Cu}_{42}\text{Zn}_{13}$ clusters. . . . .	132
Figure 41 – Lowest energy structures for the adsorbed species involving in the reaction paths to ethanol and ethylene on $\text{Cu}_{55}$ and $\text{Cu}_{42}\text{Zn}_{13}$ clusters. The number below each structure is the adsorption energy ( $E_{ad}$ ) in eV. . . . .	134

## LIST OF TABLES

Table 1 – Structural, energetic, and electronic parameters for CO <sub>2</sub> , CO, H <sub>2</sub> O, H <sub>2</sub> , Fe <sub>13</sub> , Co <sub>13</sub> , Ni <sub>13</sub> , and Cu <sub>13</sub> : bond lengths ( $d_0$ ), angles, effective coordination number (ECN), average bond distance ( $d_{av}$ ), binding energy ( $E_b$ ), and magnetic moment ( $m_{tot}$ ). In parentheses are the deviations with respect to experimental data and DFT-PBE calculations in %.	48
Table 2 – Energetic properties for the lowest energy structures using PBE and PBE+TS of CO <sub>2</sub> , CO, H <sub>2</sub> O, and H <sub>2</sub> adsorbed on Fe <sub>13</sub> , Co <sub>13</sub> , Ni <sub>13</sub> , and Cu <sub>13</sub> clusters. Adsorption energy ( $E_{ad}$ ); interaction energy ( $E_{int}$ ); difference between the total energy of the molecule after adsorption and in the gas-phase ( $\Delta E_{tot}^{Mol}$ ); difference between the total energy of the TM <sub>13</sub> after adsorption and in the gas-phase ( $\Delta E_{tot}^{TM_{13}}$ ).	54
Table 3 – Electronic and structural properties for the lowest energy structures calculated with PBE and PBE+TS of CO <sub>2</sub> , CO, H <sub>2</sub> O, and H <sub>2</sub> on Fe <sub>13</sub> , Co <sub>13</sub> , Ni <sub>13</sub> , and Cu <sub>13</sub> clusters. Net charge at molecules obtained from the Hirshfeld charge analysis ( $\Delta q_{Mol}$ ); bond length for adsorbed molecules ( $d_0$ ); angle of CO <sub>2</sub> and H <sub>2</sub> O after adsorption (Angle); smallest Mol–TM <sub>13</sub> bond distance ( $d_{Mol-TM_{13}}$ ); relative changes in the bond lengths average weighted on adsorption site of TM <sub>13</sub> after adsorption ( $\Delta d_{av}$ ); relative changes in the TM <sub>13</sub> effective coordination number on adsorption site after adsorption ( $\Delta ECN$ ). The numbers in parenthesis are the relative change in percentages with respect to the equilibrium values in gas-phase ( $\Delta d_0$ ) and ( $\Delta Angle$ ).	58
Table 4 – Activation energies ( $E_a$ ) and imaginary( $i$ ) frequencies for transition states ( $\ddagger_{frequency}$ ).	70
Table 5 – Energetic and some structural properties for all the species studied in the selected reaction paths. Absolute value for binding energy ( $ E_b $ ); zero point energy ( $E_{energy}^{ZPE}$ ); absolute value for binding energy with $E_{energy}^{ZPE}$ correction ( $ E_b^{ZPE} $ ); experimental binding energy ( $E_b^{Exp}$ ) at two different temperatures ( $T$ ) both from reference [2]; minimum oxygen bond distance with X=H or C ( $d^{O-X}$ ); minimum carbon-carbon bond distance ( $d^{C-C}$ ); and angle between the fragment OCC ( $\angle^{OCC}$ ).	79

Table 6 – Comparison of energetic, structural, and electronic properties for $\text{Cu}_{55}$ and $\text{Cu}_{42}\text{Zn}_{13}$ clusters. Binding energy per atom ( $E_b$ ); highest occupied molecular orbital (HOMO); lowest unoccupied molecular orbital (LUMO); HOMO-LUMO gap (Gap); average effective coordination number ( $\text{ECN}_{av}$ ); average interatomic distance ( $d_{av}$ ); Radius (Radius); charge at shell surface ( $q_s$ ); and total magnetic moment ( $m_{tot}$ ). . . . .	81
Table 7 – Self-consistent Field (SCF) convergence tests varying: charge_mix_param, $n_{\text{max\_pulay}}$ , and occupation_type gaussian. SCF convergence threshold used: total energy at $10^{-6}$ eV, charge density at $10^{-5} e \text{ \AA}^{-3}$ , sum of eigenvalues at $10^{-3}$ eV, and forces at $10^{-4} \text{ eV \AA}^{-1}$ . . . . .	110
Table 8 – Comparison between set of parameters A and B for CHCO adsorbed on $\text{Cu}_{55}^{\text{ICO}}$ clusters. Relative energy ( $\Delta E_{tot}$ ); adsorption energy ( $E_{ad}$ ); highest occupied molecular orbital (HOMO); lowest unoccupied molecular orbital (LUMO); HOMO-LUMO gap (Gap); minimum bond distance of C to $\text{Cu}_{55}$ ( $d^{\text{C-Cu}}$ ); minimum bond distance of O to $\text{Cu}_{55}$ ( $d^{\text{O-Cu}}$ ); minimum bond distance of H to $\text{Cu}_{55}$ ( $d^{\text{H-Cu}}$ ); total magnetic moment ( $m_{tot}$ ). . . . .	113
Table 9 – Comparison between set of parameters A and B for CHCHO adsorbed on $\text{Cu}_{55}^{\text{ICO}}$ clusters. Relative energy ( $\Delta E_{tot}$ ); adsorption energy ( $E_{ad}$ ); highest occupied molecular orbital (HOMO); lowest unoccupied molecular orbital (LUMO); HOMO-LUMO gap (Gap); minimum bond distance of C to $\text{Cu}_{55}$ ( $d^{\text{C-Cu}}$ ); minimum bond distance of O to $\text{Cu}_{55}$ ( $d^{\text{O-Cu}}$ ); minimum bond distance of H to $\text{Cu}_{55}$ ( $d^{\text{H-Cu}}$ ); total magnetic moment ( $m_{tot}$ ). . . . .	114
Table 10 – Comparison between set of parameters A and B for CHCO adsorbed on $\text{Cu}_{42}\text{Zn}_{13}^{\text{ICO}}$ clusters. Relative energy ( $\Delta E_{tot}$ ); adsorption energy ( $E_{ad}$ ); highest occupied molecular orbital (HOMO); lowest unoccupied molecular orbital (LUMO); HOMO-LUMO gap (Gap); minimum bond distance of C to $\text{Cu}_{42}\text{Zn}_{13}$ ( $d^{\text{C-Cu}_{42}\text{Zn}_{13}}$ ); minimum bond distance of O to $\text{Cu}_{42}\text{Zn}_{13}$ ( $d^{\text{O-Cu}_{42}\text{Zn}_{13}}$ ); minimum bond distance of H to $\text{Cu}_{42}\text{Zn}_{13}$ ( $d^{\text{H-Cu}_{42}\text{Zn}_{13}}$ ); total magnetic moment ( $m_{tot}$ ). . . . .	115
Table 11 – Comparison between set of parameters A and B CHCHO adsorbed on $\text{Cu}_{42}\text{Zn}_{13}^{\text{ICO}}$ clusters. Relative energy ( $\Delta E_{tot}$ ); adsorption energy ( $E_{ad}$ ); highest occupied molecular orbital (HOMO); lowest unoccupied molecular orbital (LUMO); HOMO-LUMO gap (Gap); minimum bond distance of C to $\text{Cu}_{42}\text{Zn}_{13}$ ( $d^{\text{C-Cu}_{42}\text{Zn}_{13}}$ ); minimum bond distance of O to $\text{Cu}_{42}\text{Zn}_{13}$ ( $d^{\text{O-Cu}_{42}\text{Zn}_{13}}$ ); minimum bond distance of H to $\text{Cu}_{42}\text{Zn}_{13}$ ( $d^{\text{H-Cu}_{42}\text{Zn}_{13}}$ ); total magnetic moment ( $m_{tot}$ ). . . . .	116



Table 12 – Comparison of energetic, structural, and electronic properties for $\text{Cu}_{55}^{\text{ICO}}$ clusters using PBE, PBE with van der Waals corrections, TS or D3 approaches, and different levels of numerical atomic orbitals wave functions, namely <i>light1</i> , 2, 3, and plane-waves, PW. Binding energy per atom ( $E_b$ ); average effective coordination number ( $\text{ECN}_{av}$ ); average interatomic distance ( $d_{av}$ ); total magnetic moment ( $m_{tot}$ ). . . . .	131
Table 13 – Values of $E_{energy}^{\text{ZPE}}$ , $E_{vib}$ , and $TS$ for all gas-phase species involved in this study. All energetic quantities are given in eV. . . . .	133
Table 14 – Solvation corrections according to the functional group of the chemical species [3]. . . . .	133

## LIST OF ABBREVIATIONS AND ACRONYMS

BEP	Brønsted–Evans–Polany
CI	climbing image
CHE	computational hydrogen electrode
CORR	electrochemical reduction of CO
CO <sub>2</sub> RR	electrochemical reduction of CO <sub>2</sub>
CUB	cuboctahedron
DFT	density functional theory
DRC	disordered reduced-core
DRIFTS	<i>in-situ</i> diffuse reflectance infrared spectroscopy
ECN	effective coordination number
ESD	Euclidean similarity distance
XC	exchange-correlation
FCCf	face-centered cubic fragment
FHI-aims	Fritz-Haber Institute <i>Ab initio</i> Molecular Simulations
FT	Fischer–Tropsch
GGA	generalized gradient approximation
HK	Hohenberg–Kohn
KS	Kohn–Sham
ICO	icosahedron
IR	infrared
MEP	minimum energy path
NAO	numerical orbitals centered on the atoms
NEB	nudged elastic band
NNN	number of nearest neighbors

PBE	Perdew–Burke–Ernzenhof
PCET	proton-coupled electron transfer
PDOS	projected density of states
PDS	potential-determining step
pGMC	putative global minimum configuration
RDS	rate-determining step
	RHE reversible hydrogen electrode
RWGS	reverse water-gas shift
TS	Tkatchenko–Scheffler
TSS	transition states scaling
THL	tetrahedral-like
TM	transition metal
vdW	van der Waals

## CONTENTS

<b>1</b>	<b>INTRODUCTION</b> . . . . .	<b>22</b>
<b>1.1</b>	<b>CO<sub>2</sub> as Carbon Source for Fuel Synthesis</b> . . . . .	<b>22</b>
<b>1.2</b>	<b>Transition Metal Catalysts for CO<sub>2</sub> Reduction</b> . . . . .	<b>23</b>
<b>1.3</b>	<b>Advances in the CO<sub>2</sub> Reduction Mechanism</b> . . . . .	<b>24</b>
1.3.1	Adsorption and Activation of CO <sub>2</sub> . . . . .	25
1.3.2	Reduction of CO <sub>2</sub> via RWGS . . . . .	26
1.3.3	Electroreduction of CO <sub>2</sub> to C <sub>2</sub> Products . . . . .	27
<b>1.4</b>	<b>Open Questions</b> . . . . .	<b>29</b>
<b>1.5</b>	<b>Objectives</b> . . . . .	<b>30</b>
1.5.1	General Objectives . . . . .	30
1.5.2	Specific Objectives . . . . .	30
<b>2</b>	<b>METHODOLOGY</b> . . . . .	<b>31</b>
<b>2.1</b>	<b>Many-body Problem and Born–Oppenheimer Approximation</b> . . . . .	<b>31</b>
<b>2.2</b>	<b>Electronic Wave Function and the Electron Density</b> . . . . .	<b>33</b>
<b>2.3</b>	<b>Density Functional Theory</b> . . . . .	<b>34</b>
2.3.1	Hohenberg–Kohn Theorems . . . . .	34
2.3.2	Kohn–Sham Method . . . . .	35
2.3.3	Exchange-correlation Functionals . . . . .	36
2.3.4	van der Waals Corrections . . . . .	37
<b>2.4</b>	<b>Computational Implementation</b> . . . . .	<b>39</b>
<b>2.5</b>	<b>Searching Transition States: Climbing Image-Nudged Elastic Band Method</b> . . . . .	<b>40</b>
<b>2.6</b>	<b>Modeling in Electrocatalysis: The Computational Hydrogen Electrode Approach</b> . . . . .	<b>41</b>
<b>2.7</b>	<b>Atomic Structures Generation and Clustering Algorithms</b> . . . . .	<b>42</b>
<b>2.8</b>	<b>Analysis</b> . . . . .	<b>44</b>
2.8.1	Energetic Properties . . . . .	44
2.8.2	Structural Properties . . . . .	45
2.8.3	Electronic Properties . . . . .	46
<b>3</b>	<b>ACTIVATION OF SMALL MOLECULES VIA ADSORPTION ON 3d TRANSITION-METAL 13-ATOM CLUSTERS: THE EXAMPLE OF CO<sub>2</sub>, CO, H<sub>2</sub>O, AND H<sub>2</sub></b> . . . . .	<b>47</b>
<b>3.1</b>	<b>Gas-phase Molecules and Clusters</b> . . . . .	<b>47</b>
<b>3.2</b>	<b>Adsorption on TM<sub>13</sub> Clusters</b> . . . . .	<b>50</b>

3.2.1	Adsorption Site Preference . . . . .	52
3.2.2	Energetic Parameters . . . . .	52
3.2.3	Partial Charge Transfer Analysis . . . . .	55
3.2.4	Structural Parameters . . . . .	57
3.2.5	Vibrational Analysis . . . . .	59
<b>3.3</b>	<b>Molecular Descriptors in the Activation of Small Molecules . . . . .</b>	<b>61</b>
<b>3.4</b>	<b>Summary . . . . .</b>	<b>62</b>
<b>4</b>	<b>C–O BOND DISSOCIATION MECHANISM IN CO<sub>2</sub> REDUCTION VIA REDOX AND CARBOXYL ROUTES ON 3d TRANSITION- METAL 13-ATOM CLUSTERS . . . . .</b>	<b>64</b>
<b>4.1</b>	<b>Adsorption Study for Species Involved in the C–O Dissociation Mechanism . . . . .</b>	<b>64</b>
<b>4.2</b>	<b>Revealing the C–O Dissociation Mechanism on TM<sub>13</sub> Clusters . . . . .</b>	<b>68</b>
4.2.1	Redox Route: Mechanistic Details for C–O Dissociation . . . . .	68
4.2.2	Redox Route: the Diffusion Matters . . . . .	70
4.2.3	Carboxyl Route: Mechanistic Details for C–O Dissociation . . . . .	71
4.2.4	CO Desorption via Redox and Carboxyl Routes . . . . .	71
<b>4.3</b>	<b>Brønsted–Evans–Polanyi and Transition states Scaling Relations for Redox and Carboxyl Routes . . . . .</b>	<b>72</b>
<b>4.4</b>	<b>Routes Competition: Redox versus Carboxyl . . . . .</b>	<b>74</b>
<b>4.5</b>	<b>Summary . . . . .</b>	<b>75</b>
<b>5</b>	<b>STUDY OF THE CO<sub>2</sub> ELECTROREDUCTION ON Cu Zn ALLOYS: THE ROLE OF Zn ON THE LAST STAGES OF PATHS TOWARD C<sub>2</sub> PRODUCTS . . . . .</b>	<b>76</b>
<b>5.1</b>	<b>Systems in Gas-phase: Intermediates in the Selected Paths to Ethy- lene, Acetaldehyde, and Ethanol Production . . . . .</b>	<b>76</b>
<b>5.2</b>	<b>Clusters: Cu<sub>55</sub> and the Cu<sub>42</sub>Zn<sub>13</sub> Alloy . . . . .</b>	<b>78</b>
<b>5.3</b>	<b>Free Energy Diagrams of the Selected Reaction Paths on Cu<sub>55</sub> and Cu<sub>42</sub>Zn<sub>13</sub> . . . . .</b>	<b>81</b>
5.3.1	Reaction Paths on Cu <sub>55</sub> . . . . .	81
5.3.2	Reaction Paths on Cu <sub>42</sub> Zn <sub>13</sub> . . . . .	85
<b>5.4</b>	<b>The Effect of Zn on Late Stages of the Preferred Path Toward Ethanol . . . . .</b>	<b>85</b>
<b>5.5</b>	<b>Summary . . . . .</b>	<b>87</b>
<b>6</b>	<b>CONCLUSIONS . . . . .</b>	<b>89</b>
<b>6.1</b>	<b>Papers and Manuscripts in Progress . . . . .</b>	<b>90</b>
6.1.1	Published papers . . . . .	90

6.1.2	Manuscripts in progress . . . . .	91
	<b>REFERENCES . . . . .</b>	<b>93</b>
	<b>APPENDIX</b>	<b>107</b>
	<b>APPENDIX A – COMPUTATIONAL TESTS AND PARAMETERS</b>	<b>108</b>
	<b>APPENDIX B – CLIMBING IMAGE-NUDGED BAND ELASTIC CALCULATIONS USING FHI-AIMS PACKAGE .</b>	<b>118</b>
	<b>APPENDIX C – SUPPLEMENTARY DATA: CHAPTER 3 . . . . .</b>	<b>120</b>
	<b>APPENDIX D – SUPPLEMENTARY DATA: CHAPTER 4 . . . . .</b>	<b>126</b>
	<b>APPENDIX E – SUPPLEMENTARY DATA: CHAPTER 5 . . . . .</b>	<b>130</b>

## 1 INTRODUCTION

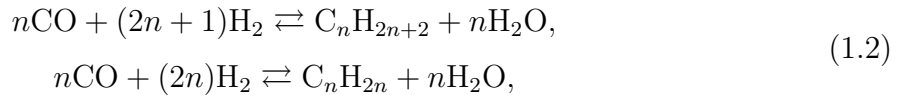
The CO<sub>2</sub> as a raw material to obtain value-added products is a relevant topic given the negative environmental impact caused by this greenhouse gas. Then, this thesis focus on the study of CO<sub>2</sub> conversion on finite-size particles based on 3*d* transition metals (TMs). This introduction provides an overview of the potential use of CO<sub>2</sub> as a chemical to produce alcohols and even long-chain hydrocarbons, which is a motivation to address the topic in this study. Followed by a general summary of the potential use of TM-based catalysts for CO<sub>2</sub> conversion, and then a review of current advances and challenges to make this process efficient will be presented. Finally, some open problems have been highlighted that lead to the objectives of this investigation.

### 1.1 CO<sub>2</sub> as Carbon Source for Fuel Synthesis

The excess of CO<sub>2</sub> concentration in the atmosphere, derived from anthropogenic factors, is the main responsible for global warming and climate change [4]. Nowadays, the CO<sub>2</sub> concentration increase rate is between 2 to 3 ppm per year [5], allow us to estimate that at 2030 would be reach the 450 ppm, which is pointed out as risk concentration [4,6]. From this perspective, to stabilize the atmospheric levels of CO<sub>2</sub> in safe values, 350 ppm, two actions are needed: to stop the anthropogenic CO<sub>2</sub> emissions and the effective remove of this gas from the atmosphere. In this context, the CO<sub>2</sub> conversion into value-added products is considered a promising strategy to move toward a circular carbon economy [7], mitigating the environmental damage, providing raw materials, and even renewable fuels to supply the global energy demand [8].

Currently, there is no commercially viable process for converting CO<sub>2</sub> into high value-added products due to problems associated with: i) high costs of capture CO<sub>2</sub>, separation, purification, transportation; and ii) high energy requirements for CO<sub>2</sub> conversion [9]. Concerning the second point, electrochemical and thermal reduction of CO<sub>2</sub> is a feasible way to supply the energy demand and move to the production of fuels [9]. Then, the electrochemical approach uses electricity to drive the process, while the thermal procedure employs temperature and pressure to provide energy for the reduction. Beyond the energy required, CO<sub>2</sub> reduction suffers problems such as slow conversion, parallel reactions, and low products selectivity, which compromise the overall efficiency of the CO<sub>2</sub> reduction. The most desired products from the CO<sub>2</sub> reduction are long-chain hydrocarbons due to their high energy density, which would be employed to produce energy in a sustainable scenario [8]. Direct Fischer–Tropsch (FT) synthesis from CO<sub>2</sub> (CO<sub>2</sub>-FT) has been proposed as a reaction scheme for thermocatalytic CO<sub>2</sub> conversion. First, CO<sub>2</sub> is reduced to CO via reverse water-gas shift (RWGS), equation (1.1), then the CO is further reduced via FT

reaction, equation (1.2) [10]. While, CH<sub>3</sub>OH production is a direct route for CO<sub>2</sub> utilization since this alcohol can be a fuel additive, substitute, and precursor in the other chemicals synthesis [11]. But, although the synthesis of CH<sub>3</sub>OH from CO<sub>2</sub> is thermodynamically favored, equation (1.3), it is slow at low temperatures, and at high temperatures, parallel reactions like RWGS are favored [11].



The conversion of CO<sub>2</sub> to CO via RWGS is another flexible option since CO is a component of syngas and a common intermediate involved in the production of fuels like ethanol and methanol [12–14]. However, the production of CO from CO<sub>2</sub> is thermodynamically disfavored,  $\Delta G_{298}^0 = 0.21 \text{ eV}$ , requiring high energy expenditure but without satisfactory conversions percentages associated to kinetic limitations, e.g., 23% at 300 °C and 1 MPa [15, 16]. In general, there are several points to solve before incorporate the CO<sub>2</sub> in a circular economy. One of those field to put efforts is developing catalysts, which would help to improve the rate reactions and reduce the energy required for the conversion.

## 1.2 Transition Metal Catalysts for CO<sub>2</sub> Reduction

Considering that Gibbs energy of formation for CO<sub>2</sub> is  $\Delta G_{298\text{K}}^{\circ} = -4.09 \text{ eV}$ , this molecule is classified as stable and almost inert [17], for instance, the energy required to break a C–O bond is about 5.50 eV [18]. In this sense, for the reduction of CO<sub>2</sub> is necessary to achieve a molecular state prone to react, which we called the CO<sub>2</sub> activation [19]. Processes like the activation, cleavage, or formation of bonds can be carried out using a reducing agent and appropriate catalysts. In this context, transition metals (TM) based materials are the most studied catalysts for the CO<sub>2</sub> reduction [20], since they showed to be active for the CO<sub>2</sub> conversion, e.g., Pt [21], Au [22], Rh [23], Pd [24], Fe [25], Ni [26], and Cu [27].

Transition metals catalysts as a single-crystal surface are widely employed to study reactions. However, especially for the CO<sub>2</sub> reduction, they have been reported poor reactivity due to CO<sub>2</sub> interacting weakly on most metals, keeping its linearity (physisorption) [28–30]. Then, different strategies to enhance the CO<sub>2</sub> reactivity on single-crystal surfaces have been employed, e.g., the use of promoters as alkali metals (K, Cs,



Na) [10, 31–33]. The exceptional case is the use of single-crystal metal electrodes for the electrochemical reduction of CO<sub>2</sub> (CO<sub>2</sub>RR), specially Cu-based, that have been shown an interesting performance to produce C<sub>2</sub> and C<sub>2</sub>+ products [34]. Another strategy used is to favor undercoordinated sites by reducing the size of catalysts.

Several studies using TM particles and nanoparticles, typically supported on a substrate, demonstrate a better reactivity for CO<sub>2</sub> reduction compared with the crystal-single surfaces [16, 35, 36]. The particle size strongly affects the selectivity of the catalysts, being a consequence of the mark changes in the electronic structure [37], and also due to the atoms coordination that modified the interaction strength with the intermediates [38, 39]. Also, the techniques to synthesize catalysts allow reducing the particle size until achieving the single-atom catalysts regimen [40], or to sculpt the particle in a set of forms like spheres, cubes, dendrites, etc[36]. Then, the power to manipulate the materials brings an opportunity to design catalysts with desired properties.

Beyond the particle size and shape, the use of a second metal is a strategy widely implemented to tune the catalysts' properties [16, 41]. The addition of a second TM induces geometric changes and modifies the electronic structure creating a synergetic effect that changes catalytic properties like the intermediates' adsorption strength. Among the vast research using bimetallic catalysts, we center our attention on modified Cu-based catalysts for the CO<sub>2</sub>RR [42], since alloying system such as Cu–Ag, Cu–Au, and Cu–Zn [43–46] have been demonstrated a highlighted activity to obtain C<sub>2</sub> products and improve the selectivity into ethanol [47, 48].

The use of 3*d* TM for the CO<sub>2</sub> conversion has gained attention due to their low-cost and disponibility compared with noble metals. Also, early experimental studies on clean surfaces revealed the potential of 3*d* late metals like Fe, Ni, Co, and Cu to activate and dissociate CO<sub>2</sub> compared with other metals [49–51]. Despite the progress achieved in the search for materials for CO<sub>2</sub> reduction, a better understanding of the catalytic process is crucial to guide the synthesis of catalysts, being necessary to put efforts into the elucidation of the reaction mechanisms on these materials.

### 1.3 Advances in the CO<sub>2</sub> Reduction Mechanism

The reactions on catalysts surface evolute in a series of elementary steps that include, for example, the physical or chemical adsorption of the species, their diffusion, the dissociation and formation of bonds, and the desorption of products. Drawing a complete picture of those stages on each material is crucial to control the reaction course; then, several experimental and theoretical studies address the identification of reactive sites, adsorbed intermediates, the calculation or measurement of rate constant, etc. Especially the development of computing architecture and methods based on the density functional theory (DFT) allows the exploration of a large number of potential materials, contributing

to our understanding and guiding the development of enhanced catalysts for CO<sub>2</sub> reduction.

### 1.3.1 Adsorption and Activation of CO<sub>2</sub>

Experiments of photo-electron spectroscopy and infrared spectroscopy have reported both the chemical and physical adsorption of CO<sub>2</sub> on surfaces of Fe, Ni, and Cu. Although the physisorbed CO<sub>2</sub> was mainly observed, the chemisorbed CO<sub>2</sub> appears at specific conditions, being influenced by the CO<sub>2</sub> concentration and the material facet, e.g., 5.0 L at 85 K on Fe(111), 0.5 L at 80 K on Ni(110), 115.0 L at 80 K on polycrystalline Cu [49,52]. Also the increase of temperature promote not only chemisorption of CO<sub>2</sub> but its dissociation to CO, as reported on Fe(111) at 300 K [28]. CO<sub>2</sub> activation via adsorption on TM surfaces was characterized by identification of two adsorption modes associated to bent CO<sub>2</sub> that suggested the chemisorption of the molecule [53]. Then, CO<sub>2</sub> chemisorption conduce an activated state that has been also proposed as a precursor in the CO<sub>2</sub> dissociation.

From DFT calculations, the adsorption and transformation of CO<sub>2</sub> has been also studied. The decomposition of CO<sub>2</sub> into CO + O was evaluated on Fe, Co, Ni, and Cu surfaces. The results pointed that upon adsorption, the surfaces transfer an electronic charge toward CO<sub>2</sub>, which is directly correlated with the adsorption energies and follow a trend with the TM, Fe > Co > Ni > Cu [54]. Other results on TM surfaces concluded that the degree of activation and adsorption strength of CO<sub>2</sub> could be adjusted by the *d*-band centers of the catalysts [55], and that the transfer of electronic charge to CO<sub>2</sub> from TM materials generates its anionic specie CO<sub>2</sub><sup>δ-</sup> when chemisorption occurs [56,57].

Most theoretical studies about the CO<sub>2</sub> adsorption on late 3*d* metals employed periodic surface models, and there are few studies about this process employing clusters. In this context, the evaluation of size effects on CO<sub>2</sub> adsorption was reported on Cu clusters at different sizes [58]. The CO<sub>2</sub> adsorption strength increased monotonically from Cu(111) to Cu<sub>13</sub>. Even that, the CO<sub>2</sub> adsorbed kept its physisorption characteristics, at least for the lowest energy structures. In contrast, other study informed the CO<sub>2</sub> chemisorption thermodynamically favored on Cu clusters with 7, 13, and 19 [59]; however, this study does not clarify if those structures reported corresponded to the lowest energy structures or were selected based on the activation of CO<sub>2</sub>.

The adsorption on Co clusters with 13, 38, and 55 atoms also showed activated CO<sub>2</sub> via chemisorption and a monotonic increases of the interaction strength as the size of cluster decreased [60]. On the other hand, Cu<sub>4</sub> cluster and Cu<sub>4-x</sub>Pt<sub>x</sub> alloys was explored to evaluate the CO<sub>2</sub> adsorption. The results indicated that CO<sub>2</sub> becomes bent on the Cu<sub>4</sub> cluster and presents a negative partial charge. When Pt was included in the clusters, the Cu<sub>2</sub>Pt<sub>2</sub> shows the maximum value for the adsorption energy, revealing the effect of the alloy. Also, the adsorption energy as a function of the Pt composition exhibits a volcano-type plot, which is useful as a predictive tool [61].

The experimental and theoretical evidence shows the potential capability of the late 3d TM clusters with few atoms to promote the activation of the CO<sub>2</sub> via adsorption and also catalyze its reduction. To contribute in the understanding and characterization of CO<sub>2</sub> activation on small clusters, chapter 3 of this thesis addressed the adsorption of small molecules involved in the RWGS reaction (CO<sub>2</sub>, CO, H<sub>2</sub>O, H<sub>2</sub>) on 3d 13-atom TM clusters using Fe, Co, Ni, and Cu. We selected TM<sub>13</sub> clusters due to their predicted relative energetic stability when compared with 12- and 14-atom TM clusters [62]. In addition, experimental studies about the synthesis and characterization of Fe, Co, Ni, and Cu particles at different sizes, which includes 13-atom clusters, validated the clusters stability with few atoms and the possibility of using those materials as potential catalysts [63–65].

### 1.3.2 Reduction of CO<sub>2</sub> via RWGS

The CO<sub>2</sub> conversion via RWGS has been widely studied, since the CO produced can be a raw material to obtain long-chain hydrocarbons via FT synthesis [66]. The identification of reaction intermediates like oxygen (O), formate (HCOO), and carboxyl (COOH) allowed propose a general reaction scheme for RWGS based mainly in two routes [21, 25, 27]: the redox and associative [14]. For the redox route, CO<sub>2</sub> directly dissociates to CO and O while the oxidation of the catalyst occurs. A second step is required to recover the catalyst by its reduction with H<sub>2</sub>. Those steps were early suggested on Cu-based catalysts where the CO<sub>2</sub> dissociation was identified as the rate-determining step (RDS) [67, 68]. Afterward, since the oxides exhibited readily to reduce and to oxidize under specific reaction conditions, for CO<sub>2</sub> reduction on TM particles supported on oxides, the redox mechanism was also suggested [69, 70].

The route associative involves adsorption of CO<sub>2</sub>, H<sub>2</sub> or both on the catalyst's surface, and then the H bond formation either with the C or the O. Some intermediates detected are the HCOO, COOH, or bicarbonate (HCO<sub>3</sub><sup>-</sup>), the later mainly when oxides are used [14]. Further hydrogenation of those species would end in the formation of CO and H<sub>2</sub>O. The preference for one intermediate could depend on the catalysts and also on the operating conditions like temperature, pressure, electrode potential, etc [16]. For instance, the formation of formate has been favored using promoters and supports [71]; however, the HCOO is considered as spectator in the mechanism toward CO on TM surfaces such as Ni, Rh, and Cu [72–74], reducing preferentially to formic acid (HCOOH).

On the other hand, carboxyl species postulates as the active intermediate to obtain CO. It is formed via CO<sub>2</sub> adsorption assisted by the adsorbed H to form the adsorbed COOH [75]. Formation of CO occurs via direct dissociation of the carboxyl [14], as was observed on Cu and Pt catalysts via experiments of *in-situ* diffuse reflectance infrared spectroscopy (DRIFTS). Also, the kinetic analysis showed a correspondence between the

exchange time for carboxyl species and the CO production [74, 76]. More insights were provided with DFT calculations, that pointed out the dissociation of COOH as the RDS via carboxyl route on Pt and Ni substrates [77, 78]. However, since the experimental studies have given a lot of attention to the effect of the oxides as supports on the CO<sub>2</sub> conversion [21, 79], the mechanism on the metals alone is less understood.

In this context, studies using DFT have employed TM surfaces to explore the redox and carboxyl route for the RWGS reaction, e.g., Fe(100), Co(100), Ni(100), Ni(111), Cu(100), Cu(111), Rh(111), Pd(111), Ag(111), and Pt(111) [54, 80]. Specifically on *3d* TMs, the activation energies for CO<sub>2</sub> dissociation presented the following trend: Ni  $\approx$  Co < Cu < Fe. This study highlighted the balance between the exothermic character of the reaction step and the CO<sub>2</sub> adsorption strength. For instance, although Fe provided the most exothermic process, the CO<sub>2</sub> over-binds on this metal and increases the activation energy for dissociation [54]. Other study comparing the redox and carboxyl routes on *3d*, *4d*, and *5d* TMs concluded that the redox route is favored on metals with oxygen affinity like Ni, Rh, and Cu [80].

There are few studies about CO<sub>2</sub> reduction on TM clusters [58, 60, 81] focused on the size effect and reaction mechanisms towards the formation of methanol; however, the competition of the routes and how the C–O bond dissociation of the CO<sub>2</sub> occurs have been less explored. That limits our understanding at small scales that are important to develop improved materials, especially when the experimental research highlights the potential of single-atom catalysts for the CO<sub>2</sub> catalysis [82, 83]. Then, in chapter 4 we focus on the C–O bond dissociation in the CO<sub>2</sub> reduction via the redox and carboxyl routes on Fe<sub>13</sub>, Co<sub>13</sub>, Ni<sub>13</sub>, and Cu<sub>13</sub> clusters.

### 1.3.3 Electroreduction of CO<sub>2</sub> to C<sub>2</sub> Products

Since the capability of Cu catalysts to obtain C<sub>2</sub> and C<sub>2</sub>+ products from CO<sub>2</sub> electroreduction was reported [84, 85], the study of materials based on this metal gained a lot of attention looking to develop new catalysts with higher selectivity and at smaller overpotentials. The general reaction scheme follows similar idea discussed above with the RWG reaction, first the CO<sub>2</sub> reduces to CO and then the CO is the raw material to obtain hydrocarbons and alcohols [86]. Both experimental and theoretical results have been bringing insights in the CO<sub>2</sub>RR mechanism on Cu-based catalysts. Some proposed intermediates were: CO\*, COH\*, CHOH\*, C\*, CH<sub>2</sub>\*, and CH<sub>3</sub>\* [87, 88]. Later, from spectroscopy experiments, the CO\*, COCOH\*, and CH<sub>3</sub>CHO were also identified [89], informing possible intermediates that lead to C<sub>2</sub> products.

The first mechanism proposed for C<sub>1</sub> products formation from DFT calculations and computational hydrogen electrode method (CHE) reveals a preference to CH<sub>4</sub> production on Cu(211) surfaces with the following steps: CO<sub>2</sub>  $\longrightarrow$  COOH\*  $\longrightarrow$  CO\*  $\longrightarrow$  CHO\*  $\longrightarrow$

$\text{CH}_2\text{O}^* \longrightarrow \text{CH}_3\text{O}^* \longrightarrow \text{CH}_4 + \text{O}^*$  [87]. This path helps to explain the experimental results and also postulated the hydrogenation of CO as the possible potential-determining step [85]. From these results, several studies focused on the effect of different Cu facets, finding that the intermediates species were more (less) stabilized on (211) ((111)), exhibiting an effect related to the surface atoms coordination [47].

Recently, our group performed a detailed study about the coordination number (CN) effect on different paths into C<sub>1</sub> products like CO, HCOOH, CH<sub>4</sub>, and CH<sub>3</sub>OH [39,90]. Those results informed different pathways favoring the production of HCOOH according to the adsorption site coordination via COOH intermediate on the step region and HCOO on terrace region of Cu(533) surface. Also, the solvation correction influenced the path to CH<sub>4</sub> on CN = 9, which allows consistency with the experimental findings. Differently for the PDS reported on Cu(211), the PDS on CN = 5 was the water formation from OH\*, estimating larger onset potentials compared with more coordinated adsorption sites.

The selectivity to C<sub>1</sub> or C<sub>2</sub> products on Cu-based electrodes is structural sensitive. For instance, Cu(100) favor the conversion into C<sub>2</sub>H<sub>4</sub> with CH<sub>3</sub>CH<sub>2</sub>OH and CH<sub>3</sub>CHO as side products, Cu(111) is more active to CH<sub>4</sub> and HCOOH, and Cu(110) enhances the Faradaic efficiencies for C<sub>2</sub> products like CH<sub>3</sub>COOH, CH<sub>3</sub>CHO, and CH<sub>3</sub>CH<sub>2</sub>OH [91]. Studies about the electroreduction of CO on Cu(100) showed preferential formation of C<sub>2</sub>H<sub>4</sub> without CH<sub>4</sub> evolution, concluding that the path bifurcation into CH<sub>4</sub> and C<sub>2</sub>H<sub>4</sub> occurs before the CO formation [92]. Also, the CO electroreduction showed the formation of C<sub>2</sub> products like ethylene, acetaldehyde, and ethanol, suggesting that those products share a similar path and bifurcate in later stages [3,93–95].

Focusing on the later stages (after C–C bond formation) for the CO<sub>2</sub> and CO reduction, by CHE method the OCCOH\* was proposed as the intermediate that determines the onset potential to produce C<sub>2</sub> species on Cu(100) electrodes [3]. Later, this intermediate was detected using Fourier transform infrared spectroscopy during the CORR, supporting a possible path via OCCOH\* [89]. Regarding the path bifurcation between ethanol and ethylene, the CH<sub>2</sub>CHO\* specie seems to precede the bifurcation on Cu-based catalysts; explaining both, the preference formation of ethylene on Cu(100) single-crystal, or either ethanol formation on OD-Cu electrodes [3,96]. Recently, ethylene oxide has been proposed as a key species to produce ethylene selectively, and the acetaldehyde formation leads to the selective production of ethanol [97]. This study also suggested the importance of undercoordinated sites to favor ethanol production, which could guide the design of catalysts with site specifics to favor one or another intermediate.

Several studies informed the wide set of parameters that could tune product selectivity and the onset potentials for the CO<sub>2</sub>RR, for instance: experimental conditions related to the pH, temperature, pressure; modifications on the catalysts as the surface reconstruction during the electrocatalysis or the formation of alloys by the inclusion of a

second metal[88]. Regarding to the later, electrodes bases on cooper and a second metal, e.g., Au, Ag, or Zn, has increased the CO<sub>2</sub>RR efficiency compared to Cu by enhancing the production of C<sub>2</sub> and C<sub>2</sub>+ products [43–46]. Most of the studies explained this improvement due to the higher CO\* coverage observed on the alloy compared to the Cu electrodes. The higher amount of CO promotes its dimerization and consequently increases the C<sub>2</sub> species production.

As observed on Cu catalysts, CO<sub>2</sub>RR products selectivity on CuZn alloys are also composition- and structure-dependent. For instance, by in-situ extended X-ray absorption fine structure spectroscopy, the products distribution for CO<sub>2</sub>RR on CuZn nanoparticles showed that shorter interatomic distances favor the production of CH<sub>4</sub>, while nanoparticles with longer Cu–Zn distances favor the production of CO, which is then reduced to C<sub>2</sub> products [98]. Further, other properties evaluated to understand what is the most important characteristic for the synthesis of C<sub>2</sub> and C<sub>2</sub>+ compounds were the nanoparticle shape/surface morphology, chemical composition, and surface roughness [36]. The shape showed to be the biggest factor, where the nanocubes at the composition of Cu<sub>86.4</sub>Zn<sub>13.6</sub> led to higher Faradaic efficiency to C<sub>2</sub>+ products.

Although there are studies that mainly reported selectivity to C<sub>1</sub> products on CuZn alloys, it was attributed to the use of Zn-rich alloys [99, 100], while Cu-rich CuZn alloys showed more selectivity to ethanol and ethylene [47, 48]. In terms of mechanism, the CO<sub>2</sub>RR on Cu<sub>4</sub>Zn<sub>1</sub> showed maximized ethanol formation and the followed mechanism was proposed [47]: firstly, CO\* forms on copper and zinc, the CO\* on copper is further reduced to CH<sub>2</sub>\* while the CO\* on Zn migrates close to CH<sub>2</sub>\* to form CH<sub>2</sub>CO\*. Then, the CH<sub>2</sub>CO\* reduces to CH<sub>3</sub>CHO and finally to CH<sub>3</sub>CH<sub>2</sub>OH. The theoretical investigation of CuZn alloys at finite-size is still unexplored, as well as the second metal effects on the path stages after the C–C coupling. In chapter 5 we addressed this topic on nanoclusters of 55-atoms aiming to use a model with size that could be comparable with small nanoparticles, typically used experimentally.

## 1.4 Open Questions

To know how to promote the conversion of CO<sub>2</sub> to higher value-added products is necessary to have a better understanding of the elementary steps of the reaction mechanism, CO<sub>2</sub> adsorption, formation, and dissociation of bonds, desorption, etc. This knowledge could help answer open questions such as:

- i) What are the mechanisms that drive the CO<sub>2</sub> activation on TM-based materials at finite-size particles?
- ii) How OC–O bond dissociation occurs on TM-based materials at finite-size particles?

iii) What are the preferred reaction paths to  $C_2$  products, and how CuZn alloys could impact the last stages of  $CO_2$  conversion?

The answers to those and other questions could enable the selection of the materials based on rational design. However, this information is still incomplete, mainly on finite-size particles.

## 1.5 Objectives

### 1.5.1 General Objectives

This thesis contributes to the atomistic understanding of the activation and reaction path characterization for the  $CO_2$  reduction on finite-size particles based on  $3d$  TM. The points addressed were: the identification of descriptors to characterize the activation of small molecules important in the RWGS reaction; the mechanism elucidation and identification of scaling-relations for the C–O bond dissociation of the  $CO_2$  via redox and carboxyl routes; and the role of the nanoclusters of Cu and CuZn alloy on the later stages of the path to  $C_2$  products. The specific objectives are below, and each topic is discussed separately in different chapters.

### 1.5.2 Specific Objectives

- Study the activation of  $CO_2$ , CO,  $H_2$ , and  $H_2O$  via adsorption on  $Fe_{13}$ ,  $Co_{13}$ ,  $Ni_{13}$ , and  $Cu_{13}$  clusters to identify the atomistic descriptors that characterize their activation on  $3d$  13-atom TM clusters.
- Elucidate the reaction mechanism for the C–O bond dissociation of the  $CO_2$  on  $Fe_{13}$ ,  $Co_{13}$ ,  $Ni_{13}$ , and  $Cu_{13}$  clusters to evaluate the competition between routes and to identify scaling-relationships.
- Construct  $Cu_{55}$  and  $Cu_{42}Zn_{13}$  clusters models to evaluate the effect of the alloy on the later stages of the reaction paths to  $C_2$  products like acetaldehyde, ethanol, and ethylene.

## 2 THEORETICAL APPROACH AND COMPUTATIONAL DETAILS

Computational simulations at the atomic scale are a powerful tool to improve our understanding of the physical and chemical properties of the materials and their correlations with the molecular structure. Beyond identifying correlations between properties, it is possible to discover new materials, predict their behavior, and support the explanations for experimental observations. This chapter overviews the fundamentals of the theoretical approach as well as the description of methods and strategies used to study the CO<sub>2</sub> adsorption and conversion on transition-metals clusters. It covers the following sections: in (2.1) and (2.3) are including the theoretical basis of density functional theory; (2.4) computational implementation, (2.5) the climbing image-nudged elastic band method for the activation barriers calculations; (2.6) the computational hydrogen electrode model; (2.7) atomic structures generation and clustering algorithms; and (2.8) analysis.

### 2.1 Many-body Problem and Born–Oppenheimer Approximation

The quantum mechanics formalism describes the behavior of the subatomic particles, which allows studying systems at atomic and molecular scales. Within this formalism, the state of a system is characterized by its wave function,  $\Psi$ , then, to obtain information about the system in its stationary state, it must be solved the time-independent Schrödinger equation,

$$\widehat{H}\Psi(\mathbf{r}_1, \mathbf{r}_2, \dots, \mathbf{r}_N, \mathbf{R}_1, \mathbf{R}_2, \dots, \mathbf{R}_M) = E\Psi(\mathbf{r}_1, \mathbf{r}_2, \dots, \mathbf{r}_N, \mathbf{R}_1, \mathbf{R}_2, \dots, \mathbf{R}_M), \quad (2.1)$$

where,  $\widehat{H}$  is the Hamiltonian operator,  $\Psi$  is the wave function dependent of the positions for the  $N$  electrons and  $M$  nuclei,  $(\mathbf{r}_1, \mathbf{r}_2, \dots, \mathbf{r}_N)$  and  $(\mathbf{R}_1, \mathbf{R}_2, \dots, \mathbf{R}_M)$ , respectively, and  $E$  is the energy (eigenvalue) of the system in a given quantum mechanical state (eigenstate).

The Hamiltonian operator applied to the wave function provides the total energy of the system, defined as [101],

$$\begin{aligned} \widehat{H} &= \widehat{T}_{el} + \widehat{T}_{nuc} + \widehat{V}_{el-el} + \widehat{V}_{nuc-nuc} + \widehat{V}_{el-nuc} \\ &= \sum_{i=1}^N -\frac{1}{2}\nabla_{\mathbf{r}_i}^2 - \sum_{\alpha=1}^M \frac{1}{2M_{\alpha}}\nabla_{\mathbf{R}_{\alpha}}^2 + \sum_{i=1}^{N-1} \sum_{j=i+1}^N \frac{1}{|\mathbf{r}_i - \mathbf{r}_j|} + \\ &\quad \sum_{\alpha=1}^{M-1} \sum_{\beta=\alpha+1}^M \frac{Z_{\alpha}Z_{\beta}}{|\mathbf{R}_{\alpha} - \mathbf{R}_{\beta}|} - \sum_{i=1}^N \sum_{\alpha=1}^M \frac{Z_{\alpha}}{|\mathbf{r}_i - \mathbf{R}_{\alpha}|}; \end{aligned} \quad (2.2)$$

the expression (2.2) in atomic units includes contributions from the kinetic energy of electrons ( $\widehat{T}_{el}$ ), nuclei ( $\widehat{T}_{nuc}$ ), as well as the terms for Coulomb interactions between electrons ( $\widehat{V}_{el-el}$ ), nuclei ( $\widehat{V}_{nuc-nuc}$ ), and electrons-nuclei ( $\widehat{V}_{el-nuc}$ ).  $M_{\alpha}$  is the mass of



$\alpha$  nucleus, and the Laplacian operators ( $\nabla_{\mathbf{r}_i}^2, \nabla_{\mathbf{R}_\alpha}^2$ ) are:  $\nabla_{\mathbf{r}_i}^2 = \frac{\partial^2}{\partial x_i^2} + \frac{\partial^2}{\partial y_i^2} + \frac{\partial^2}{\partial z_i^2}$  and  $\nabla_{\mathbf{R}_\alpha}^2 = \frac{\partial^2}{\partial X_\alpha^2} + \frac{\partial^2}{\partial Y_\alpha^2} + \frac{\partial^2}{\partial Z_\alpha^2}$ .

However, the analytic solution of equation (2.1) is only possible for simple systems such as hydrogen-like atoms. For many-electron systems, the interaction between two or more electrons leads to coupling terms, difficulting its solution. A practical way to solve equation (2.1) for many-electron systems involves some simplifications, for instance, separating the electronic and nuclei motion, which is a consequence of the adiabatic and Born–Oppenheimer approximations [102, 103].

Although the quantitative details of the approximations are omitted here, below is provided a qualitative perspective and the derived results. The concept behind the approximations is that the electrons move faster than nuclei, implying that the nuclei cannot adapt instantaneously to the quick motion of the electrons, and they could be considered approximately fixed relative to the electrons. Under this assumption, the wave function is approximated as a product between the electronic and nuclear functions, written as

$$\Psi(\mathbf{r}_1, \mathbf{r}_2, \dots, \mathbf{r}_N, \mathbf{R}_1, \mathbf{R}_2, \dots, \mathbf{R}_M) = \Phi^{el}(\{\mathbf{r}_i\}; \{\mathbf{R}_\alpha\}') \varphi^{nuc}(\{\mathbf{R}_\alpha\}), \quad (2.3)$$

where the electronic function has a parametric dependence of the nuclear positions ( $\{\mathbf{r}_i\}; \{\mathbf{R}_\alpha\}'$ ). Equation (2.3) corresponds to the decoupling of the wave function in the electronic and nuclear problem, which are solved separately. Then, under the Born–Oppenheimer approximation, the following Schrödinger equations are obtained:

$$\widehat{H}_{el} \Phi^{el}(\{\mathbf{r}_i\}; \{\mathbf{R}_\alpha\}') = E^{el}(\{\mathbf{R}_\alpha\}') \Phi^{el}(\{\mathbf{r}_i\}; \{\mathbf{R}_\alpha\}'), \quad (2.4)$$

$$\widehat{H}_{nuc} \varphi^{nuc}(\{\mathbf{R}_\alpha\}) = (\widehat{T}_{nuc} + E(\{\mathbf{R}_\alpha\}')) \varphi^{nuc}(\{\mathbf{R}_\alpha\}) = E' \varphi^{nuc}(\{\mathbf{R}_\alpha\}), \quad (2.5)$$

with  $\widehat{H}_{el} = \widehat{T}_{el} + \widehat{V}_{el-el} + \widehat{V}_{el-nuc}$ ,  $E^{el}(\{\mathbf{R}_\alpha\}')$  as the electronic energy,  $E'$  the total energy of the system, and  $E(\{\mathbf{R}_\alpha\}')$  as the electronic energy for fixed nuclei positions including the nuclear repulsion term:

$$E(\{\mathbf{R}_\alpha\}') = E^{el}(\{\mathbf{R}_\alpha\}') + \sum_{\alpha=1}^{M-1} \sum_{\beta=\alpha+1}^M \frac{Z_\alpha Z_\beta}{|\mathbf{R}_\alpha - \mathbf{R}_\beta|}. \quad (2.6)$$

In summary, the Born–Oppenheimer approximation allows the solution for the electronic problem of a molecular system as follows: first, the nuclei positions are defined, then, in this nuclear environment, the electronic wave function is obtained using the Schrödinger equation (2.4). Since the coupling terms between different electronic states are neglected within the approximation, it would fail to properly describe the behavior when two or more potential surfaces approach or intersect one another [104, 105]. The sections below focus on the solution of the electronic problem constituted by equations (2.4) and (2.6).

## 2.2 Electronic Wave Function and the Electron Density

Now the problem focuses on the motion of the electrons at the fixed nuclei positions. The complete description of an electron involves the specification of the spin. Then, the spin-orbital is a function for one electron that describes its spatial coordinates and its spin [106],

$$u_i = \phi_i(\mathbf{r}_i)\xi(\omega), \quad (2.7)$$

where,  $u_i$  is the spin-orbital of the electron  $i$ ,  $\phi_i(\mathbf{r}_i)$  is the spatial function, and  $\xi(\omega)$  the spin function that can be spin-up or spin-down.

Thus, the electronic wave function of  $N$  electrons depends on their spatial and spin coordinates and can be constructed using spin-orbitals. Due to the fermionic nature of the electrons, the electronic wave function must be antisymmetric to the exchange between the coordinates of any two electrons. The way to guarantee this requirement is by the rearranging of the spin-orbitals in a Slater determinant,

$$\Phi(\{\mathbf{r}_i\}; \{\mathbf{R}_\alpha\}; \xi(\omega)) = \frac{1}{\sqrt{N!}} \begin{vmatrix} \phi_1(\mathbf{r}_1)\xi(\omega) & \phi_2(\mathbf{r}_1)\xi(\omega) & \dots & \phi_N(\mathbf{r}_1)\xi(\omega) \\ \phi_1(\mathbf{r}_2)\xi(\omega) & \phi_2(\mathbf{r}_2)\xi(\omega) & \dots & \phi_N(\mathbf{r}_2)\xi(\omega) \\ \vdots & \vdots & \ddots & \vdots \\ \phi_1(\mathbf{r}_N)\xi(\omega) & \phi_2(\mathbf{r}_N)\xi(\omega) & \dots & \phi_N(\mathbf{r}_N)\xi(\omega) \end{vmatrix}. \quad (2.8)$$

The equation (2.8) provides some important consequences. *i)* The determinant becomes equal to zero if two columns are identical, which could be interpreted as the electrons with the same spin cannot occupy the same orbital. *ii)* The Slater determinant could be different from zero if two electrons occupy the same orbital but with opposite spin values. Thus, when the equation (2.4) uses the electronic wave function with the form of the equation (2.8) in addition to the Coulomb term for the electrostatic interaction, appears an important term known as the exchange term. The exchange term typically has been attributed to the antisymmetry of the wave function; however, it is a consequence of the permutation symmetry of the Hamiltonian of a many-electron system.

Formalisms using the electronic wave function to treat the equation (2.4) have been proposed, for instance, Hartree–Fock [106]. However, this formalism presents limitations to include the electronic correlation effects, and the use of methods to treat this problem is computationally expensive. To tackle those issues from a different perspective, methodologies that employ electron density have been developed. The electron density,  $\rho(\mathbf{r})$ , can be obtained by,

$$\rho(\mathbf{r}) = \sum_{i=1}^N |\phi_i|^2. \quad (2.9)$$

In this context, the formalism of our interest in this study is the density functional theory [107], which allows describing  $N$ -electrons systems employing  $\rho(\mathbf{r})$ , that depends on 3

variables, instead of the electronic wave function, that depends on  $3N$  variables, reducing the dimensionality of the problem.

### 2.3 Density Functional Theory

The DFT is grounded in two theorems proposed by Pierre C. Hohenberg and Walter Kohn, known as Hohenberg–Kohn (HK) theorems.

#### 2.3.1 Hohenberg–Kohn Theorems

For a collection of  $N$ -electrons under the influence of an external potential,  $v_{ext}(\mathbf{r})$ , and their mutual Coulomb repulsion, the first theorem states that [107]: "*two external potentials that differ by more than an additive constant cannot provide the same ground state electron density,  $\rho_0(\mathbf{r})$ .*" Implying an uniquely correspondence between the  $\rho_0(\mathbf{r})$  and the  $v_{ext}(\mathbf{r})$ . Where the external potential  $v_{ext}(\mathbf{r})$  is defined by:

$$v_{ext}(\mathbf{r}) = - \sum_{\alpha=1}^M \frac{Z_{\alpha}}{|\mathbf{r} - \mathbf{R}_{\alpha}|}. \quad (2.10)$$

Considering that the external potential fixes the Hamiltonian, it is deduced from the theorem that the ground state energy of the system is determined by the ground state electron density. Then, the ground state energy,  $E_0$ , is a functional of  $\rho_0(\mathbf{r})$ , that is written as  $E_0 = E[\rho_0(\mathbf{r})]$ , where the square brackets denote a functional relation. In this sense, a functional is a mathematical rule that take functions as arguments, which is used in DFT to calculate  $E_0$  from  $\rho_0(\mathbf{r})$  by

$$E[\rho_0(\mathbf{r})] = T_{el}[\rho_0(\mathbf{r})] + V_{el}[\rho_0(\mathbf{r})] + V_{ext}[\rho_0(\mathbf{r})], \quad (2.11)$$

where  $V_{ext}[\rho_0(\mathbf{r})]$  is obtained by:

$$V_{ext}[\rho_0(\mathbf{r})] = \left\langle \Phi \left| \sum_{i=1}^N v_{ext}(\mathbf{r}) \right| \Phi \right\rangle = \int \rho_0(\mathbf{r}) v_{ext}(\mathbf{r}) d\mathbf{r}. \quad (2.12)$$

Thus,  $V_{ext}[\rho_0(\mathbf{r})]$  is known, however, the functionals  $T_{el}[\rho_0(\mathbf{r})]$  and  $V_{el}[\rho_0(\mathbf{r})]$  are unknown. Then:

$$\begin{aligned} E[\rho_0(\mathbf{r})] &= \int \rho_0(\mathbf{r}) v_{ext}(\mathbf{r}) d\mathbf{r} + T_{el}[\rho_0(\mathbf{r})] + V_{el}[\rho_0(\mathbf{r})] \\ &= \int \rho_0(\mathbf{r}) v_{ext}(\mathbf{r}) d\mathbf{r} + F_{HK}[\rho_0(\mathbf{r})], \end{aligned} \quad (2.13)$$

where  $F_{HK}[\rho_0(\mathbf{r})] \equiv T_{el}[\rho_0(\mathbf{r})] + V_{el}[\rho_0(\mathbf{r})]$  is independent of the external potential.

To obtain  $E[\rho(\mathbf{r})]$  from (2.11), it is necessary a second theorem. This theorem provides the variational principle [107]: "*For a trial density  $\rho(\mathbf{r})$  such that  $\int \rho(\mathbf{r}) d\mathbf{r} = N$  and  $\rho(\mathbf{r}) \geq 0$ , the following inequality is valid:  $E[\rho_0(\mathbf{r})] \leq E[\rho(\mathbf{r})]$ .*" Which can be written as:

$$\langle \Phi | \widehat{H}_{el} | \Phi \rangle = \int \rho(\mathbf{r}) v_{ext}(\mathbf{r}) d\mathbf{r} + F_{HK}[\rho(\mathbf{r})] = E[\rho(\mathbf{r})] \geq E[\rho_0(\mathbf{r})]. \quad (2.14)$$

To minimize  $E[\rho(\mathbf{r})]$  the Lagrange multipliers method is used, assuming differentiability of  $E[\rho(\mathbf{r})]$ :

$$\delta \left\{ E[\rho(\mathbf{r})] - \mu \left[ \int \rho(\mathbf{r}) d\mathbf{r} - N \right] \right\} = 0. \quad (2.15)$$

Equation (2.14) is used in equation (2.15) to obtain the following Euler-Lagrange equation:

$$\frac{\delta E[\rho(\mathbf{r})]}{\delta \rho(\mathbf{r})} = v_{ext}(\mathbf{r}) + \frac{\delta F_{HK}[\rho(\mathbf{r})]}{\delta \rho(\mathbf{r})} = \mu, \quad (2.16)$$

where  $\mu$  is a Lagrange multiplier associated with the constrain condition  $\int \rho(\mathbf{r}) d\mathbf{r} - N = 0$ , which is interpreted as the chemical potential of the system.

The Hohenberg–Kohn formalism affords the bases of DFT but does not provide a practical way to calculate the energy from the electron density, because the functional  $F_{HK}[\rho(\mathbf{r})]$  is unknown. To apply this theory was necessary to devise a method to carry out the calculations with DFT.

### 2.3.2 Kohn–Sham Method

The Kohn–Sham (KS) method considered an auxiliary reference system *ref* of  $N$  non-interacting electrons feeling the external potential  $v_{ext,ref}(\mathbf{r})$ . This  $v_{ext,ref}(\mathbf{r})$  is such that the electronic density of the reference system  $\rho_{ref}(\mathbf{r})$  is the same electronic density  $\rho(\mathbf{r})$  in the real system of interest,  $\rho_{ref}(\mathbf{r}) = \rho(\mathbf{r})$  [108]. Taking account of this, the Hohenberg–Kohn equation (2.13) can be rewritten as follow. First,  $\Delta T$  is defined as:

$$\Delta T[\rho] \equiv T_{el}[\rho(\mathbf{r})] - T_{ref}[\rho(\mathbf{r})], \quad (2.17)$$

where  $T_{el}[\rho(\mathbf{r})]$  and  $T_{ref}[\rho(\mathbf{r})]$  are the kinetic electronic energies of the real system in the ground state and the reference system *ref*, respectively. A second definition is  $\Delta V_{el}[\rho(\mathbf{r})]$ :

$$\Delta V_{el}[\rho(\mathbf{r})] \equiv V_{el}[\rho(\mathbf{r})] - \frac{1}{2} \int \int \frac{\rho(\mathbf{r})\rho(\mathbf{r}')}{|\mathbf{r} - \mathbf{r}'|} d\mathbf{r}d\mathbf{r}', \quad (2.18)$$

where,  $|\mathbf{r} - \mathbf{r}'|$ , in the classical expression for the electrostatic repulsion, is the distance between the points of coordinates  $x, y, z$  and  $x', y', z'$ .

With the definitions (2.17) and (2.18), (2.13) becomes:

$$E[\rho(\mathbf{r})] = \int \rho(\mathbf{r})v_{ext}(\mathbf{r})d\mathbf{r} + T_{ref}[\rho(\mathbf{r})] + \frac{1}{2} \int \int \frac{\rho(\mathbf{r})\rho(\mathbf{r}')}{|\mathbf{r} - \mathbf{r}'|} d\mathbf{r}d\mathbf{r}' + \Delta T[\rho(\mathbf{r})] + \Delta V_{el}[\rho(\mathbf{r})]. \quad (2.19)$$

$\Delta T[\rho(\mathbf{r})]$ ,  $\Delta V_{el}[\rho(\mathbf{r})]$  functionals are unknown. Thus, the exchange-correlation energy functional,  $E_{xc}[\rho(\mathbf{r})]$ , is defined as:

$$E_{xc}[\rho(\mathbf{r})] \equiv \Delta T[\rho(\mathbf{r})] + \Delta V_{el}[\rho(\mathbf{r})], \quad (2.20)$$

and (2.19) can be written as:

$$E[\rho(\mathbf{r})] = \int \rho(\mathbf{r})v_{ext}(\mathbf{r})d\mathbf{r} + T_{ref}[\rho(\mathbf{r})] + \frac{1}{2} \int \int \frac{\rho(\mathbf{r})\rho(\mathbf{r}')}{|\mathbf{r} - \mathbf{r}'|} d\mathbf{r}d\mathbf{r}' + E_{xc}[\rho(\mathbf{r})]. \quad (2.21)$$

The minimization of the equation (2.21) leads to the following expression:

$$\frac{\delta E[\rho(\mathbf{r})]}{\delta \rho(\mathbf{r})} = v_{ext}(\mathbf{r}) + \frac{\delta T_{ref}[\rho(\mathbf{r})]}{\delta \rho(\mathbf{r})} + \int \frac{\rho(\mathbf{r}')}{|\mathbf{r} - \mathbf{r}'|} d\mathbf{r}' + \frac{\delta E_{xc}[\rho(\mathbf{r})]}{\delta \rho(\mathbf{r})}. \quad (2.22)$$

The equation (2.9) provided the form for  $\rho(\mathbf{r})$ , where the spatial part of the spin-orbital is known as Kohn–Sham (KS) orbital in the KS formulation,  $\phi_i^{KS}$ . Combining the equations (2.21) and (2.9), the following single-particle Schrödinger equation is obtained:

$$\hat{h}^{KS} \phi_i^{KS}(\mathbf{r}) = \left[ -\frac{1}{2} \nabla_{\mathbf{r}_i}^2 + v_{eff}(\mathbf{r}) \right] \phi_i^{KS}(\mathbf{r}) = \varepsilon_i^{KS} \phi_i^{KS}(\mathbf{r}), \quad (2.23)$$

$$v_{eff} = v_{ext}(\mathbf{r}) + \int \frac{\rho(\mathbf{r}')}{|\mathbf{r} - \mathbf{r}'|} d\mathbf{r}' + \frac{\delta E_{xc}[\rho(\mathbf{r})]}{\delta \rho(\mathbf{r})}. \quad (2.24)$$

The last term in the right side is the exchange-correlation potential denoted by  $v_{xc}(\mathbf{r})$ .

The expression 2.23 is known as the Kohn–Sham equation, and its solution involves a self-consistent process [109]: first begins assuming a density  $\rho(\mathbf{r})$ , constructed from (2.9), that providing the  $v_{eff}$  from (2.24), allowing the solution of equation (2.23) to find a new  $\rho(\mathbf{r})$ , from which effective potential can be obtained to restart the cycle until achieve convergence. After solving the KS equations and obtaining the electron density, the total energy of the system, including the constant energy term of nuclei-nuclei interactions, is calculated by:

$$E[\rho(\mathbf{r})] = \sum_{i=1}^N \varepsilon_i - \int \rho(\mathbf{r})v_{xc}(\mathbf{r})d\mathbf{r} - \frac{1}{2} \int \int \frac{\rho(\mathbf{r})\rho(\mathbf{r}')}{|\mathbf{r} - \mathbf{r}'|} d\mathbf{r}d\mathbf{r}' + E_{xc}[\rho(\mathbf{r})] + \sum_{\alpha=1}^{M-1} \sum_{\beta=\alpha+1}^M \frac{Z_{\alpha}Z_{\beta}}{|\mathbf{R}_{\alpha} - \mathbf{R}_{\beta}|}. \quad (2.25)$$

### 2.3.3 Exchange-correlation Functionals

As mentioned earlier, the  $E_{xc}[\rho(\mathbf{r})]$  functional is unknown, even so, the information it contains is related to the following components:

1. **The kinetic energy correction:** the term  $\Delta T[\rho(\mathbf{r})]$  in (2.20) is related with the quantity of kinetic energy needed to correct  $T_{ref}[\rho(\mathbf{r})]$  to obtain the kinetic energy of the real system  $T_{el}[\rho(\mathbf{r})]$ .
2. **The exchange energy:** associated with the requirement of antisymmetry in the electronic wave function.

3. **The electronic correlation energy:** Consider the interaction between the electrons as a function of the correlation of their movements. That means that the behavior of one electron can affect the interaction between them.
4. **Self-interaction correction (SIC):** necessary to correct the self-interaction that derives from the fact that the expression of electrostatic repulsion of the classical charge cloud erroneously allows that a portion of  $\rho(\mathbf{r})$  in  $d\mathbf{r}$ , interact with other portion of the charge contributions of the same electron.

Finding accurate approximations for the exchange-correlation energy is a key aspect for the applicability of the KS formalism and to perform DFT calculations. Then, different formulations for  $E_{xc}$  have been developed. In this context, we have the generalized gradient approximations (GGA) which consider semi-local corrections, meaning that besides the information of  $\rho(\mathbf{r})$  in a particular point  $\mathbf{r}$ , it includes a gradient dependence,  $\nabla\rho(\mathbf{r})$ , to take into account the variation of  $\rho(\mathbf{r})$  with  $\mathbf{r}$ , thus considering the non-homogeneity of the true electron density. The general expression for  $E_{xc}^{\text{GGA}}$  is:

$$E_{xc}^{\text{GGA}}[\rho(\mathbf{r})] = \int f(\rho(\mathbf{r}), |\nabla\rho(\mathbf{r})|) d\mathbf{r}. \quad (2.26)$$

Usually, the expressions for  $E_{xc}^{\text{GGA}}$  involve the sum of the exchange and correlation parts that are modeling separately:

$$E_{xc}^{\text{GGA}} = E_x^{\text{GGA}} + E_c^{\text{GGA}}. \quad (2.27)$$

In this investigation,  $E_{xc}^{\text{GGA}}$  proposed by Perdew, Burke, and Ernzerhof, known as PBE functional, was employed [110]. In the PBE functional the  $E_x^{\text{PBE}}$  is defined by:

$$E_x^{\text{PBE}}[\rho(\mathbf{r})] = \int \rho(\mathbf{r}) \epsilon_x^{\text{unif}}(\rho(\mathbf{r})) F_x(s) d\mathbf{r}, \quad (2.28)$$

where  $\epsilon_x^{\text{unif}} = -\frac{3k_F}{4\pi}$  is the exchange energy of the uniform electron gas approximation,  $k_F = (3\pi^2\rho(\mathbf{r}))^{\frac{1}{3}}$  is the local Fermi wave vector, and  $F_x(s) = 1 + \kappa - \frac{\kappa}{1 + \frac{\mu s^2}{\kappa}}$  with  $s = \frac{|\nabla\rho(\mathbf{r})|}{2k_F\rho(\mathbf{r})}$ ,  $\mu = 0.21951$ , and  $\kappa = 0.804$ . While the correlation part  $E_c^{\text{PBE}}$  is written as:

$$E_c^{\text{PBE}}[\rho(\mathbf{r})] = \int \rho(\mathbf{r}) [\epsilon_c^{\text{unif}}(r_s) + H(r_s, \zeta, t)] d\mathbf{r}, \quad (2.29)$$

where  $\epsilon_c^{\text{unif}}$  expression is obtained from the Perdew-Wang parameterization [111],  $r_s = (\frac{3}{4\pi\rho(\mathbf{r})})^{\frac{1}{3}}$  is the local Seitz radius, and the gradient contribution  $H(r_s, \zeta, t)$  was constructed from three conditions discussed in details in the Perdew, Burke, and Ernzerhof paper [110].

### 2.3.4 van der Waals Corrections

Standard local and semi-local functionals, such as LDA and GGA, can hardly provide a suitable description of the asymptotic long-range interatomic behavior that

is characteristic of van der Waals (vdW) dispersion interactions [112]. The vdW forces are distance-dependent interactions between atoms or molecules. Distinct from ionic or covalent bonds, vdW attractions do not result in a chemical bond and are comparatively weak. For instance, vdW forces appear from the fluctuation in the polarizations of two molecules close to each other and quickly vanishes at longer distances. The term includes dipole-dipole, dipole-induced dipole, and London dispersion forces. Those forces could be crucial in determining the structural, electronic, and energetic properties of several weak interacting systems, including DNA, and the interaction of some molecules with surfaces [113–115].

In the last decade, some approaches emerged to improve the accuracy in the description of vdW interactions [112]. Some common used methods adding a pairwise interatomic term,  $E_{\text{disp}}$ , to the energy of equation (2.25),  $E_{\text{DFT}}$ . The energy then reads:

$$E_{\text{tot}} = E_{\text{DFT}} + E_{\text{disp}}, \quad (2.30)$$

where the  $E_{\text{disp}}$  has the following general expression,

$$E_{\text{disp}} = -\frac{1}{2} \sum_{A,B} f_{\text{damp}}(R_{AB}, R_A^0, R_B^0) \frac{C_{6AB}}{R_{AB}^6}. \quad (2.31)$$

The expression (2.31) includes: the attractive vdW pair potential form by including the  $R_{AB}^{-6}$  term, which describes the behavior of the energy decay as a function of the interatomic distance,  $R_{AB}$ , between atoms  $A$  and  $B$ ;  $R_A^0$  and  $R_B^0$  are the vdW radii; the  $f_{\text{damp}}$  is a damping function employed to avoid the singularity at zero distance; and  $C_{6AB}$  are the interatomic dispersion coefficients, which can be obtained from different formulas using the ionization potentials and polarizabilities [116,117]. Compared with other approaches such as non-local correlation functionals or many-body dispersion, the pairwise-additive provides a slighter increase in the computational cost [112].

Studies about adsorption and catalytic processes on metal surfaces for several systems reported that the simples pairwise-additive corrections provide reasonably good vdW forces description [118]. In this context, the most used approaches are the D3 correction method of Grimme [119] and the Tkatchenko–Scheffler correction (TS) [120]. Since this study involved the adsorption of species that weakly interact with the transition metals clusters, we employed in our calculations the vdW Tkatchenko–Scheffler correction available in the software used.

The Tkatchenko–Scheffler approach uses reference values of atomic polarizabilities and atomic dispersion coefficients to obtain the  $C_{6AB}$  coefficient. Also, it considers the environment-dependency of atomic dispersion coefficient by including a correction involving the effective volume of the atoms based on the Hirshfeld partitioning scheme, and the damping function employed is Fermi-type [120],

$$f_{damp}(R_{AB}, R_{AB}^0) = \frac{1}{1 + \exp \left[ -d \left( \frac{R_{AB}}{s_R R_{AB}^0} - 1 \right) \right]}, \quad (2.32)$$

where  $R_{AB}^0 = R_A^0 = R_B^0$ ,  $d$  and  $s_R$  are empirical parameters [120].

## 2.4 Computational Implementation

There are several packages to carry out the solution of the Kohn–Sham equations (2.23). In this investigation, the Fritz-Haber Institute *Ab initio* Molecular Simulations package (FHI-aims) was used for all electronic structure calculations [121]. For this, the first step is to choose the set of basis functions to represent the Kohn–Sham orbitals  $\phi_i^{KS}$  by their linear combination,

$$\phi_i^{KS} = \sum_k^n C_{ki} \psi_k(\mathbf{r}), \quad (2.33)$$

here,  $\psi_k(\mathbf{r})$  represents the basis functions and  $C_{ki}$  are the coefficients in the linear combination.

Within the basis sets provided by the FHI-aims code are the numerical orbitals centered on the atoms (NAOs) [121]. The general shape of NAOs basis functions is:

$$\psi_k(\mathbf{r}) = \frac{u_k(r)}{r} Y_{lm}(\Omega), \quad (2.34)$$

with  $Y_{lm}(\Omega)$  as the spherical harmonics obtained from the solution of the Schrödinger equation for hydrogenoid systems, and  $u_k(r)$  is the radial part that includes both analytically and numerically defined functions.  $u_k(r)$  comes from the numerical solution of the following equation:

$$\left[ -\frac{1}{2} \frac{d^2}{dr^2} + \frac{l(l+1)}{r^2} + \nu_k(r) + \nu_{cut}(r) \right] u_k(r) = \varepsilon_k u_k(r), \quad (2.35)$$

where  $\nu_k(r)$  is a potential that provides the behavior of  $u_k(r)$ ,  $\nu_{cut}(r)$  is a confining potential, which guarantees the decay of each radial function to zero, taken into account the confining radius  $r_{cut}$ . The  $\nu_{cut}(r)$  used in FHI-aims have the following shape:

$$\nu_{cut}(r) = \begin{cases} 0 & r \leq r_{onset} \\ s \times \exp \left( \frac{w}{r - r_{onset}} \right) \times \frac{1}{(r - r_{cut})^2} & r_{onset} < r < r_{cut} \\ \infty & r \geq r_{cut}, \end{cases} \quad (2.36)$$

which mean that,  $\nu_{cut}(r)$  grows exponentially from a value  $r_{onset}$  up to cutting radius  $r_{cut}$ . At  $r_{cut}$ ,  $\nu_{cut}(r)$  is infinity and the function decays to zero.  $s$  and  $w$  are default values, 200 Ha and 2.0 Å, respectively. The definition of  $\nu_{cut}(r)$  is an advantage when using NAO, because it allows the radial functions to be localized. Depending on  $\nu_{cut}(r)$ , the type of basis set are established, called *Light* and *Tight*. One of the differences between the two



sets of bases is the extension of each radial function defined by  $\nu_{cut}(r)$ , which for the set *Light* it is 5.0 Å, while for the set *Tight* it is 6.0 Å. On the other hand, the  $Y_{lm}(\Omega)$  are organized in levels of basis function groups of different angular momenta  $l$  namely *tier 1*, *tier 2*, and *tier 3*. More details about the type of functions in each group for specific atom could be found in the paper: *Ab initio* molecular simulations with numeric atom-centered orbitals [121].

All calculations were performed within spin-polarized DFT using the exchange-correlation (XC) energy functional proposed by Perdew–Burke–Ernzerhof (PBE) [110], employing the vdW correction formulated by Tkatchenko–Scheffler [120] and the *light-tier2* basis set. The detailed computational parameters and the convergences tests performed to guide their selection are in Appendix A.

## 2.5 Searching Transition States: Climbing Image-Nudged Elastic Band Method

We employed the nudged elastic band algorithm (NEB) combined with climbing image (CI) to identify transition states by finding the minimum energy path (MEP) that connects two minimum points on the potential energy surface (initial and final state) [122]. For CI-NEB calculations, firstly, the atomic position for the initial and final states are specified. Then, a path between those states can be discretized by creating a number of replicas (defined by the user) from the interpolation between the states, for instance, a linear interpolation. The set of replicas, commonly called images, compound the initial path to be optimized iteratively until converging to the MEP.

During relaxation of the MEP, the images are moved in each iteration according to the forces, i.e., the negative gradient of the energy concerning the atomic coordinates,  $-\nabla E(\mathbf{R}_\alpha)$ , which comes from the DFT calculations in this study. The total force on each image has a parallel ( $F_{\parallel}$ ) and a perpendicular ( $F_{\perp}$ ) component as:

$$\mathbf{F} = F_{\parallel} + F_{\perp} = \kappa r + F_{\perp}, \quad (2.37)$$

where  $\kappa$  is a spring constant and  $r$  is the distance between images. In this study, the value of  $\kappa$  was defined based on the tests reported in the Appendix. Then, each image interacts with its neighbor in the parallel direction to the path by spring forces. Hence, the  $F_{\parallel}$  prohibits the image’s relaxation down to a local minimum, and  $F_{\perp}$  ensures the image relaxation into the MEP.

The part with the most interest along the MEP is the highest energy point, which is the possible first-order saddle point along the path connecting the initial and final states. The CI method allows refining the saddle point by using the highest energy image, releasing it from all spring forces, and forcing it to “climb” upward until converging to the highest saddle point [122]. Finally, the maximum energy image is verified as a potential transition

state if it has one imaginary vibration frequency parallel to the MEP. Details about the strategies employed in this study to perform these calculations are in the Appendix B.

## 2.6 Modeling in Electrocatalysis: The Computational Hydrogen Electrode Approach

The computational hydrogen electrode model enables the study of the electrocatalytic process from first-principles calculations [87,123]. Within the CHE approach, firstly the reaction mechanism must be specified to evaluate the Gibbs free energy changes in each elementary step,  $\Delta G = \Delta H - T\Delta S$ . Within this model, the free energy for each component  $i$  in the elementary step is computed by

$$G_i = H_i - TS_i, \quad (2.38)$$

where the enthalpy for the component  $i$  is:

$$H_i = E_{tot} + E_{sol} + E_{energy}^{ZPE} + E_{thermal} + PV. \quad (2.39)$$

In the equation (2.39), the  $E_{tot}$  is the total energy from electronic structure calculations,  $E_{sol}$  the solvation energy,  $E_{energy}^{ZPE}$  the zero-point energy,  $E_{thermal}$  the thermal energy, and the last term refers to pressure,  $P$ , and volume,  $V$ . In this study we used DFT calculation to obtain  $E_{tot}$ , the  $E_{energy}^{ZPE}$ ,  $E_{thermal}$  and  $PV$  information were obtained from the vibrational frequencies calculations, and the  $E_{sol}$  values comes from a previous study [3] that provided values for the adsorbed species according to their functional groups. In the  $H_i$  for molecule in the gas-phase,  $E_{sol}$  is neglected in equation (2.39), while for adsorbed species  $E_{sol}$  is included and the  $PV$  term is excluded. Thus, the free energy for the species in the gas-phase,  $G_i^{gp}$ , and adsorbed,  $G_i^{ad}$ , are:

$$G_i^{gp} = E_{tot} + E_{energy}^{ZPE} + E_{thermal} - TS + PV \text{ and} \quad (2.40)$$

$$G_i^{ad} = E_{tot} + E_{sol} + E_{energy}^{ZPE} + E_{thermal} - TS. \quad (2.41)$$

The term  $(E_{energy}^{ZPE} + E_{thermal} - TS)$  for adsorbed molecules is typically obtained at 298 K and can be calculated within the harmonic limit using the following equations:

$$E_{energy}^{ZPE} = \sum_l \frac{1}{2} \epsilon_l, \quad (2.42)$$

$$E_{thermal} = \sum_l \frac{\epsilon_l}{e^{\epsilon_l/k_B T} - 1}, \quad (2.43)$$

$$S = k_B \sum_l \frac{\epsilon_l}{k_B T (e^{\epsilon_l/k_B T} - 1)} - \ln(1 - e^{-\epsilon_l/k_B T}), \quad (2.44)$$

where  $\epsilon_l$  are the energies associated with the vibrational frequencies,  $k_B$  the Boltzmann constant, and  $T$  the temperature. For gas-phase systems,  $E_{thermal}$  and  $S$  terms, are calculated under gas ideal limit.

In the CHE method, each elementary step within a given reaction pathway is formulated as the removal (oxidation) or addition (reduction) of a proton and an electron,  $\text{H}^+ + \text{e}^-$ . Since the chemical potentials of proton and electron are still less straightforward to determine in *ab initio* calculations, Rossmeisl and Nørskov proposed following an analogous idea to experiments. To compare different setups of experiments, the potentials are measured with respect to a known reference potential of a well-defined standard reaction, typically the hydrogen formation:



Under this consideration, it is possible to set up the free energy reference by assuming the free energy of protons and electrons as the free energy of  $\text{H}_2$ ,  $\frac{1}{2}G_{\text{H}_2} = G_{(\text{H}^+ + \text{e}^-)}$ . Also, the contribution from the influence of applied electrical potential,  $U$ , it is included by setting the total energy of the electron in the electrode as  $-qU$  where  $q$  is the fundamental charge. Thus, the free energy of each step will vary with  $U$  according to  $\Delta G(U) = \Delta G(U = 0) - eU$ . Therefore, changes in the electrode potential can be adjusted by changing the energy of a proton-electron pair by  $-eU$ .

Finally, the highest positive free energy value between all the steps is the potential-determining step (PDS), which provides the lowest electrode potential that should be applied to obtain a target product via the reaction pathway studied,  $U_{\text{PDS}}$ :

$$U_{\text{PDS}} = -\Delta G_{\text{MAX}}/e^- . \quad (2.46)$$

## 2.7 Atomic Structures Generation and Clustering Algorithms

To obtain the trial structures for molecules, Mol, adsorbed on transition metal clusters with 13 and 55 atoms, namely,  $\text{TM}_{13} = \text{Fe}_{13}, \text{Co}_{13}, \text{Ni}_{13}, \text{Cu}_{13}$ , and  $\text{TM}_{55} = \text{Cu}_{55}, \text{Cu}_{42}\text{Zn}_{13}$ , we combined a procedure developed in-house that automatically generates a huge number of structures [124–126], the K-means algorithm [127], and no-automatic design of structures. The workflow proceeded as follow:

1. **Optimized TM clusters and molecules:** for all TM clusters employed in this study, we selected the lowest energy structures among the optimized sets. For  $\text{TM}_{13}$  clusters, a set of 52 configurations were re-optimized, which included low and high symmetry structures from a previous study performed in the group [62, 115]. For  $\text{Cu}_{55}$  clusters, the icosahedral, cuboctahedral, and distorted models were explored. Further, to design the  $\text{Cu}_{42}\text{Zn}_{13}$  cluster alloys, we used the icosahedral model as this configuration presents the lowest energy for  $\text{Cu}_{55}$ . The clusters alloys considering core-shell types structures with most Zn atoms at the core ( $C_{\text{Zn}}S_{\text{Cu}}$ ), with most of the Zn at the shell ( $C_{\text{Cu}}S_{\text{Zn}}$ ), and a segregated cluster ( $Seg_{\text{Cu-Zn}}$ ). Also, we employed all the molecules and intermediates previously optimized.

2. **Molecules around the clusters:** considering the fixed atomic positions of the TM clusters (TM<sub>13</sub> and TM<sub>55</sub>), the molecule was randomly positioned around the cluster at 2.00 Å of distance, which was selected based on previous test calculations of CO<sub>2</sub>, CO, H<sub>2</sub>O, and H<sub>2</sub> on Fe<sub>13</sub> cluster and provided a bond distance about 2.00 Å. We generated 10<sup>8</sup> configurations, that later was reduced to a smaller set. This reduction was guided by the modified Euclidean similarity distance (ESD) algorithm [128, 129], employed in previous studies [125, 130], which compares the structures in pairs and identify the structural similarity based on defined ESD criteria,  $\Delta_{a,b}$ , equation (2.47),

$$\Delta_{a,b} > \frac{\sum_{i=1}^N (d_{i,a} - d_{i,b})^2}{\sum_{i=1}^N d_{i,a}^2 + d_{i,b}^2}, \quad (2.47)$$

where  $N$  is the number of atoms in the structure  $a$  and  $b$ ,  $d_{i,a}$  and  $d_{i,b}$  are the distances of the  $i$ th atom to the geometric center of the structures  $a$  and  $b$ , respectively. The denominator allows the normalization and removes the dimensionality, which provides a quantity independent of the species and cluster size.  $\Delta_{a,b}$  values was tested for each case in order to keep sets from 4 to 30 configurations, according to the molecule complexity and TM cluster symmetry.

3. **K-means algorithm:** specifically for the study of molecules/TM<sub>55</sub>, we employed the K-means algorithm to perform an additional reduction of the trial configurations from thousand to dozens based only on the structural information.

K-means is a widely used method to clustering information [127]. The essence of algorithm is partitioning the  $n$  observables or samples into a set of  $K$  groups. Considering  $X = x_i, i = 1, \dots, n$  as a set of  $n$   $d$ -dimensional points to be grouped into a  $K$  sets,  $C = c_k, k = 1, \dots, K$ , the partition aims to minimize the squared error between samples  $x_i$  and the centroids ( $\mu_k$ ) of each  $c_k$  group by:

$$J(C) = \sum_{k=1}^K \sum_{x_i \in c_k} \|x_i - \mu_k\|^2. \quad (2.48)$$

Then, the algorithm follow two steps:

- a) Each  $x_i$  is assigning to its closest centroid between the  $c_k$  groups.
- b) The centroid of each  $c_k$  group is re-compute taken the mean of samples assigned to it.

The process is iterative until the assigned of all samples to the  $c_k$  groups.

4. **Designed trial configurations:** the CO<sub>2</sub>/TM<sub>13</sub> set was extended using additional orientations of the bent CO<sub>2</sub> around the TM<sub>13</sub>. Furthermore, to find the transition

state for a reaction step, we need molecule/TM<sub>13</sub> structures to represent the reactants and products, i.e., initial and final states, respectively. Then, After the CO<sub>2</sub> adsorption study, we selected the preferred adsorption site of CO<sub>2</sub> chemisorption on each TM<sub>13</sub> to study the reaction steps. For systems involving in the reaction steps, we designed their trial configurations as follow:

- (i) For CO<sub>2</sub> → CO + O: the initial states considered the preferred adsorption site of CO<sub>2</sub> chemisorption; for the final states, we increased the CO–O bond length along with different directions.
- (ii) For CO<sub>2</sub> + H → COOH: for the initial states, we placed the CO<sub>2</sub> on its preferred site for chemisorption, while the H was placed close to the same site, with at least one TM<sub>13</sub> atom being shared between H and CO<sub>2</sub>; for the final states, we considered different orientations for COOH in *trans*- and *cis*- conformations.
- (iii) For COOH → CO + OH: the initial states were the same as the final states from (ii); while for the final states, we increased the CO–OH bond length along different directions.
- (iv) For all co-adsorption systems, we included additional structures where we added one molecule (CO<sub>2</sub> or CO) on the preferred adsorption site of CO<sub>2</sub> chemisorption and placed the second adsorbate (H, O, and OH) around the cluster.
- (v) The structures for single species such as H, O, CO, and OH, were obtained from the co-adsorption optimized structures by removing one of the species.

## 2.8 Analysis

In this section the properties employed in the analysis and data interpretation are briefly indicated.

### 2.8.1 Energetic Properties

All the energetic properties derived from the total energy  $E_{tot}^{\text{DFT-PBE}}$  or  $E_{tot}^{\text{DFT-PBE+disp}}$ , according to the case. To characterize and compare the energetic properties of the Mol and TM clusters in gas-phase, the binding energy per atom,  $E_b$ , was calculated. The  $E_b$  is related to the amount of energy required to disassemble a chemical substance into its constituent atoms, which was obtained by,

$$E_b = \frac{E_{tot}^{\text{AxBy}} - xE_{tot}^{\text{A}} - yE_{tot}^{\text{B}}}{x+y}, \quad (2.49)$$

where A, B are the atoms species of the system, and x, y represent the atomicity.

For the adsorbed systems the adsorption energy,  $E_{ad}$ , was calculated as well the interaction energy,  $E_{int}$ .  $E_{ad}$  is the total energy difference between Mol/TM ( $E_{tot}^{\text{Mol/TM}}$ ), and the relaxed configurations of TM ( $E_{tot}^{\text{TM}}$ ) and molecules ( $E_{tot}^{\text{Mol}}$ ):

$$E_{ad} = E_{tot}^{\text{Mol/TM}} - E_{tot}^{\text{TM}} - E_{tot}^{\text{Mol}}. \quad (2.50)$$

In similar way, the  $E_{int}$  is:

$$E_{int} = E_{tot}^{\text{Mol/TM}} - E_{tot}^{\text{TM}^{\text{ad}}} - E_{tot}^{\text{Mol}^{\text{ad}}}, \quad (2.51)$$

where  $E_{tot}^{\text{TM}^{\text{ad}}}$  and  $E_{tot}^{\text{Mol}^{\text{ad}}}$  are the total energies for the TM and the molecule using the atomic positions acquired after the Mol–TM interaction.

Both  $E_{ad}$  and  $E_{int}$  evaluate the strength of the interaction between the molecules and the TM. The negative values indicate that the adsorbed structures present lower energy than the molecules and TM separated, and as larger are the absolute values, the stronger is the interaction. The main difference between  $E_{ad}$  and  $E_{int}$  is the energy variation related to the structural distortion experimented by Mol and TM after the adsorption, which were defined as  $\Delta E_{tot}^{\text{Mol}} \equiv E_{tot}^{\text{Mol}^{\text{ad}}} - E_{tot}^{\text{Mol}}$ ,  $\Delta E_{tot}^{\text{TM}} \equiv E_{tot}^{\text{TM}^{\text{ad}}} - E_{tot}^{\text{TM}}$ , and could be interpreted in terms of a energetic cost necessary to achieve the adsorbed configuration. Thus, the distortion energy can be used to relate the  $E_{ad}$  and  $E_{int}$  by:

$$E_{ad} \equiv E_{int} + \Delta E_{tot}^{\text{Mol}} + \Delta E_{tot}^{\text{TM}}. \quad (2.52)$$

With the definition in (2.52) is possible to evaluate how much more favorable the adsorbed configuration is concerning the energy expenditure of Mol and TM to get that configuration.

Finally, the activation energy,  $E_a$ , is computing as:

$$E_a = E_{tot}^{\ddagger} - E_{tot}^{\text{initial-state}}, \quad (2.53)$$

where  $\ddagger$  represents the transition state, and initial-state superscript refers to the reactants in a particular reaction step.

## 2.8.2 Structural Properties

To evaluate the grade of structural perturbation in the molecules due to the adsorption, we used the bond length ( $d_0$ ), angles, and changes concerning the equilibrium values. Also, for the TM the changes in the effective coordination number ( $\Delta\text{ECN}$ ) and the average bond length ( $\Delta d_{av}$ ) were evaluated. In the ECN concept for each bond length between atom  $i$  and the surrounding atoms  $j$ ,  $d_{ij}$ , it is calculating a weight that accounts for the  $d_{ij}$  contributions in the coordination calculation. The weight is larger as the bond lengths are shorter [131–134]. In this context, the ECN for a particular atom  $i$  is obtained by:

$$\text{ECN}_i = \sum_j \exp \left[ 1 - \left( \frac{d_{ij}}{d_{av}^i} \right)^6 \right], \quad (2.54)$$

with  $d_{av}^i$  defined as:

$$d_{av}^i = \frac{\sum_j d_{ij} \exp \left[ 1 - \left( \frac{d_{ij}}{d_{av}^i} \right)^6 \right]}{\sum_j \exp \left[ 1 - \left( \frac{d_{ij}}{d_{av}^i} \right)^6 \right]}, \quad (2.55)$$

thus  $d_{av}^i$  must be obtained in a self-consistent way. Then, the ECN and  $d_{av}$  results from the average of  $\text{ECN}_i$  and  $d_{av}^i$ :

$$\text{ECN} = \frac{1}{n} \sum_i^n \text{ECN}_i, \quad d_{av} = \frac{1}{n} \sum_i^n d_{av}^i, \quad (2.56)$$

where  $n$  is the number of atoms.

### 2.8.3 Electronic Properties

To understand the electronic changes generated by the adsorption on  $\text{TM}_{13}$  clusters, the electron density difference was analyzed:

$$\Delta\rho = \rho^{\text{Mol}/\text{TM}_{13}} - \rho^{\text{Mol}^{\text{ad}}} - \rho^{\text{TM}_{13}^{\text{ad}}}, \quad (2.57)$$

where  $\rho^{\text{Mol}/\text{TM}_{13}}$  is the total electron density of the adsorbed system,  $\rho^{\text{Mol}^{\text{ad}}}$  and  $\rho^{\text{TM}_{13}^{\text{ad}}}$  are the total electron densities of Mol and  $\text{TM}_{13}$ , respectively, fixed in the atomic positions found in  $\text{Mol}/\text{TM}_{13}$ .

Additionally, the net charge in the molecules,  $\Delta q_{\text{Mol}}$ , was determined, calculated from the sum of the charge at the atoms in the  $\text{Mol}^{\text{ad}}$ ,

$$\Delta q_{\text{Mol}} = \sum_i^n Q_{H,i}^{\text{Mol}}, \quad (2.58)$$

where  $Q_{H,i}^{\text{Mol}}$  is the charge at the atom  $i$  in the  $\text{Mol}^{\text{ad}}$  with  $n$  atoms, which was obtained from the Hirshfeld population analysis [135].

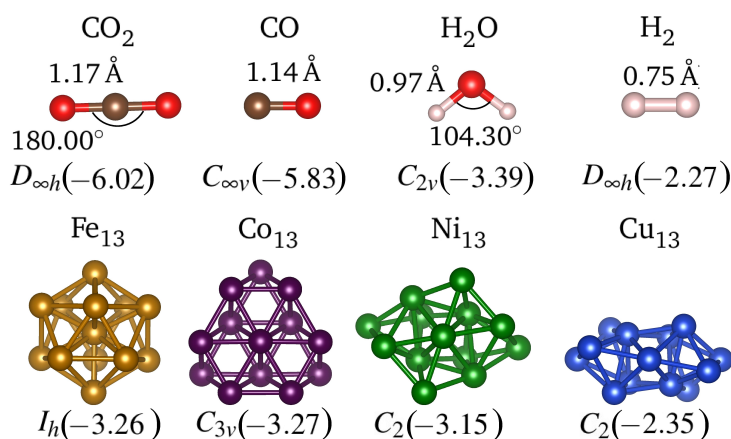
### 3 ACTIVATION OF SMALL MOLECULES VIA ADSORPTION ON 3d TRANSITION-METAL 13-ATOM CLUSTERS: THE EXAMPLE OF CO<sub>2</sub>, CO, H<sub>2</sub>O, AND H<sub>2</sub>

Understanding the adsorption process is crucial in material science since it is involved in almost all technological applications. The heterogeneous catalysis is an example of our interest, where usually the reactants adsorb on catalysts before their transformation. Beyond the adsorption of reactants, the adsorption of the intermediates and even the products can affect subsequent steps, either promoting or inhibiting them. Specifically, within the CO<sub>2</sub> utilization framework, any process that makes this stable molecule more reactive would facilitate its conversion, which is associated with the concept of activation, and where the adsorption process could play a crucial role. Hence, this chapter discusses the adsorption process on 3d TM<sub>13</sub> clusters and its role in the activation of reactants and products involved in the CO<sub>2</sub> reduction via reverse water-gas shift reaction [115].

#### 3.1 Gas-phase Molecules and Clusters

The optimized molecules and the lowest energy structure for TM<sub>13</sub> clusters in gas-phase are shown in Figure 1, including their space group, the binding energy in eV per atom ( $E_b$ ) and some bond lengths and angles. Additional structural and electronic parameters are in Table 1.

Figure 1 – Optimized structures for CO<sub>2</sub>, CO, H<sub>2</sub>O, and H<sub>2</sub> along with their bond lengths and angles, and the lowest energy structures for Fe<sub>13</sub>, Co<sub>13</sub>, Ni<sub>13</sub>, and Cu<sub>13</sub> clusters. Below each structures are their space groups and the numbers in parenthesis are the binding energies ( $E_b$ ) in eV/atom.



Source: Reprinted from OCAMPO-RESTREPO, V. K.; ZIBORDI-BESSE, L.; DA SILVA, J. L. F. *The Journal of Chemical Physics*, v. 151, p. 214301, 2019 [115]. Copyright 2019 with the permission of AIP Publishing.



Table 1 – Structural, energetic, and electronic parameters for CO<sub>2</sub>, CO, H<sub>2</sub>O, H<sub>2</sub>, Fe<sub>13</sub>, Co<sub>13</sub>, Ni<sub>13</sub>, and Cu<sub>13</sub>: bond lengths ( $d_0$ ), angles, effective coordination number (ECN), average bond distance ( $d_{av}$ ), binding energy ( $E_b$ ), and magnetic moment ( $m_{tot}$ ). In parentheses are the deviations with respect to experimental data and DFT-PBE calculations in %.

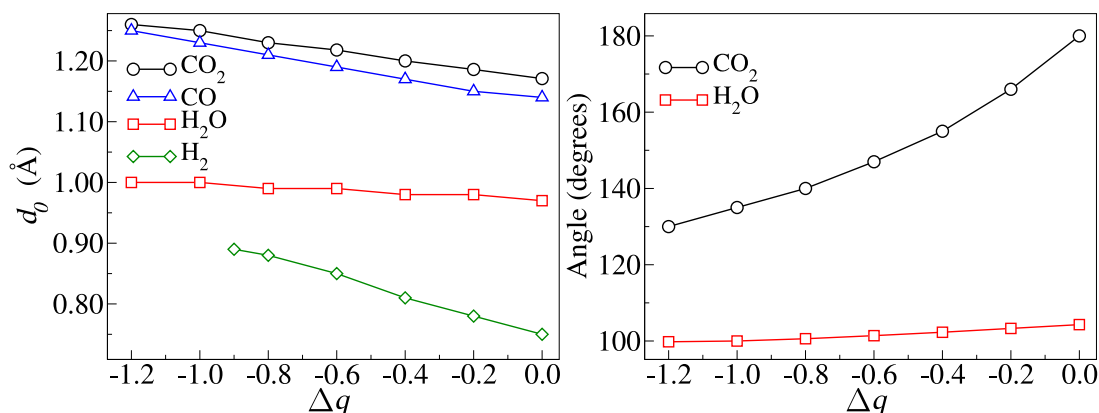
Molecules		CO <sub>2</sub>		CO		H <sub>2</sub> O		H <sub>2</sub>	
$d_0$ (Å)	DFT-PBE	1.17	(0.86)	1.14	(0.88)	0.97	(1.04)	0.75	(1.35)
	Expt. [136]	1.16		1.13		0.96		0.74	
Angle (degrees)	DFT-PBE	180.00	(0.00)			104.30	(-0.17)		
	Expt. [136]	180.00				104.48			
$E_b$ (eV/atom)	DFT-PBE	-6.02	(8.27)	-5.83	(4.48)	-3.39	(5.94)	-2.27	(0.44)
	DFT-PBE [110]			-5.83		-3.38		-2.28	
	Expt.[137]	5.56		5.58		3.20		2.26	
Clusters		Fe <sub>13</sub>		Co <sub>13</sub>		Ni <sub>13</sub>		Cu <sub>13</sub>	
ECN (NNN)	DFT-PBE	6.30	(0.00)	5.40	(0.00)	5.70	(0.00)	5.70	(0.00)
	DFT-PBE [62]	6.30		5.40		5.70		5.70	
$d_{av}$ (Å)	DFT-PBE	2.50	(0.00)	2.30	(0.00)	2.40	(0.00)	2.50	(0.00)
	DFT-PBE [62]	2.50		2.30		2.40		2.50	
$E_b$ (eV/atom)	DFT-PBE	-3.26	(3.16)	-3.27	(0.31)	-3.15	(0.64)	-2.35	(0.86)
	DFT-PBE [62]	-3.16		-3.26		-3.13		-2.33	
$m_{tot}$ ( $\mu_B$ )	DFT-PBE	44	(0)	27	(0)	10	(0)	1	(0)
	DFT-PBE [62]	44		27		10		1	

Source: Reprinted from OCAMPO-RESTREPO, V. K.; ZIBORDI-BESSE, L.; DA SILVA, J. L. F. **The Journal of Chemical Physics**, v. 151, p. 214301, 2019 [115]. Copyright 2019 with the permission of AIP Publishing.

As expected from previous studies for TM<sub>13</sub> [62, 138], the binding energy per atom decreases from Fe to Cu, which can be explained by an increasing occupation of the high energy anti-bonding states as the atomic number (number of valence electrons) increases. Our results deviate by 3.15, 0.31, 0.64, and 0.86 %, respectively, compared with previous DFT-PBE results [62, 138], which were obtained with a larger NAO basis set, such as the *tight-tier1*.

From our analysis, we identified the following space groups,  $I_h$ ,  $C_{3v}$ ,  $C_2$ ,  $C_2$ , for Fe<sub>13</sub>, Co<sub>13</sub>, Ni<sub>13</sub>, and Cu<sub>13</sub>, that have 2, 4, 6, and 6 non-equivalent atoms, respectively. Thus, there is a correlation between compact high-symmetry structures with the magnitude of the binding energy, which explain the group space differences from Fe to Cu. Comparing with experimental data and previous DFT-PBE results for CO<sub>2</sub>, CO, H<sub>2</sub>O, and H<sub>2</sub> in gas-phase [110, 136, 137], the average deviations in the geometrical (bond lengths and angles) and energetic parameters are smaller than 1.30 % and 8.50 %, respectively, see Table 1.

Figure 2 – The left side displays the bond lengths of the CO<sub>2</sub>, CO, H<sub>2</sub>O, and H<sub>2</sub> as a function of their charge state, while the right side shows the angles for the triatomic molecules as a function of their charge state.



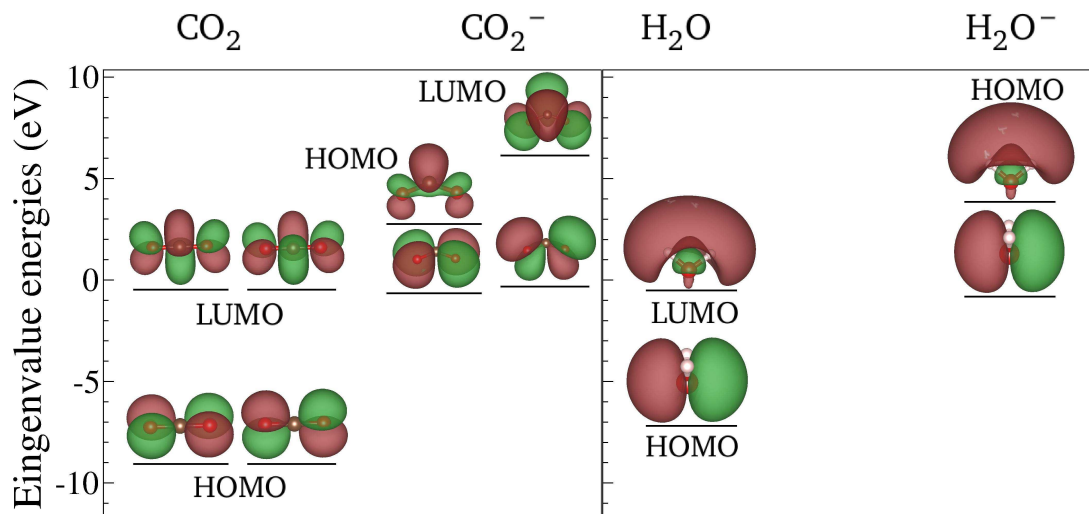
Source: Reprinted from OCAMPO-RESTREPO, V. K.; ZIBORDI-BESSE, L.; DA SILVA, J. L. F. **The Journal of Chemical Physics**, v. 151, p. 214301, 2019 [115]. Copyright 2019 with the permission of AIP Publishing.

Previous studies for CO<sub>2</sub> adsorbed on TM surfaces reported an electronic charge transfer from the substrate to the CO<sub>2</sub> molecule [54–57], that involves the structural change of the CO<sub>2</sub> from linear to angular configuration, and it has been assumed that affect the CO<sub>2</sub> activation [56,57]. Thus, inspired by those results, we evaluated the changes of bond lengths and angles as a function of the charge states,  $\Delta q$ , on the CO<sub>2</sub>, CO, H<sub>2</sub>O, and H<sub>2</sub> molecules by including fractions of charge via charge functionality available in FHI-aims package, results displayed in Figure 2

The addition of electronic charge to the molecules (anionic systems) increased the equilibrium bond lengths, in particular, for H<sub>2</sub>, CO, and CO<sub>2</sub>, but less pronounced for H<sub>2</sub>O. All the studied molecules have the lowest unoccupied molecular orbital (LUMO) with anti-bonding nature, which explains this observation. Hence, the occupation of LUMO leads to weaker bonds, and it reflects in the increase of bond distances.

We observed a large reduction in the angle by the addition of the electronic charge, especially for CO<sub>2</sub> and in less proportion for H<sub>2</sub>O. Results shown in Figure 3 could explained the trends. Comparing the molecular orbitals LUMO for CO<sub>2</sub> and HOMO for CO<sub>2</sub><sup>-</sup> (anionic), the electron addition modified the electronic density redistribution, affecting mainly the density over the carbon.

The greater electronic density on C in CO<sub>2</sub><sup>-</sup>, compared with the neutral CO<sub>2</sub>, increased the electronic repulsion changing the angle OCO until 134.74°, which is consistent with experimental characterization of this anionic species [139]. While in H<sub>2</sub>O<sup>-</sup> the shape of the orbital remained unchanged, conserving the space group  $C_{2v}$  and showing a decrease in only 4.00° for HOH angle. In general, charge transferred to molecules promotes their activation, suggesting that any mechanism that mimics the charge transfer process should

Figure 3 – Diagram for the HOMO and LUMO of  $CO_2$ ,  $CO_2^-$ ,  $H_2O$ , and  $H_2O^-$ .

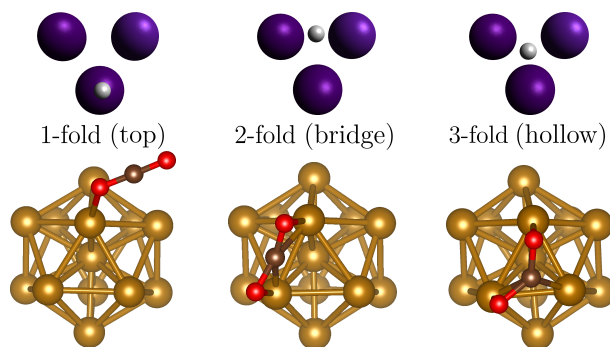
Source: Reprinted from OCAMPO-RESTREPO, V. K.; ZIBORDI-BESSE, L.; DA SILVA, J. L. F. *The Journal of Chemical Physics*, v. 151, p. 214301, 2019 [115]. Copyright 2019 with the permission of AIP Publishing.

provide similar responses.

### 3.2 Adsorption on $TM_{13}$ Clusters

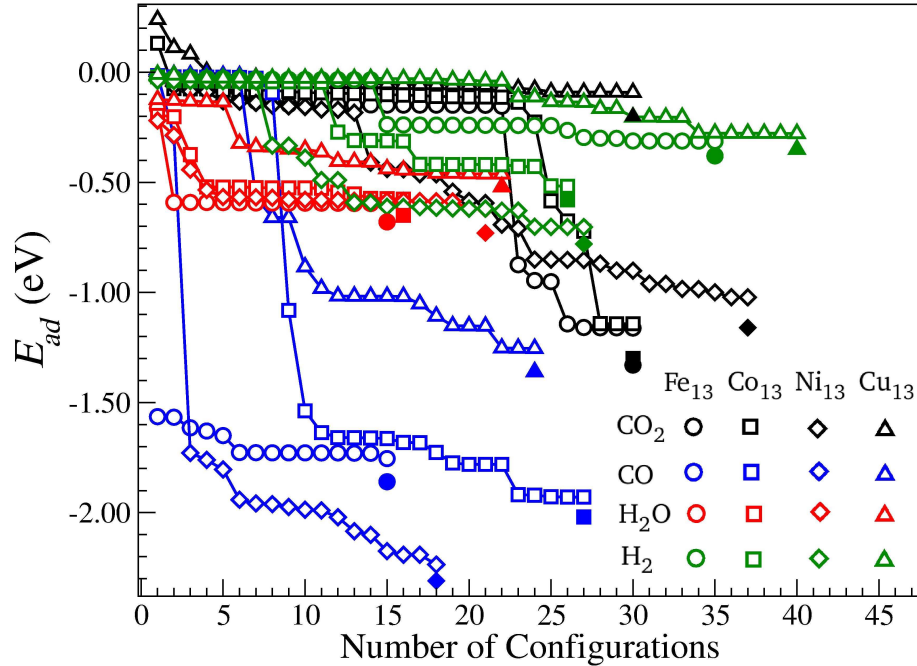
We calculated around 25 adsorption configurations for each Mol/ $TM_{13}$  system. Three types of adsorption sites were identified: 1-fold (top), 2-fold (bridge), and 3-fold (hollow), Figure 4. The different adsorption sites provide variations in the adsorption energies ( $E_{ad}$ ) are in details in the Appendix C and summarized in Figure 5. Concerning

Figure 4 – Representation for adsorption sites identified in this study. The interactions between the molecule and  $TM_{13}$  are 1-fold sites (top), 2-fold sites (bridge), and 3-fold sites (hollow) when this interaction is directly with one, two, or three atoms of the  $TM_{13}$ , respectively. Example for  $CO_2/Fe_{13}$ .



Source: Adapted from OCAMPO-RESTREPO, V. K.; ZIBORDI-BESSE, L.; DA SILVA, J. L. F. *The Journal of Chemical Physics*, v. 151, p. 214301, 2019 [115]. Copyright 2019 with the permission of AIP Publishing.

Figure 5 – Adsorption energy ( $E_{ad}$ ) for all calculated configurations. Open and solid symbols are results with PBE and PBE+TS calculations, respectively.



Source: Reprinted from OCAMPO-RESTREPO, V. K.; ZIBORDI-BESSE, L.; DA SILVA, J. L. F. **The Journal of Chemical Physics**, v. 151, p. 214301, 2019 [115]. Copyright 2019 with the permission of AIP Publishing.

to  $CO_2/TM_{13}$ , particularly for  $TM = Fe, Co,$  and  $Ni$ , the more negative values for  $E_{ad}$  was obtained for the bridge and hollow adsorptions sites, where the  $CO_2$  binding via C and both O atoms. The top site corresponds to values close to zero and the  $CO_2$  interacting via one O atom. Contrary to the observed on  $Cu_{13}$ , where the top sites leads negative values, and the bridge and hollow sites positive values of  $E_{ad}$ .

Regarding the rest of  $Mol/TM_{13}$  systems, all configurations exhibited negative values of  $E_{ad}$ . The  $CO/TM_{13}$  mainly interacts via the carbon and the differences in the  $E_{ad}$  values derives from the CO orientations on the  $TM_{13}$ . In  $H_2O/TM_{13}$ , the water interacted via the O or via the H atoms, with most negative values of  $E_{ad}$  when the former interacts. Finally, the  $H_2$  adsorbed in a parallel way on all  $TM_{13}$  presented a stronger interaction than its perpendicular adsorption.

Among the wide set of adsorbed structures explored, our discussion below mainly focused on the most important physical-chemical properties for the lowest energy configurations. In particular for  $CO_2$ , we discussed both 1-fold and 2-fold sites to explain the positive values observed of adsorption energy for  $CO_2$  on  $Cu_{13}$ . Also, since the results obtained with PBE functional and PBE with van der Waals correction from Tkatchenko-Scheffler (PBE+TS) followed similar trends, only the results from PBE+TS calculations were discussed.

### 3.2.1 Adsorption Site Preference

Figure 6 displays the lowest energy structures for Mol/ $TM_{13}$  along with their adsorption energies. The preferential adsorption of  $CO_2$  on  $Fe_{13}$ ,  $Co_{13}$ , and  $Ni_{13}$  occurs via C and O on 2-fold sites, while on  $Cu_{13}$  the molecule retains its linearity and coordinates by one oxygen atom to one cluster atom on 1-fold site. The same adsorption sites preferences were reported on periodic surfaces of Fe, Co, Ni, and Cu [20, 54, 58], suggesting that the TM specie has high influence in the adsorption site preference.

The two types of preferential sites observed suggest that the  $CO_2$  adsorption proceed via different mechanisms as the  $d$  states filled for  $3d$  TM series. Then, uncompleted  $d$ -states systems like  $Fe_{13}$ ,  $Co_{13}$ , and  $Ni_{13}$  tends to form a chemical bond with  $CO_2$  via LUMO state, which have electron density localization from both C and O atoms, Figure 3. While, the  $Cu_{13}$  cluster have characteristics of closed-shell system, being less reactive and interacting weakly with  $CO_2$ . The main characteristics of those mechanisms are discussed within this chapter.

The CO interacts via C atom with all  $TM_{13}$  clusters and preferentially adsorbs 1-fold site on  $Cu_{13}$ , 2-fold site on  $Co_{13}$  and  $Ni_{13}$ , and 3-fold site on  $Fe_{13}$ . The carbon participation can be explained by the electron density localization of C atoms in the LUMO states of CO [140]. While  $H_2O$  molecule shown a preference to adsorb with the oxygen atom on the 1-fold site for all studied cases, being consistent with the results informed in the literature using  $Ni_{13}$ ,  $Cu_{13}$ , and additional  $TM_{13}$  clusters [124]. According to Figure 3, it is suggested the participation of HOMO state of water in this interaction due to the electron density is localized at O atom.

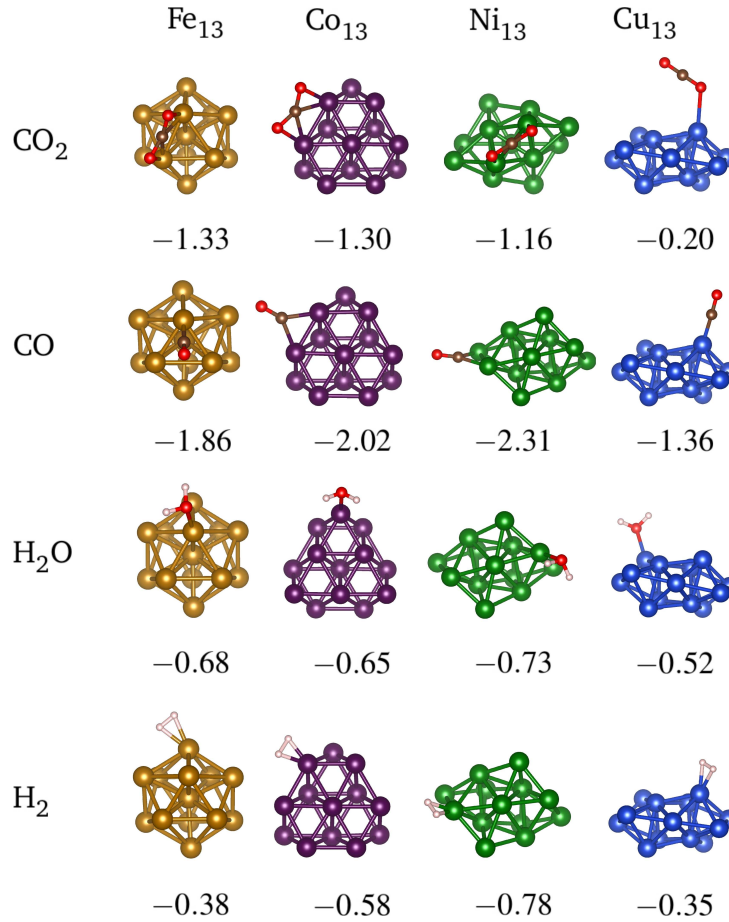
Regarding  $H_2$  adsorption, the 1-fold site was preferred on all  $TM_{13}$  with both H atoms binding at the same  $TM_{13}$  atom. Which could involve the participation of both HOMO and LUMO state in the adsorption. The same behavior has been observed on Fe(110) surfaces and clusters with 55 atoms of Au, Pd, and AuPd [141, 142], suggesting that the preferred adsorption site of  $H_2$  is barely affected by the TM species and the size scale.

### 3.2.2 Energetic Parameters

The energetic characterization of the lowest energy structures for Mol/ $TM_{13}$  systems included the calculation of the adsorption energy ( $E_{ad}$ ), interaction energy ( $E_{int}$ ), and deformation energies for the Mol and  $TM_{13}$  clusters ( $\Delta E_{tot}^{Mol}$ , and  $\Delta E_{tot}^{TM_{13}}$ ), data informed in Table 2. We observed distinct differences in the magnitude of all energetic properties among the studied systems, which is a consequence of the nature of the electronic states involved in the interactions.

The adsorption of all molecules on  $Cu_{13}$  exhibited the smallest values for  $|E_{ad}|$  and

Figure 6 – Lowest energy structures for the Mol/ $TM_{13}$  systems. The adsorption energy ( $E_{ad}^{PBE+TS}$ ) is below each structures in eV.



Source: Reprinted from OCAMPO-RESTREPO, V. K.; ZIBORDI-BESSE, L.; DA SILVA, J. L. F. **The Journal of Chemical Physics**, v. 151, p. 214301, 2019 [115]. Copyright 2019 with the permission of AIP Publishing.

$|E_{int}|$  among all  $TM_{13}$  studied. It can be associated to the closed-shell  $3d$ -states in Cu, making it less prone to react in presence of the molecules compared with the remaining clusters (Fe<sub>13</sub>, Co<sub>13</sub>, Ni<sub>13</sub>) with uncompleted  $d$ -states. Comparing with a study informed in literature for CO<sub>2</sub>, CO, and H<sub>2</sub>O on the Cu(111) and Cu(211) [58], those molecules binds stronger on Cu<sub>13</sub> since our adsorption energies are larger in magnitude, which could be expected due to the lower coordination of the adsorption sites provided by the clusters.

For CO<sub>2</sub>, the  $E_{ad}$  is about the same on Fe<sub>13</sub>, Co<sub>13</sub>, Ni<sub>13</sub>, from  $-1.33$  to  $-1.16$  eV, while on Cu<sub>13</sub> differs substantially,  $-0.20$  eV. Those differences match with the way as the CO<sub>2</sub> adsorbs on each  $TM_{13}$  cluster, as discussed in the adsorption site preference section. Then, there is a relation between the deformation of CO<sub>2</sub> upon adsorption and the strength of the interaction. The bond formation involves stronger interaction which changes CO<sub>2</sub> structure into a bent configuration while weaker interaction, no chemical bond formation, keep the CO<sub>2</sub> in linear configuration, i.e.  $E_{ad}^{CO_2}$  decreased from Fe to Cu.

Table 2 – Energetic properties for the lowest energy structures using PBE and PBE+TS of  $CO_2$ ,  $CO$ ,  $H_2O$ , and  $H_2$  adsorbed on  $Fe_{13}$ ,  $Co_{13}$ ,  $Ni_{13}$ , and  $Cu_{13}$  clusters. Adsorption energy ( $E_{ad}$ ); interaction energy ( $E_{int}$ ); difference between the total energy of the molecule after adsorption and in the gas-phase ( $\Delta E_{tot}^{Mol}$ ); difference between the total energy of the  $TM_{13}$  after adsorption and in the gas-phase ( $\Delta E_{tot}^{TM_{13}}$ ).

		Mol/ $Fe_{13}$		Mol/ $Co_{13}$		Mol/ $Ni_{13}$		Mol/ $Cu_{13}$	
		PBE	PBE+TS	PBE	PBE+TS	PBE	PBE+TS	PBE	PBE+TS
$E_{ad}$ (eV)	$CO_2$	-1.16	-1.33	-1.14	-1.30	-1.02	-1.16	-0.09	-0.20
	$CO$	-1.75	-1.86	-1.93	-2.02	-2.24	-2.31	-1.25	-1.36
	$H_2O$	-0.60	-0.68	-0.58	-0.65	-0.62	-0.73	-0.46	-0.52
	$H_2$	-0.31	-0.38	-0.52	-0.58	-0.70	-0.78	-0.28	-0.35
$E_{int}$ (eV)	$CO_2$	-3.09	-3.23	-2.86	-3.01	-2.70	-2.85	-0.10	-0.20
	$CO$	-1.98	-2.06	-2.10	-2.19	-2.39	-2.49	-1.31	-1.42
	$H_2O$	-0.57	-0.64	-0.55	-0.62	-0.61	-0.72	-0.46	-0.52
	$H_2$	-0.65	-0.70	-1.06	-1.12	-0.95	-1.04	-0.34	-0.43
$\Delta E_{tot}^{Mol}$ (eV)	$CO_2$	1.78	1.79	1.71	1.71	1.59	1.58	0.00	0.00
	$CO$	0.11	0.11	0.12	0.12	0.12	0.12	0.00	0.00
	$H_2O$	0.00	0.00	0.00	0.00	0.00	0.00	0.00	0.00
	$H_2$	0.20	0.20	0.53	0.53	0.23	0.23	0.05	0.05
$\Delta E_{tot}^{TM_{13}}$ (eV)	$CO_2$	0.15	0.11	0.01	0.00	0.09	0.11	0.01	0.00
	$CO$	0.12	0.09	0.05	0.05	0.03	0.06	0.06	0.06
	$H_2O$	-0.03	-0.04	-0.03	-0.03	-0.01	-0.01	0.00	0.00
	$H_2$	0.14	0.12	0.01	0.01	0.02	0.03	0.01	0.03

Source: Reprinted from OCAMPO-RESTREPO, V. K.; ZIBORDI-BESSE, L.; DA SILVA, J. L. F. **The Journal of Chemical Physics**, v. 151, p. 214301, 2019 [115]. Copyright 2019 with the permission of AIP Publishing.

Regarding to the magnitude of  $E_{ad}$  among  $CO$ ,  $H_2O$ , and  $H_2$  on  $TM_{13}$ , there are a large differences in the values, but except small deviations, the magnitude of adsorption energies increase as follows,  $Cu_{13} < Fe_{13} < Co_{13} < Ni_{13}$ . Those similarities in the general trend of  $E_{ad}$  are associated to the adsorption sites, e.g. on  $Ni_{13}$  the three molecules preferentially adsorb on the same TM atoms, different to  $CO_2$ , which suggests that the  $TM_{13}$  clusters play an important role in the control of adsorption strength on those molecules.

The large differences observed between  $|E_{ad}^{CO_2}|$  and  $|E_{int}^{CO_2}|$  for  $Fe_{13}$ ,  $Co_{13}$ , and  $Ni_{13}$  are mainly attributed to the structural distortions of  $CO_2$  quantified by  $\Delta E_{tot}^{Mol}$ , which is about the same on  $Fe_{13}$ ,  $Co_{13}$ , and  $Ni_{13}$ , but zero on  $Cu_{13}$ . Although the  $TM_{13}$  distortion contributes to the  $|E_{int}^{CO_2}|$ , it is negligible compared with the  $CO_2$ , as shown the  $\Delta E_{tot}^{TM_{13}}$  results. Beyond lowest energy structures, we found high energy structures where  $CO_2$  adsorbs on 2-fold sites on  $Cu_{13}$  but with positive values for adsorption energies,  $E_{ad} > 0$ . Similar behavior was previously report on  $Cu(111)$  surface [20].

From equation (2.52), one of cases to obtain  $E_{ad} > 0$  would be when  $\Delta E_{tot}^{Mol}$  is larger than the magnitude of  $E_{int}$ . It means that the strength of the interaction between  $CO_2$  and  $Cu_{13}$  does not compensate for the energetic increase due to the  $CO_2$  deformation. In those cases, the  $E_{ad}$  provides an idea that the interaction is weak, being unable to characterize the strength of the adsorption by itself. The  $E_{ad}$  as a measure of the adsorption strength is widely employed, being consistent when the energy increases due to the structural distortion of the individual systems is smaller than the interaction energy.

For CO on  $Fe_{13}$ ,  $Co_{13}$ , and  $Ni_{13}$ , the adsorption and interaction energies differ by 0.17 to 0.20 eV. Differently to  $CO_2/TM_{13}$ , for  $TM = Fe, Co, \text{ and } Ni$ , the  $\Delta E_{tot}^{CO}$  is substantially smaller, i.e., 0.11 to 0.12 eV, which indicates that the structural changes on CO are smaller than on  $CO_2$  after the adsorption. Particularly for  $CO/Cu_{13}$ , the  $E_{ad}$  and  $E_{int}$  differ by 0.06 eV, which is entirely associate with the distortion of  $Cu_{13}$ , thus, the CO remain without distortions.

For  $H_2O$ , the adsorption and interaction energies exhibited the smaller differences, being the sole system with negatives values for  $\Delta E_{tot}^{TM_{13}}$  (zero on  $Cu_{13}$ ) and  $\Delta E_{tot}^{Mol} = 0$  eV on all clusters, indicating a different adsorption mechanism compared to remaining systems. For  $H_2$ , although the  $E_{ad}$  and  $E_{int}$  values are smaller than ones for CO, the  $\Delta E_{tot}^{H_2}$  rise from 0.05 eV ( $Cu_{13}$ ) up to 0.53 eV ( $Co_{13}$ ), showing the large impact of the adsorption on the structural distortion of  $H_2$ , which is not represented by the  $E_{ad}$  since exhibited the smaller values among studied molecules.

Our results of  $E_{ad}$  with PBE for  $CO_2$ , CO, and  $H_2O$  are comparable with the data reported on the icosahedral ( $I_h$ )  $Cu_{13}$  cluster, being  $-0.09$  eV,  $-1.30$  eV, and  $-0.49$  eV, respectively [58]. The deviations are associated with the differences in the  $Cu_{13}$  structure, since we used the putative global minimum configuration (pGMC) ( $C_2$ ) in this study lower in energy by 78 eV that the  $I_h$  structure. Despite the differences in the magnitude for  $E_{ad}$  of  $CO_2$  adsorption on  $TM_{13}$  clusters, our trends are consistent with the reported on the respective surfaces [20, 54].

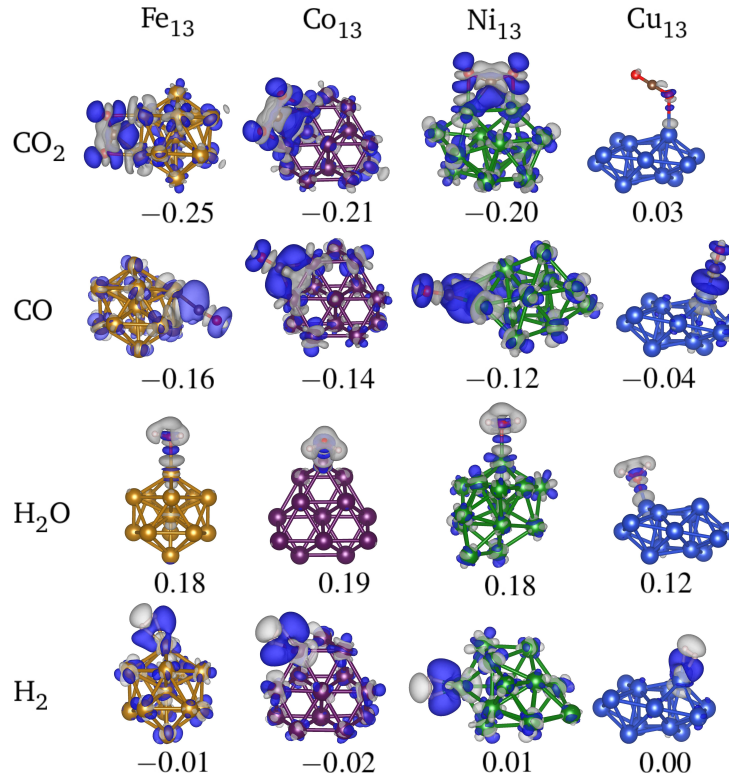
### 3.2.3 Partial Charge Transfer Analysis

To improve our understanding on the electronic properties, we calculated for lowest energy configurations the electron density difference,  $\Delta\rho$ , which identify the space region where the electron density increases or decreases upon the adsorption, and the results are shown in Figure 7. Furthermore, based on the Hirshfeld analysis, we calculated the charge transfer among the systems, which will be characterized by the effective charge on the molecules,  $\Delta q_{Mol}$ , and the results are summarized in Table 3.

As expected, main changes in the isosurfaces occurs near to the adsorption sites, and the adsorption on the top sites mainly involves the  $d_{z^2}$  TM orbital, e.g.,  $H_2O/Ni_{13}$ , while in the bridge sites participate the  $d_{xy}$ ,  $d_{xz}$ , and  $d_{yz}$  orbitals, e.g.,  $CO_2/Ni_{13}$ , which has been



Figure 7 – Electron density difference for  $\text{CO}_2$ ,  $\text{CO}$ ,  $\text{H}_2\text{O}$ , and  $\text{H}_2$  on the  $TM_{13}$  clusters. Blue and gray colors represent the charge accumulation and depletion, respectively. The charge transfer from cluster to molecule obtained from the Hirshfeld charge density analysis is below the structure in the number of  $e$ . The charge density used for the isosurface plots was  $1.50 \times 10^{-2} e \text{ \AA}^{-3}$ .

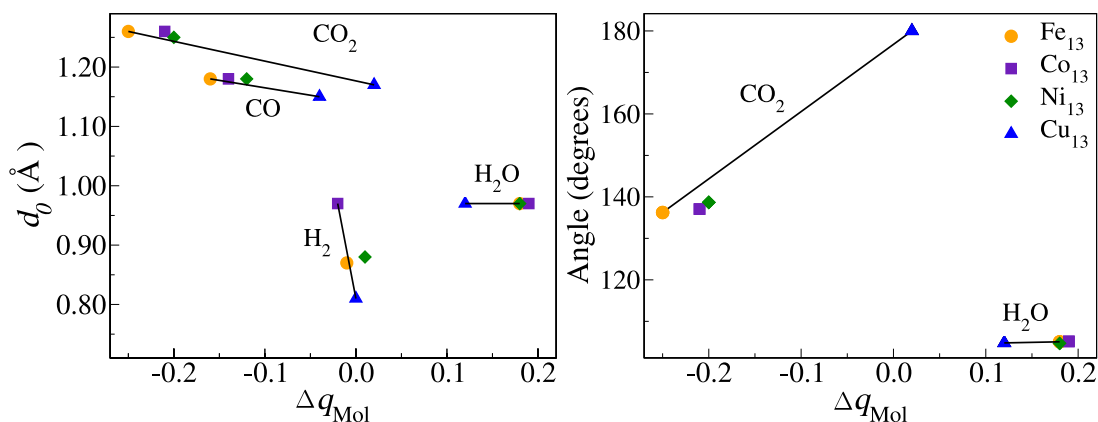


Source: Reprinted from OCAMPO-RESTREPO, V. K.; ZIBORDI-BESSE, L.; DA SILVA, J. L. F. **The Journal of Chemical Physics**, v. 151, p. 214301, 2019 [115]. Copyright 2019 with the permission of AIP Publishing.

reported previously for the adsorption of  $\text{CO}_2$  on metallic complexes [143]. Concerning the molecules, the LUMO of bent  $\text{CO}_2$  is analogous to the HOMO of  $\text{CO}_2^-$  [144], and we found similarities with the shape of the electron distribution for  $\text{CO}_2^{\text{ad}}$  on  $\text{Fe}_{13}$ ,  $\text{Co}_{13}$ , and  $\text{Ni}_{13}$ . Hence, we infer that the molecule is binding to these clusters through  $\text{CO}_2$  LUMO. For  $\text{CO}_2/\text{Cu}_{13}$ , the charge variation in the molecule is small suggesting the slightly perturbation due to the molecule and cluster interaction.

For both  $\text{CO}_2$  and  $\text{CO}$  on  $\text{Fe}_{13}$ ,  $\text{Co}_{13}$ , and  $\text{Ni}_{13}$ , the  $\Delta q_{\text{Mol}}$  values are negative, which indicates a charge donation from the clusters to molecules while  $\Delta q_{\text{Mol}}$  is negligible on  $\text{Cu}_{13}$ . Thus, there is a correlation between the magnitude of the charge transferred and the  $\text{CO}_2$  configuration upon adsorption, i.e., bent on  $\text{Fe}_{13}$ ,  $\text{Co}_{13}$ , and  $\text{Ni}_{13}$ , and linear on  $\text{Cu}_{13}$ , that is also consistent with the magnitude of  $\Delta E_{\text{tot}}^{\text{Mol}}$ , for both,  $\text{CO}_2$  and  $\text{CO}$ . To support this observation, we calculate the  $\Delta q_{\text{Mol}}$  for the higher energy configuration of  $\text{CO}_2/\text{Cu}_{13}$ , where the  $\text{CO}_2$  is bent. We found that the  $\text{Cu}_{13}$  also transferred charge to  $\text{CO}_2$ ,  $\Delta q_{\text{Mol}} = -0.18$ , which confirm that the charge donation to  $\text{CO}_2$  affects its configuration

Figure 8 – Angles and bond lengths for  $CO_2$ ,  $CO$ ,  $H_2O$ , and  $H_2$  upon adsorption on each  $TM_{13}$  as a function of  $\Delta q_{Mol}$ . The lines for each molecule connect the more negative or less positive with the more positive value of  $\Delta q_{Mol}$ .



Source: Reprinted from OCAMPO-RESTREPO, V. K.; ZIBORDI-BESSE, L.; DA SILVA, J. L. F. **The Journal of Chemical Physics**, v. 151, p. 214301, 2019 [115]. Copyright 2019 with the permission of AIP Publishing.

after the adsorption, and an appropriate adsorption site could promote this process on all  $TM_{13}$ .

In the case of  $H_2O$ , its HOMO and LUMO are shown in Figure 3 and, compared to the isosurfaces for  $H_2O/TM_{13}$ , we infer the HOMO participation in the  $H_2O$  adsorption. Further, the positive net charge in the molecule suggests that  $H_2O$  acts as a donor specie on all  $TM_{13}$  clusters. As it has been mentioned, for  $H_2O/TM_{13}$  systems a negative  $\Delta E_{tot}^{TM_{13}}$  was found, that could be explained by the charge transferred toward  $TM_{13}$ . In the case of  $H_2$  on  $TM_{13}$  clusters, the net charge at  $H_2^{ad}$  is close to zero and becomes difficult to infer the flux of the charge on those systems by this analysis.

### 3.2.4 Structural Parameters

Table 3 includes the bond lengths,  $d_0$ , and angles of the molecules upon adsorption and in parenthesis their relative error with respect to the equilibrium parameters in gas-phase. Also, Figure 8 shows the  $d_0$  and angles as a function of  $\Delta q_{Mol}$  on each  $TM_{13}$ . Similarly to discussed from the energetic parameters for  $CO_2$  and  $CO$  on  $Fe_{13}$ ,  $Co_{13}$ , and  $Ni_{13}$ , the adsorption on any of those clusters provides the same C–O bond length increase while for the  $CO_2$  angle decrease, slightly variations between the clusters were observed, being a parameter more sensitive than bond lengths. The correlation between the structural parameters of  $CO_2^{ad}$  and  $CO^{ad}$  with  $\Delta q_{Mol}$  allow us to infer that the charge transferred toward molecules from  $TM_{13}$  promotes those structural modifications, since the adsorption on  $Cu_{13}$  does not involve appreciable charge transfer and, consequently, the  $d_0$  and angles remains unaltered, contrary to  $Fe_{13}$ ,  $Co_{13}$ , and  $Ni_{13}$ .

Those results are similar to the observed from Figure 2. However, although for  $CO_2$

Table 3 – Electronic and structural properties for the lowest energy structures calculated with PBE and PBE+TS of  $CO_2$ ,  $CO$ ,  $H_2O$ , and  $H_2$  on  $Fe_{13}$ ,  $Co_{13}$ ,  $Ni_{13}$ , and  $Cu_{13}$  clusters. Net charge at molecules obtained from the Hirshfeld charge analysis ( $\Delta q_{Mol}$ ); bond length for adsorbed molecules ( $d_0$ ); angle of  $CO_2$  and  $H_2O$  after adsorption (Angle); smallest Mol– $TM_{13}$  bond distance ( $d_{Mol-TM_{13}}$ ); relative changes in the bond lengths average weighted on adsorption site of  $TM_{13}$  after adsorption ( $\Delta d_{av}$ ); relative changes in the  $TM_{13}$  effective coordination number on adsorption site after adsorption ( $\Delta ECN$ ). The numbers in parenthesis are the relative change in percentages with respect to the equilibrium values in gas-phase ( $\Delta d_0$ ) and ( $\Delta Angle$ ).

		Mol/ $Fe_{13}$		Mol/ $Co_{13}$		Mol/ $Ni_{13}$		Mol/ $Cu_{13}$	
		PBE	PBE+TS	PBE	PBE+TS	PBE	PBE+TS	PBE	PBE+TS
$\Delta q_{Mol}$ (e)	$CO_2$	-0.25	-0.25	-0.21	-0.21	-0.20	-0.20	0.02	0.02
	$CO$	-0.16	-0.16	-0.14	-0.14	-0.12	-0.12	-0.04	-0.04
	$H_2O$	0.18	0.18	0.19	0.19	0.19	0.18	0.15	0.12
	$H_2$	-0.01	-0.01	-0.02	-0.02	0.01	0.01	0.00	0.00
$d_0$ (Å)	$CO_2$	1.26	1.26	1.26	1.26	1.25	1.25	1.17	1.17
		(7.70)	(7.70)	(7.70)	(7.70)	(6.84)	(6.84)	(0.00)	(0.00)
	$CO$	1.18	1.18	1.18	1.18	1.18	1.18	1.15	1.15
		(3.51)	(3.51)	(3.51)	(3.51)	(3.51)	(3.51)	(0.88)	(0.88)
	$H_2O$	0.97	0.97	0.97	0.97	0.97	0.97	0.97	0.97
(0.00)		(0.00)	(0.00)	(0.00)	(0.00)	(0.00)	(0.00)	(0.00)	
$H_2$	0.87	0.87	0.97	0.97	0.88	0.88	0.81	0.81	
		(16.00)	(16.00)	(29.33)	(29.33)	(17.33)	(17.33)	(8.00)	(8.00)
Angle (degrees)	$CO_2$	136.26	136.23	137.04	137.05	138.52	138.68	180.00	180.00
		(-24.30)	(-24.32)	(-23.87)	(-23.86)	(-23.04)	(-22.96)	(0.00)	(0.00)
	$H_2O$	105.20	105.06	105.14	105.16	105.05	104.71	105.66	104.79
		(0.86)	(0.73)	(0.81)	(0.82)	(0.72)	(0.39)	(1.30)	(0.47)
$d_{Mol-TM_{13}}$ (Å)	$CO_2$	2.03	2.03	2.00	2.00	1.98	1.25	2.46	2.40
	$CO$	1.81	1.81	1.90	1.90	1.84	1.84	1.81	1.81
	$H_2O$	2.13	2.12	2.11	2.09	2.06	2.05	2.11	2.12
	$H_2$	1.70	1.69	1.57	1.57	1.57	1.57	1.72	1.72
$\Delta d_{av}$ (%)	$CO_2$	-0.08	-0.22	0.86	0.71	2.08	1.88	0.41	0.27
	$CO$	-0.22	-0.35	-0.13	-0.13	1.28	1.15	2.36	2.14
	$H_2O$	0.44	0.32	0.54	0.42	1.27	0.96	0.77	0.39
	$H_2$	-1.00	-1.04	0.61	0.66	2.65	2.45	1.49	1.22
$\Delta ECN$ (%)	$CO_2$	-5.30	-5.00	-0.24	-0.41	-1.21	-0.96	-0.02	0.08
	$CO$	-1.44	-1.39	1.22	1.38	-0.07	0.02	-0.84	-0.42
	$H_2O$	-2.43	-2.32	0.21	0.11	-0.22	-0.23	-0.73	-0.87
	$H_2$	-6.69	-6.58	0.98	1.07	0.76	0.70	-0.33	-0.04

Source: Reprinted from OCAMPO-RESTREPO, V. K.; ZIBORDI-BESSE, L.; DA SILVA, J. L. F. *The Journal of Chemical Physics*, v. 151, p. 214301, 2019 [115]. Copyright 2019 with the permission of AIP Publishing.

and  $CO$  behavior are consistent in both analyses cannot be numerically compared. Beyond that, the chemical environment imposed by the adsorption makes possible a significant structural variation in those molecules, which only can be reached in the gas phase when the molecule receives at least one electron. For  $H_2O/TM_{13}$  the  $H-O$  bond length remains unaltered, and the  $HOH$  angle tends to increase slightly, which is associated with the charge

donation toward  $TM_{13}$ . On the other hand, for  $H_2^{ad}$ , the H–H bond length increases on all  $TM_{13}$  which correlates with the magnitude for  $\Delta E_{tot}^{Mol}$ , i.e., the larger H–H bond distance correspond to the larger  $\Delta E_{tot}^{Mol}$  (on  $Co_{13}$ ). However, these results do not correlate with the  $\Delta q_{Mol}$  due to the almost zero values obtained from our analysis, being still difficult to infer what mechanism promotes the  $H_2$  structural modification.

Regarding the smallest distance between molecules and  $TM_{13}$  clusters,  $d_{Mol-TM_{13}}$ , no general trends were identified. Furthermore, to evaluate the structural effects on the TM atoms directly involved in the adsorption, we calculated their relative changes of weighted bond length,  $\Delta d_{av}$ , and effective coordination number,  $\Delta ECN$ . In general, the  $\Delta d_{av}$  reaches a maximum of 2.65 % (DFT-PBE), but there is no clear tendency for this parameter. In the case of  $\Delta ECN$ , the variation shows a dependence with the  $TM_{13}$  symmetry, indicating that clusters with higher symmetry are more affected. However, these changes in the  $TM_{13}$  clusters indicate small perturbations in their structures, which is consistent with the small  $\Delta E_{tot}^{TM_{13}}$ , showing that the studied clusters present high stability in the adsorption process.

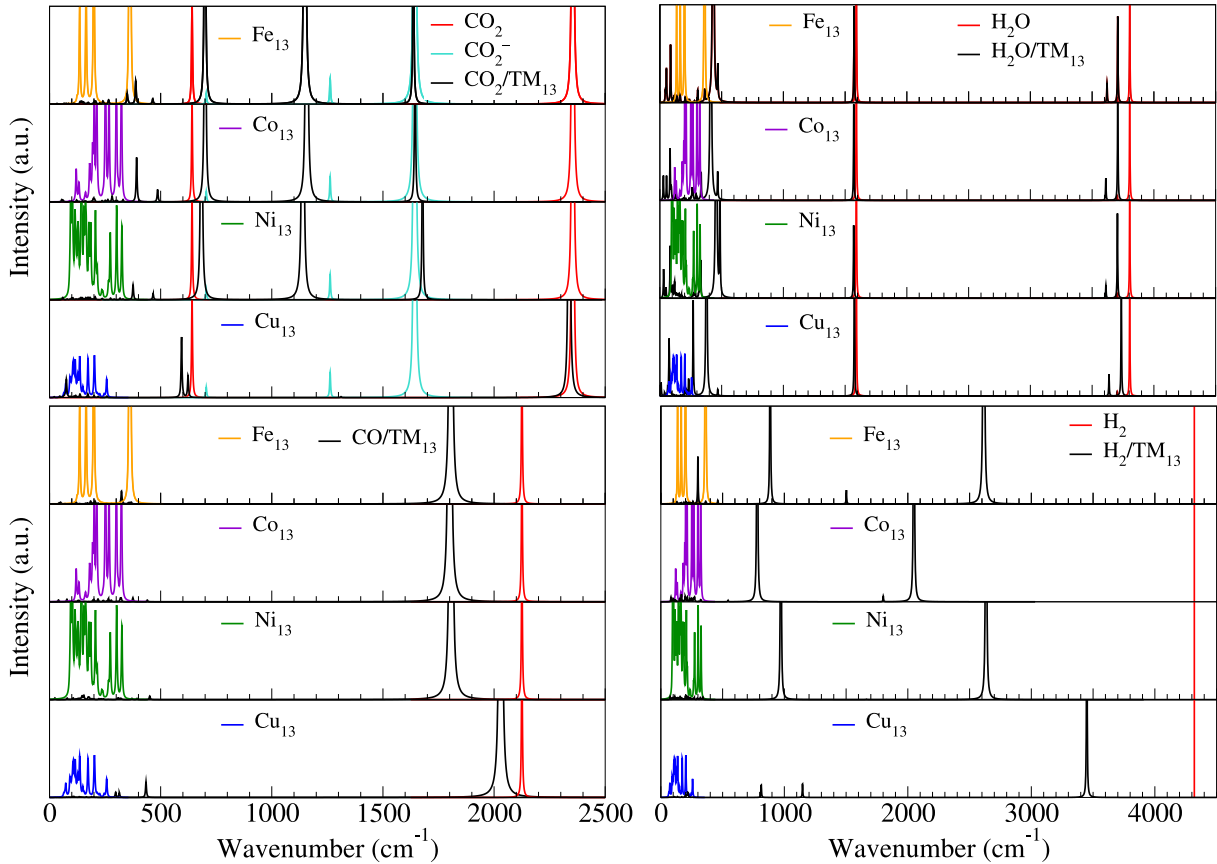
### 3.2.5 Vibrational Analysis

To improve the characterization of the molecules upon adsorption on the 13-atom clusters, we calculated the infrared (IR) spectra, which yields the vibrational frequencies and the intensities for the modes active in the IR. Our results are shown in Figure 9 for molecules and  $TM_{13}$  clusters in gas-phase, and for Mol/ $TM_{13}$ . The vibrational modes of  $CO_2$  in gas-phase are the symmetric stretching ( $\nu_s$ :  $1320\text{ cm}^{-1}$ ), antisymmetric stretching ( $\nu_{as}$ :  $2353\text{ cm}^{-1}$ ), and the bending ( $\nu_b$ :  $641\text{ cm}^{-1}$ ), where only the two last ones are active in the IR, and deviate from experimental data by 0.17 % and  $-3.90\%$ , respectively [145].

Upon the adsorption on  $Fe_{13}$ ,  $Co_{13}$ , and  $Ni_{13}$  clusters, three characteristics bands related to  $CO_2^{ad}$  are observed. The  $\nu_s$  mode becomes active near to  $1100\text{ cm}^{-1}$ , the wavenumber referent to the  $\nu_{as}$  presents a red-shift, while the one referent to  $\nu_b$  a blue-shift compared with  $CO_2$  in gas-phase. The red-shift indicates a weakening of C–O bonds, which is consistent with an increase in  $d_0$ . Performing these comparisons of  $CO_2^{ad}$  with the  $CO_2^-$ , the bands have better coincidence as more similar the geometry of  $CO_2^{ad}$  to the radical anion, principally for the  $\nu_{as}$  ( $1643\text{ cm}^{-1}$ ) and  $\nu_b$  ( $705\text{ cm}^{-1}$ ) modes. In addition, the wavenumber corresponding to  $\nu_s$  mode is red-shifted compared with  $\nu_s$  for  $CO_2^-$ , which is interpreted as a damping of the vibrational frequency of this mode due to the interaction with the clusters.

In contrast, for  $CO_2/Cu_{13}$ , the vibrational modes related to  $CO_2^{ad}$  are closer to the results obtained for  $CO_2$  in the gas-phase. However, the  $\nu_b$  mode splits into two bands, suggesting that the interaction with the cluster breaks the degeneracy of that mode. Further, bands corresponding to C– $TM_{13}$  and O– $TM_{13}$  interactions appear at the low-frequency region, but usually, they are not used to characterize the adsorption. The

Figure 9 – Infrared spectra of molecules,  $TM_{13}$ , and Mol/ $TM_{13}$ . The infrared intensities for the  $TM_{13}$  clusters were multiplied by 50 for visualization purposes.



Source: Adapted from OCAMPO-RESTREPO, V. K.; ZIBORDI-BESSE, L.; DA SILVA, J. L. F. **The Journal of Chemical Physics**, v. 151, p. 214301, 2019 [115]. Copyright 2019 with the permission of AIP Publishing.

$CO_2$  activation can be characterized by the shifts in the  $\nu_{as}$  and  $\nu_b$  modes, and appearance of the  $\nu_s$  mode in the IR spectra. Similar behavior has been informed for  $CO_2$  adsorption on mononuclear complex and surfaces [20, 146, 147]. Nevertheless, our results suggested by the first time that the adsorption of  $CO_2$  when the molecule is not activated could characterize through the variations in the  $\nu_b$  mode.

Using C–O stretching of CO in gas-phase ( $2125\text{ cm}^{-1}$ ) as reference, we found a red-shifted for CO on all clusters, and the displacement is directly related to the increase in  $d_0^{C-O}$  upon the adsorption. In the case of  $H_2O$  in gas-phase, the  $\nu_s$  ( $3704\text{ cm}^{-1}$ ),  $\nu_{as}$  ( $3804\text{ cm}^{-1}$ ), and  $\nu_b$  ( $1591\text{ cm}^{-1}$ ) were found, and deviate about 1.30 % from experimental results [145]. After the adsorption, we identified a small red-shift in the wavenumber of  $\nu_s$  and  $\nu_{as}$  modes, which is consistent with the insignificant structural modifications. However, the band observed around  $500\text{ cm}^{-1}$  can be used to characterize the  $H_2O-TM_{13}$  interaction, which was previously reported [124], and correspond to the asymmetric and symmetric bending through the equatorial plane of the molecule.

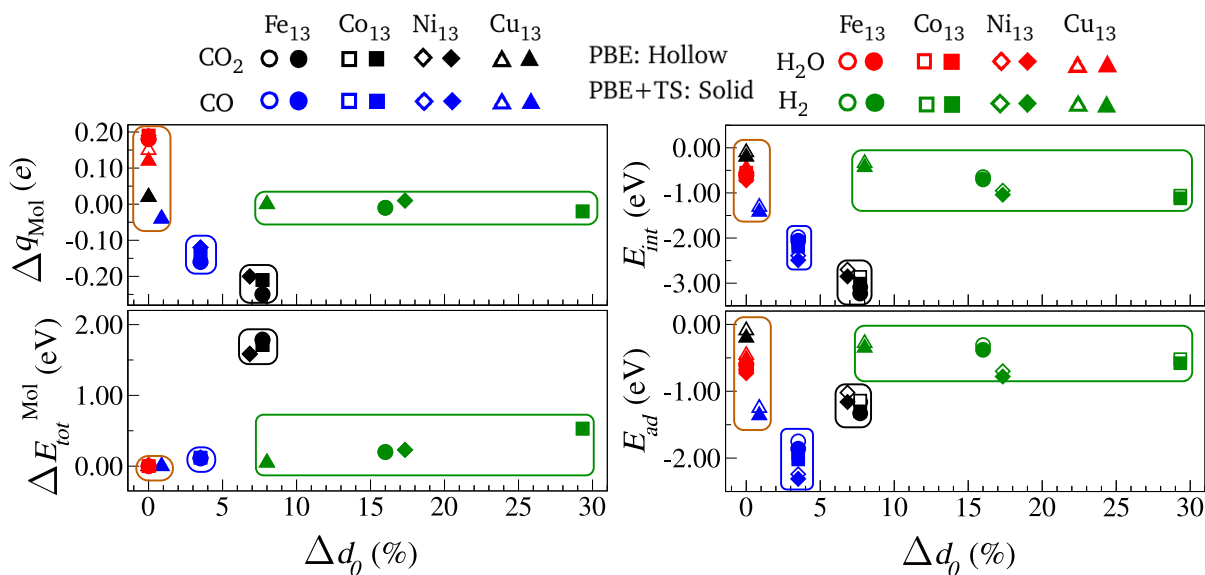
Finally, the  $\text{H}_2$  in the gas-phase has a stretching mode ( $4320\text{ cm}^{-1}$ ) inactive in the IR, that was represented by a red line in Figure 9 for reference. For  $\text{H}_2/\text{TM}_{13}$ , two additional bands appear in the region  $800\text{-}1900\text{ cm}^{-1}$ , corresponding to the  $\text{H}_2\text{-TM}_{13}$  symmetric and antisymmetric stretching. Those bands permit to characterize the participation of the two hydrogen atoms in the adsorption. Additionally, the band correspond to  $\text{H-H}$  stretching appears, with significant displacement compared to the red line, the magnitude of the red-shift is consistent with the increase in  $d_0^{\text{H-H}}$  for  $\text{H}_2/\text{TM}_{13}$ .

### 3.3 Molecular Descriptors in the Activation of Small Molecules

Among the properties used to characterize the adsorption process, we observed that the structural and energetic modification of the  $\text{TM}_{13}$  clusters upon the adsorption are small in contrast with the  $\Delta d_0$  parameter. Since the activation of the molecules should lead to more reactive species, prone to breaking bonds and forming new ones, the changes in bond lengths could be considered an appropriate parameter to evaluate the effect of the adsorption on the activation. Hence, to improve our understanding of the relationship between the descriptors calculated, we analyze the relation between  $\Delta d_0$  and the following properties:  $\Delta q_{\text{Mol}}$ ,  $\Delta E_{\text{tot}}^{\text{Mol}}$ ,  $E_{\text{ad}}$ , and  $E_{\text{int}}$ , Figure 10.

Among the common characteristics of the lowest energy configurations of  $\text{H}_2\text{O}/\text{TM}_{13}$ ,

Figure 10 – The relative change for bond lengths of adsorbed molecules regarding to the gas-phase configuration, as a function of net charge at molecule upon adsorption ( $\Delta q_{\text{Mol}}$ ), deformation energy for the molecules ( $\Delta E_{\text{tot}}^{\text{Mol}}$ ), interaction energy ( $E_{\text{int}}$ ), and adsorption energy ( $E_{\text{ad}}$ ).



Source: Adapted from OCAMPO-RESTREPO, V. K.; ZIBORDI-BESSE, L.; DA SILVA, J. L. F. *The Journal of Chemical Physics*, v. 151, p. 214301, 2019 [115]. Copyright 2019 with the permission of AIP Publishing.

CO<sub>2</sub>/Cu<sub>13</sub>, and CO/Cu<sub>13</sub> systems, we found the following trends,  $\Delta d_0 < 1.00\%$ ,  $\Delta q_{\text{Mol}} > 0$  or close to zero, and  $\Delta E_{\text{tot}}^{\text{Mol}} = 0$ , which indicate negligible perturbations in the molecules upon adsorption. Therefore, those parameters allow us to infer the no activation of molecules on those TM<sub>13</sub>. However, since some higher energy configurations for CO<sub>2</sub>/Cu<sub>13</sub> promote the distortion of CO<sub>2</sub> with negative  $\Delta q_{\text{Mol}}$ , we infer that the activation of CO<sub>2</sub> on Cu<sub>13</sub> have similar characteristics than found on Fe<sub>13</sub>, Co<sub>13</sub>, and Ni<sub>13</sub>.

Regarding to H<sub>2</sub>/TM<sub>13</sub>, CO<sub>2</sub> and CO on Fe<sub>13</sub>, Co<sub>13</sub>, and Ni<sub>13</sub>, there were an increase in the H–H and C–O bond length higher than 1.00%, respectively, the diminish in the CO<sub>2</sub> angle, and also  $\Delta E_{\text{tot}}^{\text{Mol}} > 0$ , indicating perturbations at molecules after the adsorption, and according with our interpretation, the molecules are activated. However, parameters as  $E_{\text{int}}$  and  $E_{\text{ad}}$  are not negligible in none of the previous cases (activated or not activated), suggesting that the magnitude of strength of the adsorption is unable to characterize the activation of those molecules.

The effect of the charge transfer in the H<sub>2</sub><sup>ad</sup> activation cannot be assessed by  $\Delta q_{\text{Mol}}$  analysis. However, it is important to emphasize that the adsorption on clusters allowed a greater H–H bond length elongation than adding charge to H<sub>2</sub> in gas-phase, suggesting additional effects related to the chemical environment provided by the TM<sub>13</sub>. Differently, for CO<sub>2</sub><sup>ad</sup> and CO<sup>ad</sup>, we observed that the charge transfer toward these molecules is the driving force of their activation, since the molecules present structural modifications when negative net charges are found in CO<sub>2</sub><sup>ad</sup> and CO<sup>ad</sup>, e.g., on Fe<sub>13</sub>, Co<sub>13</sub>, and Ni<sub>13</sub>, while no structural changes observed when  $\Delta q_{\text{Mol}}$  were close to zero, as for Cu<sub>13</sub> cases.

Some insights were remarked based on the following mechanism informed for the reduction of CO<sub>2</sub> using H<sub>2</sub> on iron catalysts [10]. The CO<sub>2</sub> interaction with the iron(II) leads to the formation of CO<sub>2</sub><sup>-</sup>, this attacks the H<sub>2</sub> in the gas-phase producing the –COOH species while occurring the homolytic cleavage of H–H bond. When the residual H· attacks carbonyl or hydroxyl group of –COOH, there is the respective formation of formic acid or CO. With the information above, we highlight some features from our results that suggest the potential use of TM<sub>13</sub> in the CO<sub>2</sub> conversion. The charge donor character found for TM<sub>13</sub> clusters could be the driving force to promote the CO<sub>2</sub> activation and formation of the CO<sub>2</sub><sup>-</sup> species. Also, both the CO<sub>2</sub><sup>ad</sup> with a partial negative charge and the weakening of H–H bond, resulting from the adsorption on 3d TM<sub>13</sub> clusters, could promote the formation of COOH species.

### 3.4 Summary

We identified atomistic descriptors in the activation of small molecules induced by their adsorption on 3d TM<sub>13</sub> clusters. The crucial descriptor associated with the activation is the structural variations of the molecules upon their adsorption, i.e., the increase of bond lengths and the angles decreases. The energetic quantification of structural distortion can

be assessed by the distortion energy, which is the energy difference between the structure of molecules in the gas phase and their structure achieved due to the adsorption. Also, for the  $\text{CO}_2^{\text{ad}}$  and  $\text{CO}^{\text{ad}}$  the activation is a consequence of the electronic charge transferred from the  $\text{TM}_{13}$  to molecule. The participation of the carbon atom in the activation mechanism was confirmed by the electron density difference analysis, which reveals the accumulation of charge on the C as well as along C– $\text{TM}_{13}$  bond. However, our analysis of adsorption energy indicates that the strength of the interaction is not necessarily proportional to the activation. Particularly for  $\text{H}_2$  is difficult to infer the participation of the charge transfer mechanism in its activation, although the adsorption on all  $\text{TM}_{13}$  clusters results in a large H–H bond length, suggesting other possible mechanisms related to the chemical environment provided by the  $\text{TM}_{13}$ .



## 4 C–O BOND DISSOCIATION MECHANISM IN CO<sub>2</sub> REDUCTION VIA REDOX AND CARBOXYL ROUTES ON 3d TRANSITION-METAL 13-ATOM CLUSTERS

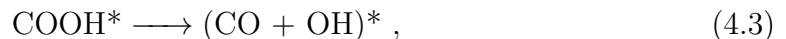
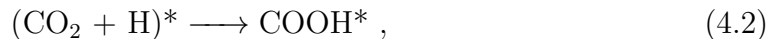
The conversion of CO<sub>2</sub> to CO via the reverse water gas shift reaction, Equation (1.1), has been suggested as the main reaction to produce the CO detected during the CO<sub>2</sub> reduction [12–14]. Since the CO could be a final product or an intermediate toward other products like methanol, understanding the mechanism that involves its production is crucial to enhance the design of catalysts active and with desired features (low-cost, stable, so on) for the CO<sub>2</sub> reduction.

Within the RWGS reaction, the production of CO involves the C–O bond cleavages either from CO<sub>2</sub> or a hydrogenated intermediate, being an important step to be understood in the mechanism, then, in this chapter, we focus our attention on the understanding of C–O bond dissociation using DFT combined with climbing image-nudged elastic band algorithm to find the transition states and to calculate the activation energies of the following reaction steps:

- *Reaction steps from redox route:*



- *Reaction steps from carboxyl route:*



where \* represents the interaction of the species with the TM<sub>13</sub> clusters, and the parenthesis encloses co-adsorbed species.

Results and discussion are organized as follows: (i) adsorption study of the reactants, products, and individual species involved in the reaction steps studied; (ii) detailed mechanism of the C–O bond dissociation by redox and carboxyl routes; (iii) scaling relations analyses for redox and carboxyl routes; and (iv) discussion about routes competition.

### 4.1 Adsorption Study for Species Involved in the C–O Dissociation Mechanism

To study the C–O bond dissociation, we need structures to represent the reactants and products, or, the initial and final states, respectively, according to the Equations 4.1 to 4.3. Beyond that, we included additional systems to support the explanation of trends, co-adsorption effects, and identification of descriptors. Thus, we optimized 9 systems,

namely, the adsorption of single species such as H, O, CO, OH, CO<sub>2</sub>, and COOH and co-adsorbed structures like the (CO<sub>2</sub> + H), (CO + O), and (CO + OH).

The discussion in this section focuses on the adsorption site characterization of the molecule-TM<sub>13</sub> interaction using the adsorption energy,  $E_{ad}$  since this property is commonly used in the analyses of the scaling relation. Also, this discussion involved selected structures for each system according to the reaction steps from equations (4.1)-(4.3). We defined that the adsorbed structures selected as initial and final states, i.e., reactants and products, must be close to adsorption sites predefined according to the CO<sub>2</sub> adsorption results. Then, our initial and final states include both lowest and some high-energy structures.

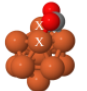
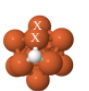
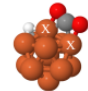
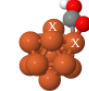
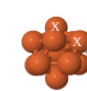
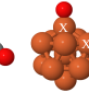
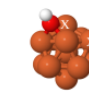
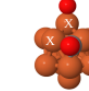
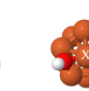
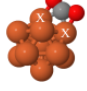
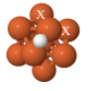
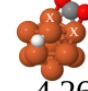
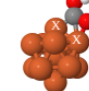
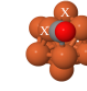

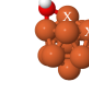
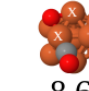
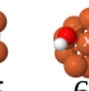
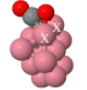
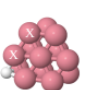
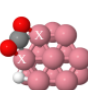
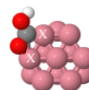
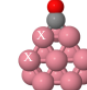
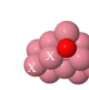
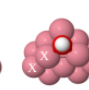
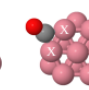
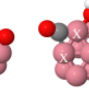
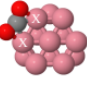
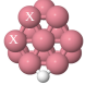
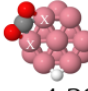
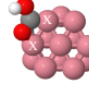
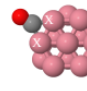
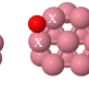
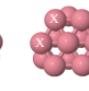
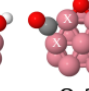
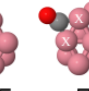
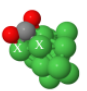
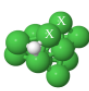
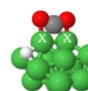
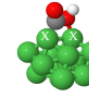
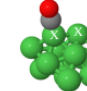
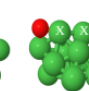
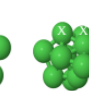
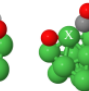
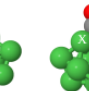
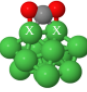
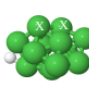
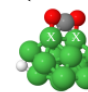
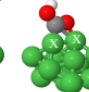
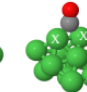
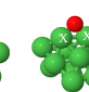
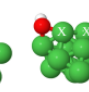
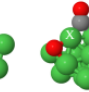
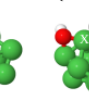
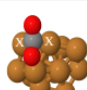
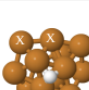
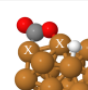
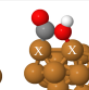
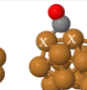
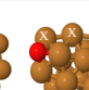

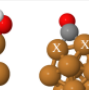
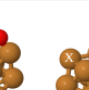
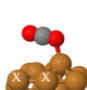
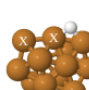
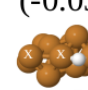
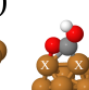
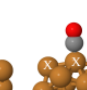
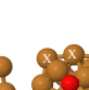
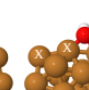
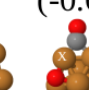
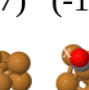
This chapter discussed the representative structures involved in the minimum energy path for the C–O bond dissociation. However, our study explored several initial and final states that are in detail in the supporting information of the reference: OCAMPO-RESTREPO, V. K.; VERGA, L. G.; DA SILVA, J. L. F. **The Journal of Physical Chemistry C**, v. 125, n. 48, p. 26296-26306, 2021 [148]. It is worth informing that all structures used as initial and final states were minima, confirmed by the vibrational frequencies calculations with positive values for the eigenvalues of the Hessian matrix for all normal modes.

Figure 11 shows the lowest energy and one high energy configuration for each system, including co-adsorbed and individual species (i.e., 72 systems). In the previous chapter, we made a wide discussion about the lowest energy structures of CO<sub>2</sub>/TM<sub>13</sub>. Here, we extended the discussion to high energy structures important in the C–O dissociation mechanism. Recapping, the CO<sub>2</sub> adsorbs on Fe<sub>13</sub>, Co<sub>13</sub>, and Ni<sub>13</sub> preferentially via C and O on 2-fold sites, and via one O atom on 1-fold sites on Cu<sub>13</sub>. The adsorption strength decreased from Fe<sub>13</sub> to Cu<sub>13</sub>, which is consistent with previous trends reported on 3d transition metal materials [20, 115, 149].

For high energy configurations, we also observed CO<sub>2</sub> adsorbed via 3-fold sites on all TM<sub>13</sub> clusters characterized by CO<sub>2</sub> deformation, similar to the observed when adsorbed on 2-fold sites. As common characteristic, the interaction via 2- and 3-fold sites yield significant structural and electronic changes on the CO<sub>2</sub> upon the adsorption, suggesting chemisorption of the molecule. To illustrate the structural changes induced by the TM<sub>13</sub> compared with CO<sub>2</sub> in the gas phase, Figure 12 shows the C–O bond distance for all CO<sub>2</sub> adsorbed systems. In general, the C–O bonds suffer symmetric elongation on all TM<sub>13</sub>, and also we observed asymmetric elongation on Ni<sub>13</sub> and Cu<sub>13</sub>.

As discussed early, the chemisorption on Cu<sub>13</sub> leads positive adsorption energies for particular cases, that is mainly explained by the CO<sub>2</sub> deformation energy. Rewriting the adsorption energy in terms of deformation energies,  $E_{ad} = E_{int} + \Delta E_{tot}^{Mol} + \Delta E_{tot}^{TM_{13}}$  [115], the interaction strength can be also characterized by the interaction energy,  $E_{int}$ . Then, the chemisorption afford a strong interaction between the molecule-substrate and induces

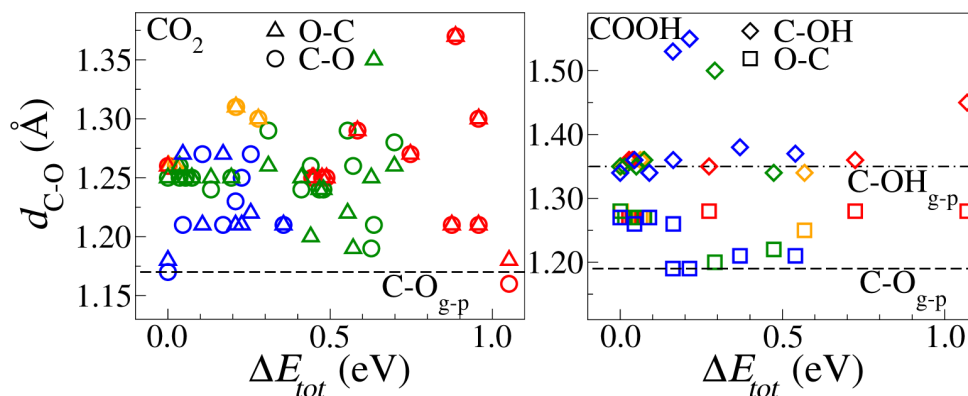
Figure 11 – Lowest and high energy structures for adsorbed and co-adsorbed systems. The TM atoms highlighted with white x are the preferred sites for the lowest energy CO<sub>2</sub> chemisorption. Numbers below the structures are the adsorption energies ( $E_{ad}$ ) and in parentheses the adsorption energy for CO<sub>2</sub> and CO ( $E_{ad}^{CO_2, CO}$ ) obtained due to the co-adsorption effect.

	CO <sub>2</sub>	H	(CO <sub>2</sub> +H)	COOH	CO	O	OH	(CO+O)	(CO+OH)
Fe <sub>13</sub>	High 								
	-1.12	-2.82	-4.24 (-1.24)	-3.02	-1.74	-5.48	-4.37	-7.31 (-1.67)	-6.49 (-1.76)
Fe <sub>13</sub>	Lowest 								
	-1.33	-2.86	-4.26 (-1.28)	-3.08	-1.86	-6.60	-4.75	-8.65 (-1.52)	-6.75 (-1.73)
Co <sub>13</sub>	High 								
	-0.41	-2.77	-4.06 (-1.22)	-3.12	-1.72	-6.03	-4.45	-8.23 (-1.94)	-6.57 (-1.84)
Co <sub>13</sub>	Lowest 								
	-1.30	-3.07	-4.38 (-1.26)	-3.15	-2.02	-6.19	-5.01	-8.25 (-1.82)	-7.04 (-1.97)
Ni <sub>13</sub>	High 								
	-0.46	-2.77	-3.99 (-1.12)	-2.83	-2.07	-5.75	-3.90	-7.96 (-1.91)	-6.18 (-1.97)
Ni <sub>13</sub>	Lowest 								
	-1.16	-2.98	-4.08 (-1.11)	-3.13	-2.17	-5.84	-4.83	-8.29 (-2.05)	-7.00 (-2.07)
Cu <sub>13</sub>	High 								
	0.05	-2.57	-2.67 (-0.03)	-2.54	-1.07	-4.97	-3.98	-5.69 (-0.67)	-5.27 (-1.06)
Cu <sub>13</sub>	Lowest 								
	-0.20	-2.83	-3.03 (-0.13)	-2.75	-1.14	-5.13	-4.44	-6.65 (-0.58)	-5.80 (-1.29)

Source: Reprinted with permission from OCAMPO-RESTREPO, V. K.; VERGA, L. G.; DA SILVA, J. L. F. *The Journal of Physical Chemistry C*, v. 125, n. 48, p. 26296-26306, 2021 [148]. Copyright © 2021, American Chemical Society.

the CO<sub>2</sub> deformation, characterized by  $\Delta E_{tot}^{Mol}$ . As larger the structural deformation is the  $\Delta E_{tot}^{Mol}$  becomes larger and positive. Specifically for the CO<sub>2</sub>/Cu<sub>13</sub> in Figure 11, the values for  $E_{int}$ ,  $\Delta E_{tot}^{Mol}$ , and  $\Delta E_{tot}^{TM_{13}}$  are  $-1.74$ ,  $1.69$ , and  $0.10$  eV, respectively, which explains

Figure 12 – C–O bond lengths ( $d_{\text{C-O}}$ ) for all optimized structures of  $\text{CO}_2$  and  $\text{COOH}$  upon adsorption on  $\text{TM}_{13}$  as a function of the relative energy ( $\Delta E_{\text{tot}}$ ). Open circles and triangles symbols for  $\text{CO}_2$  bonds; open squares and diamonds symbols for  $\text{COOH}$  bonds. Yellow, red, green, and blue indicates the  $\text{Fe}_{13}$ ,  $\text{Co}_{13}$ ,  $\text{Ni}_{13}$ , and  $\text{Cu}_{13}$  clusters, respectively. The dashed (dashed-dots) lines are the C–O (C–OH) bonds length in gas-phase.



Source: Reprinted with permission from OCAMPO-RESTREPO, V. K.; VERGA, L. G.; DA SILVA, J. L. F. **The Journal of Physical Chemistry C**, v. 125, n. 48, p. 26296-26306, 2021 [148]. Copyright © 2021, American Chemical Society.

the positive value of  $E_{\text{ad}}$ . To study the C–O bond dissociation, we selected the preferred adsorption site for  $\text{CO}_2$  chemisorption on each  $\text{TM}_{13}$  as the reactive site since this site provided an activated  $\text{CO}_2$

For the lowest energy structures, H atom interacts on all  $\text{TM}_{13}$  clusters via 2-fold sites, while its interaction via 3-fold sites is observed in high energy structures. The O preferentially adsorbs on  $\text{Fe}_{13}$  and  $\text{Cu}_{13}$  via 3-fold sites, while on  $\text{Co}_{13}$  and  $\text{Ni}_{13}$  via 2-fold sites. For lowest energy structures, we observed that the interaction strength decreased from  $\text{Fe}_{13}$  to  $\text{Cu}_{13}$ , and this trend is consistent with the oxygen affinity trend for transition metals reported based on the bond enthalpies for  $\text{TM-O}$  systems [150].

CO and OH interact by the C and O atoms, respectively, independently of the  $\text{TM}_{13}$  cluster. This well defined interaction behavior is due to the C and O electron density contributions to the LUMO states in the CO and OH, respectively [140], facilitating the charge transfer from  $\text{TM}_{13}$  to molecules. Furthermore, the OH always binds on the 2-fold sites on the  $\text{TM}_{13}$  in contrast with CO that presents an adsorption site dependence with the TM, i.e., binds on 1-fold site on  $\text{Cu}_{13}$ , 2-fold on  $\text{Co}_{13}$  and  $\text{Ni}_{13}$ , and 3-fold site on  $\text{Fe}_{13}$ .

Both *cis*- and *trans*-COOH conformation bind to all  $\text{TM}_{13}$  via C and one O atom on 2-fold sites, being the *cis*- isomer lowest in energy. We also observed that the  $\text{TM}_{13}$  influenced in the stabilization of different adsorption orientations, showing that the adsorption of *cis*-COOH occurs only by the C–O bond on  $\text{Fe}_{13}$  and  $\text{Co}_{13}$ , while it also occurs by the C–OH bond on  $\text{Ni}_{13}$  and  $\text{Cu}_{13}$ , inducing significant structural changes as informed in Figure 12.

For all  $(CO + O)/TM_{13}$  and  $(CO + OH)/TM_{13}$  systems except for  $(CO + OH)/Co_{13}$ , the co-adsorbates preferentially adsorbed on close sites, sharing one TM atom. Differently for  $(CO_2 + H)/TM_{13}$  systems, in the lowest energy structures adsorbates did not share atoms. However, in high energy structures with  $CO_2$  adjacent to the H, the later prefers the 3-fold site rather than 2-fold, as in  $H/TM_{13}$  systems, except on  $Cu_{13}$ . We also quantify the influence of the co-adsorbate on the adsorption energy for  $CO_2$  and CO by the procedure below.

First, we excluded the co-adsorbed specie, i.e. H, O, OH, of the structures obtained from  $(CO_2 + H)/TM_{13}$ ,  $(CO + O)/TM_{13}$ , and  $(CO + OH)/TM_{13}$ ; we performed the energy calculation keeping the structures of  $CO_2/TM_{13}$  and  $CO/TM_{13}$  without relaxation; the energies from previous step were used as  $E_{tot}^{Mol/TM_{13}}$  in the adsorption energy equation. In general, the co-adsorption of H,O and OH decrease the magnitude for  $|E_{ad}^{CO_2;CO}|$  when compared with similar adsorption sites of the systems without co-adsorption; however, small effects on C- $TM_{13}$  and C-O distances were observed. Similar results have been reported on close-packed Rh, Pd, Pt, Ir, and Cu surfaces [151, 152].

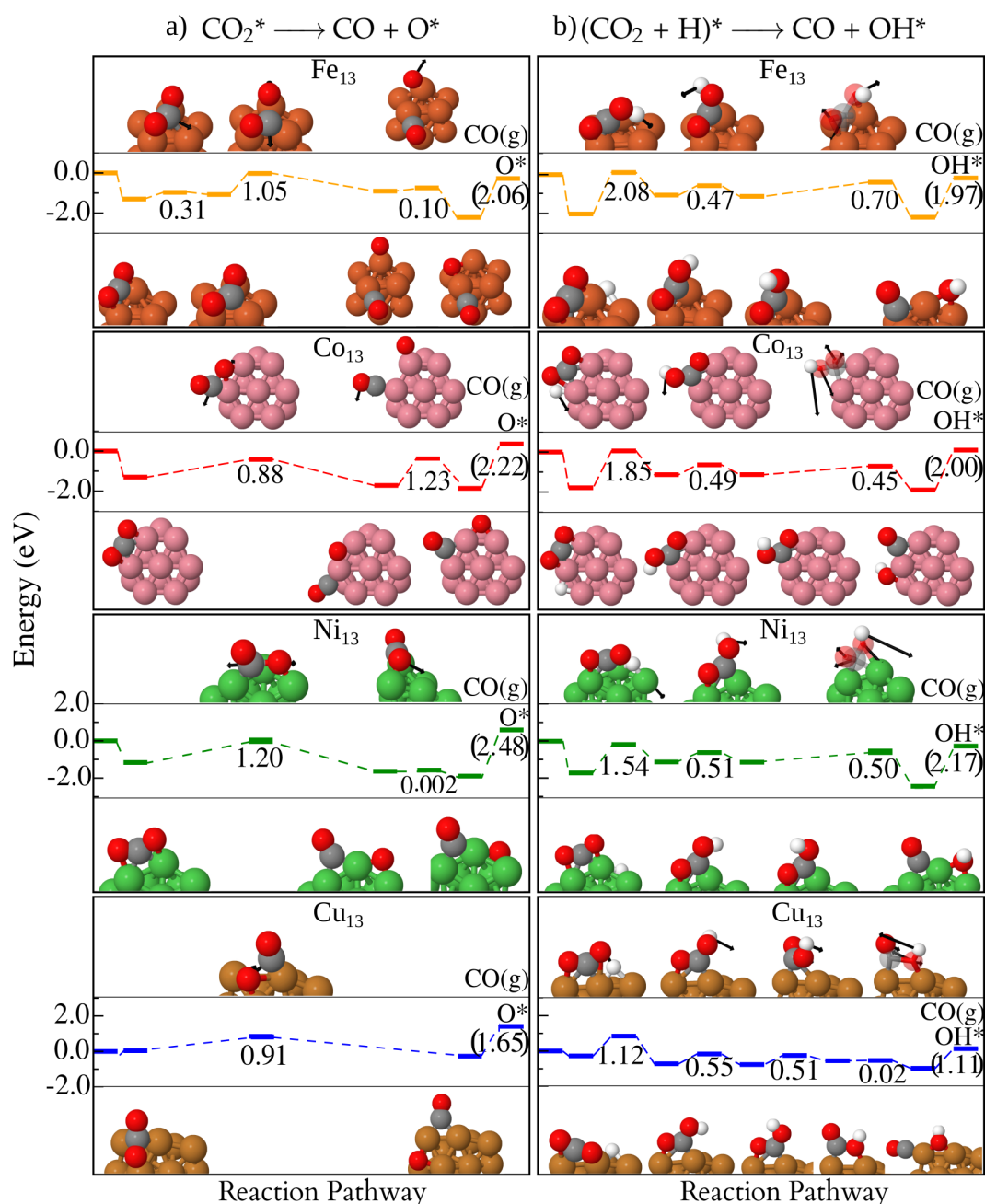
## 4.2 Revealing the C–O Dissociation Mechanism on $TM_{13}$ Clusters

Figures 13 displays the potential energy profiles for redox and carboxyl routes on  $TM_{13}$  clusters and Table 4 contents the activation energies,  $E_a$ , for the reaction steps toward CO, and the imaginary frequencies values for the transition states. All energies plotted in the potential energy profiles are relative to the sum of  $E_{tot}^{TM_{13}}$  and  $\sum E_{tot}^{Mol}$ , where the last term is equal to  $E_{tot}^{CO_2}$  and  $E_{tot}^{CO_2} + E_{tot}^H$  for the redox and carboxyl routes, respectively. The activation energies are given by  $E_a = E_{tot}^\ddagger - E_{tot}^{initial-state}$ . We explored several paths to find the minimum energy path (MEP), the additional paths found are reported in the Appendix D. In this section, we focus on the characterization of the MEP found for each step on each  $TM_{13}$ .

### 4.2.1 Redox Route: Mechanistic Details for C–O Dissociation

Figures 13 a) details the  $CO_2^* \longrightarrow CO + O^*$  reaction. Comparing the reaction step for OC–O dissociation, we find differences between  $TM_{13}$  clusters in the adsorption site for the chemisorbed  $CO_2$  that preceded the bond dissociation. The C-O bond dissociation on  $Co_{13}$  and  $Ni_{13}$  occurs from a  $CO_2$  adsorbed on 2-fold sites, while on  $Fe_{13}$  and  $Cu_{13}$  from the  $CO_2$  adsorbed on 3-fold sites. However, the stabilization of all the transition states preferentially occurs on 3-fold sites, except on  $Co_{13}$ . Based on the  $E_a$  values, the MEP for direct  $CO_2$  dissociation is provided by  $Co_{13}$ ,  $E_a = 0.88$  eV, and the activation energy trend between the studied clusters is:  $E_a^{Co_{13}} < E_a^{Cu_{13}} < E_a^{Fe_{13}} < E_a^{Ni_{13}}$ .

Figure 13 – Potential energy profiles for C–O dissociation: a) via redox route; b) via carboxyl route on  $TM_{13}$ . The structures for all intermediates and transition states are at the bottom and top of their potential energy diagram, respectively. The activation energies ( $E_a$ ) values are the number below boxes, while the CO desorption energy is the number in parenthesis. For comparison purposes, we aligned the transition states for the same elementary step, and the black arrows indicate the vibrational movement in the direction of the reaction coordinate.



Source: Reprinted with permission from OCAMPO-RESTREPO, V. K.; VERGA, L. G.; DA SILVA, J. L. F. *The Journal of Physical Chemistry C*, v. 125, n. 48, p. 26296-26306, 2021 [148]. Copyright © 2021, American Chemical Society.

Table 4 – Activation energies ( $E_a$ ) and imaginary( $i$ ) frequencies for transition states ( $\ddagger_{frequency}$ ).

Reaction Step	$TM_{13}$	$\ddagger_{frequency}$ ( $cm^{-1}$ )	$E_a$ (eV)
$CO_2^* \longrightarrow (CO + O)^*$	Fe <sub>13</sub>	383.5 $i$	1.05
	Co <sub>13</sub>	420.6 $i$	0.88
	Ni <sub>13</sub>	431.5 $i$	1.20
	Cu <sub>13</sub>	225.0 $i$	0.91
$(CO_2 + H)^* \longrightarrow trans-COOH^*$	Fe <sub>13</sub>	1442.0 $i$	2.08
	Co <sub>13</sub>	1351.4 $i$	1.85
	Ni <sub>13</sub>	1312.0 $i$	1.54
	Cu <sub>13</sub>	1535.1 $i$	1.12
$trans-COOH^* \longrightarrow cis-COOH^*$	Fe <sub>13</sub>	597.5 $i$	0.47
	Co <sub>13</sub>	604.3 $i$	0.49
	Ni <sub>13</sub>	624.4 $i$	0.51
	Cu <sub>13</sub>	676.9 $i$	0.55
$cis-COOH^* \longrightarrow cis-COOH^*$	Cu <sub>13</sub>	80.2 $i$	0.51
$cis-COOH^* \longrightarrow (CO + OH)^*$	Fe <sub>13</sub>	237.7 $i$	0.70
	Co <sub>13</sub>	92.4 $i$	0.45
	Ni <sub>13</sub>	114.7 $i$	0.50
	Cu <sub>13</sub>	148.2 $i$	0.02

Source: Reprinted with permission from OCAMPO-RESTREPO, V. K.; VERGA, L. G.; DA SILVA, J. L. F. **The Journal of Physical Chemistry C**, v. 125, n. 48, p. 26296-26306, 2021 [148]. Copyright © 2021, American Chemical Society.

#### 4.2.2 Redox Route: the Diffusion Matters

The lowest energy structure for  $CO_2$  chemisorption not always provided the active site where the C–O dissociation occurs. As our results on the Fe<sub>13</sub> cluster inform, the  $CO_2$  diffusion could precede its direct dissociation when the lowest energy structures for initial and final states were connected. The  $CO_2$  adsorption on Fe<sub>13</sub> is stronger than the rest of  $TM_{13}$ , which can induce this difficulty to direct react and the necessity to arise more reactive intermediates, like the  $CO_2$  adsorbed on a 3-fold site, to allow the C–O dissociation.

We also explored the diffusion after dissociation of both CO and O species. A small barrier for CO diffusion was observed only on Ni<sub>13</sub>, while the O presented diffusion barriers on all metals, Appendix D. We relate these results to the stronger oxygen adsorption on  $TM_{13}$ , difficulting the O- $TM_{13}$  bond dissociation to move from one site to another. On periodic surfaces similar trends have been reported and a good correlation between diffusion barriers and adsorption energies [153]. The differences between CO and O diffusion behavior play an important role in the entropic contribution treatment, as has been informed in previous studies[154], and our results at small sizes cluster models suggest similar behavior.

### 4.2.3 Carboxyl Route: Mechanistic Details for C–O Dissociation

Figure 13 b) describes the C–O bond dissociation via carboxyl intermediate,  $(CO_2 + H)^* \longrightarrow CO + OH^*$ . To produce CO, at least two steps must occur: (1) the COO–H formation, and (2) OC–OH bond breaking. Since the adsorption study suggested that  $CO_2$  chemisorbed was favorable on most of the  $TM_{13}$ , we adopted the Langmuir–Hinshelwood mechanism[155]. Our results suggested that the C–O dissociation via carboxyl route proceed in three (four) elementary steps on  $Fe_{13}$ ,  $Co_{13}$ , and  $Ni_{13}$  (Cu). There are two common processes involving the COOH specie that occur on all studied  $TM_{13}$  that: the COO–H bond formation into *trans*-COOH conformation, followed by OC–OH bond rotation to *cis*- conformation. The bond rotation is less energy demanding, smaller activation energies, than the *trans*-COOH formation. The  $E_a$  for COO–H bond formation decreases while  $E_a$  for OC–OH bond rotation increases from Fe to Cu clusters.

For OC–OH bond dissociation on  $Fe_{13}$ ,  $Co_{13}$ , and  $Ni_{13}$ , the *cis*-COOH intermediate stabilized when C–O fragment interacted with the cluster. The C–O dissociation occurs directly from *cis*-COOH via its rotation until C–OH fragment bonded to the cluster. Differently to most  $TM_{13}$ , the  $Cu_{13}$  provided an additional step involving a more activated *cis*-COOH intermediate, due to its interaction via C–OH fragment, with only 0.21 eV higher than the lowest energy structure. The alternative path proceeds as follow: *cis*-COOH rotates until interacting via C–OH fragment, then the OC–OH bond dissociation occurs from this activated intermediate with a small barrier of 0.02 eV. This result evidenced the importance of the adsorption in the intermediates activation, since the OC–OH bond elongates about 15 % when interacting with the  $TM_{13}$ , compared to COOH in the gas phase. The  $E_a$  trend for OC–OH dissociation is:  $E_a^{Cu_{13}} \ll E_a^{Co_{13}} < E_a^{Ni_{13}} < E_a^{Fe_{13}}$ .

### 4.2.4 CO Desorption via Redox and Carboxyl Routes

The desorption energies for CO were calculated by the difference energies between  $CO + O^*$  and  $(CO + O)^*$  or  $CO + OH^*$  and  $(CO + OH)^*$  for redox or carboxyl routes, respectively. The energies for  $O^*$  and  $OH^*$  come from their relaxation keeping the same adsorption site that when they were co-adsorbed with CO. Either by redox or carboxyl routes, the CO desorption energy increased as follow:  $Cu_{13} < Fe_{13} < Co_{13} < Ni_{13}$ . The desorption energies range from 1.11 to 2.48 eV, being higher than the activation barriers for previous steps on most of the  $TM_{13}$ , except on  $Fe_{13}$  and  $Cu_{13}$  by carboxyl route. Then, even if we provided enough energy to overcome the C–O dissociation, its desorption could be a limiting step, suggesting that CO tend to be likely an intermediate toward other products or a poison rather than a final product on  $TM_{13}$  clusters.



### 4.3 Brønsted–Evans–Polanyi and Transition states Scaling Relations for Redox and Carboxyl Routes

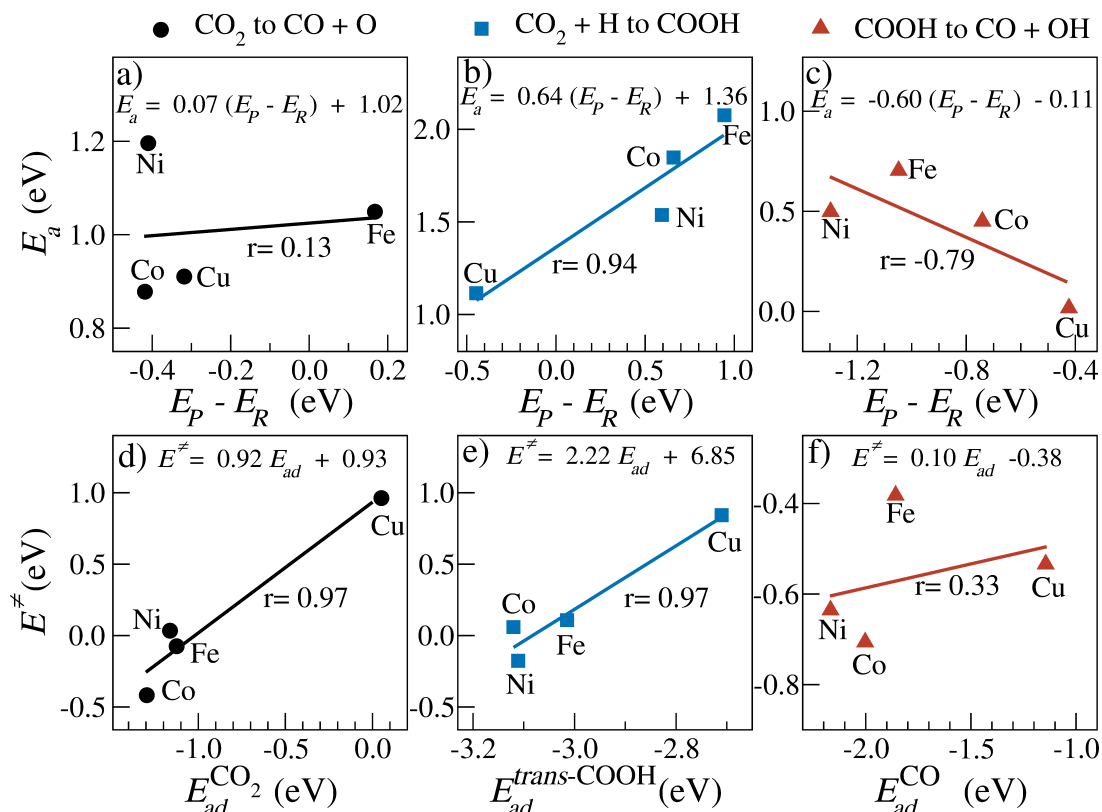
Within heterogeneous catalysis, the concept of the scaling relation suggests the existence of an empirical mathematical relationship of the adsorption energies between different adsorbed species, including intermediates and transition states, involved in a reaction step studied on different catalyts[156]. We employed the well-known Brønsted–Evans–Polanyi (BEP) and the transition states scaling (TSS) relation to identify the adsorbates that could be good descriptors for the C–O bond dissociation within RWGS reaction. The BEP relates the activation energy with the energy difference between product and reactant, while TSS analyzes the relationship between the transition state energy and the intermediates adsorption energies. Specifically for TSS relations, we used all adsorbed species involved in the studied reaction step, results informed in Appendix D. In this section, it is discussed the results for BEP relations and the most correlated TSS relations.

Figure 14 shows the BEP and TSS relations for CO<sub>2</sub> dissociation in a) and d), for COOH formation in b) and e), for CO–OH dissociation in c) and f), respectively. For CO<sub>2</sub> dissociation, the analysis from BEP indicates that activation energy could not be well predicted by the reaction energy, as the small value for Pearson coefficient ( $r$ ) informs poor correlation. It is expected due to the high dependence of BEP relation with similarities in the process among the compared materials [157], e.g., similar adsorption sites for reactants, products, and transition state. As characterized in the section above, the CO<sub>2</sub> dissociation presented differences in between TM<sub>13</sub> in both, the reactants and transition states adsorption sites.

However, the TSS analysis points out the CO<sub>2</sub> adsorption energy as the most correlated with the transition state energy for the CO<sub>2</sub> dissociation process. It suggests that the CO<sub>2</sub>–TM<sub>13</sub> interaction influences the transition state stabilization and could be used as a catalytic descriptor for the direct C–O bond dissociation of the CO<sub>2</sub>. Then, it would be expected that stronger CO<sub>2</sub> adsorption induces stronger transition state interaction with the TM<sub>13</sub> clusters. Beyond CO<sub>2</sub> adsorption, the O energy adsorption also shows good correlation with  $E^{[\text{CO}-\text{O}]^\ddagger}$ , informing that the O–TM interactions also provide information about the strength of transition state interaction with the cluster. Same to CO<sub>2</sub>, as stronger (weaker) the O adsorption is, stronger (weaker) the  $[\text{CO}-\text{O}]^\ddagger$  interaction with clusters should be.

For carboxyl route the steps involving the COOH formation and its dissociation presented substantial  $E_a$  variation with the TM<sub>13</sub>, contrary to the step related to the *trans*- to *cis*-COOH rotation. Hence, to analyze the scaling relations, we choose only the first steps mentioned above. As expected for the *trans*-COOH formation, the results from BEP informed good correlations with  $r = 0.94$ . Then, the activation energy for this step scales with the reaction energy, decreasing when the exothermicity of the reaction step

Figure 14 – BEP and TSS relations for: CO<sub>2</sub> dissociation in a), d); COOH formation in b), e); and for CO–OH dissociation in c), f).  $E_a$  is the activation energy, while  $E^\ddagger$  is the transition state energy obtained by:  $E^\ddagger = E_{tot}^\ddagger - E_{tot}^{TM_{13}} - \sum E_{tot}^{reactants}$ . The products and reactants are represented by  $P$  and  $R$ , respectively, and the equation inside each plot comes from the linear regression.



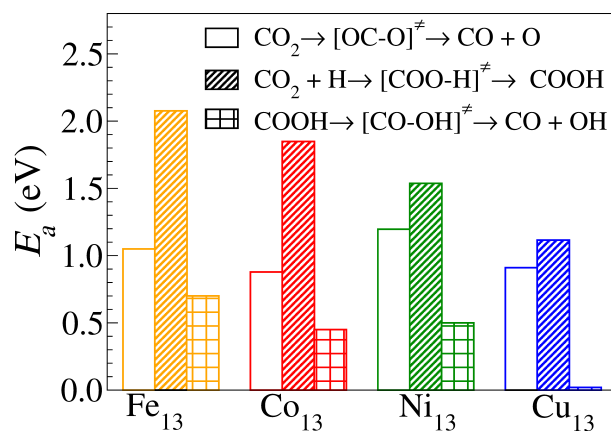
Source: Reprinted with permission from OCAMPO-RESTREPO, V. K.; VERGA, L. G.; DA SILVA, J. L. F. *The Journal of Physical Chemistry C*, v. 125, n. 48, p. 26296-26306, 2021 [148]. Copyright © 2021, American Chemical Society.

increased. Also, the slope from the equation allows to infer that the transition state tends to be more like products [158], since the variations in the final state highly impact the activation energies.

The TSS analysis supports the result above, showing a good correlation with the adsorption energy of the *trans*-COOH product. Stronger adsorption of *trans*-COOH also implies stronger transition state interaction with the TM<sub>13</sub>, and then this intermediate could be suggested as a descriptor in the COOH formation step. Beyond the influence of the product on the transition state energy, the reactants can play an important role in modulating the exothermicity change for this step. The adsorption strength of (CO<sub>2</sub> + H)\* decreased from Fe to Cu matching with the exothermicity increase of the step, and hence, with the  $E_a$  decreased trend. It would indicate that the weak interaction of reactants-TM<sub>13</sub> also favors the  $E_a^{[COO-H]^\ddagger}$  decrease.

For the *cis*-CO–OH dissociation, both BEP and TSS analysis shows substantial

Figure 15 – Comparison of the activation energies ( $E_a$ ) between  $\text{CO}_2$  dissociation,  $\text{CO}_2$  hydrogenation, and  $\text{CO-OH}$  dissociation on  $\text{TM}_{13}$  represented by open bar, diagonal line filled bar, and squares filled bar, respectively.



Source: Reprinted with permission from OCAMPO-RESTREPO, V. K.; VERGA, L. G.; DA SILVA, J. L. F. *The Journal of Physical Chemistry C*, v. 125, n. 48, p. 26296-26306, 2021 [148]. Copyright © 2021, American Chemical Society.

poor correlation, being difficult to postulate a descriptor for this step, at least from these results. Again, the different alternative paths, earlier described for this dissociation, breaks the predictive power of the BEP linear relationship. Similar to the  $\text{CO}_2$  dissociation, the activation energy for  $\text{CO-OH}$  dissociation on  $\text{TM}_{13}$  could not be predicted by the reaction energy.

#### 4.4 Routes Competition: Redox versus Carboxyl

We compared the lowest  $E_a$  found for the C–O bonds dissociation on the  $\text{TM}_{13}$  clusters by redox and carboxyl routes in Figure 15. The lower activation energies for  $\text{CO}_2$  dissociation on all studied clusters suggested the redox route as the preferred for C–O bond dissociation, with the  $\text{Co}_{13}$  as the best candidate to provide the lowest energy path. The highlighted results on Co could be due to its capability to strongly adsorb both  $\text{CO}_2$  and O compared with remaining clusters, as suggested from TSS scaling relation. Other studies have reported smaller  $E_a$  values on Co and Ni periodic systems [54] than our data. The discrepancy comes from the differences in the  $\text{CO}_2$  adsorption sites used, being the  $\text{CO}_2$  more coordinated to the surface than the reported in this study. However, comparing similar adsorption sites for  $\text{CO}_2$  on Fe and Cu periodic systems, we reported  $E_a$  values lower by 0.18 eV and 0.05 eV on  $\text{Fe}_{13}$   $\text{Cu}_{13}$ , respectively, indicating the impact of low coordination sites on the activation energy.

To evaluate the competition between redox and carboxyl routes for the C–O bond dissociation, we compared the higher activation energies of each route. The activation energies differences between the  $\text{CO}_2$  dissociation (redox) and its hydrogenation into

carboxyl species decreased from Fe<sub>13</sub> to Cu<sub>13</sub>, which has been also reported on 3d TM periodic surfaces [80,159]. It suggests that on early 3d TM, the redox route doubtless provides an easier path, while on later metals, both routes could arise. We attributed this competitive behavior on Cu<sub>13</sub> to the weaker CO<sub>2</sub> + H-TM interaction, that facilitates the H-Cu<sub>13</sub> bond scission and then the COO-H bond formation, compared to remained clusters.

Finally, to evaluate the effect of the CO<sub>2</sub> hydrogenation on the C-O dissociation, the activation energies for related to [OC-O]<sup>‡</sup> and [CO-OH]<sup>‡</sup> were compared. The C-O bond dissociation from carboxyl species presented smaller  $E_a$  than from CO<sub>2</sub> on all clusters. Compared with the CO<sub>2</sub> activation via adsorption, the formation of COOH provides larger C-O bonds length, requiring less energy to its dissociation. Additionally, the COOH adsorption provided large elongation of the C-OH bond on carboxyl species, which drastically reduces its dissociation activation energy, especially on Cu<sub>13</sub>. Even so, the carboxyl route is limiting by the COOH formation on all TM<sub>13</sub> and enhancing this first step could help in the production of CO.

## 4.5 Summary

The C-O bond dissociation is a critical process within the reverse water gas shift reaction to obtain CO as the final product or either as intermediate in the synthesis of renewable fuels. In this study, we characterized the C-O bond dissociation on 3d TM<sub>13</sub> clusters via redox and carboxyl routes. The redox route presented the lower activation energies for the C-O bond dissociation from CO<sub>2</sub> compared with the carboxyl route on all studied TM<sub>13</sub>. Among TM<sub>13</sub> clusters, Co provided the lowest reaction path, being attributed to its capability to strongly adsorb both CO<sub>2</sub> and O species. Furthermore, we identified a competitive trend between redox and carboxyl routes, since the difference between activation energies of CO<sub>2</sub> dissociation and COOH formation decreased from Fe<sub>13</sub> to Cu<sub>13</sub>. Our results suggested that this behavior is consequence of the (CO<sub>2</sub> + H)-TM interaction strength, that decreased from Fe to Cu as well. Then, as weaker is the H-TM interaction, easier is the bond scission, facilitating the COOH formation. Finally, we pointed out the CO<sub>2</sub> and *trans*-COOH species as the best descriptors for the C-O bond dissociation via the redox and carboxyl routes, respectively.

## 5 STUDY OF THE CO<sub>2</sub> ELECTROREDUCTION ON Cu Zn ALLOYS: THE ROLE OF Zn ON THE LAST STAGES OF PATHS TOWARD C<sub>2</sub> PRODUCTS

The interest to obtain heavier hydrocarbons from CO<sub>2</sub> reduction is motivated by their larger energy density, which can be exploited to supply the global energy demand in a more sustainable scenario. In this context, understanding the reaction mechanism until C<sub>2</sub> products like ethylene, acetaldehyde, and ethanol is crucial to guide the design of the catalysts. Despite the extensive research on the CO<sub>2</sub>RR, there is not yet a consensus about the complete reaction mechanism toward C<sub>2</sub> products. Also, there are some challenges to address aiming to improve process efficiency, such as the reducing of the large overpotentials that limit the use of those materials at industrial scale [160]. For instance, the thermodynamic potential required for the CO<sub>2</sub> reduction into C<sub>2</sub> products like ethylene (C<sub>2</sub>H<sub>4</sub>) and ethanol (CH<sub>3</sub>CH<sub>2</sub>OH) are 0.064 V and 0.084 V versus the reversible hydrogen electrode (RHE) at 298 K, respectively. However, the experimental overpotentials reported on Cu polycrystalline are  $-1.13$  V for C<sub>2</sub>H<sub>4</sub> and  $-1.14$  V for CH<sub>3</sub>CH<sub>2</sub>OH [161], being necessary the improvement of Cu-based electrocatalysts to reduce the input energy and increase the products selectivity.

In this chapter, we addressed the last stages in the CO<sub>2</sub>RR to understand the role of Zn on the ethanol and ethylene selectivity using DFT and the computational hydrogen electrode method [87]. The discussion begins with the systems in gas-phase: Cu<sub>55</sub>, Cu<sub>42</sub>Zn<sub>13</sub> clusters and the species involved in the reaction paths studied; this is followed by the discussion of the free energy diagrams for the reaction paths studied on Cu<sub>55</sub> and Cu<sub>42</sub>Zn<sub>13</sub> clusters; finally, the analysis of the effect of Zn on the paths toward C<sub>2</sub> products.

### 5.1 Systems in Gas-phase: Intermediates in the Selected Paths to Ethylene, Acetaldehyde, and Ethanol Production

In this study we mainly put our attention on the later stages of the possible paths to C<sub>2</sub> products, since previous studies of the CO<sub>2</sub>RR and CO electroreduction reaction (CORR) suggested that the C<sub>2</sub> products mentioned share a similar path and bifurcate in later stages (after C–C coupling) [3, 93–95]. Also, the similar onset potentials observed for ethylene and ethanol production on Cu catalysts could indicate a common potential-determining step (PDS), attributed to the OCCOH formation, including the CO dimerization and a proton-coupled electron transfer (PCET) step [3].

The mechanisms suggested in the literature for the C–C bond formation from the CORR are controversial. For instance, the CHO + CO  $\longrightarrow$  COCHO coupling has been reported as favored on Cu(111) surfaces over CO + CO  $\longrightarrow$  COCO + H  $\longrightarrow$  COCOH

formation. That find contrasts with the experimental identification of COCOH species using FTIR; however, it is well known that COCHO can tautomerize into COCOH, opening another possible path to obtain the species experimentally observed. Further steps proposed from COCHO intermediate included the CCO followed by the CHCO intermediate as the starting point for the hydrogenation to ethanol and ethylene formation [3]. However, recent study explored other paths for C–C coupling on Cu(111) surface via: CO dimerization or coupling CO and CH<sub>x</sub> species. The CO–CH coupling via Langmuir–Hinshelwood mechanism is favored over CO–CH<sub>2</sub> and CO–CH<sub>3</sub> with the smaller activation energy of 0.70 eV [162], providing additional evidences of the CHCO as a possible intermediate to C<sub>2</sub> products.

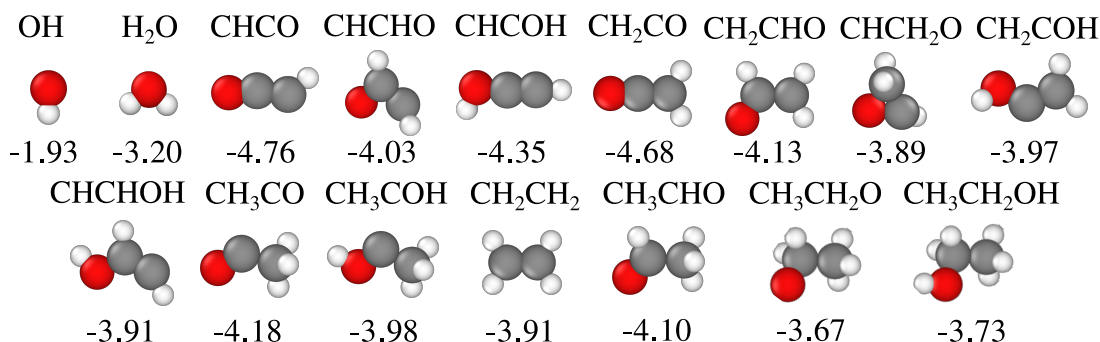
Herein, we explored several PCET steps from CHCO until ethylene, acetaldehyde, and ethanol considering the following species:

- First hydrogenation of the CHCO into CH<sub>2</sub>CO, CHCOH, and CHCHO.
- All the option for the hydrogenation of the species in the item above, considering key reported intermediates as CH<sub>2</sub>CHO and CHCH<sub>2</sub>O [163]: CH<sub>3</sub>CO, CH<sub>2</sub>COH, CH<sub>2</sub>CHO, CHCH<sub>2</sub>O, and CHCHOH.
- The next PCET considered provided the direct formation of acetaldehyde and ethylene. This stage is one of the ways proposed for the paths bifurcation into C<sub>2</sub> products, and acetaldehyde is reported as an intermediate to producing ethanol selectively [97].
- In the last stages was only considered the intermediates reported as the most favored on Cu(111) following the paths: from acetaldehyde to CH<sub>3</sub>CH<sub>2</sub>O and then CH<sub>3</sub>CH<sub>2</sub>OH; from ethylene to OH and then the H<sub>2</sub>O.

Figure 16 displays all the intermediates and products studied, and Table 5 presents some energetic and structural properties. For the C<sub>2</sub> species, the calculated binding energies are slightly overestimated with a maximum relative error about 5.0% compared to the experimental values for: CH<sub>2</sub>CO, CH<sub>3</sub>CO, C<sub>2</sub>H<sub>4</sub>, CH<sub>3</sub>CHO, CH<sub>3</sub>CH<sub>2</sub>O, and CH<sub>3</sub>CH<sub>2</sub>OH. Contrary, the values for OH and H<sub>2</sub>O are underestimated with a larger relative error of 13.00% for the hydroxide [2].

The most stable species, more negative values for  $E_b$ , are CHCO, CHCOH, and CH<sub>2</sub>CO, that presented the shorter bond lengths between the carbons and oxygen atoms since the central carbon is prone to keep its valence complete. Although the central carbon only binds to the other carbon and oxygen atoms, those species have differences in their OCC angle. The smaller angle for CHCO can be explained by its radical nature and the electron delocalization over the central carbon atom. While the CH<sub>2</sub>CO and CHCOH

Figure 16 – Species in gas-phase that participate in the reaction paths studied, where the carbon, oxygen, and hydrogen atoms are the gray, red, and white balls, respectively. The number below each species is the binding energy with  $E_{energy}^{ZPE}$  correction ( $E_b^{ZPE}$ ) in eV per atom.



Source: Own authorship.

presented OCC angle close to 180.00°, the slightly difference could be explained by a possible hybridization changes on the O atom from  $sp^2$  to  $sp^3$ , respectively.

As expected, the hydrogenation on the central carbon in the CHCHO species provided the smaller OCC angle among the species with a molecular formula of  $C_2H_2O$ , a consequence of the central carbon hybridization that also impacts the binding energy, reducing the strength of their bonds compared with the other isomers. Comparing the species with the molecular formula of  $C_2H_3O$  the most stable species keep the shorter C–O bond length:  $CH_2CHO$  and  $CH_3CO$ . The remaining isomers presented additional O- bonds, weakening the C–O bond and providing less stability to the species. A similar trend for the  $C_2H_4O$  species was observed, where the acetaldehyde is more stable than  $CH_3COH$ . Finally, comparing the ethylene and ethanol stability, the former presented a stronger C–C bond, typically characterized as a double bond that provides more stability for this species as evidenced by comparing the binding energy values.

## 5.2 Clusters: $Cu_{55}$ and the $Cu_{42}Zn_{13}$ Alloy

To obtain our model for the  $Cu_{55}$  cluster, we reoptimized a set of 9 different structures from a previous study developed in our group [1]. Structures with high and low-symmetry were included, namely: icosahedron (ICO), cuboctahedron (CUB), disordered reduced-core (DRC), that includes models with 7 to 11 atoms in the core, tetrahedral-like models (THL), and a fragment of the FCC structure (FCCf). As expected, our putative global minimum configuration was the ICO structure with small differences in their properties as compared with previous results [1]. Then, we selected the  $Cu_{55}$  ICO as our reference model to study the effect of the Zn in the CuZn alloy. Most of the studies have reported higher Faradaic efficiencies for  $C_2$  products on CuZn alloys, specifically on Cu-rich alloys with Cu:Zn ratio of 3:1 and 4:1 [47, 48].

Table 5 – Energetic and some structural properties for all the species studied in the selected reaction paths. Absolute value for binding energy ( $|E_b|$ ); zero point energy ( $E_{energy}^{ZPE}$ ); absolute value for binding energy with  $E_{energy}^{ZPE}$  correction ( $|E_b^{ZPE}|$ ); experimental binding energy ( $E_b^{Exp}$ ) at two different temperatures ( $T$ ) both from reference [2]; minimum oxygen bond distance with X=H or C ( $d^{O-X}$ ); minimum carbon-carbon bond distance ( $d^{C-C}$ ); and angle between the fragment OCC ( $\angle^{OCC}$ ).

Species	$ E_b $ (eV)	$E_{energy}^{ZPE}$ (eV)	$ E_b^{ZPE} $ (eV)	$E_b^{Exp}$ (eV)		$d^{O-X}$ (Å)	$d^{C-C}$ (Å)	$\angle^{OCC}$ (°)
				$T=298\text{ K}$	$T=0\text{ K}$			
OH	4.09	0.22	3.87	4.46	4.41	0.98		
H <sub>2</sub> O	10.16	0.56	9.59	9.61	9.51	0.97		
CHCO	19.55	0.50	19.05			1.18	1.30	169.40
CHCHO	20.95	0.79	20.16			1.29	1.35	90.80
CHCOH	22.57	0.83	21.73			1.31	1.21	175.30
CH <sub>2</sub> CO	24.22	0.83	23.39	22.45	22.24	1.17	1.31	180.00
CH <sub>2</sub> CHO	25.91	1.11	24.79			1.24	1.43	123.20
CHCH <sub>2</sub> O	24.50	1.16	23.34			1.37	1.45	63.30
CH <sub>2</sub> COH	24.93	1.13	23.80			1.34	1.32	130.90
CHCHOH	24.56	1.11	23.45			1.39	1.31	124.20
CH <sub>3</sub> CO	26.20	1.13	25.07	24.32	24.05	1.19	1.50	129.20
CH <sub>3</sub> COH	27.89	1.44	26.45			1.33	1.49	107.60
C <sub>2</sub> H <sub>4</sub>	24.81	1.35	23.47	23.35	23.07		1.33	
CH <sub>3</sub> CHO	30.15	1.45	28.70	28.25	27.92	1.21	1.50	124.80
CH <sub>3</sub> CH <sub>2</sub> O	31.06	1.68	29.38	28.88	28.50	1.35	1.53	117.30
CH <sub>3</sub> CH <sub>2</sub> OH	35.67	2.10	33.57	33.43	32.98	1.44	1.52	92.6

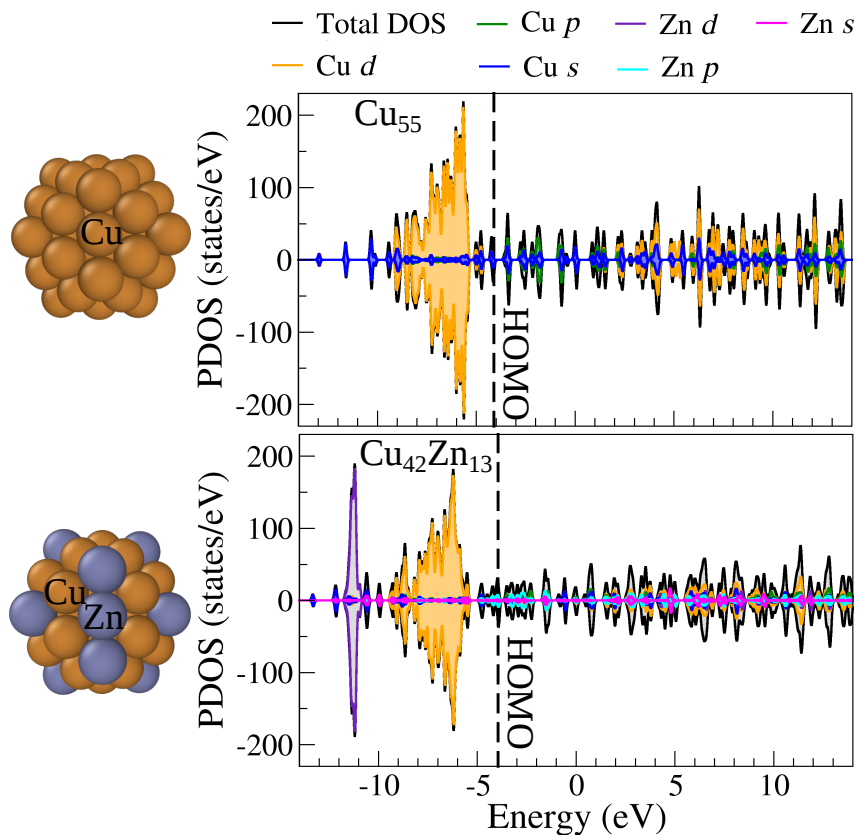
Source: Own authorship.

To use a composition close to the experimental observations, we employed a composition of  $Cu_{42}Zn_{13}$  that leads a Cu:Zn ratio of 3.2:1. We used as a base structure the ICO model to design the alloys configurations considering core-shell types structures with most Zn atoms at the core ( $C_{Zn}S_{Cu}$ ), with most of the Zn at the shell ( $C_{Cu}S_{Zn}$ ), and a segregated cluster ( $Seg_{Cu-Zn}$ ). Our pGMC for the  $Cu_{42}Zn_{13}$  presented all the Zn atoms at the shell, 12 at the vertex and 1 at the edge. The greater stabilization of  $C_{Cu}S_{Zn}$  model described above compared to the  $C_{Zn}S_{Cu}$  models can be explained by the larger covalent radius of Zn compared to Cu, 1.63 and 1.11 Å, respectively. The Zn atoms in the core create a strain providing more open structures and then weaker bonds. Additional details comparing all the alloys structures calculated can be found in Appendix E.

Figure 17 shows the pGMC for the  $Cu_{55}$  and  $Cu_{42}Zn_{13}$  clusters with their plots of projected density of states, and Table 6 contains data related to energetic, structural, and electronic properties. About the structural properties, the  $Cu_{42}Zn_{13}$  cluster presented small



Figure 17 –  $\text{Cu}_{55}$  and  $\text{Cu}_{42}\text{Zn}_{13}$  cluster models with their projected density of states (PDOS). The dashed line in each PDOS plot refers to the HOMO energy.



Source: Own authorship.

differences compared with the  $\text{Cu}_{55}$ , e.g., larger radius and  $d_{av}$  values. It is a consequence of the larger Zn–Zn and Cu–Zn bond lengths, compared to  $\text{Cu}_{55}$  cluster, that deviates the average value of the bond distances. Contrarily, the binding energy is more affected, where the alloy requires less energy to be atomized.

Regarding the electronic properties, the magnetic moment is reduced by the introduction of the Zn while the HOMO-LUMO gap keeps unaltered. However, the HOMO and LUMO energies suffer small shifts induced by Zn. The HOMO and LUMO states in the alloy have contributions from the  $s$  and  $p$  states from both Cu and Zn atoms, as observed in the PDOS plot. Also, we identified that the  $d$  states from the Cu and the Zn do not contribute to the HOMO and LUMO states; however, in the alloy, new states appeared formed mainly by  $d$  states from the Zn. Finally, we analyzed the charge at the cluster surface, observing that the alloy presented a less negative net charge at the surface compared to the  $\text{Cu}_{55}$  cluster. It could be an effect induced by the electronegativity differences, where the Cu tends to accumulate charge while the Zn tends to donate it when they are together.

Table 6 – Comparison of energetic, structural, and electronic properties for  $\text{Cu}_{55}$  and  $\text{Cu}_{42}\text{Zn}_{13}$  clusters. Binding energy per atom ( $E_b$ ); highest occupied molecular orbital (HOMO); lowest unoccupied molecular orbital (LUMO); HOMO-LUMO gap (Gap); average effective coordination number ( $\text{ECN}_{av}$ ); average interatomic distance ( $d_{av}$ ); Radius (Radius); charge at shell surface ( $q_S$ ); and total magnetic moment ( $m_{tot}$ ).

Clusters	$E_b$ (eV/atom)	HOMO (eV)	LUMO (eV)	Gap (eV)	$\text{ECN}_{av}$ (NNN)	$d_{av}$ (Å)	Radius (Å)	$q_S$ (e)	$m_{tot}$ ( $\mu_B$ )
$\text{Cu}_{55}$	-3.12	-4.11	-4.07	0.04	8.39	2.50	4.75	-0.19	3.00
$\text{Cu}_{42}\text{Zn}_{13}$	-2.63	-3.95	-3.91	0.04	8.43	2.52	4.82	-0.14	2.00

Source: Own authorship.

### 5.3 Free Energy Diagrams of the Selected Reaction Paths on $\text{Cu}_{55}$ and $\text{Cu}_{42}\text{Zn}_{13}$

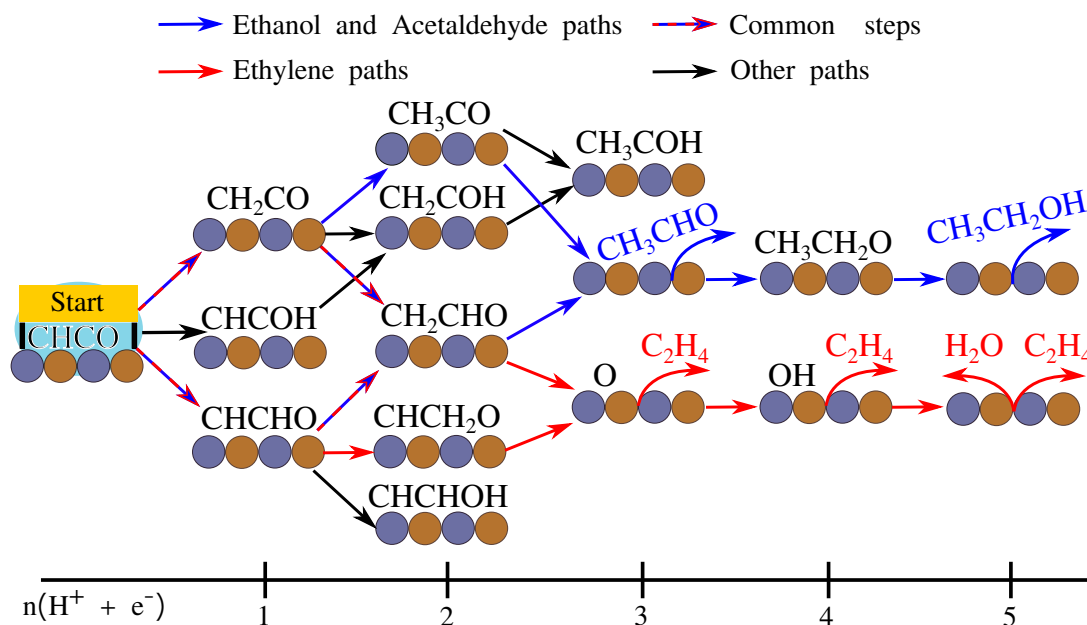
The  $\text{CO}_2\text{RR}$  on  $\text{CuZn}$  alloys have shown an increase in the Faradaic efficiencies to  $\text{C}_2$  and also  $\text{C}_2+$  products, which is explained by an improvement in the  $\text{CO}$  production. Then, an increase in the  $\text{CO}$  coverage favors the  $\text{C}-\text{C}$  coupling; however, very negative potentials are still required to promote the production of  $\text{C}_2$  products. Figure 18 displays the general reaction scheme explored on  $\text{Cu}_{55}$  and  $\text{Cu}_4\text{Zn}_{13}$  clusters. We explored two paths sharing common intermediates to  $\text{CH}_3\text{CH}_2\text{OH}$  and  $\text{C}_2\text{H}_4$ , red and blue overlapped lines, and additional paths bifurcated in earlier intermediates than  $\text{CH}_2\text{CHO}$ , red lines for ethylene and blue lines for ethanol. In this section, we discussed our findings in line with different experimental and theoretical studies, comparing and contrasting the preferred reaction paths toward  $\text{C}_2$  products. All the potentials informed are versus the RHE.

#### 5.3.1 Reaction Paths on $\text{Cu}_{55}$

To explore more than one reaction path, we adsorbed and optimized all the intermediates informed in Figure 18 on the  $\text{Cu}_{55}$  cluster. However, we employed the lowest energy adsorbed structures to plot only the free energy diagram for the complete sequential steps until  $\text{CH}_3\text{CHO}$ ,  $\text{CH}_3\text{CH}_2\text{OH}$ , and  $\text{C}_2\text{H}_4$  in Figure 19. For ethanol, we compare three possible paths, observing that all paths shared the same step with the larger positive  $\Delta G$  (0.30 eV): the formation of  $\text{CH}_3\text{CH}_2\text{OH}$ . Assuming no kinetic limitations, we could infer that the applied potential to produce ethanol is enough to open those three paths, which typically is about  $-1.00\text{ V}$ . For ethylene the paths via  $\text{CH}_2\text{CHO}$  have the same step with larger positive  $\Delta G$  (0.55 V): formation of  $\text{C}_2\text{H}_4$ . The remained path presented the formation of  $\text{CHCH}_2\text{O}$  as the step with larger  $\Delta G$  and almost 2.5 times greater than the other paths, indicating that this path is inhibiting until applying a potential of  $-1.35\text{ V}$ .

Comparing the most favorable paths for ethanol and ethylene, we observed a

Figure 18 – Possible reaction pathways via proton-coupled electron transfer steps after CH–CO coupling for CO<sub>2</sub>RR or CORR toward ethylene, acetaldehyde, and ethanol production. The final products are highlighted in blue for ethanol and acetaldehyde and red for ethylene and water.



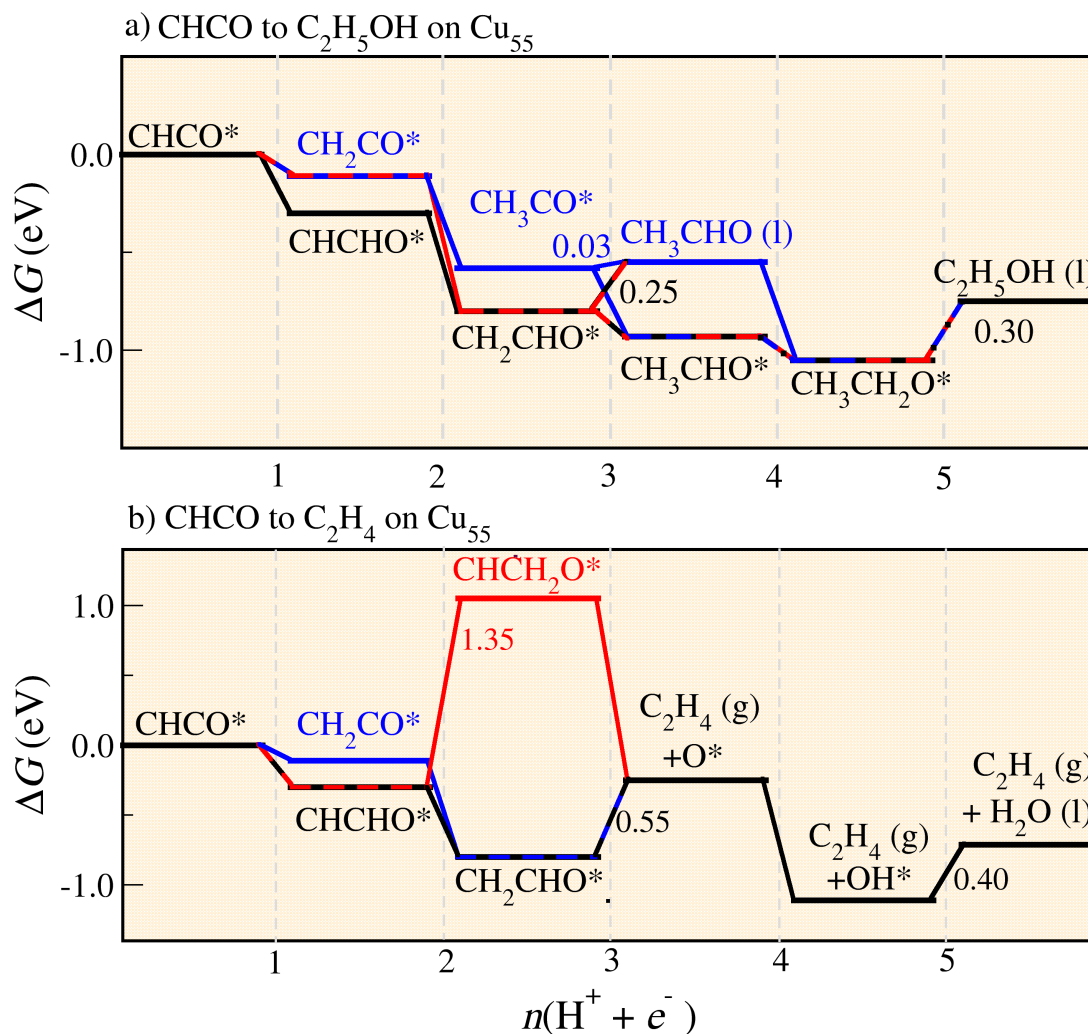
Source: Own authorship.

preference for the path toward ethanol on  $\text{Cu}_{55}$  clusters. Our results followed the same preferred path reported by Ting *et al.* on  $\text{Cu}(111)$  [162]. In contrast with our results, they informed that each step in the path into ethanol presented negative values for  $\Delta G$  and desorbed acetaldehyde was reported as intermediate. Similarly, for the ethylene path, they also obtained the formation of ethylene as a step with positive  $\Delta G$  although with a smaller value than our results. Then it suggests an effect induced by the size that influences more on the path to ethanol than to ethylene, being a possible strategy to tune the product's selectivity.

A previous study suggested a path bifurcation into ethylene and ethanol after OHC–CO formation, being the ethanol produced via  $\text{CH}_2\text{CHO}$  specie while ethylene via  $\text{CHCH}_2\text{O}$  on  $\text{Cu}(100)$  surface [163]. However, our results on  $\text{Cu}_{55}$  showed the path to ethylene that proceeds via  $\text{CHCH}_2\text{O}$  intermediate as less favored, and at least at this size scale, the preferred paths to ethanol and ethylene have common intermediates:  $\text{CHCHO}$  and  $\text{CH}_2\text{CHO}$ . Our findings are consistent with several studies that reported experimental evidences suggesting common pathway into  $\text{C}_2$  products, for instance, similar shift in the Faradaic efficiency of ethanol and ethylene as a function of the cations in the electrolyte [93], and both products have about the same onset potential [89, 161, 164], which indicates a common potential-determining step.

A previous study for the CORR on nanocrystalline oxide-derived copper (OD-Cu)

Figure 19 – Free energy diagram from CHCO to a)  $\text{CH}_3\text{CH}_2\text{OH}$  and b)  $\text{C}_2\text{H}_4$  on  $\text{Cu}_{55}$ . The steps with positive  $\Delta G$  are indicated with their values in eV. Black lines connect the preferred reaction path, while red and blue lines connected other paths explored.

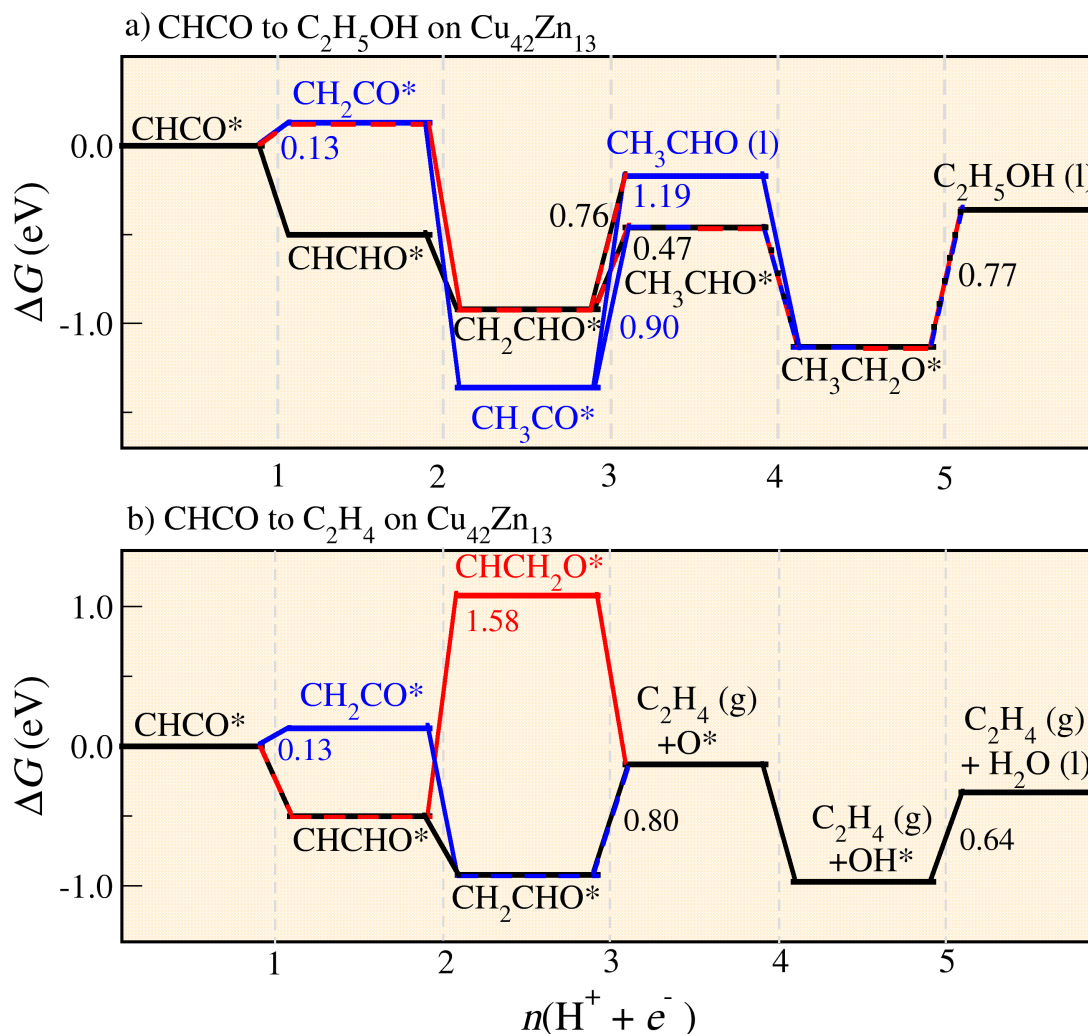


Source: Own authorship.

and Cu nanoparticles electrodes reported the ethanol formation at low overpotentials and no  $\text{C}_1$  side products [165]. Those experiments used a saturated atmosphere of CO at 1.00 atm, and the absence of  $\text{C}_1$  products suggesting a fast C–C coupling, indicating that this step is not a PDS. Then, we compared our results and found a good agreement with the onset potential for each product on the Cu nanoparticles. For instance, they reported the production of acetate at  $-0.30$  V and suggested that the mechanism acetate formation occurs via  $-\text{OH}$  attack to a carbonyl-containing intermediate. Our results suggested that this intermediate could be the acetaldehyde since the predicted potential for its formation is at  $-0.25$  V, equation (2.46) using the  $\Delta G$  of 0.25 eV.

The production of ethanol was detected at  $-0.35$  V with a large amount between up to  $-0.45$  V, while the acetate decreased and it started the increase of ethylene production

Figure 20 – Free energy diagram from CHCO to a)  $\text{CH}_3\text{CH}_2\text{OH}$  and b)  $\text{C}_2\text{H}_4$  on  $\text{Cu}_{42}\text{Zn}_{13}$ . The steps with positive  $\Delta G$  are indicated with their values in eV. Black lines connect the preferred reaction path, while red and blue lines connected other paths explored.



Source: Own authorship.

up to  $-0.50$  V [165]. According to our data, the path to ethanol on small nanoparticles should proceed via adsorbed acetaldehyde and suggested that the potential-determining step would be ethanol formation with an onset potential of  $-0.30$  V. Meanwhile, in the path to ethylene, we predicted that its formation is the potential-determining step and would occur at more negative potentials at  $-0.55$  V. Our observations also are consistent with a recent study about ethanol and ethylene selectivity and site coordination dependence [97]. It is expected ethanol formation to be favored over ethylene on undercoordinated sites with generalized coordination numbers smaller than 5.90, typically observed on step edges and kinks defects surfaces.

### 5.3.2 Reaction Paths on $\text{Cu}_{42}\text{Zn}_{13}$

To study the reaction paths on  $\text{Cu}_{42}\text{Zn}_{13}$ , we followed the same procedure informed for  $\text{Cu}_{55}$ . Figure 20 shows the free energy diagram for the complete sequential steps until  $\text{CH}_3\text{CHO}$ ,  $\text{CH}_3\text{CH}_2\text{OH}$ , and  $\text{C}_2\text{H}_4$  on CuZn alloy. Similar to the observed on  $\text{Cu}_{55}$ , the preferred path toward ethanol on the alloy has the same step with the larger positive  $\Delta G$ : the formation of  $\text{CH}_3\text{CH}_2\text{OH}$ . Meanwhile, the path that proceeds via  $\text{CH}_3\text{CO}$  intermediate suggested a different PDS and, to be favored, it requires to go until more negative potentials than the needed for remaining paths, which contrasts with the early discussion on  $\text{Cu}_{55}$ . For the paths toward ethylene, the trend observed on  $\text{Cu}_{42}\text{Zn}_{13}$  is similar to that on  $\text{Cu}_{55}$ , keeping the same PDSs although with higher values for  $\Delta G$ .

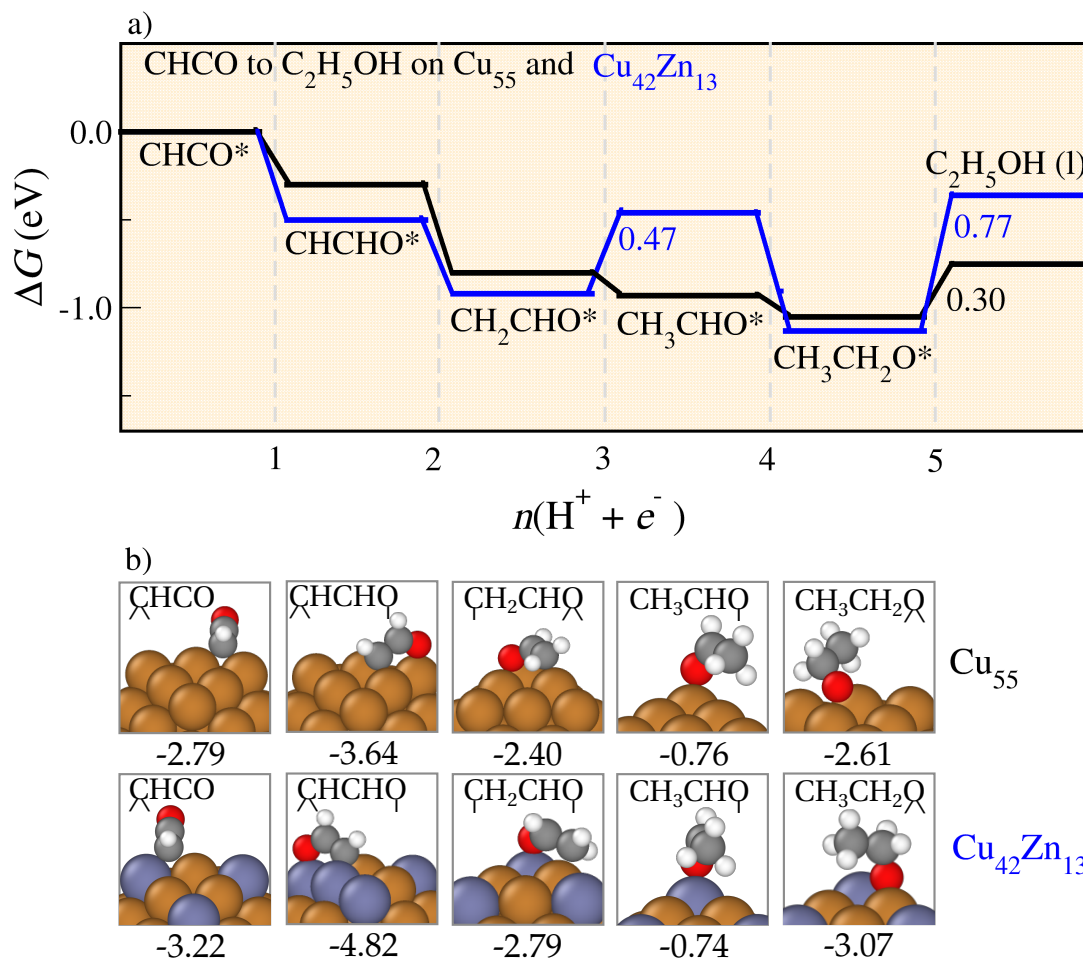
The inclusion of Zn in copper electrodes has been pointed out as an alternative to enhance the  $\text{CO}_2\text{RR}$  selectivity to ethanol [36, 47]. An experimental study proposed a mechanism for  $\text{CO}_2$  reduction to explain the highlighted ethanol selectivity on  $\text{Cu}_4\text{Zn}$  catalyst [166]. The Zn increases the CO production and favor its spillover to Cu sites, while the CO produced on Cu atoms is further reduced to  $\text{CH}_2$  species. The CO that migrates from Zn to Cu sites form the  $\text{CH}_2\text{CO}$  by its coupling with  $\text{CH}_2$  species. Further  $\text{CH}_2\text{CO}$  reduction favor the  $\text{CH}_3\text{CHO}$  formation and finally forms  $\text{CH}_3\text{CH}_2\text{OH}$ .

The increase of Faradaic efficiency for ethanol occurred at the same time that the Faradaic efficiency decreased for CO, suggesting that the potential-determining step for  $\text{C}_2$  products is the C–C coupling [166]. After overcoming this step, ethanol production is favored over ethylene. From our results, it would be expected that the path via  $\text{CH}_2\text{CO}$  prefers the acetaldehyde formation than the ethylene sharing a common intermediate ( $\text{CH}_2\text{CHO}$ ). The trends experimentally reported and the predicted by our model are consistent, although similar to the observed on  $\text{Cu}_{55}$  when the crucial intermediate is  $\text{CH}_2\text{CO}$ . That supports the idea that improvement due to Zn occurs in early stages, formation of CO and C–C coupling [166, 167], rather than on later stages.

## 5.4 The Effect of Zn on Late Stages of the Preferred Path Toward Ethanol

Figure 21 a) displays the preferred path toward ethanol on  $\text{Cu}_{55}$  and  $\text{Cu}_{42}\text{Zn}_{13}$ . Compared with the  $\text{Cu}_{55}$ , the  $\text{Cu}_{42}\text{Zn}_{13}$  alloy provided a more exergonic path until the formation of  $\text{CH}_2\text{CHO}$  species. But, the step that forms adsorbed acetaldehyde from  $\text{CH}_2\text{CHO}$  is endergonic, differently than on  $\text{Cu}_{55}$ . However, the more endergonic step is still associated with the ethanol formation with a larger value of  $\Delta G$  than on  $\text{Cu}_{55}$ . Then, in case that the final step of the studied paths becomes the PDS, it would be expected larger onset potentials on  $\text{Cu}_{42}\text{Zn}_{13}$  alloy than on  $\text{Cu}_{55}$  cluster. The differences in  $\Delta G$  along the paths on  $\text{Cu}_{55}$  and  $\text{Cu}_{42}\text{Zn}_{13}$  can be explained by the Zn effect on their adsorption strength.

Figure 21 – a) Free energy diagram for the preferred path from CHCO to CH<sub>3</sub>CH<sub>2</sub>OH on Cu<sub>55</sub> and Cu<sub>42</sub>Zn<sub>13</sub>. The steps with positives  $\Delta G$  are indicated with their values in eV. Black lines connect the preferred reaction path on Cu<sub>55</sub>, while blue lines connected preferred path on Cu<sub>42</sub>Zn<sub>13</sub>. b) Structures for the adsorbed species on the preferred path toward ethanol. The numbers are the adsorption energies in eV ( $E_{ad}$ ).

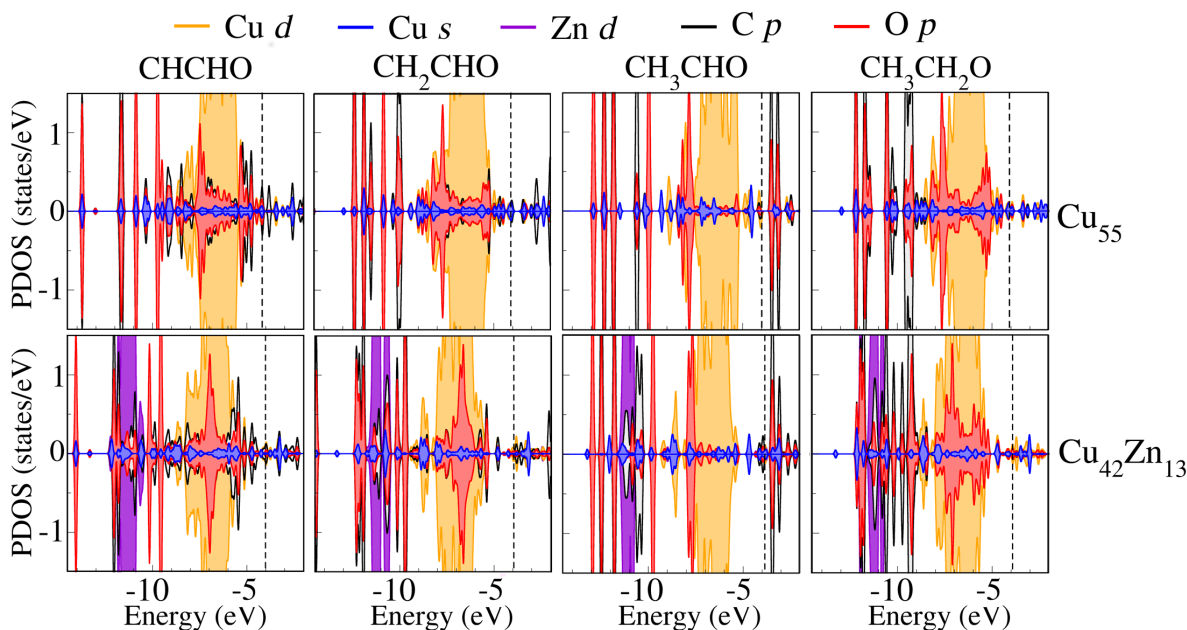


Source: Own authorship.

Figure 21 b) informs the lowest energy structures and their adsorption energies for the species involved in the path on Cu<sub>55</sub> and Cu<sub>42</sub>Zn<sub>13</sub>. Most of the species adsorbed stronger on CuZn alloy than on Cu cluster, except CH<sub>3</sub>CHO. That explains the more exergonic steps on the alloy and the differentiate behavior in the step toward CH<sub>3</sub>CHO. To understand those differences, we analyzed the PDOS for the CHCHO, CH<sub>2</sub>CHO, CH<sub>3</sub>CHO, and CH<sub>3</sub>CH<sub>2</sub>O on Cu<sub>55</sub> and Cu<sub>42</sub>Zn<sub>13</sub>, Figure 22. For all adsorbed species on Cu<sub>55</sub>, the interaction mainly occurs via *p* states from the C and O atoms with the *d* and *s* states of the Cu. The stronger adsorption observed on Cu<sub>42</sub>Zn<sub>13</sub> was associated to the *d* states from the Zn, that brings more stabilization via additional overlapping with the C and O states.

The main difference observed for the adsorbed CH<sub>3</sub>CHO is the orientation, on Cu<sub>55</sub> interacts via O along the edge, while on Cu<sub>42</sub>Zn<sub>13</sub>, the O binds to Zn and orientated above

Figure 22 – Projected density of states (PDOS) of C, O, and the TM atoms involved in the adsorption of the species on  $\text{Cu}_{55}$  and  $\text{Cu}_{42}\text{Zn}_{13}$  clusters. Only the species in the preferred path toward ethanol were analyzed.



Source: Own authorship.

the facet. Those differences also were reflected in the PDOS. For instance, on  $\text{Cu}_{55}$  the states related to C and O atoms are spread and overlapping with deeper *s* states of Cu, while on  $\text{Cu}_{42}\text{Zn}_{13}$ , those states shift to less negative energies and concentrate on the region of *d* states associated to Zn. It would explain the slight difference in the acetaldehyde adsorption strength, which tends to be stronger on  $\text{Cu}_{55}$  since the overlapping with deeper *s* states from the Cu is favored.

## 5.5 Summary

The electroreduction of  $\text{CO}_2$  to  $\text{C}_2$  products like ethanol is motivated by its potential application supplying the global energy demand more sustainable and renewable. Cooper-based catalysts have exhibited a highlighted performance obtaining  $\text{C}_2$  products, but large overpotentials and poor selectivity are still challenging. Herein, we studied the late stages in the reaction paths toward ethylene, acetaldehyde, and ethanol on  $\text{Cu}_{55}$  and  $\text{Cu}_{42}\text{Zn}_{13}$  clusters. Our result suggested that the preferred reaction path into ethanol and ethylene formation shared common intermediates species ( $\text{CH}_2\text{CHO}$ ), and it is the same on both  $\text{Cu}_{55}$  and  $\text{Cu}_{42}\text{Zn}_{13}$  clusters. Also, it was favored ethanol formation via the acetaldehyde path over the ethylene. Our observations are consistent with a recent study that predicted ethanol selectivity over ethylene on under-coordinated sites for Cu-based catalysts. Comparing our results with experimental findings of the electroreduction of



CO on Cu nanoparticles, we observed a good agreement with the onset potentials of the products. Since the C–C coupling seems to occur faster enough to avoid the formation C<sub>1</sub> products, it indicates that this is not the potential-determining step (PDS). Then, our results suggested that the PDS could be associated with the hydrogenation of the adsorbed CH<sub>3</sub>CH<sub>2</sub>O to form ethanol. Regarding the role of the Zn on the reaction path, our results follow similar trends reported experimentally: ethanol formation at lower overpotentials than ethylene. However, the similarities observed at the late stages with the Cu<sub>55</sub> cluster support the idea that the improvements due to the Zn affect previous stages like the formation of CO and the C–C coupling. Finally, the differences in the reactions paths between Cu<sub>55</sub> and Cu<sub>42</sub>Zn<sub>13</sub> were associated with the *d* states from Zn that reinforce the interaction with the adsorbed species providing more exergonic steps.

## 6 CONCLUSIONS

This investigation contributes to the understanding of the CO<sub>2</sub> activation and conversion on finite-size particles by studying the CO<sub>2</sub> adsorption, C–O bond dissociation, and reaction paths into C<sub>2</sub> products of the CO<sub>2</sub> reduction. Our findings suggested descriptors to characterize the activation of small molecules, provided the mechanistic elucidation for the C–O bond dissociation, and insights about the preferred reaction paths to C<sub>2</sub> products. Herein, we employed a theoretical approach based on the density functional theory calculations. Furthermore, the climbing image nudged elastic band algorithm allowed search the transition states to calculate the activation barriers. Lastly, the computational hydrogen electrode method provided a thermodynamic analysis for electrocatalytic conversion of CO<sub>2</sub>. Below are the main conclusions for each topic.

The adsorption of CO<sub>2</sub>, CO, H<sub>2</sub>, and H<sub>2</sub>O on Fe<sub>13</sub>, Co<sub>13</sub>, Ni<sub>13</sub>, and Cu<sub>13</sub> promoted the activation of those molecules. Among the parameters analyzed, the structural changes of each molecule upon the adsorption are a suitable descriptor for the activation since the elongation of the bonds should lead to more reactive species. The adsorption and interaction energies could not characterize the activation of the studied molecules. However, the energy difference between the structure of molecules in the gas phase and their achieved structure upon the adsorption allowed us to obtain an energetic parameter that also describes their activation. The net negative charge at CO<sub>2</sub><sup>ad</sup> and CO<sup>ad</sup> indicated that TM<sub>13</sub> clusters transferred electronic charge mainly via C atom, which drives the activation of those molecules. Although it was difficult to infer the participation of the charge transfer in the H<sub>2</sub><sup>ad</sup> activation, the adsorption on all TM<sub>13</sub> clusters resulted in a large H–H bond length, suggesting other possible mechanisms related to the chemical environment provided by the TM<sub>13</sub>, which could be explored in future studies.

The study of the C–O bond dissociation of the CO<sub>2</sub> on Fe<sub>13</sub>, Co<sub>13</sub>, Ni<sub>13</sub>, and Cu<sub>13</sub> allowed the elucidation of the mechanism. By the redox route, we identified that the diffusion process of CO<sub>2</sub> and CO are important to facilitate the dissociation of the C–O bond and the desorption of CO, especially on Fe<sub>13</sub>. About the carboxyl route, the minimum energy path starts with the formation of trans-COOH and then occurs its rotation until cis-COOH. Particularly on the Cu<sub>13</sub>, an additional rotation favored the interaction of OC–OH bond with the surface, which provided the smaller activation energy for that dissociation. Between the redox and carboxyl routes, the former followed the minimum energy reaction path on all TM<sub>13</sub>. Among the TM<sub>13</sub>, Co<sub>13</sub> exhibited the smaller activation energy for the direct OC–O dissociation given its capability to adsorb strongly the CO<sub>2</sub> and the O. An interesting trend identified was the activation energy decreased for the carboxyl formation from Fe to Cu, making the activation energy comparable with the

redox route, and would be expected competition between routes on the Cu cluster. This is the consequence of the  $(\text{CO}_2 + \text{H})\text{-TM}$  interaction, that becomes weak in from Fe to Cu facilitating the H-TM bond dissociation and also the COO-H bond formation. The scaling relationships analyzed suggested the  $\text{CO}_2$  as a good descriptor for the redox route while the *trans*-COOH for the carboxyl route. From this study, the understanding of the spin effect on the activation barriers can be a remaining topic to explore, not addressed within this thesis.

Lastly, the late stages, after C-C coupling, of the reaction path to the acetaldehyde, ethanol, and ethylene on  $\text{Cu}_{55}$  and  $\text{Cu}_{42}\text{Zn}_{13}$  provided insights about the preferred reaction path to  $\text{C}_2$  products and the how the CuZn alloy affected it. On both  $\text{Cu}_{55}$  and  $\text{Cu}_{42}\text{Zn}_{13}$ , the path favored to ethanol and ethylene shared the  $\text{CH}_2\text{CHO}$  species as a common intermediate that then splits into acetaldehyde or ethylene. However, the ethanol path via acetaldehyde would be expected to occur preferentially over ethylene. We compared our results for  $\text{Cu}_{55}$  with experimental onset potentials for the electroreduction of CO on Cu nanoparticles, assuming that the C-C coupling was not the potential determining step. Then, the calculated values for the onset potential predicted the ethanol formation at smaller values than the ethylene, which agrees with the reported in the experiments. We suggested that the potential determining step is associated with the hydrogenation of  $\text{CH}_3\text{CH}_2\text{OH}$  species to form ethanol. Finally, the CuZn makes the exergonic step more favored compared to the  $\text{Cu}_{55}$ , attributed to the *d* states from the Zn that reinforce the adsorption strength with some species. Since the trends are similar between the  $\text{Cu}_{55}$  cluster and  $\text{Cu}_{42}\text{Zn}_{13}$  alloy, our data reinforce the idea that the improvements due to the Zn in copper-rich alloys occur in early steps, like the CO formation. However, future studies evaluating the C-C coupling on those clusters would improve the atomistic understanding of the Zn effect in the  $\text{C}_2$  products formation.

## 6.1 Papers and Manuscripts in Progress

The discussion carry on this thesis have been deliver two published papers and one manuscript in progress. During the PhD studies, the author contributes to six additional published papers, and two manuscripts under preparation. Below are listed the published papers the manuscripts in progress.

### 6.1.1 Published papers

Papers discussed in this thesis:

- OCAMPO-RESTREPO, V. K.; ZIBORDI-BESSE, L.; DA SILVA, J. L. F. *Ab initio* investigation of the atomistic descriptors in the activation of small molecules on 3d transition-metal 13-atom clusters: The example of  $\text{H}_2$ , CO,  $\text{H}_2\text{O}$ , and  $\text{CO}_2$ . **The Journal of Chemical Physics**, v. 151, p. 214301, 2019.

- OCAMPO-RESTREPO, V. K.; VERGA, L. G.; DA SILVA, J. L. F. *Ab initio* Study of the C–O bond dissociation in CO<sub>2</sub> reduction by redox and carboxyl routes on 3d transition-metal systems. **The Journal of Physical Chemistry C**, v. 125, n. 48, p. 26296-26306, 2021.

Collaborations:

- VERGA, L. G.; MENDES, P. C. D.; OCAMPO-RESTREPO, V. K.; DA SILVA, J. L. F. Exploring the adsorption site coordination as a strategy to tune copper catalysts for CO<sub>2</sub> electro-reduction. **Catalysis Science & Technology**, 2022.
- RASTEIRO, L. F.; DE SOUSA, R. A.; VIERA, L. H.; OCAMPO-RESTREPO, V. K.; VERGA, L. G.; ASSAF, J. M.; DA SILVA, J. L.; ASSAF, E. M. Insights into the alloy-support synergistic effects for the CO<sub>2</sub> hydrogenation towards methanol on oxide-supported Ni<sub>5</sub>Ga<sub>3</sub> catalysts: An experimental and DFT study. **Applied Catalysis B: Environmental**, v. 302, p. 120842, 2022.
- VERGA, L. G.; MENDES, P. C. D.; OCAMPO-RESTREPO, V. K.; DA SILVA, J. L. F. The role of site coordination on the CO<sub>2</sub> electroreduction pathway on stepped and defective copper surfaces. **Catalysis Science & Technology**, v. 11, p. 2770-2781, 2021.
- MENDES, P. C. D.; OCAMPO-RESTREPO, V. K.; DA SILVA, J. L. F. *Ab initio* investigation of quantum size effects on the adsorption of CO<sub>2</sub>, CO, H<sub>2</sub>O, and H<sub>2</sub> on transition-metal particles. **Physical Chemistry Chemical Physics**, v. 22, p. 8998-9008, 2020.
- BATISTA, K. E. A.; OCAMPO-RESTREPO, V. K.; SOARES, M. D.; QUILLES, M. G.; PIOTROWSKI, M. J.; DA SILVA, J. L. F. *Ab initio* investigation of CO<sub>2</sub> adsorption on 13-atom 4d clusters. **Journal of Chemical Information and Modeling**, v. 60, n. 2, p. 537–545, 2020.
- ZIBORDI-BESSE, L.; VERGA, L. G.; OCAMPO-RESTREPO, V. K.; DA SILVA, J. L. F. *Ab initio* investigation of the formation mechanism of nano-interfaces between 3d-late transition-metals and ZrO<sub>2</sub> nanoclusters. **Physical Chemistry Chemical Physics**, v. 22, n. 15, p. 8067-8076, 2020.

### 6.1.2 Manuscripts in progress

Papers discussed in this thesis:

- OCAMPO-RESTREPO, V. K.; VERGA, L. G.; DA SILVA, J. L. F. *Ab initio* investigation of Cu-rich CuZn alloys for electro-reduction of CO<sub>2</sub> to on C<sub>2</sub> products.

Collaborations:

- DE SOUSA, R. A.; OCAMPO-RESTREPO, V. K.; VERGA, L. G.; DA SILVA, J. L. F. *Ab initio* study of the adsorption properties of CO<sub>2</sub> reduction intermediates: The effect of Ni<sub>5</sub>Ga<sub>3</sub> alloy and the Ni<sub>5</sub>Ga<sub>3</sub>/ZrO<sub>2</sub> interface.
- COLLACIQUE, M. N.; OCAMPO-RESTREPO, V. K.; DA SILVA, J. L. F. *Ab initio* investigation of the role of the *d*-states on the adsorption and activation properties of CO<sub>2</sub> on 3*d*, 4*d*, and 5*d* transition-metal clusters.

## REFERENCES

- 1 PIOTROWSKI, M. J.; UNGUREANU, C. G.; TERESHCHUK, P.; BATISTA, K. E. A.; CHAVES, A. S.; GUEDES-SOBRINHO, D.; DA SILVA, J. L. F. Theoretical study of the structural, energetic, and electronic properties of 55-atom metal nanoclusters: A DFT investigation within van der waals corrections, spin-orbit coupling, and PBE+U of 42 metal systems. **The Journal of Physical Chemistry C**, Washington, DC, v. 120, n. 50, p. 28844–28856, 2016.
- 2 COMPUTATIONAL Chemistry Comparison and Benchmark DataBase (CCCBDB). cited Jul 2020.
- 3 CALLE-VALLEJO, F.; KOPER, M. T. M. Theoretical considerations on the electroreduction of CO to C<sub>2</sub> species on cu(100) electrodes. **Angewandte Chemie International Edition**, Weinheim, v. 52, n. 28, p. 7282–7285, 2013.
- 4 SOLOMON, S.; PLATTNER, G.-K.; KNUTTI, R.; FRIEDLINGSTEIN, P. Irreversible climate change due to carbon dioxide emissions. **Proceedings of the National Academy of Sciences of the United States of America**, Washington, DC, v. 106, n. 6, p. 1704–1709, 2009.
- 5 NOAA. **Trends in Atmospheric Carbon Dioxide**. cited Jul 2019.
- 6 SOLOMON, S.; DANIEL, J. S.; SANFORD, T. J.; MURPHY, D. M.; PLATTNER, G.-K.; KNUTTI, R.; FRIEDLINGSTEIN, P. Persistence of climate changes due to a range of greenhouse gases. **Proceedings of the National Academy of Sciences of the United States of America**, Washington, DC, v. 107, n. 43, p. 18354–18359, Oct. 2010.
- 7 WICH, T.; LUEKE, W.; DEERBERG, G.; OLES, M. Carbon2chem@-CCU as a step toward a circular economy. **Frontiers in Energy Research**, Lausanne, v. 7, p. 162, 2020.
- 8 NOCITO, F.; DIBENEDETTO, A. Atmospheric CO<sub>2</sub> mitigation technologies: Carbon capture utilization and storage. **Current Opinion in Green and Sustainable Chemistry**, Amsterdam, v. 21, p. 34–43, 2020.
- 9 POROSOFF, M. D.; YAN, B.; CHEN, J. G. Catalytic reduction of CO<sub>2</sub> by H<sub>2</sub> for synthesis of CO, methanol and hydrocarbons: challenges and opportunities. **Energy & Environmental Science**, London, v. 9, n. 1, p. 62–73, 2016.
- 10 YANG, H.; ZHANG, C.; GAO, P.; WANG, H.; LI, X.; ZHONG, L.; WEI, W.; SUN, Y. A review of the catalytic hydrogenation of carbon dioxide into value-added hydrocarbons. **Catalysis Science & Technology**, London, v. 7, n. 20, p. 4580–4598, 2017.
- 11 PAN, S.-Y.; CHIANG, P.-C.; PAN, W.; KIM, H. Advances in state-of-art valorization technologies for captured CO<sub>2</sub> toward sustainable carbon cycle. **Critical Reviews in Environmental Science and Technology**, London, v. 48, n. 5, p. 471–534, 2018.
- 12 TAYLOR, P. A.; RASMUSSEN, P. B.; CHORKENDORFF, I. Is the observed hydrogenation of formate the rate-limiting step in methanol synthesis? **Journal of the Chemical Society, Faraday Transactions**, London, v. 91, n. 8, p. 1267, 1995.

- 13 LI, Y.; CHAN, S. H.; SUN, Q. Heterogeneous catalytic conversion of CO<sub>2</sub>: a comprehensive theoretical review. **Nanoscale**, London, v. 7, n. 19, p. 8663–8683, 2015.
- 14 CHEN, X.; CHEN, Y.; SONG, C.; JI, P.; WANG, N.; WANG, W.; CUI, L. Recent advances in supported metal catalysts and oxide catalysts for the reverse water-gas shift reaction. **Frontier in Chemistry**, Lausanne, v. 8, p. 1–21, 2020.
- 15 RIEDEL, T.; SCHAUB, G.; JUN, K.-W.; LEE, K.-W. Kinetics of CO<sub>2</sub> hydrogenation on a K-promoted Fe catalyst. **Industrial & Engineering Chemistry Research**, Washington, DC, v. 40, n. 5, p. 1355–1363, 2001.
- 16 ZHU, M.; GE, Q.; ZHU, X. Catalytic reduction of CO<sub>2</sub> to CO via reverse water gas shift reaction: Recent advances in the design of active and selective supported metal catalysts. **Transactions of Tianjin University**, Hong Kong, v. 26, n. 3, p. 172–187, 2020.
- 17 HOMS, N.; TOYIR, J.; PISCINA, P. R. de la. Catalytic processes for activation of CO<sub>2</sub>. *In: New and Future Developments in Catalysis*. Amsterdam: Elsevier, 2013. p. 1–26.
- 18 HAYNES, W. M. **CRC Handbook of Chemistry and Physics**. 95th. ed. Boca Raton, FL, USA: CRC Press, 2014. ISBN 978-1-4822-0868-9.
- 19 LAIDLER, K. J. A glossary of terms used in chemical kinetics, including reaction dynamics (IUPAC recommendations 1996). **Pure and Applied Chemistry**, Berlin, v. 68, n. 1, p. 149–192, 1996.
- 20 KO, J.; KIM, B.-K.; HAN, J. W. Density functional theory study for catalytic activation and dissociation of CO<sub>2</sub> on bimetallic alloy surfaces. **The Journal of Physical Chemistry C**, Washington, DC, v. 120, n. 6, p. 3438–3447, 2016.
- 21 KATTEL, S.; YAN, B.; CHEN, J. G.; LIU, P. CO<sub>2</sub> hydrogenation on Pt, Pt/SiO<sub>2</sub> and Pt/TiO<sub>2</sub>: Importance of synergy between Pt and oxide support. **Journal of Catalysis**, Amsterdam, v. 343, p. 115–126, 2016.
- 22 SAKURAI, H.; TSUBOTA, S.; HARUTA, M. Hydrogenation of CO<sub>2</sub> over gold supported on metal oxides. **Applied Catalysis A General**, Amsterdam, v. 102, n. 2, p. 125–136, 1993.
- 23 WANG, C.; GUAN, E.; WANG, L.; CHU, X.; WU, Z.; ZHANG, J.; YANG, Z.; JIANG, Y.; ZHANG, L.; MENG, X.; GATES, B. C.; XIAO, F.-S. Product selectivity controlled by nanoporous environments in zeolite crystals enveloping rhodium nanoparticle catalysts for CO<sub>2</sub> hydrogenation. **Journal of the American Chemical Society**, Washington, DC, v. 141, n. 21, p. 8482–8488, 2019.
- 24 YE, J.; GE, Q.; LIU, C. jun. Effect of PdIn bimetallic particle formation on CO<sub>2</sub> reduction over the Pd–In/SiO<sub>2</sub> catalyst. **Chemical Engineering Science**, London, v. 135, p. 193–201, 2015.
- 25 SENGUPTA, S.; JHA, A.; SHENDE, P.; MASKARA, R.; DAS, A. K. Catalytic performance of Co and Ni doped Fe-based catalysts for the hydrogenation of CO<sub>2</sub> to CO via reverse water-gas shift reaction. **Journal of Environmental Chemical Engineering**, London, v. 7, n. 1, p. 102911, 2019.

- 26 LI, J.; LIN, Y.; PAN, X.; MIAO, D.; DING, D.; CUI, Y.; DONG, J.; BAO, X. Enhanced CO<sub>2</sub> methanation activity of Ni/anatase catalyst by tuning strong metal–support interactions. **ACS Catalysis**, Washington, DC, v. 9, n. 7, p. 6342–6348, 2019.
- 27 YANG, S.-C.; PANG, S. H.; SULMONETTI, T. P.; SU, W.-N.; LEE, J.-F.; HWANG, B.-J.; JONES, C. W. Synergy between ceria oxygen vacancies and Cu nanoparticles facilitates the catalytic conversion of CO<sub>2</sub> to CO under mild conditions. **ACS Catalysis**, Washington, DC, v. 8, n. 12, p. 12056–12066, 2018.
- 28 BEHNER, H.; SPIESS, W.; WEDLER, G.; BORGMANN, D. Interaction of carbon dioxide with fe(110), stepped fe(100) and fe(111). **Surface Science**, Amsterdam, v. 175, n. 2, p. 276–286, 1986.
- 29 BARTOS, B.; FREUND, H.-J.; KUHLENBECK, H.; NEUMANN, M.; LINDNER, H.; MÜLLER, K. Adsorption and reaction of CO<sub>2</sub> and CO<sub>2</sub>/O CO-adsorption on Ni(110): Angle resolved photoemission (ARUPS) and electron energy loss (HREELS) studies. **Surface Science**, Amsterdam, v. 179, n. 1, p. 59–89, 1987.
- 30 FUNK, S.; HOKKANEN, B.; WANG, J.; BURGHAUS, U.; BOZZOLO, G.; GARCÉS, J. Adsorption dynamics of CO<sub>2</sub> on Cu(110): A molecular beam study. **Surface Science**, Amsterdam, v. 600, n. 3, p. 583–590, 2006.
- 31 CHERNAVSKII, P. A.; KAZAK, V. O.; PANKINA, G. V.; PERFILIEV, Y. D.; LI, T.; VIRGINIE, M.; KHODAKOV, A. Y. Influence of copper and potassium on the structure and carbidisation of supported iron catalysts for fischer–tropsch synthesis. **Catalysis Science & Technology**, London, v. 7, n. 11, p. 2325–2334, 2017.
- 32 LIU, L.; PUGA, A. V.; CORED, J.; CONCEPCIÓN, P.; PÉREZ-DIESTE, V.; GARCÍA, H.; CORMA, A. Sunlight-assisted hydrogenation of CO<sub>2</sub> into ethanol and C<sub>2</sub>+ hydrocarbons by sodium-promoted Co@C vanocomposites. **Applied Catalysis B Environmental**, Amsterdam, v. 235, p. 186–196, 2018.
- 33 VERA, E.; DUAN, Y.; PFEIFFER, H. CO<sub>2</sub>–H<sub>2</sub>O capture and cyclability on sodium cobaltate at low temperatures (30–80 °C): Experimental and theoretical analysis. **Energy Technology**, Berlin, v. 7, n. 3, p. 1800527, 2019.
- 34 TODOROVA, T. K.; SCHREIBER, M. W.; FONTECAVE, M. Mechanistic understanding of CO<sub>2</sub> reduction reaction (CO<sub>2</sub>rr) toward multicarbon products by heterogeneous copper-based catalysts. **ACS Catalysis**, Washington, DC, v. 10, n. 3, p. 1754–1768, 2020.
- 35 NI, Z.; LIANG, H.; YI, Z.; GUO, R.; LIU, C.; LIU, Y.; SUN, H.; LIU, X. Research progress of electrochemical CO<sub>2</sub> reduction for copper-based catalysts to multicarbon products. **Coordination Chemistry Reviews**, Amsterdam, v. 441, p. 213983, 2021.
- 36 FREITAS, W. da S.; D’EPIFANIO, A.; MECHERI, B. Electrocatalytic CO<sub>2</sub> reduction on nanostructured metal-based materials: Challenges and constraints for a sustainable pathway to decarbonization. **Journal of CO<sub>2</sub> Utilization**, London, v. 50, p. 101579, 2021.



- 37 LI, L.; LARSEN, A. H.; ROMERO, N. A.; MOROZOV, V. A.; GLINSVAD, C.; ABILD-PEDERSEN, F.; GREELEY, J.; JACOBSEN, K. W.; NØRSKOV, J. K. Investigation of catalytic finite-size-effects of platinum metal clusters. **The Journal of Physical Chemistry Letters**, Washington, DC, v. 4, n. 1, p. 222–226, 2012.
- 38 GAO, D.; ARÁN-AIS, R. M.; JEON, H. S.; CUENYA, B. R. Rational catalyst and electrolyte design for CO<sub>2</sub> electroreduction towards multicarbon products. **Nature Catalysis**, New York, v. 2, n. 3, p. 198–210, 2019.
- 39 VERGA, L. G.; MENDES, P. C. D.; OCAMPO-RESTREPO, V. K.; SILVA, J. L. F. D. Exploring the adsorption site coordination as a strategy to tune copper catalysts for CO<sub>2</sub> electro-reduction. **Catalysis Science & Technology**, London, 2022.
- 40 ZHANG, J.; CAI, W.; HU, F. X.; YANG, H.; LIU, B. Recent advances in single atom catalysts for the electrochemical carbon dioxide reduction reaction. **Chemical Science**, London, v. 12, n. 20, p. 6800–6819, 2021.
- 41 FU, J.; LIU, K.; LI, H.; HU, J.; LIU, M. Bimetallic atomic site catalysts for CO<sub>2</sub> reduction reactions: a review. **Environmental Chemistry Letters**, Berlin, p. 1–20, 2021.
- 42 ZHU, S.; DELMO, E. P.; LI, T.; QIN, X.; TIAN, J.; ZHANG, L.; SHAO, M. Recent advances in catalyst structure and composition engineering strategies for regulating CO<sub>2</sub> electrochemical reduction. **Advanced Materials**, Berlin, v. 33, n. 50, p. 2005484, 2021.
- 43 MORALES-GUIO, C. G.; CAVE, E. R.; NITOPI, S. A.; FEASTER, J. T.; WANG, L.; KUHL, K. P.; JACKSON, A.; JOHNSON, N. C.; ABRAM, D. N.; HATSUKADE, T.; HAHN, C.; JARAMILLO, T. F. Improved CO<sub>2</sub> reduction activity towards C<sub>2</sub>+ alcohols on a tandem gold on copper electrocatalyst. **Nature Catalysis**, New York, v. 1, n. 10, p. 764–771, 2018.
- 44 FENG, Y.; LI, Z.; LIU, H.; DONG, C.; WANG, J.; KULINICH, S. A.; DU, X. Laser-prepared CuZn alloy catalyst for selective electrochemical reduction of CO<sub>2</sub> to ethylene. **Langmuir**, Washington, DC, v. 34, n. 45, p. 13544–13549, 2018.
- 45 HUANG, J.; MENSI, M.; OVEISI, E.; MANTELLA, V.; BUONSANTI, R. Structural sensitivities in bimetallic catalysts for electrochemical CO<sub>2</sub> reduction revealed by Ag–Cu nanodimers. **Journal of the American Chemical Society**, Washington, DC, v. 141, n. 6, p. 2490–2499, 2019.
- 46 ZHANG, T.; LI, Z.; ZHANG, J.; WU, J. Enhance CO<sub>2</sub>-to-C<sub>2</sub>+ products yield through spatial management of CO transport in Cu/ZnO tandem electrodes. **Journal of Catalysis**, Amsterdam, v. 387, p. 163–169, 2020.
- 47 YE, W.; GUO, X.; MA, T. A review on electrochemical synthesized copper-based catalysts for electrochemical reduction of CO<sub>2</sub> to C<sub>2</sub>+ products. **Chemical Engineering Journal**, Amsterdam, v. 414, p. 128825, 2021.
- 48 SILVA, A. H. da; RAAIJMAN, S. J.; SANTANA, C. S.; ASSAF, J. M.; GOMES, J. F.; KOPER, M. T. Electrocatalytic CO<sub>2</sub> reduction to C<sub>2</sub>+ products on Cu and Cu<sub>x</sub>Zn<sub>y</sub> electrodes: Effects of chemical composition and surface morphology. **Journal of Electroanalytical Chemistry**, Amsterdam, v. 880, p. 114750, 2021.

- 49 SOLYMOSI, F. The bonding, structure and reactions of CO<sub>2</sub> adsorbed on clean and promoted metal surfaces. **Journal of Molecular Catalysis A Chemical**, Amsterdam, v. 65, n. 3, p. 337–358, 1991.
- 50 FREUND, H.-J.; ROBERTS, M. Surface chemistry of carbon dioxide. **Surface Science Reports**, Amsterdam, v. 25, n. 8, p. 225–273, 1996.
- 51 KWAWU, C. R.; ANIAGYEI, A. A review on the computational studies of the reaction mechanisms of CO<sub>2</sub> conversion on pure and bimetals of late 3d metals. **Journal of Molecular Modeling**, Berlin, v. 27, n. 7, p. 1, 2021.
- 52 BURGHAUS, U. Surface chemistry of CO<sub>2</sub> – adsorption of carbon dioxide on clean surfaces at ultrahigh vacuum. **Progress in Surface Science**, Amsterdam, v. 89, n. 2, p. 161–217, 2014.
- 53 NASSIR, M. H.; DWYER, D. J. Sequential carbon oxygen bond cleavage in chemisorption of CO<sub>2</sub> on Fe(100). **Journal of Vacuum Science and Technology**, New York, v. 11, n. 4, p. 2104–2109, 1993.
- 54 LIU, C.; CUNDARI, T. R.; WILSON, A. K. CO<sub>2</sub> reduction on transition metal (Fe, Co, Ni, and Cu) surfaces: In comparison with homogeneous catalysis. **The Journal of Physical Chemistry C**, Washington, DC, v. 116, n. 9, p. 5681–5688, 2012.
- 55 WANG, S.-G.; LIAO, X.-Y.; CAO, D.-B.; HUO, C.-F.; LI, Y.-W.; WANG, J.; JIAO, H. Factors controlling the interaction of CO<sub>2</sub> with transition metal surfaces. **The Journal of Physical Chemistry C**, Washington, DC, v. 111, n. 45, p. 16934–16940, 2007.
- 56 WANG, S.-G.; CAO, D.-B.; LI, Y.-W.; WANG, J.; JIAO, H. Chemisorption of CO<sub>2</sub> on nickel surfaces. **The Journal of Physical Chemistry B**, Washington, DC, v. 109, n. 40, p. 18956–18963, 2005. Available at: <https://doi.org/10.1021/jp052355g>.
- 57 LI, S. F.; GUO, Z. X. CO<sub>2</sub> activation and total reduction on titanium(0001) surface. **The Journal of Physical Chemistry C**, Washington, DC, v. 114, n. 26, p. 11456–11459, 2010. Available at: <https://doi.org/10.1021/jp100147g>.
- 58 ZHANG, X.; LIU, J.-X.; ZIJLSTRA, B.; FILOT, I. A.; ZHOU, Z.; SUN, S.; HENSEN, E. J. Optimum Cu nanoparticle catalysts for CO<sub>2</sub> hydrogenation towards methanol. **Nano Energy**, Amsterdam, v. 43, p. 200–209, 2018.
- 59 GAUTAM, S.; DHARAMVIR, K.; GOEL, N. CO<sub>2</sub> adsorption and activation over medium sized Cun (n=7, 13 and 19) clusters: A density functional study. **Computational and Theoretical Chemistry**, Amsterdam, v. 1009, p. 8–16, 2013.
- 60 YU, H.; CAO, D.; FISHER, A.; JOHNSTON, R. L.; CHENG, D. Size effect on the adsorption and dissociation of CO<sub>2</sub> on Co nanoclusters. **Applied Surface Science**, Amsterdam, v. 396, p. 539–546, 2017.
- 61 GÁLVEZ-GONZÁLEZ, L. E.; JUÁREZ-SÁNCHEZ, J. O.; PACHECO-CONTRERAS, R.; GARZÓN, I. L.; PAZ-BORBÓN, L. O.; POSADA-AMARILLAS, A. CO<sub>2</sub> adsorption on gas-phase Cu<sub>4-x</sub>Pt<sub>x</sub> (x = 0–4) clusters: A DFT study. **Physical Chemistry Chemical Physics**, London, v. 20, n. 25, p. 17071–17080, 2018.

- 62 CHAVES, A. S.; PIOTROWSKI, M. J.; DA SILVA, J. L. F. Evolution of the structural, energetic, and electronic properties of the 3d, 4d, and 5d transition-metal clusters (30  $TM_n$  systems for  $n = 2 - 15$ ): A density functional theory investigation. **Physical Chemistry Chemical Physics**, London, v. 19, n. 23, p. 15484–15502, 2017.
- 63 MORSE, M. D.; GEUSIC, M. E.; HEATH, J. R.; SMALLEY, R. E. Surface reactions of metal clusters. II. reactivity surveys with  $D_2$ ,  $N_2$ , and CO. **The Journal of Chemical Physics**, Maryland, v. 83, n. 5, p. 2293–2304, 1985.
- 64 TAYLOR, K. J.; PETTIETTE-HALL, C. L.; CHESHNOVSKY, O.; SMALLEY, R. E. Ultraviolet photoelectron spectra of coinage metal clusters. **The Journal of Chemical Physics**, Maryland, v. 96, n. 4, p. 3319–3329, 1992.
- 65 WANG, L.-S.; LI, X.; ZHANG, H.-F. Probing the electronic structure of iron clusters using photoelectron spectroscopy. **Chemical Physics**, Amsterdam, v. 262, n. 1, p. 53–63, 2000.
- 66 QI, Z.; CHEN, L.; ZHANG, S.; SU, J.; SOMORJAI, G. A. A mini review of cobalt-based nanocatalyst in fischer-tropsch synthesis. **Applied Catalysis A General**, Amsterdam, v. 602, p. 117701, 2020.
- 67 ERNST, K. Kinetics of the reverse water-gas shift reaction over cu(110). **Journal of Catalysis**, Amsterdam, v. 134, n. 1, p. 66–74, 1992.
- 68 GINÉS, M.; MARCHI, A.; APESTEGUÍA, C. Kinetic study of the reverse water-gas shift reaction over CuO/ZnO/Al<sub>2</sub>O<sub>3</sub> catalysts. **Applied Catalysis A General**, Amsterdam, v. 154, n. 1-2, p. 155–171, 1997.
- 69 BERNAL, S.; BLANCO, G.; GATICA, J.; LARESE, C.; VIDAL, H. Effect of mild re-oxidation treatments with CO<sub>2</sub> on the chemisorption capability of a Pt/CeO<sub>2</sub> catalyst reduced at 500°C. **Journal of Catalysis**, Amsterdam, v. 200, n. 2, p. 411–415, 2001.
- 70 KIM, S. S.; LEE, H. H.; HONG, S. C. A study on the effect of support's reducibility on the reverse water-gas shift reaction over Pt catalysts. **Applied Catalysis A General**, Amsterdam, v. 423-424, p. 100–107, 2012.
- 71 LIN, L.; YAO, S.; LIU, Z.; ZHANG, F.; LI, N.; VOVCHOK, D.; MARTÍNEZ-ARIAS, A.; CASTAÑEDA, R.; LIN, J.; SENANAYAKE, S. D.; SU, D.; MA, D.; RODRIGUEZ, J. A. In situ characterization of Cu/CeO<sub>2</sub> nanocatalysts for CO<sub>2</sub> hydrogenation: Morphological effects of nanostructured ceria on the catalytic activity. **The Journal of Physical Chemistry C**, Washington, DC, v. 122, n. 24, p. 12934–12943, 2018.
- 72 VESSELLI, E.; RIZZI, M.; ROGATIS, L. D.; DING, X.; BARALDI, A.; COMELLI, G.; SAVIO, L.; VATTUONE, L.; ROCCA, M.; FORNASIERO, P.; BALDERESCHI, A.; PERESSI, M. Hydrogen-assisted transformation of CO<sub>2</sub> on nickel: The role of formate and carbon monoxide. **The Journal of Physical Chemistry Letters**, Washington, DC, v. 1, n. 1, p. 402–406, 2009.
- 73 MAESTRI, M.; REUTER, K. Molecular-level understanding of WGS and reverse WGS reactions on Rh through hierarchical multiscale approach. **Chemical Engineering Science**, Amsterdam, v. 74, p. 296–299, 2012.

- 74 KARELOVIC, A.; GALDAMES, G.; MEDINA, J. C.; YÉVENES, C.; BARRA, Y.; JIMÉNEZ, R. Mechanism and structure sensitivity of methanol synthesis from CO<sub>2</sub> over SiO<sub>2</sub>-supported Cu nanoparticles. **Journal of Catalysis**, Amsterdam, v. 369, p. 415–426, 2019.
- 75 CHEN, X.; SU, X.; SU, H.-Y.; LIU, X.; MIAO, S.; ZHAO, Y.; SUN, K.; HUANG, Y.; ZHANG, T. Theoretical insights and the corresponding construction of supported metal catalysts for highly selective CO<sub>2</sub> to CO conversion. **ACS Catalysis**, Washington, DC, v. 7, n. 7, p. 4613–4620, 2017.
- 76 GOGUET, A.; MEUNIER, F. C.; TIBILETTI, D.; BREEN, J. P.; BURCH, R. Spectrokinetic investigation of reverse water-gas-shift reaction intermediates over a Pt/CeO<sub>2</sub> catalyst. **The Journal of Physical Chemistry B**, Washington, DC, v. 108, n. 52, p. 20240–20246, 2004.
- 77 ZHENG, X.; GUO, L.; LI, W.; CAO, Z.; LIU, N.; ZHANG, Q.; XING, M.; SHI, Y.; GUO, J. Insight into the mechanism of reverse water-gas shift reaction and ethanol formation catalyzed by Mo<sub>6</sub>S<sub>8</sub>-TM clusters. **Molecular Catalysis**, Amsterdam, v. 439, p. 155–162, 2017.
- 78 CADI-ESSADEK, A.; ROLDAN, A.; APARICIO-ANGLÈS, X.; LEEUW, N. H. de. CO<sub>2</sub> and H<sub>2</sub> adsorption and reaction at Ni<sub>n</sub>/YSZ(111) interfaces: A density functional theory study. **The Journal of Physical Chemistry C**, Washington, DC, v. 122, n. 34, p. 19463–19472, 2018.
- 79 KATTEL, S.; LIU, P.; CHEN, J. G. Tuning selectivity of CO<sub>2</sub> hydrogenation reactions at the metal/oxide interface. **Journal of the American Chemical Society**, Washington, DC, v. 139, n. 29, p. 9739–9754, 2017.
- 80 DIETZ, L.; PICCININ, S.; MAESTRI, M. Mechanistic insights into CO<sub>2</sub> activation via reverse water–gas shift on metal surfaces. **The Journal of Physical Chemistry C**, American Chemical Society (ACS), Washington, DC, v. 119, n. 9, p. 4959–4966, Feb. 2015.
- 81 YANG, B.; LIU, C.; HALDER, A.; TYO, E. C.; MARTINSON, A. B. F.; SEIFERT, S.; ZAPOL, P.; CURTISS, L. A.; VAJDA, S. Copper cluster size effect in methanol synthesis from CO<sub>2</sub>. **The Journal of Physical Chemistry C**, Washington, DC, v. 121, n. 19, p. 10406–10412, 2017.
- 82 MILLET, M.-M.; ALGARA-SILLER, G.; WRABETZ, S.; MAZHEIKA, A.; GIRGSDIES, F.; TESCHNER, D.; SEITZ, F.; TARASOV, A.; LEVCHENKO, S. V.; SCHLÖGL, R.; FREI, E. Ni single atom catalysts for CO<sub>2</sub> activation. **Journal of the American Chemical Society**, Washington, DC, v. 141, n. 6, p. 2451–2461, 2019.
- 83 DOHERTY, F.; WANG, H.; YANG, M.; GOLDSMITH, B. R. Nanocluster and single-atom catalysts for thermocatalytic conversion of CO and CO<sub>2</sub>. **Catalysis Science & Technology**, London, v. 10, n. 17, p. 5772–5791, 2020.
- 84 HORI, Y.; KIKUCHI, K.; MURATA, A.; SUZUKI, S. Production of methane and ethylene in electrochemical reduction of carbon dioxide at copper electrode in aqueous hydrogencarbonate solution. **Chemistry Letters**, Tokyo, v. 15, n. 6, p. 897–898, 1986.

- 85 HORI, Y.; MURATA, A.; TAKAHASHI, R. Formation of hydrocarbons in the electrochemical reduction of carbon dioxide at a copper electrode in aqueous solution. **Journal of the Chemical Society, Faraday Transactions 1: Physical Chemistry in Condensed Phases**, London, v. 85, n. 8, p. 2309, 1989.
- 86 HORI, Y. Electrochemical CO<sub>2</sub> reduction on metal electrodes. *In: Modern Aspects of Electrochemistry*. [S.l.: s.n.]: Springer, New York, 2008. p. 89–189.
- 87 PETERSON, A. A.; ABILD-PEDERSEN, F.; STUDDT, F.; ROSSMEISL, J.; NØRSKOV, J. K. How copper catalyzes the electroreduction of carbon dioxide into hydrocarbon fuels. **Energy & Environmental Science**, London, v. 3, n. 9, p. 1311, 2010.
- 88 RENDÓN-CALLE, A.; BUILES, S.; CALLE-VALLEJO, F. A brief review of the computational modeling of CO<sub>2</sub> electroreduction on Cu electrodes. **Current Opinion in Electrochemistry**, Amsterdam, v. 9, p. 158–165, 2018.
- 89 PÉREZ-GALLENT, E.; MARCANDALLI, G.; FIGUEIREDO, M. C.; CALLE-VALLEJO, F.; KOPER, M. T. M. Structure- and potential-dependent cation effects on CO reduction at copper single-crystal electrodes. **Journal of the American Chemical Society**, Washington, DC, v. 139, n. 45, p. 16412–16419, 2017.
- 90 VERGA, L. G.; MENDES, P. C. D.; OCAMPO-RESTREPO, V. K.; SILVA, J. L. F. D. The role of site coordination on the CO<sub>2</sub> electroreduction pathway on stepped and defective copper surfaces. **Catalysis Science & Technology**, London, v. 11, n. 8, p. 2770–2781, 2021.
- 91 HORI, Y.; TAKAHASHI, I.; KOGA, O.; HOSHI, N. Electrochemical reduction of carbon dioxide at various series of copper single crystal electrodes. **Journal of Molecular Catalysis A Chemical**, Amsterdam, v. 199, n. 1-2, p. 39–47, 2003.
- 92 SCHOUTEN, K. J. P.; QIN, Z.; GALLENT, E. P.; KOPER, M. T. M. Two pathways for the formation of ethylene in CO reduction on single-crystal copper electrodes. **Journal of the American Chemical Society**, Washington, DC, v. 134, n. 24, p. 9864–9867, 2012.
- 93 MURATA, A.; HORI, Y. Product selectivity affected by cationic species in electrochemical reduction of CO<sub>2</sub> and CO at a cu electrode. **Bulletin of the Chemical Society of Japan**, Tokyo, v. 64, n. 1, p. 123–127, 1991.
- 94 SCHOUTEN, K. J. P.; CALLE-VALLEJO, F.; KOPER, M. T. M. A step closer to the electrochemical production of liquid fuels. **Angewandte Chemie International Edition**, Weinheim, v. 53, n. 41, p. 10858–10860, 2014.
- 95 LEDEZMA-YANEZ, I.; GALLENT, E. P.; KOPER, M. T.; CALLE-VALLEJO, F. Structure-sensitive electroreduction of acetaldehyde to ethanol on copper and its mechanistic implications for CO and CO<sub>2</sub> reduction. **Catalysis Today**, Amsterdam, v. 262, p. 90–94, 2016.
- 96 LI, C. W.; CISTON, J.; KANAN, M. W. Electroreduction of carbon monoxide to liquid fuel on oxide-derived nanocrystalline copper. **Nature**, Springer Science and Business Media LLC, v. 508, n. 7497, p. 504–507, Apr. 2014.

- 97 PIQUÉ, O.; LOW, Q. H.; HANDOKO, A. D.; YEO, B. S.; CALLE-VALLEJO, F. Selectivity map for the late stages of CO and CO<sub>2</sub> reduction to C<sub>2</sub> species on copper electrodes. **Angewandte Chemie International Edition**, Weinheim, v. 60, n. 19, p. 10784–10790, 2021.
- 98 TIMOSHENKO, J.; JEON, H. S.; SINEV, I.; HAASE, F. T.; HERZOG, A.; CUENYA, B. R. Linking the evolution of catalytic properties and structural changes in copper–zinc nanocatalysts using operando EXAFS and neural-networks. **Chemical Science**, London, v. 11, n. 14, p. 3727–3736, 2020.
- 99 JEON, H. S.; TIMOSHENKO, J.; SCHOLTEN, F.; SINEV, I.; HERZOG, A.; HAASE, F. T.; CUENYA, B. R. Operando insight into the correlation between the structure and composition of CuZn nanoparticles and their selectivity for the electrochemical CO<sub>2</sub> reduction. **Journal of the American Chemical Society**, Washington, DC, v. 141, n. 50, p. 19879–19887, 2019.
- 100 DONGARE, S.; SINGH, N.; BHUNIA, H.; BAJPAI, P. K. Electrochemical reduction of CO<sub>2</sub> using oxide based Cu and Zn bimetallic catalyst. **Electrochimica Acta**, Amsterdam, v. 392, p. 138988, 2021.
- 101 GIRARDEAU, M. Formulation of the many-body problem for composite particles. **Journal of Mathematical Physics**, Maryland, v. 4, n. 8, p. 1096–1115, 1963.
- 102 BORN, M.; OPPENHEIMER, R. Zur quantentheorie der molekeln. **Annalen der Physik**, Berlin, v. 389, n. 20, p. 457–484, 1927.
- 103 GANGOPADHYAY, G.; DUTTA-ROY, B. The born–oppenheimer approximation: A toy version. **American Journal of Physics**, Maryland, v. 72, n. 3, p. 389–392, 2004.
- 104 YARKONY, D. R. Current issues in nonadiabatic chemistry. **The Journal of Physical Chemistry**, Washington, DC, v. 100, n. 48, p. 18612–18628, 1996.
- 105 BUNKER, P.; MOSS, R. The breakdown of the born–oppenheimer approximation: the effective vibration–rotation hamiltonian for a diatomic molecule. **Molecular Physics**, London, v. 33, n. 2, p. 417–424, 1977.
- 106 PIELA, L. **Ideas of Quantum Chemistry**. Amsterdam: Elsevier Science, 2006. ISBN 9780080466767.
- 107 HOHENBERG, P.; KOHN, W. Inhomogeneous electron gas. **Physical Review**, College Park, v. 136, n. 3B, p. B864–B871, 1964.
- 108 KOHN, W.; SHAM, L. J. Self-consistent equations including exchange and correlation effects. **Physical Review**, College Park, v. 140, n. 4A, p. A1133–A1138, 1965. ISSN 0031-899X.
- 109 BLINDER, S. M. Basic concepts of self-consistent-field theory. **American Journal of Physics**, Maryland, v. 33, n. 6, p. 431–443, 1965.
- 110 PERDEW, J. P.; BURKE, K.; ERNZERHOF, M. Generalized gradient approximation made simple. **Physical Review Letters**, College Park, v. 77, n. 18, p. 3865–3868, 1996.

- 111 PERDEW, J. P.; WANG, Y. Accurate and simple analytic representation of the electron-gas correlation energy. **Physical Review B**, College Park, v. 45, n. 23, p. 13244–13249, 1992.
- 112 KLIMEŠ, J.; MICHAELIDES, A. Perspective: Advances and challenges in treating van der Waals dispersion forces in density functional theory. **The Journal of Chemical Physics**, College Park, v. 137, n. 12, p. 120901, 2012. ISSN 0021-9606.
- 113 JUREČKA, P.; ŠPONER, J.; ČERNÝ, J.; HOBZA, P. Benchmark database of accurate (MP2 and CCSD(t) complete basis set limit) interaction energies of small model complexes, DNA base pairs, and amino acid pairs. **Physical Chemistry Chemical Physics**, London, v. 8, n. 17, p. 1985–1993, 2006.
- 114 FREIRE, R. L. H.; KIEJNA, A.; DA SILVA, J. L. F. Adsorption of water and ethanol on noble and transition-metal substrates: A density functional investigation within van der waals corrections. **Physical Chemistry Chemical Physics**, London, v. 18, n. 42, p. 29526–29536, 2016.
- 115 OCAMPO-RESTREPO, V. K.; ZIBORDI-BESSE, L.; DA SILVA, J. L. F. *Ab initio* investigation of the atomistic descriptors in the activation of small molecules on 3d transition-metal 13-atom clusters: The example of H<sub>2</sub>, CO, H<sub>2</sub>O and CO<sub>2</sub>. **The Journal of Chemical Physics**, Maryland, v. 151, n. 21, p. 214301, 2019. ISSN 0021-9606, 1089-7690.
- 116 ELSTNER, M.; HOBZA, P.; FRAUENHEIM, T.; SUHAI, S.; KAXIRAS, E. Hydrogen bonding and stacking interactions of nucleic acid base pairs: A density-functional-theory based treatment. **The Journal of Chemical Physics**, Maryland, v. 114, n. 12, p. 5149–5155, 2001.
- 117 GRIMME, S. Accurate description of van der Waals complexes by density functional theory including empirical corrections. **Journal of Computational Chemistry**, New York, v. 25, n. 12, p. 1463–1473, 2004.
- 118 YUAN, D.; ZHANG, Y.; HO, W.; WU, R. Effects of van der waals dispersion interactions in density functional studies of adsorption, catalysis, and tribology on metals. **The Journal of Physical Chemistry C**, Washington, DC, v. 124, n. 31, p. 16926–16942, 2020.
- 119 GRIMME, S. Semiempirical GGA-type density functional constructed with a long-range dispersion correction. **Journal of Computational Chemistry**, Wiley-Blackwell, New York, v. 27, n. 15, p. 1787–1799, 2006.
- 120 TKATCHENKO, A.; SCHEFFLER, M. Accurate molecular van der Waals interactions from ground-state electron density and free-atom reference data. **Physical Review Letters**, College Park, v. 102, n. 7, p. 073005, 2009.
- 121 BLUM, V.; GEHRKE, R.; HANKE, F.; HAVU, P.; HAVU, V.; REN, X.; REUTER, K.; SCHEFFLER, M. *Ab initio* molecular simulations with numeric atom-centered orbitals. **Computer Physics Communications**, Amsterdam, v. 180, n. 11, p. 2175–2196, 2009.
- 122 HENKELMAN, G.; UBERUAGA, B. P.; JÓNSSON, H. A climbing image nudged elastic band method for finding saddle points and minimum energy paths. **The Journal of Chemical Physics**, Maryland, v. 113, p. 9901–9904, 2000.

- 123 NØRSKOV, J. K.; ROSSMEISL, J.; LOGADOTTIR, A.; LINDQVIST, L.; KITCHIN, J. R.; BLIGAARD, T.; Jónsson, H. Origin of the overpotential for oxygen reduction at a fuel-cell cathode. **The Journal of Physical Chemistry B**, Washington, DC, v. 108, p. 17886–17892, 2004.
- 124 ZIBORDI-BESSE, L.; TERESHCHUK, P.; CHAVES, A. S.; DA SILVA, J. L. F. Ethanol and water adsorption on transition-metal 13-atom clusters: A density functional theory investigation within van der Waals corrections. **The Journal of Physical Chemistry A**, Washington, DC, v. 120, n. 24, p. 4231–4240, 2016.
- 125 GUEDES-SOBRINHO, D.; FREIRE, R. L. H.; CHAVES, A. S.; SILVA, J. L. F. D. Ab initio investigation of the role of CO adsorption on the physical properties of 55-atom PtCo nanoalloys. **The Journal of Physical Chemistry C**, American Chemical Society (ACS), Washington, DC, v. 121, n. 49, p. 27721–27732, Nov. 2017.
- 126 CATURELLO, N. A. M. S.; BESSE, R.; DA SILVA, A. C. H.; GUEDES-SOBRINHO, D.; LIMA, M. P.; DA SILVA, J. L. F. *Ab initio* investigation of atomistic insights into the nanoflake formation of transition-metal dichalcogenides: The examples of MoS<sub>2</sub>, MoSe<sub>2</sub> and MoTe<sub>2</sub>. **The Journal of Physical Chemistry C**, Washington, DC, v. 122, n. 47, p. 27059–27069, 2018. ISSN 1932-7447, 1932-7455.
- 127 JAIN, A. K. Data clustering: 50 years beyond k-means. **Pattern Recognition Letters**, Amsterdam, v. 31, n. 8, p. 651–666, 2010.
- 128 CHA, S.-H. Comprehensive survey on distance/similarity measures between probability density functions. **International Journal of Mathematical Models and Methods in Applied Sciences**, Bridgewater, v. 1, n. 2, p. 300–307, 2007.
- 129 GEHRKE, R.; REUTER, K. Assessing the efficiency of first-principles basin-hopping sampling. **Physical Review B**, College Park, v. 79, n. 8, p. 085412, 2009. ISSN 1098-0121, 1550-235X.
- 130 CEZAR, H. M.; RONDINA, G. G.; DA SILVA, J. L. F. Parallel tempering Monte Carlo combined with clustering euclidean metric analysis to study the thermodynamic stability of lennard–jones nanoclusters. **The Journal of Chemical Physics**, College Park, v. 146, n. 6, p. 064114, 2017.
- 131 HOPPE, R. The coordination number - an “inorganic chameleon”. **Angewandte Chemie International Edition**, Weinheim, v. 9, n. 1, p. 25–34, 1970.
- 132 HOPPE, R. Effective coordination numbers (ECoN) and mean active fictive ionic radii (MEFIR). **Zeitschrift für Kristallographie – Crystalline Materials**, Berlin, v. 150, n. 1-4, p. 23–52, 1979.
- 133 DA SILVA, J. L. F.; KIM, H. G.; PIOTROWSKI, M. J.; PRIETO, M. J.; TREMILIOSI-FILHO, G. Reconstruction of core and surface nanoparticles: The example of Pt<sub>55</sub> and Au<sub>55</sub>. **Physical Review B**, College Park, v. 82, n. 20, p. 205424, 2010.
- 134 DA SILVA, J. L. F. Effective coordination concept applied for phase change (GeTe)<sub>m</sub>(Sb<sub>2</sub>Te<sub>3</sub>)<sub>n</sub> compounds. **Journal of Applied Physics**, College Park, v. 109, n. 2, p. 023502, 2011.



- 135 HIRSHFELD, F. L. Bonded-atom fragments for describing molecular charge densities. **Theoretical Chemistry Accounts**, Berlin, v. 44, n. 2, p. 129–138, 1977.
- 136 HARMONY, M. D.; LAURIE, V. W.; KUCZKOWSKI, R. L.; SCHWENDEMAN, R. H.; RAMSAY, D. A.; LOVAS, F. J.; LAFFERTY, W. J.; MAKI, A. G. Molecular structures of gas-phase polyatomic molecules determined by spectroscopic methods. **Journal of Physical and Chemical Reference Data**, College Park, v. 8, n. 3, p. 619–721, 1979.
- 137 LUO, Y.-R. **Comprehensive Handbook of Chemical Bond Energies**. [S.l.: s.n.]: CRC Press, 2007.
- 138 PIOTROWSKI, M. J.; PIQUINI, P.; DA SILVA, J. L. F. Density functional theory investigation of *3d*, *4d*, and *5d* 13-atom metal clusters. **Physical Review B**, College Park, v. 81, n. 15, p. 155446, 2010.
- 139 COOPER, C. D.; COMPTON, R. N. Electron attachment to cyclic anhydrides and related compounds. **The Journal of Chemical Physics**, American Institute of Physics publishing, Maryland, v. 59, n. 7, p. 3550–3565, Oct. 1973. ISSN 0021-9606, 1089-7690. Available at: <https://doi.org/10.1063/1.1680519>.
- 140 CHAVES, A. S.; PIOTROWSKI, M. J.; GUEDES-SOBRINHO, D.; DA SILVA, J. L. F. Theoretical investigation of the adsorption properties of CO, NO, and OH on monometallic and bimetallic 13-atom clusters: The example of Cu<sub>13</sub>, Pt<sub>7</sub>Cu<sub>6</sub>, and Pt<sub>13</sub>. **The Journal of Physical Chemistry A**, Washington, DC, v. 119, n. 47, p. 11565–11573, 2015.
- 141 XIE, W.; PENG, L.; PENG, D.; GU, F. L.; LIU, J. Processes of H<sub>2</sub> adsorption on Fe(110) surface: A density functional theory study. **Applied Surface Science**, Amsterdam, v. 296, p. 47–52, 2014.
- 142 BATISTA, K. E. A.; DA SILVA, J. L. F.; PIOTROWSKI, M. J. Adsorption of CO, NO, and H<sub>2</sub> on the Pd<sub>n</sub>Au<sub>55-n</sub> nanoclusters: A density functional theory investigation within the van der waals d3 corrections. **The Journal of Physical Chemistry C**, Washington, DC, v. 123, n. 12, p. 7431–7439, 2019.
- 143 LIU, C.; CUNDARI, T. R.; WILSON, A. K. Periodic trends in 3d metal mediated CO<sub>2</sub> activation. *In*: **Applications of Molecular Modeling to Challenges in Clean Energy**. [S.l.: s.n.]: American Chemical Society, 2013. p. 67–88.
- 144 WANG, Y.-G.; WIBERG, K. B.; WERSTIUK, N. H. Correlation effects in EOM-CCSD for the excited states: evaluated by AIM localization index (LI) and delocalization index (DI). **The Journal of Physical Chemistry A**, Washington, DC, v. 111, n. 18, p. 3592–3601, 2007.
- 145 SHIMANOUCI, T.; SHIMANOUCI, T. **Tables of molecular vibrational frequencies**. [S.l.: s.n.]: National Bureau of Standards, Washington, DC, 1980.
- 146 ARESTA, M.; NOBILE, C. F. (carbon dioxide)bis(trialkylphosphine)nickel complexes. **Journal of the Chemical Society, Dalton Transactions**, London, n. 7, p. 708–711, 1977.

- 147 HIRANO, M.; AKITA, M.; TANI, K.; KUMAGAI, K.; KASUGA, N. C.; FUKUOKA, A.; KOMIYA, S. Activation of coordinated carbon dioxide in  $\text{Fe}(\text{CO})_2(\text{depe})_2$  by group 14 electrophiles. **Organometallics**, Washington, DC, v. 16, n. 19, p. 4206–4213, 1997.
- 148 OCAMPO-RESTREPO, V. K.; VERGA, L. G.; SILVA, J. L. F. D. Ab initio study of the c–o bond dissociation in  $\text{CO}_2$  reduction by redox and carboxyl routes on 3d transition metal systems. **The Journal of Physical Chemistry C**, Washington, DC, v. 125, n. 48, p. 26296–26306, 2021.
- 149 MENDES, P. C. D.; COSTA-AMARAL, R.; GOMES, J. F.; DA SILVA, J. L. F. The influence of hydroxy groups on the adsorption of three-carbon alcohols on Ni(111), Pd(111) and Pt(111) surfaces: A density functional theory study within the d3 dispersion correction. **Physical Chemistry Chemical Physics**, London, v. 21, n. 16, p. 8434–8444, 2019.
- 150 KEPP, K. P. A quantitative scale of oxophilicity and thiophilicity. **Inorganic Chemistry**, Washington, DC, v. 55, n. 18, p. 9461–9470, 2016.
- 151 HAN, B. C.; CEDER, G. Effect of coadsorption and Ru alloying on the adsorption of CO on Pt. **Physical Review B**, College Park, v. 74, n. 20, p. 205418, 2006.
- 152 LIU, F.; XUE, T.; WU, C.; YANG, S. Coadsorption of CO and O over strained metal surfaces. **Chemical Physics Letters**, Amsterdam, v. 722, p. 18–25, 2019.
- 153 NILEKAR, A. U.; GREELEY, J.; MAVRIKAKIS, M. A simple rule of thumb for diffusion on transition-metal surfaces. **Angewandte Chemie**, Weinheim, v. 118, n. 42, p. 7204–7207, 2006.
- 154 JØRGENSEN, M.; GRÖNBECK, H. Adsorbate entropies with complete potential energy sampling in microkinetic modeling. **The Journal of Physical Chemistry C**, Washington, DC, v. 121, n. 13, p. 7199–7207, 2017.
- 155 ROSS, J. R. The kinetics and mechanisms of catalytic reactions. *In*: ROSS, J. R. (ed.). **Contemporary Catalysis**. Amsterdam: Elsevier, 2019. p. 161–186.
- 156 MEDFORD, A. J.; VOJVODIC, A.; HUMMELSHØJ, J. S.; VOSS, J.; ABILD-PEDERSEN, F.; STUDT, F.; BLIGAARD, T.; NILSSON, A.; NØRSKOV, J. K. From the sabatier principle to a predictive theory of transition-metal heterogeneous catalysis. **Journal of Catalysis**, Amsterdam, v. 328, p. 36–42, 2015.
- 157 MONTEMORE, M. M.; MEDLIN, J. W. Scaling relations between adsorption energies for computational screening and design of catalysts. **Catalysis Science & Technology**, London, v. 4, n. 11, p. 3748–3761, 2014.
- 158 SANTEN, R. A. van; NEUROCK, M.; SHETTY, S. G. Reactivity theory of transition-metal surfaces: A brønsted-evans-polanyi linear activation energy-free-energy analysis. **Chemical Reviews**, Washington, DC, v. 110, n. 4, p. 2005–2048, 2010.
- 159 QI, Y.; ZHU, Y.-A.; CHEN, D. Mechanism investigation and catalyst screening of high-temperature reverse water gas shift reaction. **Green Chemical Engineering**, Amsterdam, v. 1, n. 2, p. 131–139, 2020.

- 160 BIRDJA, Y. Y.; PÉREZ-GALLEN, E.; FIGUEIREDO, M. C.; GÖTTLE, A. J.; CALLE-VALLEJO, F.; KOPER, M. T. M. Advances and challenges in understanding the electrocatalytic conversion of carbon dioxide to fuels. **Nature Energy**, London, v. 4, n. 9, p. 732–745, 2019.
- 161 KUHL, K. P.; CAVE, E. R.; ABRAM, D. N.; JARAMILLO, T. F. New insights into the electrochemical reduction of carbon dioxide on metallic copper surfaces. **Energy Environmental Science**, London, v. 5, n. 5, p. 7050, 2012.
- 162 TING, L. R. L.; PIQUÉ, O.; LIM, S. Y.; TANHAEI, M.; CALLE-VALLEJO, F.; YEO, B. S. Enhancing CO<sub>2</sub> electroreduction to ethanol on copper–silver composites by opening an alternative catalytic pathway. **ACS Catalysis**, Washington, DC, v. 10, n. 7, p. 4059–4069, 2020.
- 163 GARZA, A. J.; BELL, A. T.; HEAD-GORDON, M. Mechanism of CO<sub>2</sub> reduction at copper surfaces: Pathways to c<sub>2</sub> products. **ACS Catalysis**, Washington, DC, v. 8, n. 2, p. 1490–1499, 2018.
- 164 REN, D.; DENG, Y.; HANDOKO, A. D.; CHEN, C. S.; MALKHANDI, S.; YEO, B. S. Selective electrochemical reduction of carbon dioxide to ethylene and ethanol on copper(i) oxide catalysts. **ACS Catalysis**, Washington, DC, v. 5, n. 5, p. 2814–2821, 2015.
- 165 LI, C. W.; CISTON, J.; KANAN, M. W. Electroreduction of carbon monoxide to liquid fuel on oxide-derived nanocrystalline copper. **Nature**, London, v. 508, n. 7497, p. 504–507, 2014.
- 166 REN, D.; ANG, B. S.-H.; YEO, B. S. Tuning the selectivity of carbon dioxide electroreduction toward ethanol on oxide-derived Cu<sub>x</sub>Zn catalysts. **ACS Catalysis**, Washington, DC, v. 6, n. 12, p. 8239–8247, 2016.
- 167 SU, X.; SUN, Y.; JIN, L.; ZHANG, L.; YANG, Y.; KERNS, P.; LIU, B.; LI, S.; HE, J. Hierarchically porous Cu/Zn bimetallic catalysts for highly selective CO<sub>2</sub> electroreduction to liquid C<sub>2</sub> products. **Applied Catalysis B Environmental**, Amsterdam, v. 269, p. 118800, 2020.
- 168 HAVU, V.; BLUM, V.; HAVU, P.; SCHEFFLER, M. Efficient integration for all-electron electronic structure calculation using numeric basis functions. **Journal of Computational Physics**, Amsterdam, v. 228, n. 22, p. 8367–8379, 2009.
- 169 VAN LENTHE, E.; SNIJDERS, J. G.; BAERENDS, E. J. The zero-order regular approximation for relativistic effects: The effect of spin-orbit coupling in closed shell molecules. **The Journal of Chemical Physics**, College Park, v. 105, n. 15, p. 6505–6516, 1996.
- 170 HENKELMAN, G.; JÓNSSON, H. Improved tangent estimate in the nudged elastic band method for finding minimum energy paths and saddle points. **The Journal of Chemical Physics**, College Park, v. 113, p. 9978–9985, 2000.
- 171 SHEPPARD, D.; TERRELL, R.; HENKELMAN, G. Optimization methods for finding minimum energy paths. **The Journal of Chemical Physics**, College Park, v. 128, n. 13, p. 134106, 2008.

## **APPENDIX**

## APPENDIX A – COMPUTATIONAL TESTS AND PARAMETERS

In this thesis, all the total energy calculations were done based on the spin-polarized DFT framework and employed the exchange-correlation functional proposed by Perdew–Burke–Ernzerhof[110] (PBE). Also, we improved the description for the long-range dispersion interactions by employing the correction formulated by Tkatchenko–Scheffler (TS) [120]. To solve the Kohn–Sham (KS) equations, we employed the Fritz–Haber Institute *Ab initio* molecular simulations (FHI-aims) package, and the Kohn–Sham orbitals were described by numeric atom-centered orbitals (NAO) [121, 168]. To increase the basis set accuracy, we add functions with angular momenta  $l+1$ , which are called polarization functions. FHI-aims organize the addition of basis functions into levels called *tier1*, *tier2*, and so on. Based on our tests, we employed the *light-tier2* basis set, triple numeric plus polarization in the literature terminology. We used a Gaussian broadening of 0.01 eV. However, based on our convergence tests, we reduced it at 0.001 eV for calculations combining the CI-NEB The scalar-relativistic framework with the zero-order regular approximation (ZORA) was also included [169],

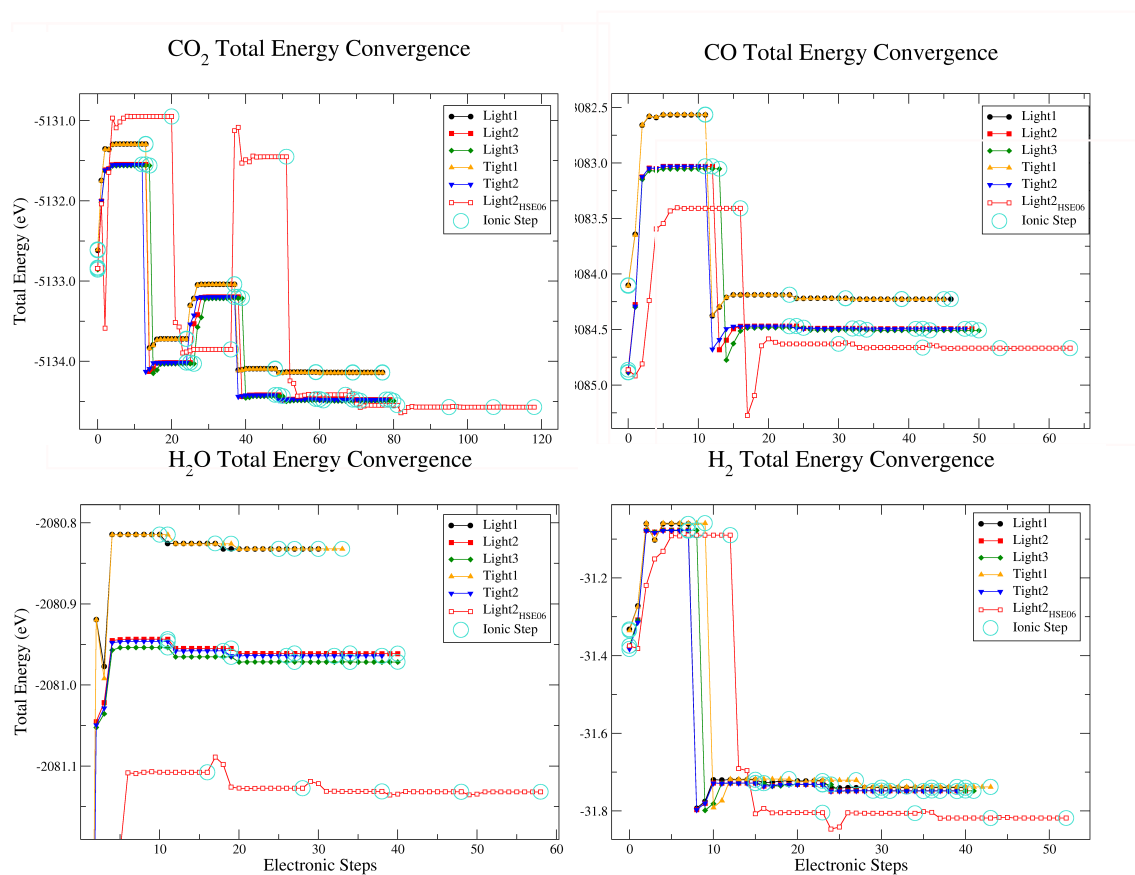
For the self-consistency of the electron density, we employed criteria like the total energy, charge density, the sum of eigenvalues, and forces. For the study discussed in Chapter 3 were setup the: total energy at  $1.0 \times 10^{-6}$  eV, charge density at  $1.0 \times 10^{-3} e \text{ \AA}^{-3}$ , and forces at  $1.0 \times 10^{-3} \text{ eV \AA}^{-1}$ . For Chapter 4: total energy at  $10^{-6}$  eV, charge density at  $10^{-5} e \text{ \AA}^{-3}$ , sum of eigenvalues at  $10^{-3}$  eV, and forces at  $10^{-4} \text{ eV \AA}^{-1}$ . For Chapter 5: total energy at  $10^{-5}$  eV, charge density at  $10^{-4} e \text{ \AA}^{-3}$ , sum of eigenvalues at  $10^{-2}$  eV, and forces at  $10^{-3} \text{ eV \AA}^{-1}$ . While the equilibrium geometries for all systems were obtained using the Broyden–Fletcher–Goldfarb–Shanno (BFGS) algorithm[121] once the atomic forces were smaller than  $10^{-2} \text{ eV \AA}^{-1}$ . Furthermore, for the vibrational frequency calculations, crucial to the identification of local minimum and transition-state configurations, we decreased the forces criteria to  $10^{-5} \text{ eV \AA}^{-1}$  to calculate the Hessian matrix elements using atomic displacements of  $2.5 \times 10^{-3} \text{ \AA}$ . To obtain the transition-states on the  $\text{Fe}_{13}$  clusters, we decreased this displacement to  $10^{-3} \text{ \AA}$  to minimize systematic errors due to the anharmonicity effects.

To search the transition-states, †, we employed the climbing image-nudge elastic band algorithm (CI-NEB)[170] and as geometry optimizer, the fast inertial relaxation engine (FIRE) [171]. We employed linear interpolation to connect the initial and final states. The force constant used for the string between the images was  $10 \text{ eV \AA}^{-1}$ . We split the procedure into two stages, given the several potential initial and final states. In the first stage, we explored several paths connecting different initial and final states at NEB framework using 7 images to connect the steps and residual forces of  $0.15 \text{ eV \AA}^{-1}$ . We found

few paths with more than one potential transition state that were later separated into the most simple steps and re-calculated. For cases with more than one path, we selected which had the lower activation energy. In the second stage, the paths from the previous stage were further refined within the climbing image functionality to achieve a residual force of  $0.01 \text{ eV \AA}^{-1}$ . We performed vibrational frequency calculations for all transition states to verify the unique negative frequency along with the reaction coordinate.

### Test performed for the results discussed in Chapter 3

Figure 23 – Total energy convergence test for small molecules using different basis set functions.



Source: Own authorship

### Test performed for the results discussed in Chapter 4

To ensure self-consistent field (SCF) convergence for a wide range of structures along the reaction path, we performed tests for electronic parameters such as the charge mix param,  $n$  max pulay, and occupation type gaussian, see FHI-aims manual. Structures 1 and 2 came from calculations with SCF convergence problems when the default setup was used, charge\_mix\_param changing,  $n$ \_max\_pulay 8, and occupation\_type gaussian 0.050 eV. Also, to verify our tests, we added a third structure without convergence problems. After our tests, the selected set up of parameters was: charge\_mix\_param 0.1,  $n$ \_max\_pulay 8, and occupation\_type gaussian 1 meV.

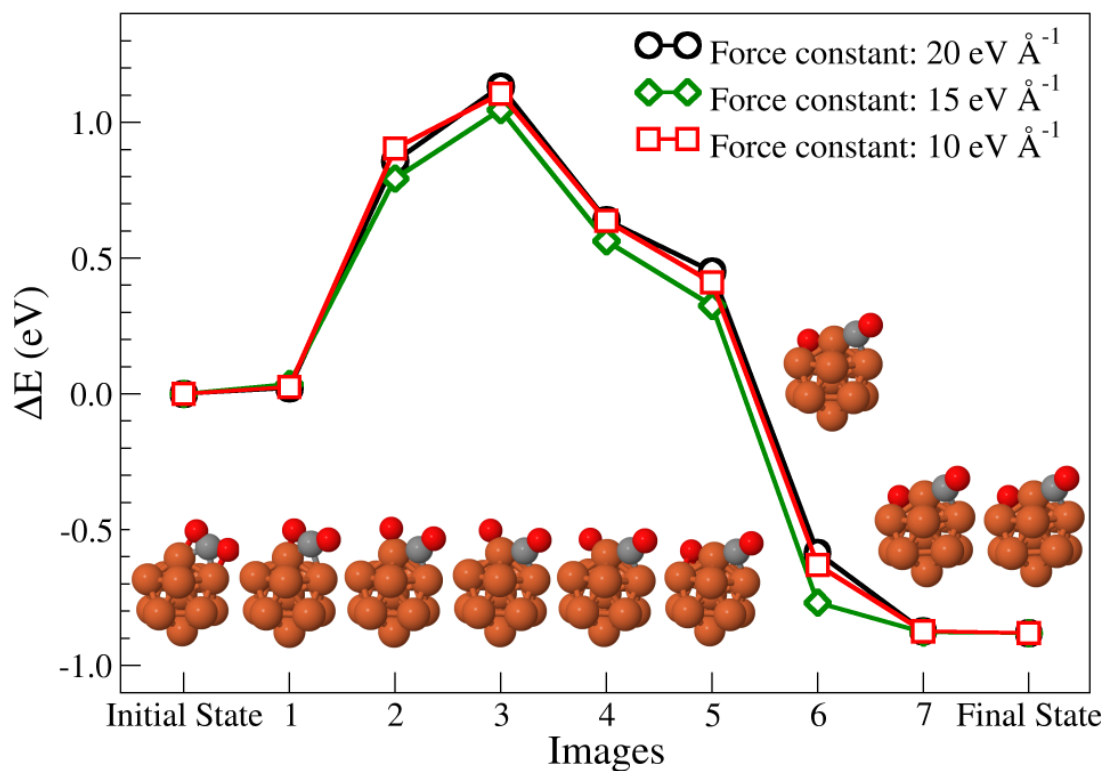
Table 7 – Self-consistent Field (SCF) convergence tests varying: charge\_mix\_param,  $n$ \_max\_pulay, and occupation\_type gaussian. SCF convergence threshold used: total energy at  $10^{-6}$  eV, charge density at  $10^{-5} e \text{ \AA}^{-3}$ , sum of eigenvalues at  $10^{-3}$  eV, and forces at  $10^{-4} eV \text{ \AA}^{-1}$ .

Parameters Fixed		charge_mix_param 0.10	occupation_type gaussian 0.01	
CO–O/Fe <sub>13</sub> structure 1	n_max_pulay	2	6	8
	SCF converged	Yes	No	No
	Number of SCF	470	500	500
	Time (h)	1.70	1.80	1.80
CO–O/Fe <sub>13</sub> structure 2	SCF converged	No	No	No
	Number of SCF	500	500	500
	Time (h)	1.60	1.70	1.70
	SCF converged	-	-	Yes
CO–O/Fe <sub>13</sub> structure 3	Number of SCF	-	-	55
	Time (h)	-	-	0.23
Parameters Fixed		occupation_type gaussian 0.01	n_max_pulay 8	
CO–O/Fe <sub>13</sub> structure 1	charge_mix_param	0.10	0.05	0.01
	SCF converged	No	No	No
	Number of SCF	500	500	500
	Time (h)	1.80	1.80	1.80
CO–O/Fe <sub>13</sub> structure 2	SCF converged	No	-	No
	Number of SCF	500	-	500
	Time (h)	1.70	-	1.60
	SCF converged	-	Yes	-
CO–O/Fe <sub>13</sub> structure 3	Number of SCF	-	50	-
	Time (h)	-	0.19	-
Parameters Fixed		charge_mix_param 0.10	n_max_pulay 8	
CO–O/Fe <sub>13</sub> structure 1	occupation_type gaussian	0.050	0.010	0.001
	SCF converged	No	No	Yes
	Number of SCF	500	500	73
	Time (h)	1.80	1.80	0.31
CO–O/Fe <sub>13</sub> structure 2	SCF converged	No	No	Yes
	Number of SCF	500	500	56
	Time (h)	1.60	1.70	0.20
	SCF converged	Yes	-	Yes
CO–O/Fe <sub>13</sub> structure 3	Number of SCF	62	-	54
	Time (h)	0.06	-	0.22

Source: Reprinted with permission from OCAMPO-RESTREPO, V. K.; VERGA, L. G.; DA SILVA, J. L. F. *The Journal of Physical Chemistry C*, v. 125, n. 48, p. 26296-26306, 2021 [148]. Copyright © 2021, American Chemical Society.

### Tests of Force Constant for Nudged Elastic Band Calculations (NEB).

Figure 24 – Reaction path of  $\text{CO}_2 \longrightarrow \text{CO} + \text{O}$  on  $\text{Fe}_{13}$  with NEB method using different force constants: red square for  $20 \text{ eV \AA}^{-1}$  (iteration 91), green diamond for  $15 \text{ eV \AA}^{-1}$  (iteration 245), and black circle for  $10 \text{ eV \AA}^{-1}$  (iteration 100). All calculations used 7 images and a residual forces threshold at  $0.15 \text{ eV \AA}^{-1}$ .



Source: Reprinted with permission from OCAMPO-RESTREPO, V. K.; VERGA, L. G.; DA SILVA, J. L. F. *The Journal of Physical Chemistry C*, v. 125, n. 48, p. 26296-26306, 2021 [148]. Copyright © 2021, American Chemical Society.



### Test performed for the study discussed in Chapter 5

Below are the results comparing the set of parameters for the scanning, A, and the set to get the final data B.

#### Set of parameters A:

basis set: light1

Total energy: *sc\_accuracy\_etot*  $1.0E - 4$

Charge density: *sc\_accuracy\_rho*  $1.0E - 3$

Sum of eigenvalues: *sc\_accuracy\_eev*  $1.0E - 1$

forces: *sc\_accuracy\_forces*  $1.0E - 2$

Nuclei forces for relaxation: *relax\_geometrytrm*  $1.0E - 1$

#### Set of parameters B:

basis set: light2;

vdW correction TS: *vdw\_correction\_hirshfeld*:on

Total energy: *sc\_accuracy\_etot*  $1.0E - 5$

Charge density: *sc\_accuracy\_rho*  $1.0E - 4$

Sum of eigenvalues: *sc\_accuracy\_eev*  $1.0E - 2$

Forces: *sc\_accuracy\_forces*  $1.0E - 3$

Nuclei forces for relaxation: *relax\_geometrytrm*  $1.0E - 2$

The tables below compare the data for CHCO and CHCHO on  $\text{Cu}_{55}$  and  $\text{Cu}_{42}\text{Zn}_{13}$  clusters. The scanning considered about 20 and 30 structures for CHCO and CHCHO. To reduce the set of structures to half for the calculation with set B, we performed a k-means analysis, including the energetic information gathered from the calculations with set A.

Figure 25 at the top shows the relative energy from set B vs. set A. The structure used as reference was the lowest energy structure provided with set B. Figure S9 at the bottom shows the relative energy difference between sets B and A for each configuration. Also, circle orange and X green highlight the lowest energy structure obtained via set A and B, respectively.

The main difference was for CHCO on  $\text{Cu}_{55}$ , where one high energy structure predicted from set A becomes degenerated with the lowest energy structure when used the set B. The properties of those structures are similar. For the rest of the systems, both sets predicted the same configuration as the lowest. Thus, we could use just the lowest energy structures predicted with set A and refine with set B to obtain the final data.

Table 8 – Comparison between set of parameters A and B for CHCO adsorbed on  $\text{Cu}_{55}^{\text{ICO}}$  clusters. Relative energy ( $\Delta E_{tot}$ ); adsorption energy ( $E_{ad}$ ); highest occupied molecular orbital (HOMO); lowest unoccupied molecular orbital (LUMO); HOMO-LUMO gap (Gap); minimum bond distance of C to  $\text{Cu}_{55}$  ( $d^{\text{C-Cu}}$ ); minimum bond distance of O to  $\text{Cu}_{55}$  ( $d^{\text{O-Cu}}$ ); minimum bond distance of H to  $\text{Cu}_{55}$  ( $d^{\text{H-Cu}}$ ); total magnetic moment ( $m_{tot}$ ).

Structures	$\Delta E_{tot}$ (eV)	$E_{ad}$ (eV)	HOMO (eV)	LUMO (eV)	Gap (eV)	$d^{\text{C-Cu}}$ (Å)	$d^{\text{O-Cu}}$ (Å)	$d^{\text{H-Cu}}$ (Å)	$m_{tot}$ ( $\mu_B$ )
CHCO/ $\text{Cu}_{55}^{\text{ICO}}$									
Set A									
4	0.57		-4.33	-4.29	0.04	1.91	3.69	2.66	2
9	0.54		-4.23	-4.19	0.04	1.97	2.10	2.81	2
10	0.53		-4.25	-4.19	0.06	1.97	2.09	2.82	2
20	0.44		-4.24	-4.13	0.11	1.96	2.15	2.76	0
3	0.11		-4.19	-4.11	0.08	2.06	3.37	2.57	0
18	0.11		-4.19	-4.11	0.08	2.06	3.41	2.48	0
23	0.00		-4.23	-4.17	0.06	2.02	3.51	2.70	2
5	0.00		-4.22	-4.17	0.05	2.02	3.61	2.70	0
12	-0.01		-4.22	-4.18	0.04	2.03	3.69	2.70	0
19	-0.02		-4.23	-4.16	0.06	2.03	3.69	2.70	2
Set B									
9	0.58	-1.42	-4.25	-4.20	0.05	1.97	2.09	2.82	2
10	0.57	-1.43	-4.26	-4.20	0.05	1.97	2.09	2.82	2
20	0.46	-1.55	-4.25	-4.15	0.10	1.96	2.14	2.75	0
18	0.09	-1.92	-4.19	-4.11	0.08	2.08	3.42	2.24	0
3	0.08	-1.92	-4.19	-4.11	0.08	2.09	3.43	2.23	0
12	0.02	-1.99	-4.22	-4.19	0.03	2.03	3.66	2.71	0
5	0.02	-1.99	-4.22	-4.19	0.03	2.03	3.66	2.70	0
4	0.02	-1.99	-4.22	-4.19	0.03	2.03	3.67	2.71	0
19	0.00	-2.01	-4.23	-4.17	0.06	2.03	3.66	2.71	2
23	0.00	-2.01	-4.23	-4.17	0.06	2.03	3.67	2.71	2

Source: Own authorship.

Table 9 – Comparison between set of parameters A and B for CHCHO adsorbed on  $\text{Cu}_{55}^{\text{ICO}}$  clusters. Relative energy ( $\Delta E_{tot}$ ); adsorption energy ( $E_{ad}$ ); highest occupied molecular orbital (HOMO); lowest unoccupied molecular orbital (LUMO); HOMO-LUMO gap (Gap); minimum bond distance of C to  $\text{Cu}_{55}$  ( $d^{\text{C-Cu}}$ ); minimum bond distance of O to  $\text{Cu}_{55}$  ( $d^{\text{O-Cu}}$ ); minimum bond distance of H to  $\text{Cu}_{55}$  ( $d^{\text{H-Cu}}$ ); total magnetic moment ( $m_{tot}$ ).

Structures	$\Delta E_{tot}$ (eV)	$E_{ad}$ (eV)	HOMO (eV)	LUMO (eV)	Gap (eV)	$d^{\text{C-Cu}}$ (Å)	$d^{\text{O-Cu}}$ (Å)	$d^{\text{H-Cu}}$ (Å)	$m_{tot}$ ( $\mu_B$ )
$\text{CHCHO}/\text{Cu}_{55}^{\text{ICO}}$									
Set A									
1	3.04		-4.27	-4.22	0.04	2.93	1.97	2.95	1
22	2.76		-4.26	-4.20	0.06	2.95	2.00	3.12	3
3	0.81		-4.33	-4.27	0.06	1.96	3.86	1.93	1
20	0.81		-4.32	-4.26	0.06	1.96	3.86	1.89	1
13	0.73		-4.36	-4.30	0.05	1.98	3.76	1.82	1
23	0.21		-4.17	-4.11	0.06	2.01	2.01	2.65	1
9	0.05		-4.23	-4.16	0.07	1.97	1.95	2.63	1
10	0.01		-4.23	-4.18	0.06	2.00	1.93	2.66	1
15	0.00		-4.23	-4.18	0.05	2.00	1.94	2.67	1
6	-0.01		-4.23	-4.18	0.06	2.00	1.94	2.67	1
Set B									
22	3.11	-0.36	-4.28	-4.23	0.05	2.97	1.98	3.06	1
1	3.11	-0.37	-4.28	-4.23	0.05	2.93	1.98	2.88	1
3	0.81	-2.66	-4.33	-4.27	0.06	1.96	3.80	1.84	1
20	0.81	-2.67	-4.33	-4.27	0.06	1.96	3.79	1.84	1
13	0.72	-2.75	-4.37	-4.31	0.05	1.99	3.70	1.78	1
23	0.16	-3.32	-4.16	-4.11	0.06	1.99	2.01	2.67	1
9	0.05	-3.42	-4.24	-4.17	0.07	1.98	1.95	2.64	1
10	0.00	-3.47	-4.24	-4.19	0.05	2.00	1.94	2.69	1
6	0.00	-3.47	-4.24	-4.19	0.05	2.00	1.94	2.68	1
15	0.00	-3.47	-4.24	-4.19	0.05	2.00	1.94	2.68	1

Source: Own authorship.

Table 10 – Comparison between set of parameters A and B for CHCO adsorbed on  $\text{Cu}_{42}\text{Zn}_{13}^{\text{ICO}}$  clusters. Relative energy ( $\Delta E_{tot}$ ); adsorption energy ( $E_{ad}$ ); highest occupied molecular orbital (HOMO); lowest unoccupied molecular orbital (LUMO); HOMO-LUMO gap (Gap); minimum bond distance of C to  $\text{Cu}_{42}\text{Zn}_{13}$  ( $d^{\text{C}-\text{Cu}_{42}\text{Zn}_{13}}$ ); minimum bond distance of O to  $\text{Cu}_{42}\text{Zn}_{13}$  ( $d^{\text{O}-\text{Cu}_{42}\text{Zn}_{13}}$ ); minimum bond distance of H to  $\text{Cu}_{42}\text{Zn}_{13}$  ( $d^{\text{H}-\text{Cu}_{42}\text{Zn}_{13}}$ ); total magnetic moment ( $m_{tot}$ ).

Structures	$\Delta E_{tot}$ (eV)	$E_{ad}$ (eV)	HOMO (eV)	LUMO (eV)	Gap (eV)	$d^{\text{C}-\text{Cu}_{42}\text{Zn}_{13}}$ (Å)	$d^{\text{O}-\text{Cu}_{42}\text{Zn}_{13}}$ (Å)	$d^{\text{H}-\text{Cu}_{42}\text{Zn}_{13}}$ (Å)	$m_{tot}$ ( $\mu_B$ )
$\text{CHCO}/\text{Cu}_{42}\text{Zn}_{13}^{\text{ICO}}$									
Set A									
15	1.39		-4.16	-4.10	0.06	2.88	1.89	5.03	1
2	0.66		-3.96	-3.91	0.05	2.05	2.19	2.82	1
22	0.60		-4.02	-3.97	0.05	1.99	3.70	2.73	1
1	0.41		-3.97	-3.90	0.07	2.10	3.50	2.79	1
19	0.41		-3.97	-3.91	0.07	2.10	3.29	2.76	1
29	0.39		-3.96	-3.92	0.04	2.01	2.41	2.80	1
13	0.26		-3.98	-3.93	0.05	2.03	2.16	2.84	1
23	0.22		-4.05	-3.99	0.06	1.95	3.70	2.74	1
20	0.22		-4.09	-4.02	0.07	1.95	3.74	2.69	1
7	0.07		-3.94	-3.91	0.04	2.09	3.71	2.70	1
3	0.03		-3.97	-3.90	0.07	2.11	3.55	2.78	1
27	0.03		-3.96	-3.90	0.06	2.10	3.68	2.79	1
8	0.03		-3.98	-3.91	0.07	2.10	3.79	2.75	1
16	0.02		-3.99	-3.92	0.07	2.10	3.79	2.75	1
21	0.00		-3.97	-3.91	0.05	2.10	3.76	2.74	1
Set B									
29	0.44	-1.44	-3.96	-3.93	0.04	2.01	2.31	2.81	1
19	0.41	-1.47	-3.98	-3.92	0.06	2.10	3.30	2.78	1
1	0.39	-1.49	-3.98	-3.91	0.07	2.10	3.37	2.78	1
15	0.37	-1.51	-4.02	-3.96	0.05	2.01	2.09	2.79	1
20	0.31	-1.57	-4.11	-4.04	0.07	1.94	3.74	2.68	1
13	0.29	-1.59	-3.99	-3.94	0.05	2.01	2.18	2.83	1
23	0.29	-1.59	-4.08	-4.01	0.07	1.94	3.73	2.68	1
22	0.21	-1.67	-3.93	-3.90	0.03	2.12	3.80	2.79	1
2	0.21	-1.67	-3.93	-3.90	0.03	2.12	3.79	2.79	1
7	0.04	-1.84	-3.95	-3.92	0.03	2.09	3.72	2.75	1
8	0.04	-1.84	-4.00	-3.92	0.07	2.10	3.72	2.76	1
27	0.02	-1.86	-3.98	-3.92	0.06	2.09	3.72	2.75	1
16	0.02	-1.86	-4.00	-3.93	0.07	2.09	3.71	2.75	1
3	0.02	-1.87	-3.99	-3.92	0.07	2.10	3.71	2.76	1
21	0.00	-1.88	-3.98	-3.93	0.05	2.09	3.73	2.75	1

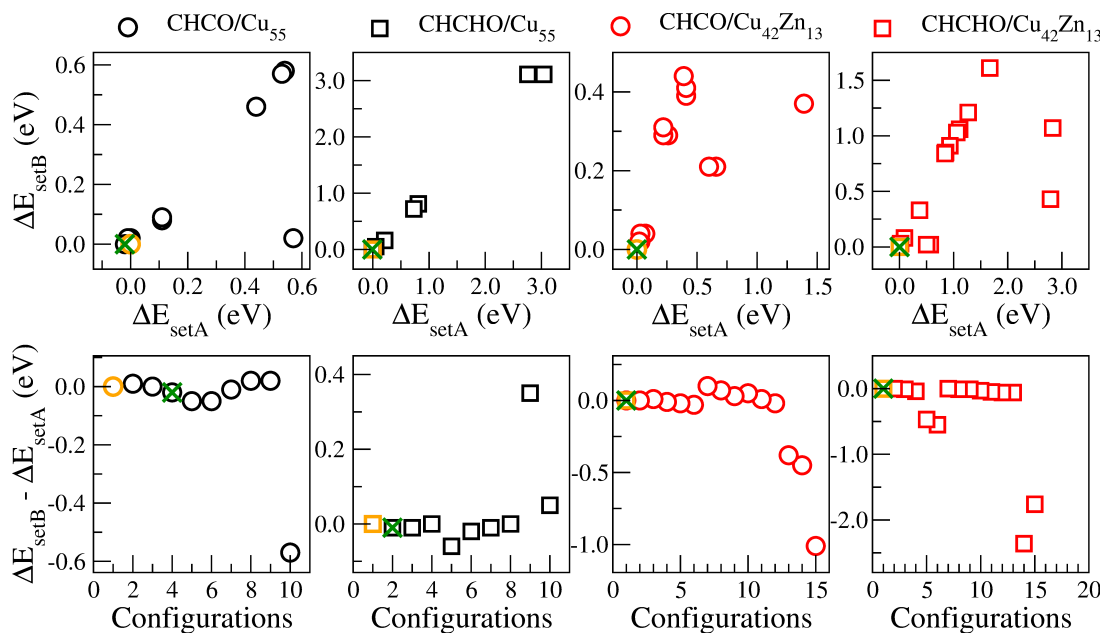
Source: Own authorship.

Table 11 – Comparison between set of parameters A and B CHCHO adsorbed on  $\text{Cu}_{42}\text{Zn}_{13}^{\text{ICO}}$  clusters. Relative energy ( $\Delta E_{tot}$ ); adsorption energy ( $E_{ad}$ ); highest occupied molecular orbital (HOMO); lowest unoccupied molecular orbital (LUMO); HOMO-LUMO gap (Gap); minimum bond distance of C to  $\text{Cu}_{42}\text{Zn}_{13}$  ( $d^{\text{C}-\text{Cu}_{42}\text{Zn}_{13}}$ ); minimum bond distance of O to  $\text{Cu}_{42}\text{Zn}_{13}$  ( $d^{\text{O}-\text{Cu}_{42}\text{Zn}_{13}}$ ); minimum bond distance of H to  $\text{Cu}_{42}\text{Zn}_{13}$  ( $d^{\text{H}-\text{Cu}_{42}\text{Zn}_{13}}$ ); total magnetic moment ( $m_{tot}$ ).

Structures	$\Delta E_{tot}$ (eV)	$E_{ad}$ (eV)	HOMO (eV)	LUMO (eV)	Gap (eV)	$d^{\text{C}-\text{Cu}_{42}\text{Zn}_{13}}$ (Å)	$d^{\text{O}-\text{Cu}_{42}\text{Zn}_{13}}$ (Å)	$d^{\text{H}-\text{Cu}_{42}\text{Zn}_{13}}$ (Å)	$m_{tot}$ ( $\mu_B$ )
<b>CHCHO/<math>\text{Cu}_{55}^{\text{ICO}}</math></b>									
<b>Set A</b>									
12	2.83		-4.12	-4.06	0.06	2.85	1.86	3.00	2
15	2.79		-3.95	-3.90	0.05	3.06	2.03	3.35	2
4	1.67		-4.16	-4.03	0.13	1.93	1.94	2.63	0
14	1.27		-4.05	-3.95	0.10	2.05	2.06	1.79	0
1	1.11		-4.13	-4.04	0.08	2.03	3.87	2.25	0
19	1.06		-4.02	-3.94	0.08	2.00	2.44	1.70	0
3	0.93		-4.15	-4.08	0.07	2.00	3.85	1.86	0
24	0.85		-4.14	-4.03	0.11	2.01	3.77	1.80	0
18	0.84		-4.16	-4.06	0.10	2.01	3.86	1.84	0
23	0.57		-3.97	-3.89	0.08	2.05	2.05	2.74	0
28	0.50		-4.13	-4.02	0.11	1.91	1.89	2.60	0
11	0.37		-4.00	-3.95	0.05	2.04	1.97	2.74	0
16	0.09		-4.02	-3.96	0.06	2.05	1.96	2.73	0
27	0.02		-4.00	-3.90	0.11	2.06	1.96	2.76	0
8	0.00		-4.00	-3.91	0.09	2.07	1.94	2.71	0
<b>Set B</b>									
4	1.61	-1.93	-4.11	-3.99	0.13	1.95	1.98	1.96	0
14	1.21	-2.33	-4.07	-3.97	0.10	2.04	2.05	1.79	0
12	1.07	-2.46	-4.05	-3.97	0.07	2.01	2.08	1.74	0
1	1.06	-2.48	-4.14	-4.05	0.08	2.04	3.93	2.01	0
19	1.03	-2.50	-4.03	-3.95	0.08	2.02	2.28	1.70	0
3	0.91	-2.62	-4.17	-4.10	0.07	2.00	3.77	1.80	0
24	0.85	-2.68	-4.16	-4.05	0.11	2.01	3.76	1.79	0
18	0.84	-2.69	-4.18	-4.07	0.11	2.00	3.77	1.79	0
15	0.43	-3.10	-4.14	-4.00	0.14	1.94	1.89	2.65	0
11	0.33	-3.20	-4.01	-3.97	0.04	2.04	1.97	2.74	0
16	0.08	-3.46	-4.04	-3.98	0.05	2.04	1.95	2.73	0
27	0.03	-3.51	-4.03	-3.91	0.11	2.06	1.96	2.75	0
23	0.02	-3.51	-4.03	-3.91	0.11	2.06	1.96	2.75	0
28	0.02	-3.51	-4.07	-3.98	0.09	2.04	1.93	2.70	0
8	0.00	-3.53	-4.02	-3.93	0.10	2.07	1.94	2.71	0

Source: Own authorship.

Figure 25 – Comparison for set of parameters A and B for CHCO and CHCHO adsorbed on  $\text{Cu}_{55}^{\text{ICO}}$  and  $\text{Cu}_{42}\text{Zn}_{13}^{\text{ICO}}$ . Circle orange and **X** green highlight the lowest energy structure obtained by set A and B, respectively.



Source: Own authorship.

## APPENDIX B – CLIMBING IMAGE-NUDGED BAND ELASTIC CALCULATIONS USING FHI-AIMS PACKAGE

For CI-NEB calculation within FHI-aims, the following files are mandatory. The optimized coordinates for the initial and final geometries, the control.in file, and the chain.in file. Below is an example for control.in and chain.in files. For more details, we direct you to the FHI-aims manual.

Figure 26 – Example for the control.in file for CI-NEB calculations.

```
#control.in
#
# Physical model
xc                pbe
charge            0.0
spin              collinear
default_initial_moment hund
relativistic      atomic_zora scalar
vdw_correction_hirshfeld

# SCF convergence
      occupation_type      gaussian 0.0010

#   ini_linear_mixing      2
#   # ini_linear_mix_param  0.01
#       mixer              pulay
#       n_max_pulay        8
#       charge_mix_param   0.10

sc_accuracy_rho      1E-5
sc_accuracy_eev      1E-3
sc_accuracy_etot     1E-6
sc_accuracy_forces   1E-4

sc_iter_limit        500
KS_method             scalapack

#relax_geometry      trm 2E-3
compute_forces       .true.
final_forces_cleaned .true.
```

Source: Own authorship.

Figure 27 – Example for the chain.in file for CI-NEB calculations.

```
run_aims mpirun -np 40 /dados/software/fhi-aims/aims.071914_7.scalapack.mpi.x
method neb
neb_spring_constant 10.0
force_thres 0.15
climb_mode 1
use_climb true
climb_thres 0.05
global_optimizer false
interpolated_climb true
optimizer FIRE
climb_global_optimizer false
climb_optimizer FIRE
restart true
initial_file ini.in
final_file fin.in
n_images 12
```


Source: Own authorship.



## APPENDIX C – SUPPLEMENTARY DATA: CHAPTER 3

This appendix provides the adsorption energy behavior for the complete set of adsorbed configurations calculated using PBE functional related to the discussion of Chapter 3. To obtain complementary information direct to OCAMPO-RESTREPO, V. K.; ZIBORDI-BESSE, L.; DA SILVA, J. L. F. *Ab initio* investigation of the atomistic descriptors in the activation of small molecules on 3d transition-metal 13-atom clusters: The example of H<sub>2</sub>, CO, H<sub>2</sub>O, and CO<sub>2</sub>. **The Journal of Chemical Physics**, v. 151, p. 214301, 2019, <https://doi.org/10.1063/1.5125769> [115].

Figure 28 – Permission request process to re-use published material in the Chapter 3.



Home | Help | Live Chat | Vivianne Ocampo-Restrepo

---



**Ab initio investigation of the atomistic descriptors in the activation of small molecules on 3d transition-metal 13-atom clusters: The example of H<sub>2</sub>, CO, H<sub>2</sub>O, and CO<sub>2</sub>**

Author: Vivianne K. Ocampo-Restrepo, Larissa Zibordi-Besse, Juarez L. F. Da Silva  
 Publication: Journal of Chemical Physics  
 Publisher: AIP Publishing  
 Date: Dec 7, 2019

*Rights managed by AIP Publishing.*

Thank you for your order.

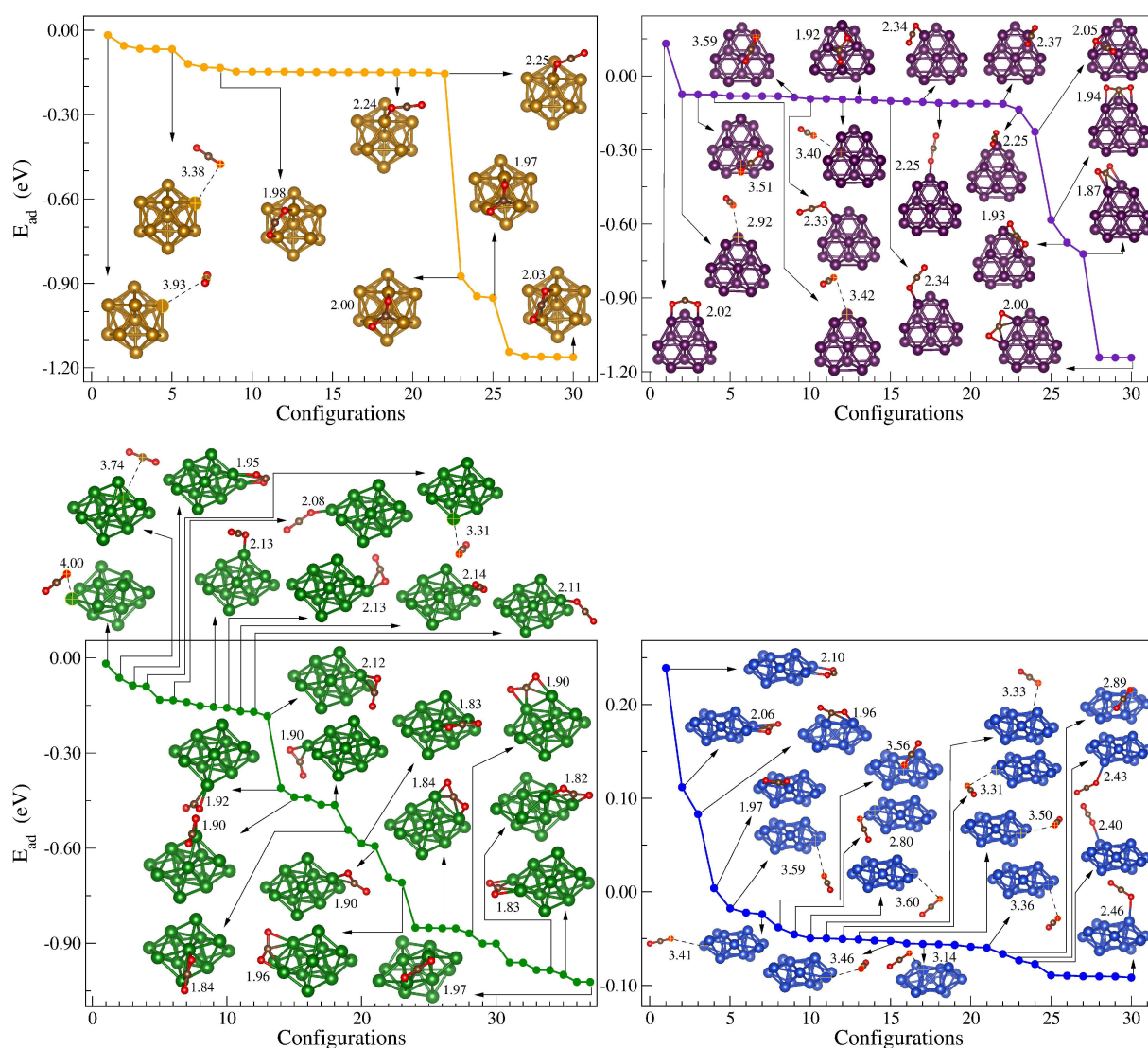
This Agreement between Vivianne Ocampo-Restrepo ("You") and AIP Publishing ("AIP Publishing") consists of your license details and the terms and conditions provided by AIP Publishing and Copyright Clearance Center.

<span style="font-size: 0.8em;">✔</span> Licensed Content	<span style="font-size: 0.8em;">📄</span> Order Details
<p><b>Licensed Content Publisher</b>      AIP Publishing</p> <p><b>Licensed Content Publication</b>      Journal of Chemical Physics</p> <p><b>Licensed Content Title</b>      Ab initio investigation of the atomistic descriptors in the activation of small molecules on 3d transition-metal 13-atom clusters: The example of H<sub>2</sub>, CO, H<sub>2</sub>O, and CO<sub>2</sub></p> <p><b>Licensed Content Author</b>      Vivianne K. Ocampo-Restrepo, Larissa Zibordi-Besse, Juarez L. F. Da Silva</p>	<p><b>Type of Use</b>      Thesis/Dissertation</p> <p><b>Requestor type</b>      Author (original article)</p> <p><b>Format</b>      Print and electronic</p> <p><b>Portion</b>      Photograph/Image</p> <p><b>Number of Photographs/Images</b>      11</p> <p><b>Will you be translating?</b>      No</p>

1. You agree to include the following copyright and permission notice with the reproduction of the Material: "Reprinted from [FULL CITATION], with the permission of AIP Publishing." For an article, the credit line and permission notice must be printed on the first page of the article or book chapter. For photographs, covers, or tables, the notice may appear with the Material, in a footnote, or in the reference list.

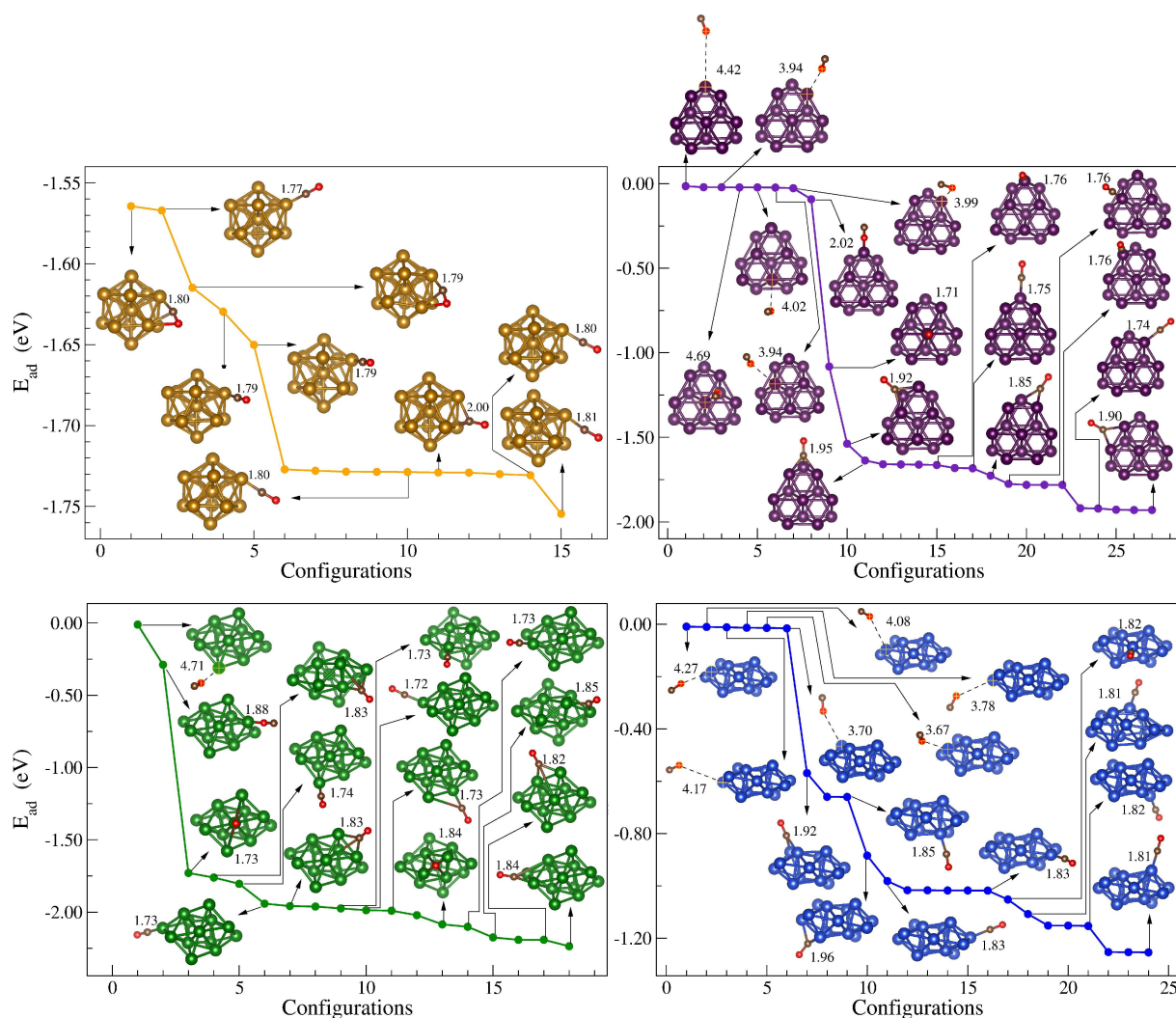
Source: Content from <https://www.copyright.com/> accessed on January (2022).

Figure 29 – Adsorption structures of  $\text{CO}_2/\text{TM}_{13}$ . Here is presented all the representative structures studied in relation to their adsorption energy. The number close to the structure is the minimum distance in Å from one atom of the molecule to one atom of the cluster. The dashed lines are used to represent the long-range interaction between molecule and cluster.



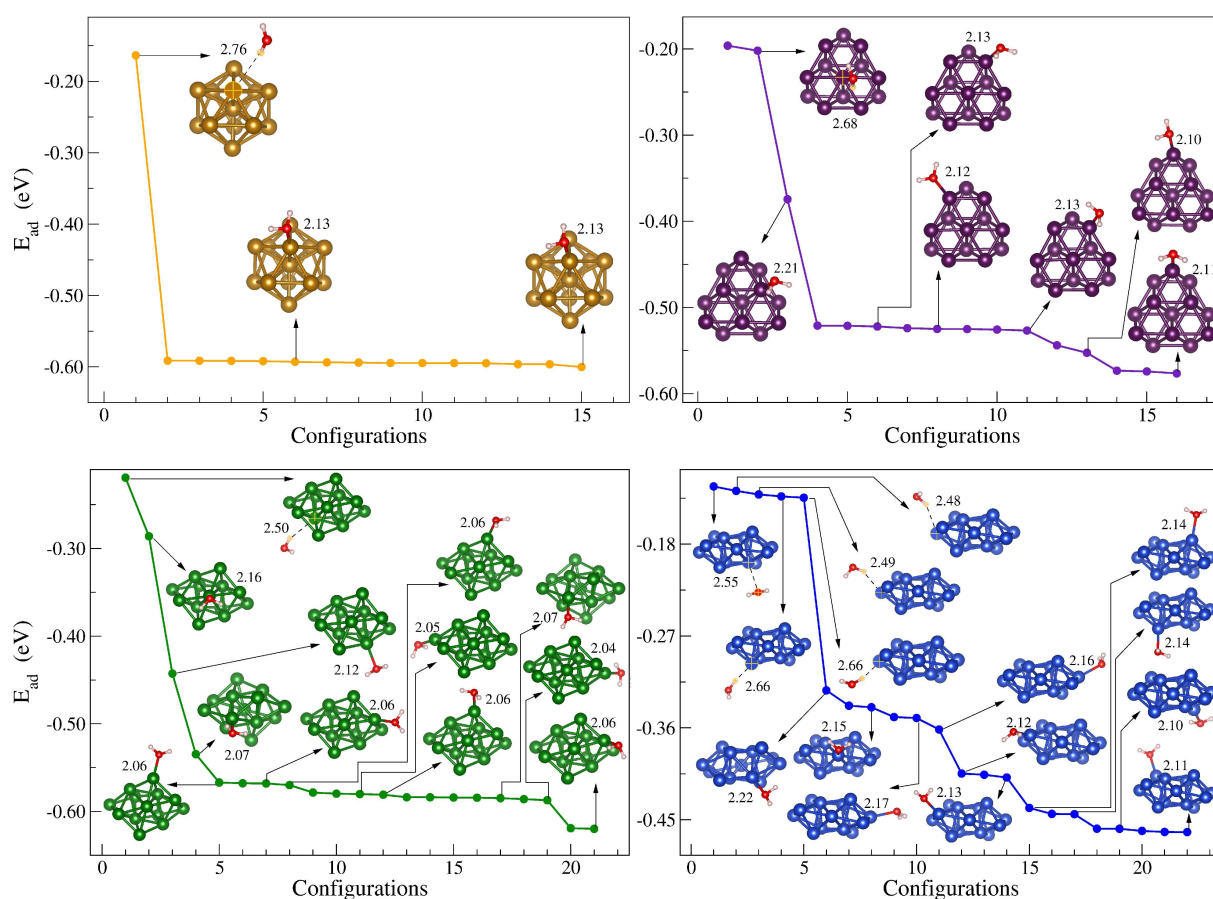
Source: Adapted from OCAMPO-RESTREPO, V. K.; ZIBORDI-BESSE, L.; DA SILVA, J. L. F. *The Journal of Chemical Physics*, v. 151, p. 214301, 2019 [115].

Figure 30 – Adsorption structures of CO/TM<sub>13</sub>. Here is presented all the representative structures studied in relation to their adsorption energy. The number close to the structure is the minimum distance in Å from one atom of the molecule to one atom of the cluster. The dashed lines are used to represent the long-range interaction between molecule and cluster.



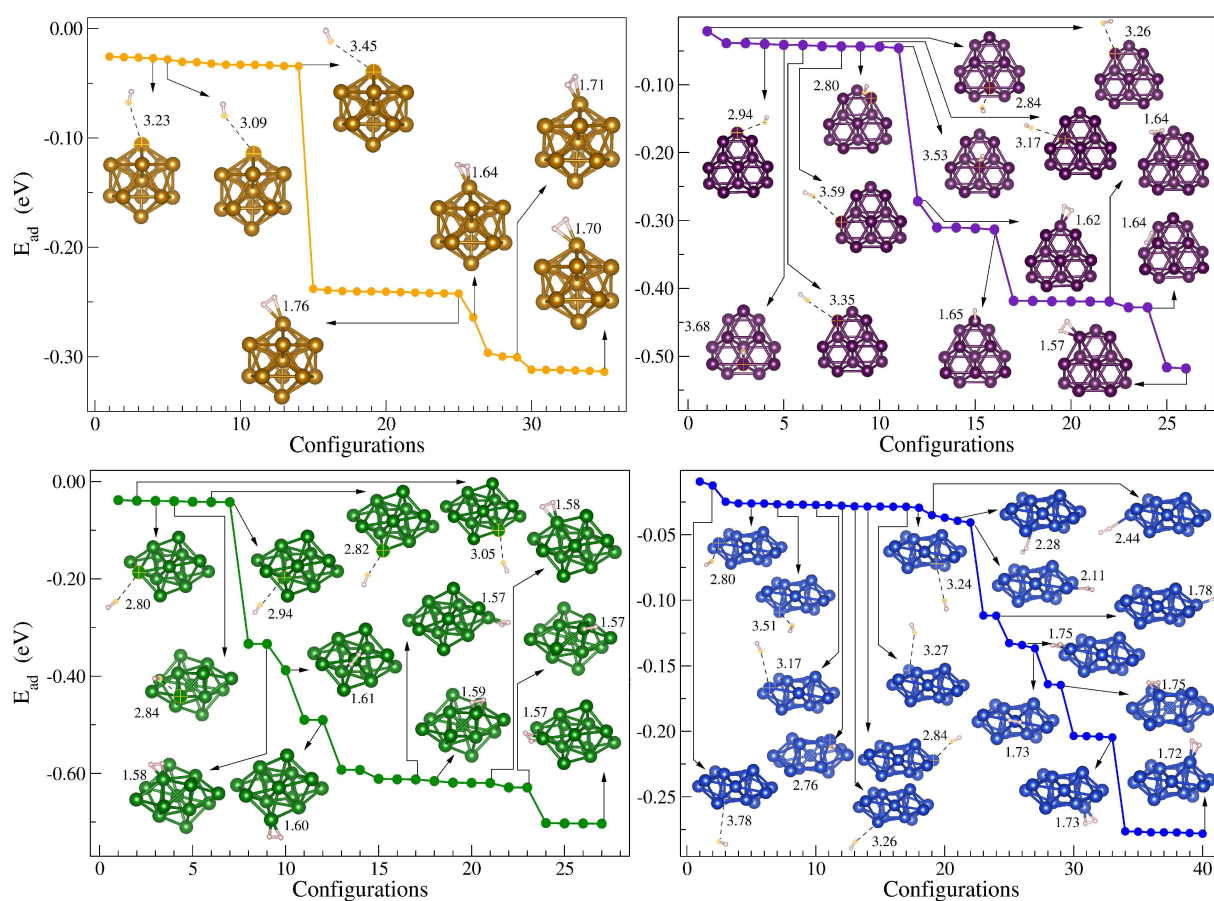
Source: Adapted from OCAMPO-RESTREPO, V. K.; ZIBORDI-BESSE, L.; DA SILVA, J. L. F. *The Journal of Chemical Physics*, v. 151, p. 214301, 2019 [115].

Figure 31 – Adsorption structures of  $\text{H}_2\text{O}/\text{TM}_{13}$ . Here is presented all the representative structures studied in relation to their adsorption energy. The number close to the structure is the minimum distance in Å from one atom of the molecule to one atom of the cluster. The dashed lines are used to represent the long-range interaction between molecule and cluster.



Source: Adapted from OCAMPO-RESTREPO, V. K.; ZIBORDI-BESSE, L.; DA SILVA, J. L. F. *The Journal of Chemical Physics*, v. 151, p. 214301, 2019 [115].

Figure 32 – Adsorption structures of  $H_2/TM_{13}$ . Here is presented all the representative structures studied in relation to their adsorption energy. The number close to the structure is the minimum distance in Å from one atom of the molecule to one atom of the cluster. The dashed lines are used to represent the long-range interaction between molecule and cluster.

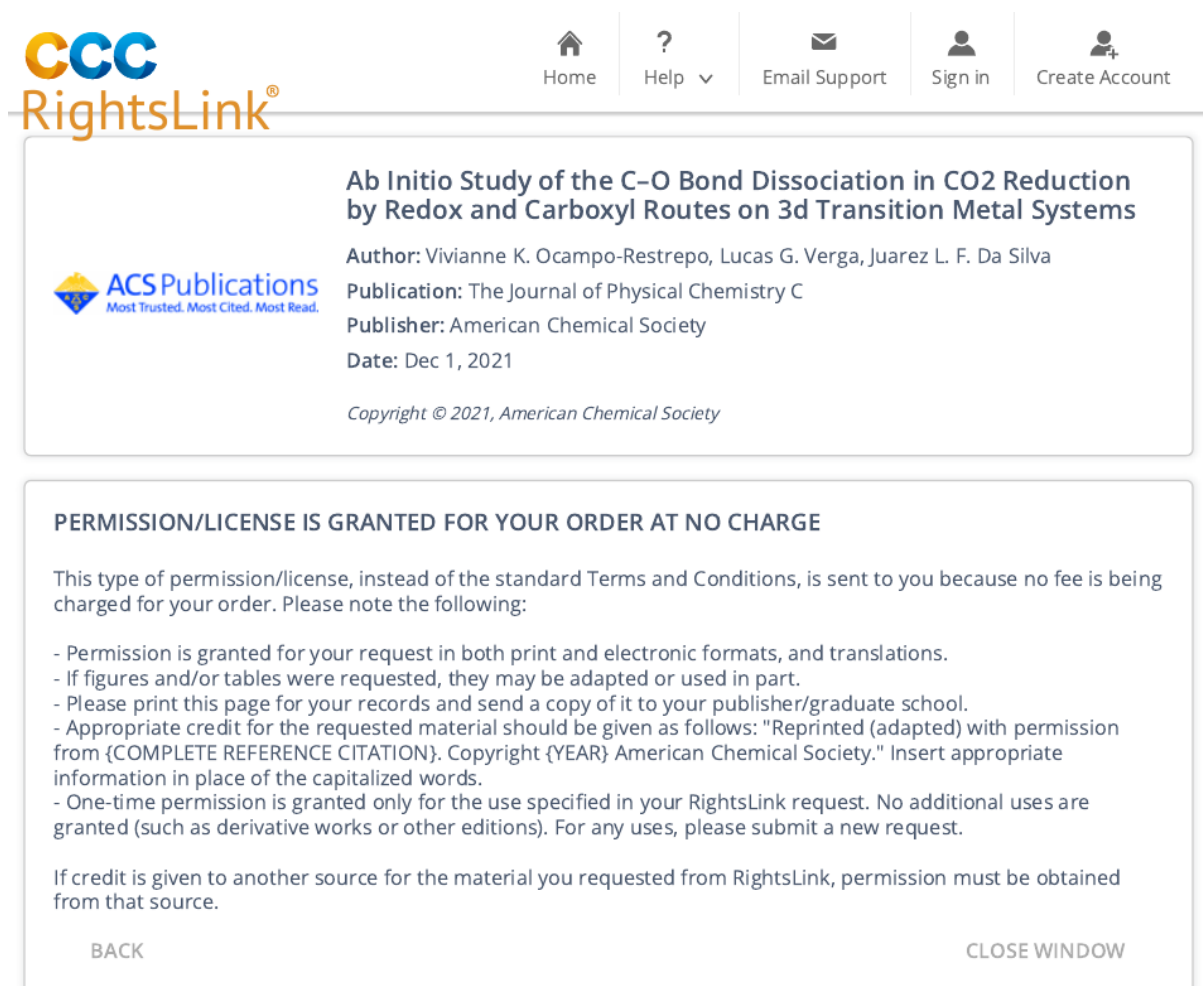


Source: Adapted from OCAMPO-RESTREPO, V. K.; ZIBORDI-BESSE, L.; DA SILVA, J. L. F. *The Journal of Chemical Physics*, v. 151, p. 214301, 2019 [115].

## APPENDIX D – SUPPLEMENTARY DATA: CHAPTER 4

This appendix provides additional results for all the potential energy profiles found and all transition-states scaling (TSS) relations explored related to the discussion of Chapter 4. To obtain complementary information of the complete set of structures calculated as well as their properties direct to OCAMPO-RESTREPO, V. K.; VERGA, L. G.; DA SILVA, J. L. F. *Ab initio* study of the C–O bond dissociation in CO<sub>2</sub> reduction by redox and carboxyl routes on 3d transition-metal systems. **The Journal of Physical Chemistry C**, v. 125, n. 48, p. 26296-26306, 2021, <https://doi.org/10.1021/acs.jpcc.1c05468> [148].

Figure 33 – Permission request process to re-use published material in the Chapter 4.



The screenshot shows the CCC RightsLink interface. At the top, there are navigation icons for Home, Help, Email Support, Sign in, and Create Account. The main content area displays the following information:

**Ab Initio Study of the C–O Bond Dissociation in CO<sub>2</sub> Reduction by Redox and Carboxyl Routes on 3d Transition Metal Systems**

Author: Vivianne K. Ocampo-Restrepo, Lucas G. Verga, Juarez L. F. Da Silva  
 Publication: The Journal of Physical Chemistry C  
 Publisher: American Chemical Society  
 Date: Dec 1, 2021

Copyright © 2021, American Chemical Society

**PERMISSION/LICENSE IS GRANTED FOR YOUR ORDER AT NO CHARGE**

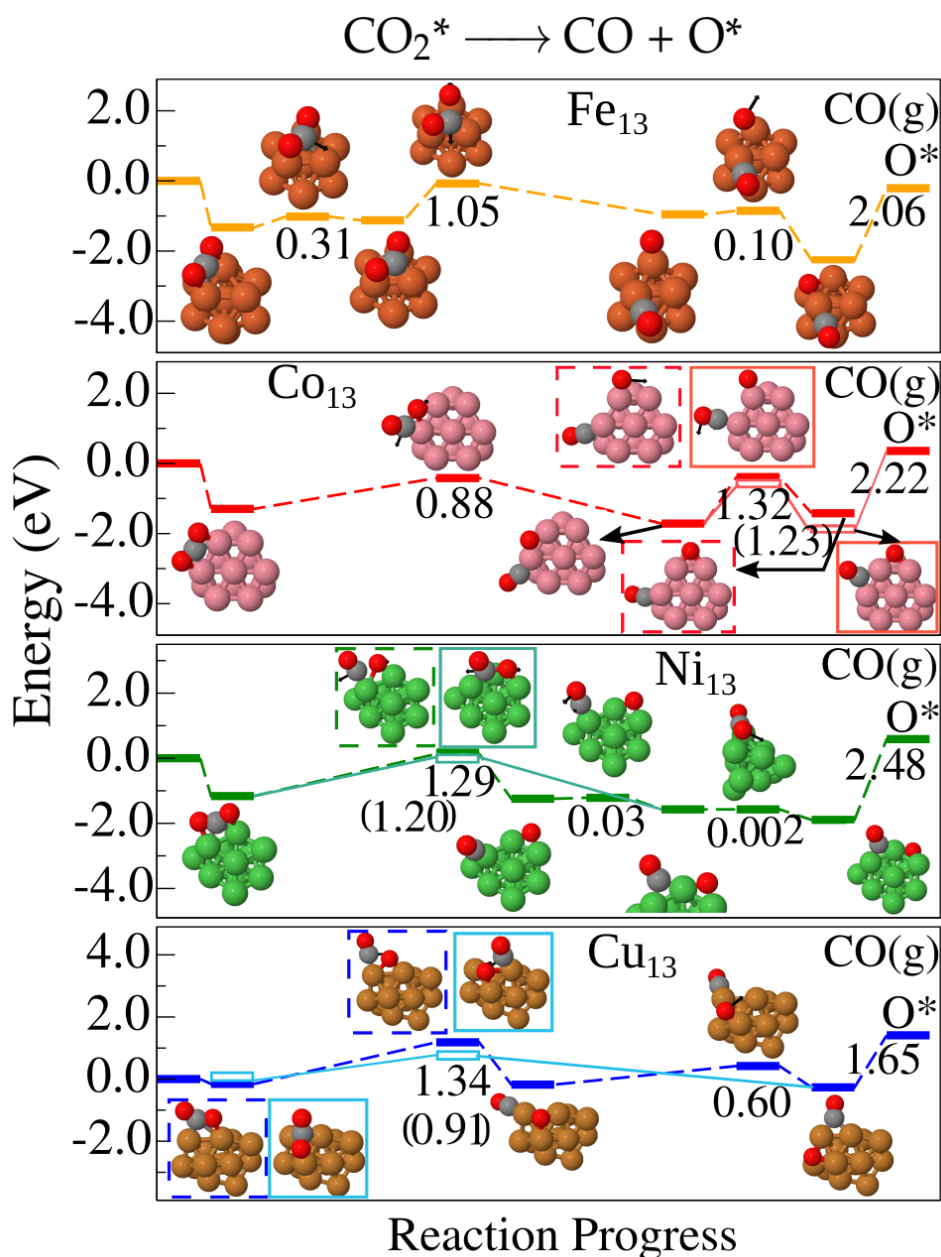
This type of permission/license, instead of the standard Terms and Conditions, is sent to you because no fee is being charged for your order. Please note the following:

- Permission is granted for your request in both print and electronic formats, and translations.
- If figures and/or tables were requested, they may be adapted or used in part.
- Please print this page for your records and send a copy of it to your publisher/graduate school.
- Appropriate credit for the requested material should be given as follows: "Reprinted (adapted) with permission from {COMPLETE REFERENCE CITATION}. Copyright {YEAR} American Chemical Society." Insert appropriate information in place of the capitalized words.
- One-time permission is granted only for the use specified in your RightsLink request. No additional uses are granted (such as derivative works or other editions). For any uses, please submit a new request.

If credit is given to another source for the material you requested from RightsLink, permission must be obtained from that source.

BACK CLOSE WINDOW

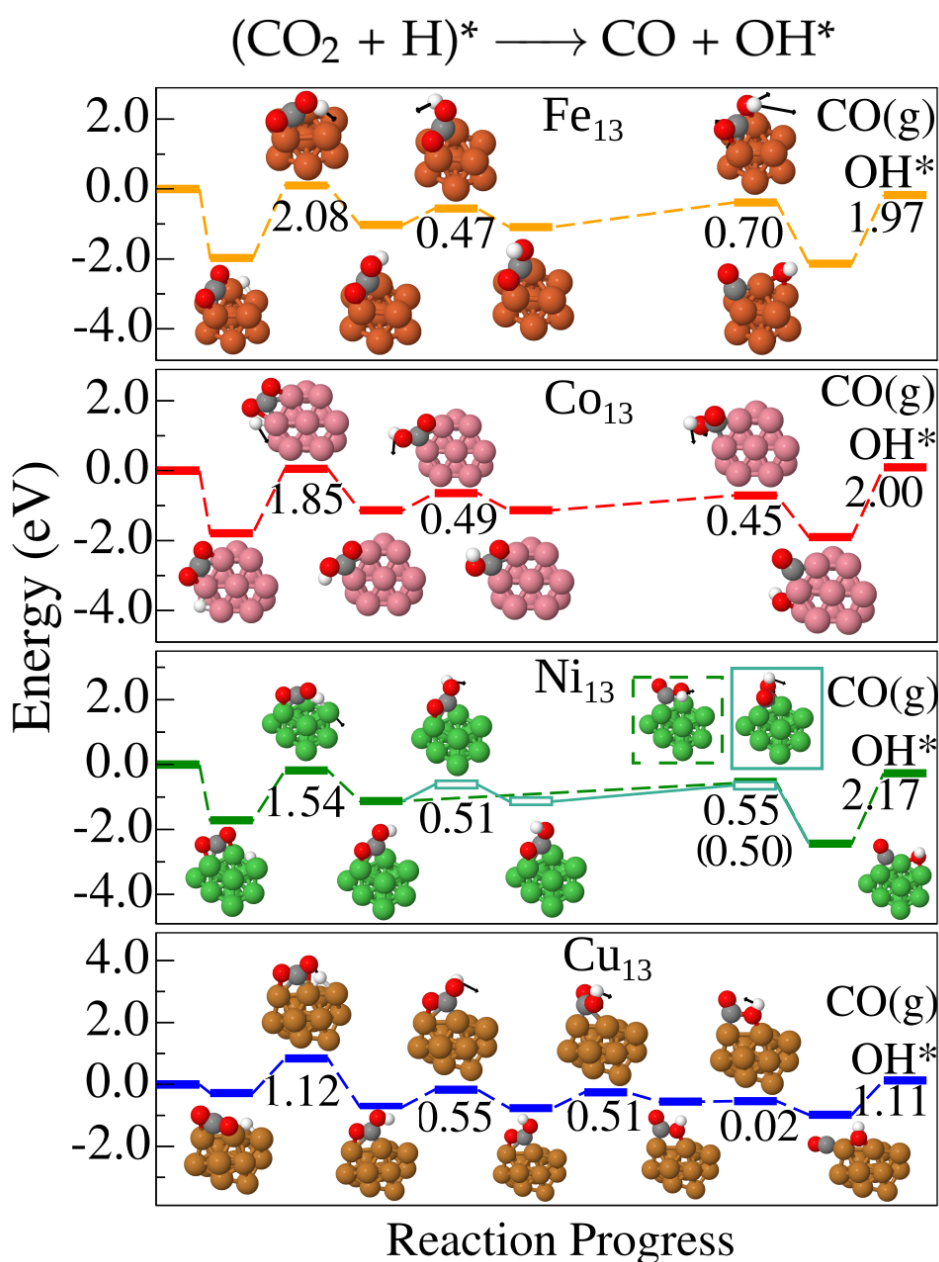
Figure 34 – Potential energy profiles for  $\text{CO}_2^* \longrightarrow \text{CO} + \text{O}^*$ . The energy reference for redox path is the total energies sum of  $\text{TM}_{13}$  with  $\text{CO}_2$ . For comparison purposes, common transition-states are aligned. All intermediates and transition-state structures are under and over the boxes, respectively. For each transition-state, black arrows indicate the vibrational movement along the reaction coordinate. The number under transitions-states are the activation energies,  $E_a$ , for solid boxes paths connected by dashed lines, and in parenthesis are the values for the alternative paths represented by open boxes connected by solid lines. The CO desorption energy is the number throughout the last step. When two structures are possible, we highlight them with a dashed square for the solid boxes paths and a solid square for the open boxes paths.



Source: Reprinted with permission from OCAMPO-RESTREPO, V. K.; VERGA, L. G.; DA SILVA, J. L. F. *The Journal of Physical Chemistry C*, v. 125, n. 48, p. 26296-26306, 2021 [148]. Copyright © 2021, American Chemical Society.

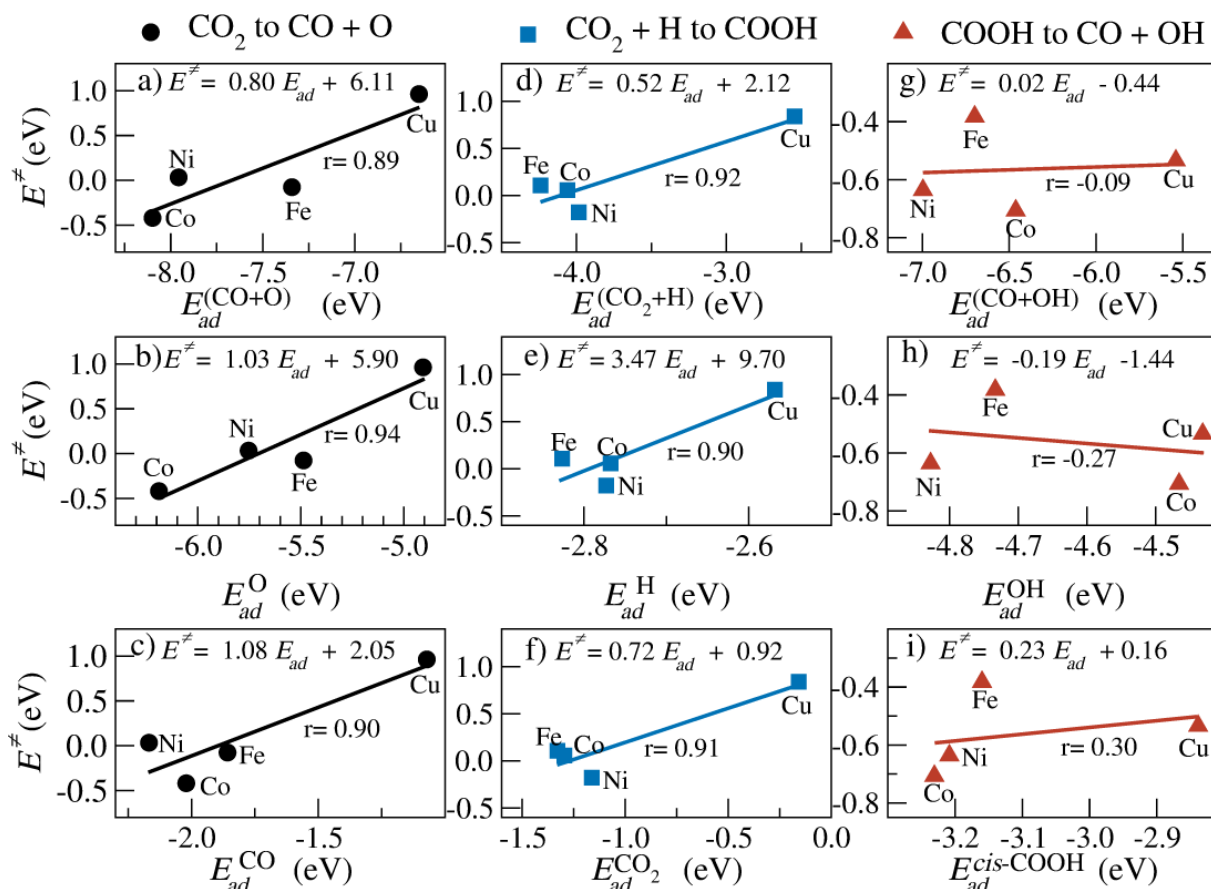


Figure 35 – Potential energy profiles for  $(\text{CO}_2 + \text{H})^* \longrightarrow \text{CO} + \text{OH}^*$  on  $\text{TM}_{13}$ . The energy reference for carboxyl path is the total energies sum of  $\text{TM}_{13}$ ,  $\text{CO}_2$ , and  $\text{H}$ . For comparison purposes, common transition-states are aligned. All intermediates and transition-state structures are under and over the boxes, respectively. For each transition-state, black arrows indicate the vibrational movement along the reaction coordinate. The number under transitions-states are the activation energies,  $E_a$ , for solid boxes paths connected by dashed lines, and in parenthesis are the values for the alternative paths represented by open boxes connected by solid lines. The  $\text{CO}$  desorption energy is the number throughout the last step. When two structures are possible, we highlight them with a dashed square for the solid boxes paths and a solid square for the open boxes paths.



Source: Reprinted with permission from OCAMPO-RESTREPO, V. K.; VERGA, L. G.; DA SILVA, J. L. F. *The Journal of Physical Chemistry C*, v. 125, n. 48, p. 26296-26306, 2021 [148]. Copyright © 2021, American Chemical Society.

Figure 36 – TSS relations for all the processes studied.  $E^\ddagger$  is the transition-state energy as a function of the adsorption energies ( $E_{ad}$ ).

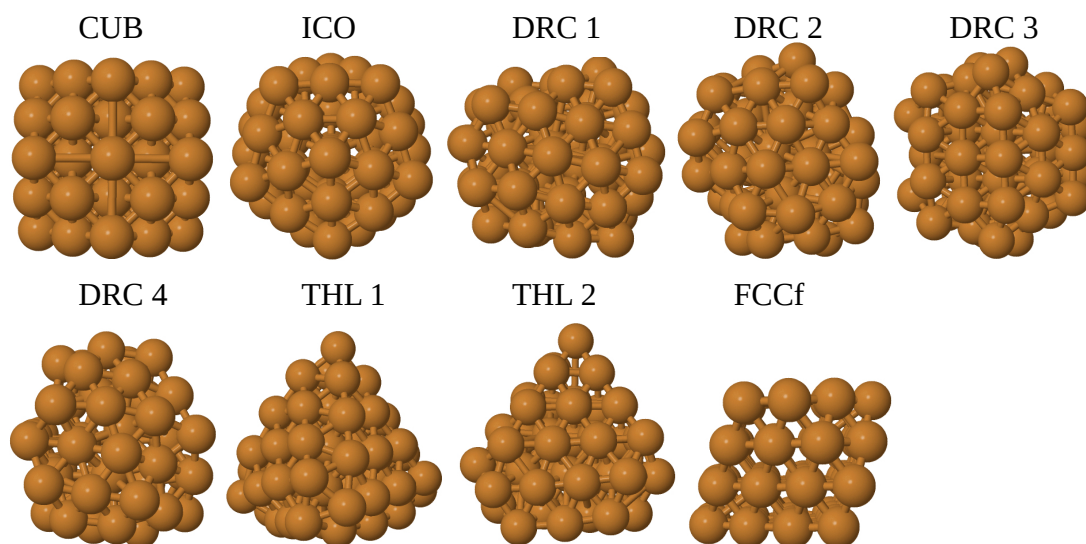


Source: Adapted with permission from OCAMPO-RESTREPO, V. K.; VERGA, L. G.; DA SILVA, J. L. F. **The Journal of Physical Chemistry C**, v. 125, n. 48, p. 26296-26306, 2021 [148]. Copyright © 2021, American Chemical Society.

## APPENDIX E – SUPPLEMENTARY DATA: CHAPTER 5

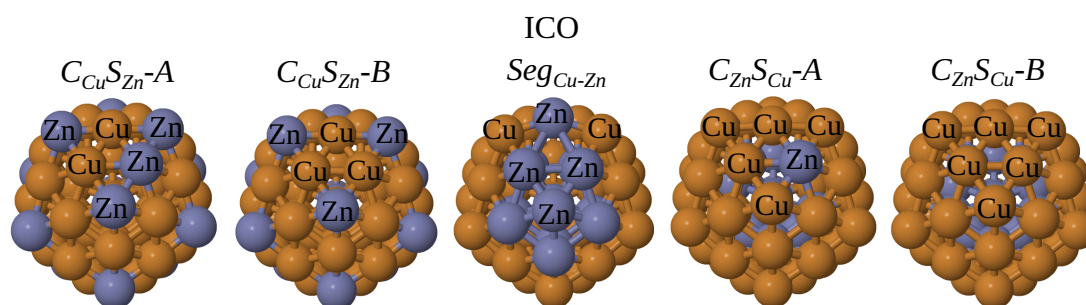
This appendix contains additional data related to the clusters models used, the values for solvation correction, and the liquid-phase correction adopted for discussion of Chapter 5. This manuscript is in progress and expected to be published in the year 2022. At the moment, the authors for this study are OCAMPO-RESTREPO, V. K.; VERGA, L. G.; DA SILVA, J. L. F. The permissions for re-use and adapting the material for this thesis will be requested.

Figure 37 –  $\text{Cu}_{55}$  clusters models. Structures with high and low-symmetry were included, namely: icosahedron (ICO), cuboctahedron (CUB), disordered reduced-core (DRC), that includes models with 7 to 11 atoms in the core, tetrahedral-like models (THL), and a fragment of the FCC structure (FCCf) [1].



Source: Own authorship.

Figure 38 –  $\text{Cu}_{42}\text{Zn}_{13}$  ICO clusters models. Core-shell type core Cu-rich,  $C_{\text{Cu}}S_{\text{Zn}}$ ; core-shell type core Zn-rich,  $C_{\text{Zn}}S_{\text{Cu}}$ ; and segregated cluster,  $Seg_{\text{Cu-Zn}}$ .



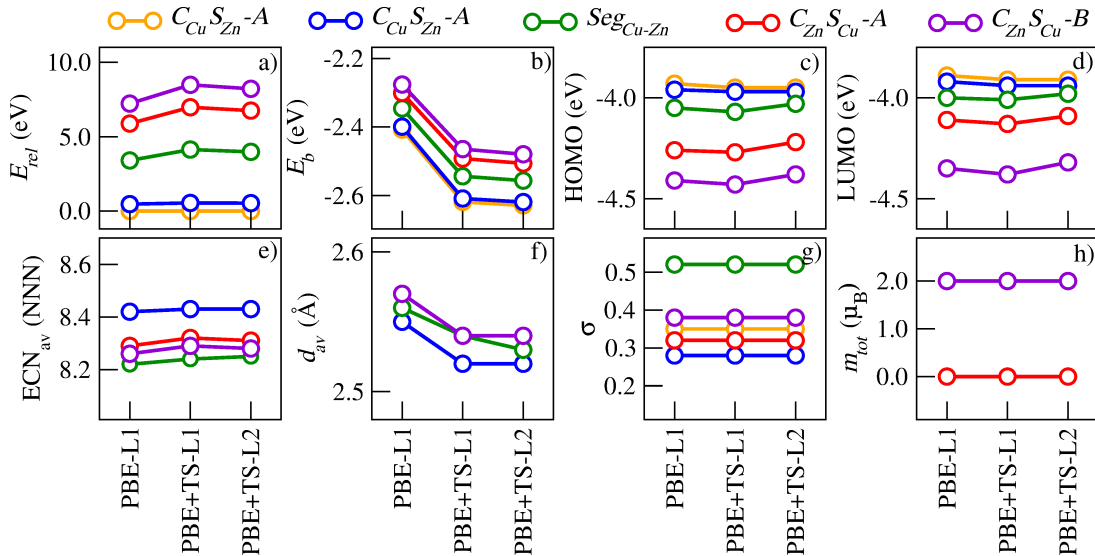
Source: Own authorship.

Table 12 – Comparison of energetic, structural, and electronic properties for  $\text{Cu}_{55}^{\text{ICO}}$  clusters using PBE, PBE with van der Waals corrections, TS or D3 approaches, and different levels of numerical atomic orbitals wave functions, namely *light1*, 2, 3, and plane-waves, PW. Binding energy per atom ( $E_b$ ); average effective coordination number ( $\text{ECN}_{av}$ ); average interatomic distance ( $d_{av}$ ); total magnetic moment ( $m_{tot}$ ).

$\text{Cu}_{55}^{\text{ICO}}$		$E_b$ (eV/atom)	$\text{ECN}_{av}$ (NNN)	$d_{av}$ (Å)	$m_{tot}$ ( $\mu_B$ )
This study	PBE- <i>light1</i>	-2.89	8.38	2.52	3.00
	PBE+TS- <i>light1</i>	-3.10	8.40	2.50	3.00
	PBE- <i>light2</i>	-2.91	8.38	2.52	3.00
	PBE+TS- <i>light2</i>	-3.12	8.39	2.50	3.00
	PBE+TS- <i>light3</i>	-3.13	8.39	2.50	3.00
Literature[1]	PBE-PW	-2.87	8.38	2.52	3.00
	PBE+D3-PW	-3.12	8.40	2.49	3.00

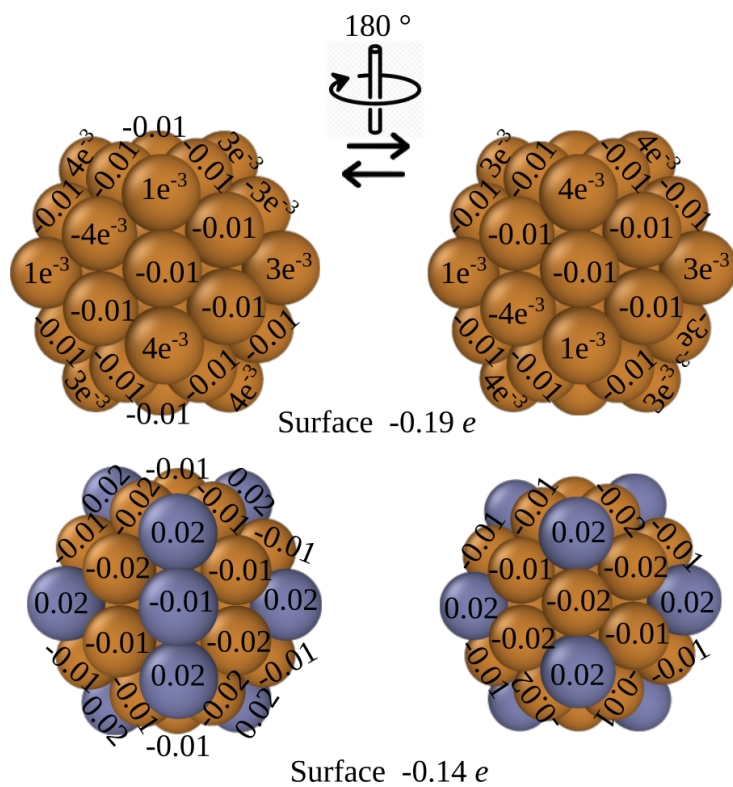
Source: Own authorship.

Figure 39 – Properties of  $\text{Cu}_{42}\text{Zn}_{13}$  ICO clusters models as a function of basis function and functionals. Energetic, structural, and electronic properties for  $\text{Cu}_{42}\text{Zn}_{13}$  ICO clusters. Relative energy ( $\Delta E_{tot}$ ); binding energy ( $E_b$ ); highest occupied molecular orbital (HOMO); lowest unoccupied molecular orbital (LUMO); HOMO-LUMO gap (Gap); average effective coordination number ( $\text{ECN}_{av}$ ); average interatomic distance ( $d_{av}$ ); Radius (Radius); chemical order parameter ( $\sigma$ ); total magnetic moment ( $m_{tot}$ ).



Source: Own authorship.

Figure 40 – Superficial charge distribution analysis for  $\text{Cu}_{55}$  and  $\text{Cu}_{42}\text{Zn}_{13}$  clusters.



Source: Own authorship.

## Gas-phase Molecules

The free energies of gas-phase molecules was obtained by:

$$G_i^{gp} = E_{tot} + E_{energy}^{ZPE} + E_{vib} - TS_{vib} \quad (\text{E.1})$$

All the  $E_{energy}^{ZPE}$  and  $TS$  calculated at 298 K and 1.00 atm. The Table 13 provides the data obtained for gas-phase species involved in this study.

Table 13 – Values of  $E_{energy}^{ZPE}$ ,  $E_{vib}$ , and  $TS$  for all gas-phase species involved in this study. All energetic quantities are given in eV.

Species	$E_{energy}^{ZPE}$	$E_{vib}$	$TS$
H <sub>2</sub>	0.27	0.00	0.42
H <sub>2</sub> O	0.56	0.00	0.58
C <sub>2</sub> H <sub>4</sub>	1.35	0.01	0.68
CH <sub>3</sub> CHO	1.45	0.03	0.81
CH <sub>3</sub> CH <sub>2</sub> OH	2.10	0.04	0.84

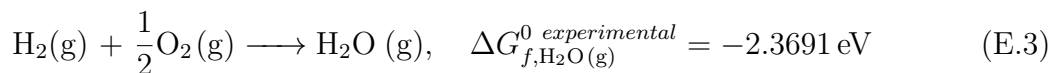
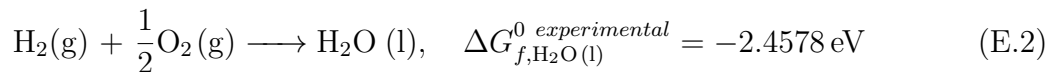
Table 14 – Solvation corrections according to the functional group of the chemical species [3].

Functional Group	Solvation Correction (eV)
RCO*	-0.10
OH*	-0.50
ROH*	-0.38
OR*	-0.25

## Liquid-phase Corrections: example for H<sub>2</sub>O

Bellow the approach employed to include the correction for liquid molecules like water, acetaldehyde, and ethanol. We add the correction to the equation (E.1) for each case.

*i)* Obtain the experimental standard Gibbs free energy of formation for the species in the gas and liquid phase. We employed the values at 298 K and 1.00 atm [18].



*ii)* Perform the difference between  $\Delta G_{f,\text{H}_2\text{O}(\text{l})}^0 \text{ experimental}$  and  $\Delta G_{f,\text{H}_2\text{O}(\text{g})}^0 \text{ experimental}$ .

$$\Delta G_{f,\text{H}_2\text{O}(l)}^{0 \text{ experimental}} - \Delta G_{f,\text{H}_2\text{O}(g)}^{0 \text{ experimental}} = -0.0887 \text{ eV} \quad (\text{E.4})$$

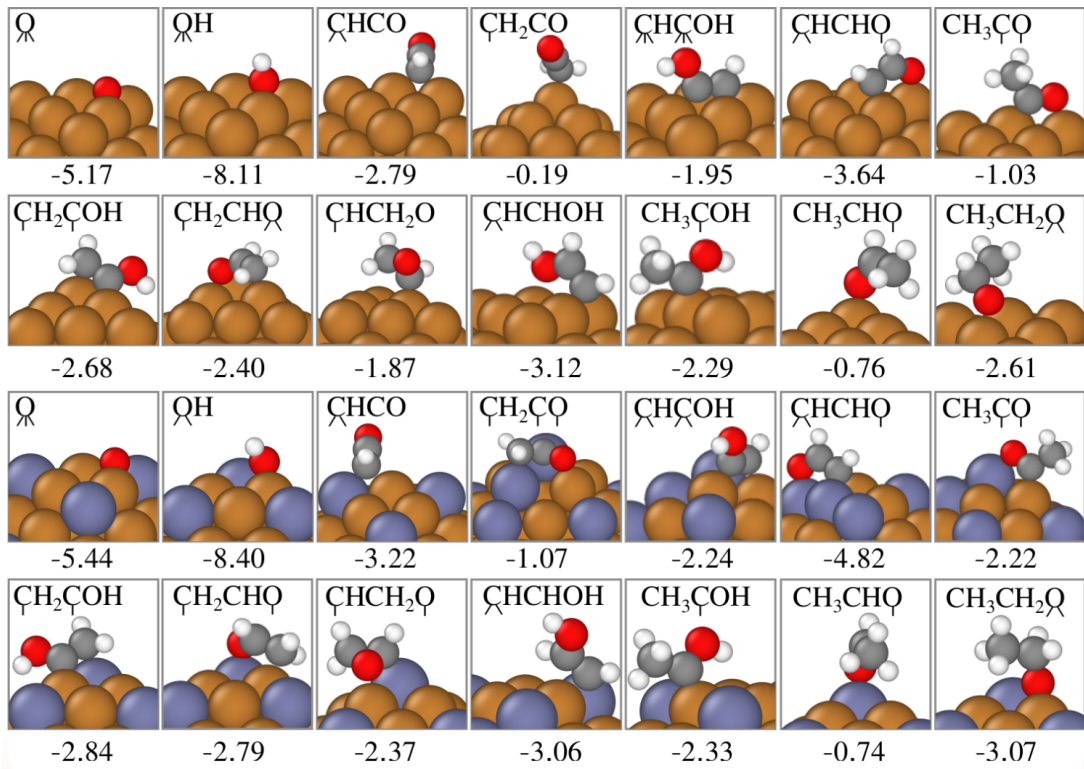
equivalent to:

$$G_{\text{H}_2\text{O}(l)} - G_{\text{H}_2\text{O}(g)} = -0.0887 \text{ eV} \quad (\text{E.5})$$

ii) Solve to get  $G_{\text{H}_2\text{O}(l)}$  and use the  $G_{\text{H}_2\text{O}(g)}$  coming from DFT calculations, equation (E.1).

$$G_{\text{H}_2\text{O}(l)} = E_{tot} + ZPE + E_{vib} - TS_{vib} - -0.0887 \text{ eV} \quad (\text{E.6})$$

Figure 41 – Lowest energy structures for the adsorbed species involving in the reaction paths to ethanol and ethylene on  $\text{Cu}_{55}$  and  $\text{Cu}_{42}\text{Zn}_{13}$  clusters. The number below each structure is the adsorption energy ( $E_{ad}$ ) in eV.



Source: Own authorship.